Technological University Dublin
ARROW@TU Dublin

Doctoral | Engineering

2011-4

Numerical Prediction of the Haemodynamic Impact of Coronary Stent Implantation

Jonathan Murphy
Technological University Dublin

Follow this and additional works at: https://arrow.tudublin.ie/engdoc

 Part of the Engineering Science and Materials Commons, and the Medicine and Health Sciences Commons

Recommended Citation

Murphy, J. (2011) *Numerical Prediction of the Haemodynamic Impact of Coronary Stent Implantation.* Doctoral Thesis. Technological University Dublin. doi:10.21427/D7532J

This Theses, Ph.D is brought to you for free and open access by the Engineering at ARROW@TU Dublin. It has been accepted for inclusion in Doctoral by an authorized administrator of ARROW@TU Dublin. For more information, please contact arrow.admin@tudublin.ie, aisling.coyne@tudublin.ie, vera.kilshaw@tudublin.ie.

Numerical Prediction of the Haemodynamic Impact of Coronary Stent Implantation

Jonathan B. Murphy B.Eng.

Department of Mechanical Engineering
Dublin Institute of Technology, Bolton St.
Dublin 1
Ireland

April 2011

Thesis Submitted in Partial Fulfilment of the Requirements for the Degree of

DOCTOR of PHILOSOPHY

ABSTRACT

Arterial restenosis limits the effectiveness of coronary stenting. Restenosis is caused by excessive tissue growth which is stimulated by arterial injury and alterations to the arterial WSS. The altered WSS results from stent-induced disturbances to the natural haemodynamics of the artery. Recent numerical studies have predicted only minor differences in altered WSS between different stent designs using a commonly employed threshold assessment technique. While it is possible that there are only minor differences, it is more likely that the assessment technique is incapable of fully elucidating the altered WSS created by stent implantation. This thesis proposes a methodology that involves a more complete level of investigation into the stent-induced alterations to the WSS by incorporating the full suite of WSS-based variables: WSS, WSS gradient (WSSG), WSS angle gradient (WSSAG) and oscillatory shear index (OSI). Each of these variables highlights a different type of alteration to the arterial WSS that could lead to excessive tissue growth. The four variables are analysed quantitatively and qualitatively using statistical methods to assess the effect of the stent implantation. The methodology is applied to three stents with contrasting designs: the Palmaz-Schatz (PS), the Gianturco-Roubin II (GR-II) and the Bx-Velocity (Bx) stents. From the results, the stents are ranked (best to worst) for WSS: GR-II, PS, Bx (Cohen's d: -0.01, -0.613), for WSSG: PS, Bx, GR-II (d: 0.159, 0.764), for WSSAG: PS GR-II Bx (d: 0.213, 0.082), and for OSI: PS, GR-II, Bx (d: 0.315, 0.380). The proposed method of analysis is shown to elucidate the alterations to the WSS created by the stents to a far greater level than with the previously used threshold technique. This method of stent assessment could be utilised to minimise WSS alterations at the design stage of future bare metal, as well as permanent and bioabsorbable drug-eluting coronary stents.

DECLARATION

I certify that this thesis which I now submit for examination for the award of Doctor of Philosophy, is entirely my own work and has not been taken from the work of others, save and to the extent that such work has been cited and acknowledged within the text of my work.

This thesis was prepared according to the regulations for postgraduate study by research of the Dublin Institute of Technology and has not been submitted in whole or in part for another award in any Institute.

The work reported on in this thesis conforms to the principles and requirements of the Institute's guidelines for ethics in research.

The Institute has permission to keep, lend or copy this thesis in whole or in part, on condition that any such use of the material of the thesis is duly acknowledged.

Signature  Date 16/06/11

ACKNOWLEDGEMENTS

Firstly, I would like to thank my supervisor Dr. Fergal Boyle for his advice and encouragement. The time and effort he has invested in guiding this work and assisting with this thesis is greatly appreciated. Special recognition must also go to my parents for their continuous support, which has managed to withstand over two decades of education.

This work has been supported by the Department of Mechanical Engineering in DIT, Bolton St. and the Irish Research Council for Science Engineering and Technology (IRCSET). Special thanks also go to Dr. David Kennedy and Dr. Steve Jerrams for their parts in supporting this work.

The technical assistance and advice of the following people over the duration of this work is gratefully acknowledged: Alan Brereton and Ian Campbell from DIT for their excellent IT support, Dr. Caitriona Lally from DCU for her helpful advice on stents and modelling of the artery wall, Derek Sweeney from IDAC and Ian Hamill from the UK technical support team for their help with ANSYS software, John Milroy for his invitation to Boston Scientific, and also Johnson and Johnson and COOK for their technical information which helped with development of the stent models. Special thanks must also go to the nameless reviewers from the journals of Computers in Biology and Medicine, Biorheology and Cardiovascular Engineering and Technology whose invaluable comments and advice greatly enhanced the quality of this work.

Finally, I'd like to thank my colleagues and friends over the years, without whose endless advice and support this thesis would have been finished in half the time.

NOMENCLATURE

Scalars (English)

A	Surface area [m^2]
C	Constitutive equation coefficient (Chap. 3); Coefficient of prolapse (Chap. 5)
D	Diameter [m]
H	Distance between plates [m] (Chap. 3); Strut height [m] (Chap. 4)
I	Indicator function
K	Kurtosis; Constitutive equation coefficient (Chap. 3)
L	Distance between stent struts [m]; Length [m] (Chap. 5, App. B)
N	Number of data points
P	Static pressure [Pa]
R	Radius [m]
T	Period of cardiac cycle [s]
U	Freestream velocity [m/s]
V	Control volume [m^3]
X	Prolapse reduction factor
a	Directional cosine; Fourier series constant (Chap. 5); Control volume coefficient (App. A)
b	Fourier series constant
e	Number of mesh faces
f	Axial strut length [m]
h	Axial distance between struts [m]
ip	Number of integration points
m	Mass [kg]
n	Number of vertices; Number of integration points (App. A); Number of surrounding nodes (App. A, C)
p	Number of timesteps
q	Carreau model constant
r	Radial coordinate [m]; Strut radius [m] (Chap. 4)
s	Control surface [m^2]
t	Time [s]

Δt	Timestep [s]
u, v, w	Component of velocity vector in the Cartesian x, y and z directions respectively [m/s]
x, y, z	Cartesian coordinates [m]
x	Axial distance along flat plate [m] (App. B)
y	Vertical height from flat plate [m] (App. B)

Scalars (Greek)

Φ	Variable value; Component of the WSS vector (App. C)
α, β, Ω	Angles of rotation [rad]
β	Specified blend factor (App. A)
γ	Shear strain rate [1/s]
η	Dimensionless Parameter
δ	Maximum tissue protrusion depth [m]; Boundary layer thickness [m] (App. B)
λ	Second coefficient of viscosity [kg/m.s]; Carreau model constant (Chap. 5)
μ	Fluid dynamic viscosity [kg/m.s]; Statistical Mean (Chap. 5, 6, 7)
ν	Fluid kinematic viscosity [m^2/s]
π	3.14159...
ρ	Density [kg/m^3]
σ	Standard deviation
ϕ	Angular difference [rad]; Fourier series constant (Chap. 5); Variable value (Chap. 5, App. A)
χ	Shear strain [rad]
Ψ	Percentage difference
φ	Flow separation parameter

Vectors

$\vec{C}$	Cartesian coordinate

$\vec{F}$	Force [N]
$\vec{L}$	Local coordinate
$\vec{V}$	Velocity [m/s^1]
$\vec{a}, \vec{b}$	Random directional vectors
$\vec{g}$	Acceleration due to gravity [m/s^2]
$\vec{i}, \vec{j}, \vec{k}$	Unit vector in the Cartesian x, y and z directions respectively
$\vec{m}, \vec{n}, \vec{l}$	Directional vectors of the local coordinate system, where $\vec{m}$ is the WSS direction, $\vec{n}$ is tangential to the surface and normal to $\vec{m}$ and $\vec{l}$ is the surface normal direction
$\vec{p}, \vec{q}, \vec{r}$	Unit vector in the local m, n and l directions respectively
$\vec{r}$	Directional vector from upwind node (App. A)
$\vec{x}, \vec{y}, \vec{z}$	Directional vectors of the Cartesian coordinate system
$\vec{\varsigma}$	Vorticity [rad/s]
$\vec{\tau}$	Wall shear stress [N/m^2]
$\vec{\omega}$	Angular velocity [rad/s]

Tensors

$\vec{\vec{\delta}}_{ij}$	Kronecker delta function
$\vec{\vec{\varepsilon}}_{ij}$	Strain rate [1/s]
$\vec{\vec{\sigma}}_{ij}$	Fluid total stress [N/m^2]
$\vec{\vec{\tau}}_{ij}$	Viscous stress [N/m^2]

Matrices

A	SVD coefficients
B	SVD known values
U	SVD matrix, orthogonal to V
V	SVD matrix, orthogonal to U
a	Linearised equation set coefficients
b	Known values from previous timesteps
s	SVD diagonal matrix

x	SVD solution
ϕ	Hydrodynamic equations solution

Subscripts

Blasius	Calculated from the Blasius solution
D	Calculated based on diameter, D
N	Reverse flow
P	Forward flow
S	Separation
cl	Centreline
d	Calculated from diameter
e	Entrance
f	Friction
i, j, k, l	Summation indices
ip	Value at integration point
j	Element number (Chap. 5)
m	Mesh
n	Neighbour node; Data point number (Chap. 5, App. B)
o	Node of interest; Outer radius (Chap. 5); Lower bound on viscosity for Carreau model (Chap. 5)
p	Number of timesteps
t	Timestep
u, v, w	Component associated with velocity vector in the Cartesian x, y and z directions respectively
up	Value at upwind node
w	Component at the wall
x, y, z	Component associated with Cartesian x, y and z directions respectively
x	Calculated based on distance, x
Pooled	RMS of values from Stent A and Stent B
Predicted	Calculated by the software
Stent A	Value from Stent A
Stent B	Value from Stent B

ϕ	Value for Variable ϕ
∞	Upper bound on viscosity for Carreau model
1,2,3	Component associated with the principle axes; Component associated with xyz axis (Cartesian system) or mnl axis (local system) (App. C)

Superscripts

i	Node number
m	Mesh number
n	Iteration number
o	Time level
s	Simulation number
T	Transpose
*	Non dimensional
'	Corrected value

Vector and Tensor Notation

$\vec{\nabla}$	Gradient operator
.	Scalar product
$\times$	Cross product
$\otimes$	Dyadic product
·	Tensor product

Abbreviations

ADP	Adenosine Diphosphate
BMS	Bare Metal Stent
Bx	Bx-Velocity
CABG	Coronary Artery Bypass Graft
CAD	Coronary Artery Disease
CE	Conformité Européenne
CFD	Computational Fluid Dynamics
CHD	Coronary Heart Disease
CSA	Cross Sectional Area

DES	Drug-Eluting Stent
EC	Endothelial Cell
ECM	Extracellular Matrix
EES	Everolimus-Eluting Stent
EU	European Union
FDA	Food and Drug Administration
FEA	Finite Element Analysis
FGF	Fibroblast Growth Factor
FSP	Flow Separation Parameter
GR-II	Gianturco-Roubin II
IH	Intimal Hyperplasia
LAD	Left Anterior Descending
LDL	Low Density Lipoproteins
ML	Multilink
MOSI	Modified Oscillatory Shear Index
OSI	Oscillatory Shear Index
PAF	Platelet Activating Factor
PCI	Percutaneous Coronary Intervention
PDGF	Platelet Derived Growth Factor
PES	Paclitaxel-Eluting Stent
PS	Palmaz-Schatz
PTCA	Percutaneous Transluminal Coronary Angioplasty
Re	Reynolds Number
RMS	Root Mean Squared
ROS	Reactive Oxygen Species
SAM	Surface Adherent Monocytes
SES	Sirolimus-Eluting Stent
SVD	Singular Value Decomposition
TIM	Tissue Infiltrating Monocytes
TIMI	Thrombolysis in Myocardial Infarction
TLR	Target Lesion Revascularisation
TNF	Tumor Necrosis Factor
VSMC	Vascular Smooth Muscle Cell
vWf	von Willebrand factor

WSS	Wall Shear Stress
WSSAG	Wall Shear Stress Angle Gradient
WSSG	Wall Shear Stress Gradient

TABLE OF CONTENTS

LIST OF FIGURES

LIST OF TABLES

CHAPTER 1

Introduction

1.1 Background

Cardiovascular diseases are the main cause of death in Europe, accounting for 48% of the mortality or approximately 4.3 million deaths in 2008 [1]. The main forms of cardiovascular disease are coronary heart disease (CHD) and stroke, responsible for 22% and 14% of the total European mortalities respectively in the same year [1]. CHD refers to a failure of the coronary circulation to supply adequate blood flow to the cardiac muscle and surrounding tissue. This coronary circulation failure is most commonly precipitated by the growth of atherosclerotic plaque in the coronary arteries, a condition known as coronary artery disease (CAD).

Implantation of one or more coronary stents is the current state-of-the-art treatment for CAD. Basically, a stent is a metal scaffold inserted into the artery and then, most commonly, expanded by a balloon to restore the blood flow originally restricted by the atherosclerotic plaque. Over two million stents are implanted annually worldwide, with a market value of approximately €4.3 billion ($5.4 billion) in 2009 and a forecast to reach €5.1 billion ($6.5 billion) in 2016 [38].

Unfortunately, the stented artery is susceptible to restenosis, which is a re-blockage of the artery. Restenosis is caused by in-stent tissue growth which is the body's response to stent implantation. Tissue growth in an artery is predominantly

stimulated by arterial injury [27, 103, 109] and by alterations to the arterial wall shear stress (WSS) [9, 13, 35, 52, 55, 56, 58, 59, 72, 92]. In a stented artery, the altered WSS results from stent-induced disturbances to the natural haemodynamics of the artery.

With the advent of powerful high-speed computers, the environment of the stented artery can be simulated using numerical techniques. Computational fluid dynamics (CFD) has recently proved useful to predict the arterial haemodynamics resulting from stent implantation. If the haemodynamic features which lead to restenosis could be predicted, CFD could be utilised to pre-clinically assess coronary stents based on their haemodynamic impact on the artery. However, the numerical methodology employed in several of the most recent attempts [4, 26, 61] found only minor differences in the altered WSS between different stent designs, even though these stents had different *in vivo* restenosis rates.

This thesis proposes a novel stent assessment methodology which provides a greater depth of analysis of the arterial WSS in the stented artery than previously conducted in this field. The methodology incorporates physiologically realistic models of the stented artery, a multi-variable approach to the identification of stent-induced alterations to the arterial WSS, and a robust statistical method of analysis of the predicted variables. The benefits of the proposed methodology over the conventional methods are demonstrated by application to three sample stents.

1.2 Coronary Artery Disease

CAD is a chronic disease which is the result of the slow formation of atherosclerotic plaque in the coronary arteries, generally over a period of decades. As shown in Figure 1-1 the disease is initiated as low-density lipoproteins (LDL), which transport

cholesterol in the blood stream, become oxidised and damage the artery wall. Oxidisation occurs as the LDL come into contact with free radicals in the blood stream, particularly reactive oxygen species (ROS). ROS are oxygen molecules with unpaired valence shell electrons which makes them highly reactive. They are produced naturally in the human body as a by-product of cellular respiration but their numbers can be increased through environmental factors such as cigarette smoking, exposure to X-rays and air pollution [66]. The oxidised LDL become trapped beneath and cause damage to the endothelial cells (ECs) which line the inner artery wall [125].

Specialised white blood cells known as macrophages travel to the site of the damaged ECs to absorb the offending oxidised LDL; these cells migrate through the ECs and situate themselves within the subendothelial layer. Once inside the artery wall the macrophages begin absorbing the oxidised LDL and turn into large foam cells. Messenger particles called cytokines are released from foam cells to attract vascular smooth muscle cells (VSMCs) from deep in the artery wall to the subendothelial layer. The foam cells eventually rupture depositing the oxidised LDL back into the artery wall, attracting more macrophages. This continual cycle leads to the accumulation of cells (foam, VSMCs) in the subendothelial layer forming fatty streaks in the artery. These streaks eventually grow into lesions or plaques narrowing the arteries as shown in Figure 1-2, a condition known as atherosclerosis. Advanced lesions usually form a fibrous cap over the fatty core, which can rupture leading to thrombus formation (blood clots), sudden myocardial infarction (heart attack) and death.

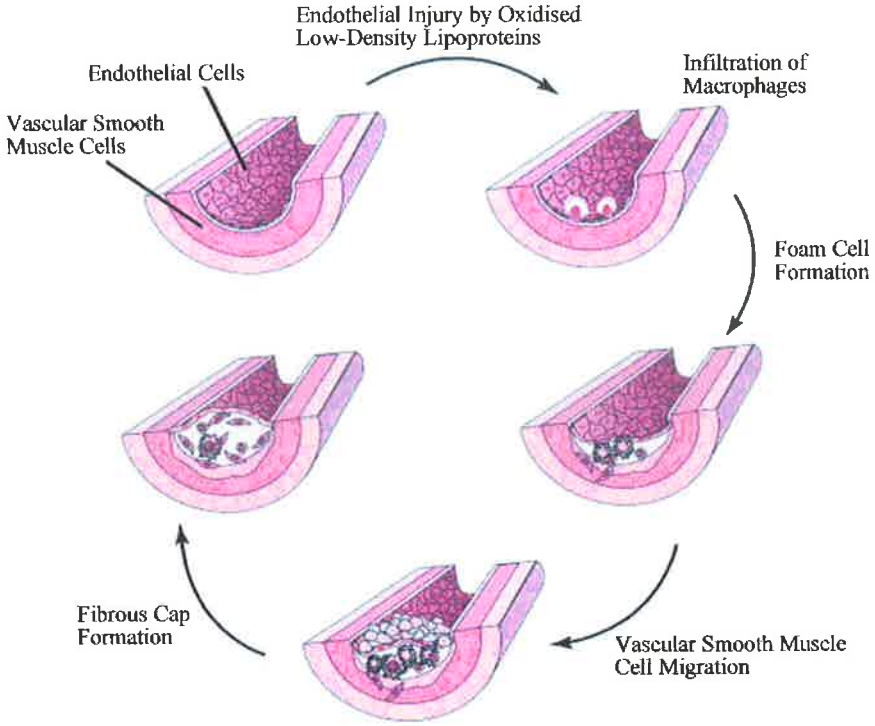

Figure 1-1: The progression of arteriosclerosis in an initially healthy coronary artery. The disease begins with endothelial injury from oxidised LDL and progresses as plaque forms consisting of foam cells and vascular smooth muscle cells (VSMCs). The plaque is finally covered by a fibrous cap (original illustration taken from Huittinen [47]).

Atherosclerosis can be accelerated through various risk factors such as cigarette smoking, high blood pressure, high blood cholesterol, physical inactivity, obesity and diabetes [1]. When coronary arteries become narrowed by more than 50% to 70%, they can no longer meet the increased blood and oxygen demand of the cardiac muscle during exercise or stress. Lack of oxygen to the heart muscle causes chest pain or angina which is usually a warning sign of the presence of significant CAD. Patients with angina are at risk of developing a myocardial infarction if left untreated. Myocardial infarction is the death of the heart muscle precipitated by the complete blockage of a diseased coronary artery by an obstruction, often plaque due to atherosclerosis.

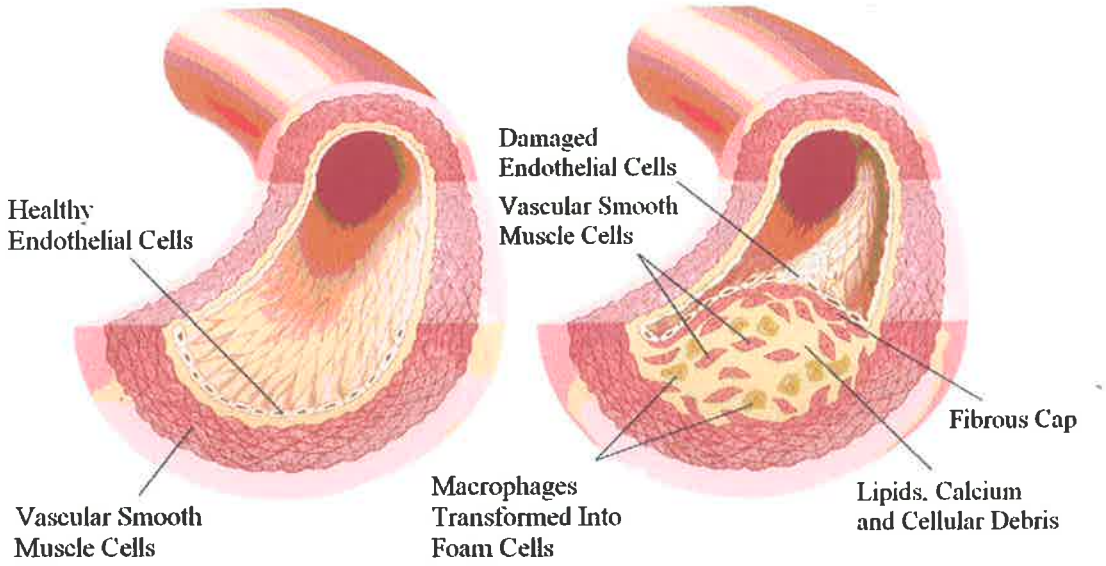

Figure 1-2: Comparison of a healthy artery and an artery with advanced CAD [28].

1.3 Therapeutic Treatments

Due to the major prevalence of CAD, several therapeutic treatments have been developed over the past half century. This section details three of the most popular treatments for CAD.

1.3.1 Coronary Artery Bypass Graft

Traditionally, a coronary artery bypass graft (CABG) was the most popular procedure for the treatment of symptomatic atherosclerosis. The first successful CABG reported in the USA [30] was performed by Dr. R. Favaloro (Cleveland Clinic, USA) in 1967, three years after Dr. V. I. Kolesov (First Leningrad Medical Institute, Russia) performed the first successful CABG in Russia in 1964. A CABG surgery begins by opening the patient's chest with an incision over the sternum, after which the sternum is opened to expose the heart, a procedure known as a median sternotomy. The patient's heart is stopped to allow the surgeon to achieve better technical results. A blood vessel is then harvested from elsewhere in the body and

used to bypass the site of the blockage as shown in Figure 1-3. Originally, the greater saphenous vein from the leg was used as the bypass graft, but now the vessels of choice are the internal mammary arteries from the chest as they are less prone to disease and subsequent re-blockage [37]. Another commonly harvested blood vessel is the radial artery from the forearm which has also shown improved results over vein grafts [137].

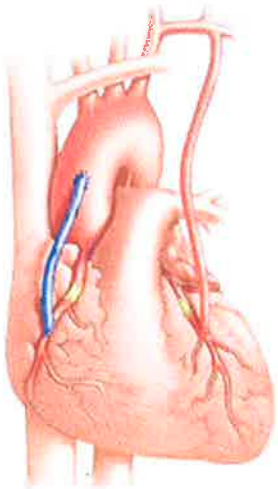

Figure 1-3: Illustration of two CABGs. During a CABG an artery (pink) or vein (blue) is grafted to bypass the site of the arterial blockage (yellow) to restore blood flow to the downstream myocardial muscle and tissue.

A cardiopulmonary bypass is usually provided by a heart-lung machine which maintains the circulation of blood and oxygenation of the body during the operation while the heart is stopped. The heart-lung machine has however been implicated in various complications associated with the CABG operation including adverse cerebral outcomes [128], renal failure [19], and systemic inflammatory response [12]. These complications have lead to a rise in popularity of off-pump procedures, where the bypass grafting is performed whilst the heart is still beating. However, a clinical study [115] comparing on-pump versus off-pump procedures with 2,203 patients revealed that patients in the off-pump group had worse outcomes

at one-year follow-up. A recent meta-analysis [122] of on-pump versus off-pump procedures revealed that off-pump CABG may increase late (>1 year) all-cause mortality by a factor of 1.37 over on-pump CABG.

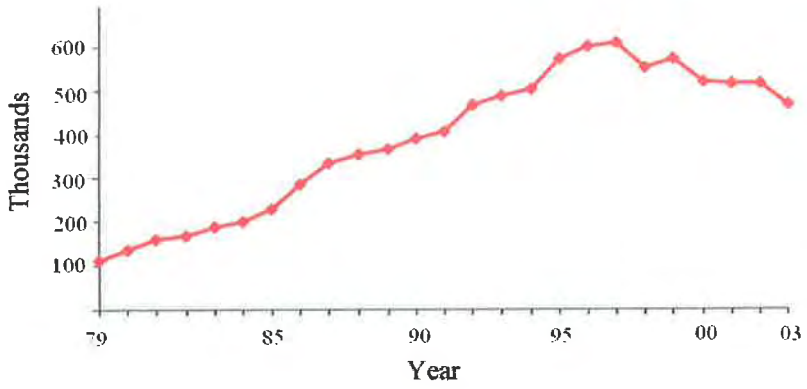

Figure 1-4: The number of CABG procedures (in thousands) conducted per year in the USA from 1979 to 2003 [15].

Reports from the National Centre for Health Statistics [15] in the USA show that the amount of CABG procedures has been declining since the mid-nineties as shown in Figure 1-4. This decline is due to the introduction of percutaneous coronary interventions (PCI).

1.3.2 Percutaneous Transluminal Coronary Angioplasty

The first minimally invasive treatment of atherosclerosis was performed in 1977 by Dr. A. Gruentzig (University Hospital Zurich, Switzerland) [40] and is known as percutaneous transluminal coronary angioplasty (PTCA) or balloon angioplasty, a subset of PCI. During PTCA, a physician guides a long thin tube called a catheter through a patient's arteries, usually entering through the groin or arm, and advances to the plaque site in the coronary artery, under fluoroscopic guidance. The catheter is tipped with an inflatable balloon. At the site of obstruction the balloon is inflated for about 1 minute, compressing the plaque and enlarging the lumen of the coronary artery. Balloon inflation pressures may vary from five atmospheres of pressure [50],

to as much as 20 atmospheres [11].

Although this revolutionary procedure greatly reduced patient trauma, restenosis (defined as >50% re-blockage of the artery) was common with PTCA, with rates as high as 30% - 40% within three to six months of the procedure [46, 95]. A comparative study by the Bypass Angioplasty Revascularisation Investigators (BARI) [124] conducted in 1997 examined the choice of treatment for multivessel disease amongst 1,829 patients. They found that by five years after study entry, 8% of the patients assigned to CABG had undergone additional revascularisation procedures, as compared with 54% of those assigned to PTCA. Restenosis after PTCA most commonly takes the form of elastic recoil of the vessel wall and also vessel contraction known as negative remodelling [75].

Another disadvantage of PTCA is the significant risk posed from weakening of the artery wall. Although the artery would be opened successfully using a balloon, in certain cases the artery would collapse after the balloon was deflated. Acute closure occurs in approximately 4 - 8% of balloon angioplasty procedures within the first 24 hours [21, 23]. When acute closure occurs, it is a medical emergency with many patients requiring emergency CABG. Elastic recoil, negative remodelling and acute closures were virtually eliminated by the introduction of stents in the early 1990s.

1.3.3 Coronary Stenting

Coronary stenting grew directly out of interventional cardiologists' experience with PTCA and acute closures during the 1980s. A coronary stent is an artificial support device used in the coronary artery to keep the artery open. Usually, the stent is mounted on a balloon catheter in a "crimped" or collapsed state. During the stenting

procedure, the balloon is threaded to the site of the blockage and inflated causing the stent to expand and push itself against the inner wall of the coronary artery. This acts as a scaffold to hold the artery open; the balloon is then deflated and removed. By forming a rigid support, the stent can prevent acute closures and also significantly reduces elastic recoil and negative remodelling.

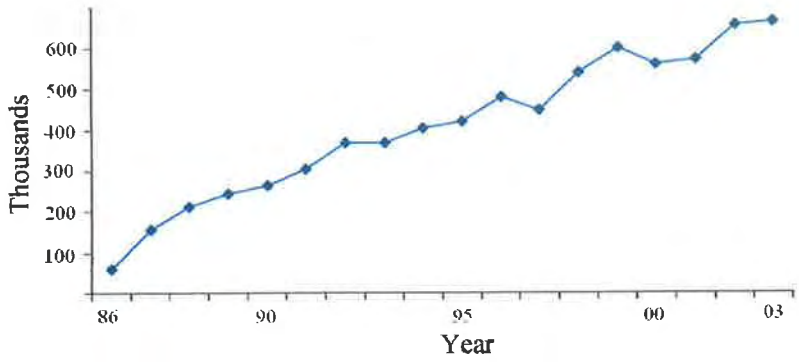

Figure 1-5: The number of PCI procedures conducted (in thousands) per year in the USA from 1986 to 2003 [15].

The first self-expanding stent was inserted into a human coronary artery in 1986 by Dr. J. Puel and Dr. U. Sigwart (Centre Hospitalier Regional Universitaire, France) [116]. The first balloon-expandable stent was developed by Dr. J. Palmaz (University of Texas Health and Science Centre, USA) and Dr. R. Schatz (Brooke Army Medical Centre, USA) in 1989 and approved for use in the USA by the Food and Drug Administration (FDA) in 1994. Approval was based on the results of two clinical trials (BENESTENT-I [112] and STRESS [31]) conducted to compare implantation of Palmaz-Schatz (PS) stents (Cordis, Johnson & Johnson, NJ, USA) to PTCA with short (<15mm) de novo lesions in large vessels (>3mm). The incidence of restenosis in the stented arm of the BENESTENT-I and STRESS trials was 22% and 31.6% respectively, significantly less than in the PTCA group (31% and 42.1% respectively). Over the next decade, a plethora of stent designs emerged as several generations of these bare metal stents (BMSs) were developed. The

growth of stent technology lead to a steady increase in the number of PCIs performed in the USA over the last two decades as shown in Figure 1-5.

While BMSs virtually eliminated the complication of acute artery closure and reduced elastic recoil and negative remodelling, restenosis persisted. Restenosis following stent implantation is mainly due to intimal hyperplasia (IH), which is the proliferation and migration of VSMCs to the inner artery wall where they proceed to narrow the lumen inside the stent. In an intravascular ultrasound study [45] of 142 patients with PS stents, late lumen loss, defined as the cross sectional area (CSA) of the lumen post intervention minus the CSA of the lumen at follow up, was shown to correlate strongly with the amount of tissue growth from IH as shown in Figure 1-6. This study demonstrates that restenosis following stent implantation is primarily due to IH in the lumen.

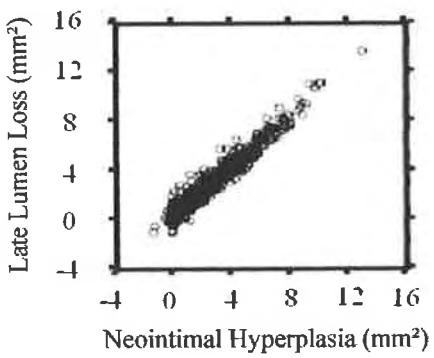

Figure 1-6: Strong correlation between IH and late lumen loss in stented coronary arteries [45].

In recent years, drug-eluting stents (DESs) have been developed to address the problem of IH. A DES typically consists of a BMS platform which has been coated in a formulation of a drug and carrier material. The drugs commonly employed are known to interrupt key cellular processes associated with VSMC proliferation. A proliferating cell undergoes a process known as mitosis, in which it

replicates itself. The drug employed on DESs target mechanisms in the VSMC proliferation cycle to inhibit IH.

To date, clinical evaluation has proven the superiority of DESs for the reduction of restenosis rates compared to BMSs, leading to the regulatory approval of a number of DESs by both the European Union (EU) Conformité Européenne (CE) and the FDA. At present there are five distinct DESs that have received both CE and FDA approval: the first-generation Cypher sirolimus-eluting stent (Cordis) and Taxus Express^2 paclitaxel-eluting stent (Boston Scientific, MA, USA), and the second generation Endeavor zotarolimus-eluting stent (Medtronic Vascular, MN, USA), Xience-V everolimus-eluting stent (Abbott Vascular, CA, USA) and Taxus Liberté paclitaxel-eluting stent (Boston Scientific). First-generation DESs showed a reduction in restenosis rates to less than 10% in equivalency trials against BMSs [18, 20, 39, 76, 77, 106, 107, 120]. However, long-term biocompatibility of these stents has been the source of much concern in recent years due to late (6-12 months) cases of poor neointimal coverage and stent thrombosis [49, 73, 94]. First-generation DESs employ permanent polymer coatings to hold and gradually release the drug into the artery. Due to the fact that most cases of late stent thrombosis occur long after the period of drug release from the DES, it has been widely postulated that permanent polymers may contribute to late adverse events by inhibiting endothelial coverage and inducing late hypersensitivity reactions.

As a result of these observations, biocompatible co-polymer coatings which actively promote healthy neointimal coverage have been employed by second-generation DESs. Furthermore, significant efforts are currently being made to improve the overall biocompatibility of DESs with research in this area currently

centred on the identification and evaluation of biocompatible and fully bioabsorbable stent platforms and coatings, improved mechanisms of drug-delivery and potent therapeutic agents capable of reducing the risk of late stent thrombosis.

BMSs, permanent and bioabsorbable DESs will ultimately always create disturbances to the arterial haemodynamics after implantation leading to altered WSS. This altered WSS has previously been known to encourage IH [55, 56, 64, 72, 92]. As different stents are known to produce different restenosis rates [2, 3, 53, 54, 67], it is reasonable to assume that this may be influenced by different levels of stent-induced alterations to the WSS.

Currently, state-of-the-art numerical investigations into haemodynamics in the stented artery employ three-dimensional (3D) and transient CFD. In most of these investigations the WSS is predicted, as the influence of this variable on IH in the artery has been well established. The wall shear stress gradient (WSSG) is the spatial rate of change of the WSS and is also frequently calculated, as this too is known to influence IH in the artery. The level of altered WSS caused by stent implantation is analysed using threshold values of the WSS ($WSS<0.5\ N/m^2$) and WSSG ($WSSG>200\ N/m^3$), as IH has been found to be more prolific in regions exceeding these thresholds [57, 58, 92]. However, in several studies this "threshold method" has not successfully identified significant differences in altered WSS between the different stents [4, 26, 59, 61, 62]. In these studies, there is evidence to suggest that there may be a difference in the level of altered WSS caused by the different stents and therefore the threshold method is not capable of identifying it.

One such study [59] investigated the haemodynamic effects of a rigid versus a flexible stent in a curved coronary artery. At mean flow, the stented area exposed

to low WSS (<0.5 N/m²) was 99.1 and 103.7 mm² and the stented area exposed to high WSSG (>200 N/m³) was 73.8 and 68.3 mm² for the flexible and rigid stents respectively. These results do not show much difference between the stents, yet Fontaine et al. [32] have shown greater neointimal thickness with the rigid compared to the flexible stent (1.08 vs 0.74 mm respectively). If altered WSS is a factor in the difference in neointimal thicknesses between these stents, this would indicate that a greater depth of analysis is required to investigate the effects of stent rigidity on arterial WSS.

Another CFD study [61] investigating the influence of stent design properties on haemodynamics reported low WSS in 0.3 and 2.4% and high WSSG in 32 and 38% of the stented area for stent strut thicknesses of 0.056 and 0.096 mm respectively. Balassino et al. [4] also analysed the haemodynamic impact of strut thickness using CFD. Analysing the JoStent Flex stent (JOMED AB, Helsingborg, Sweden), they compared strut thicknesses of 0.05 with 0.15 mm by measuring the areas exposed to low WSS. They reported 60.6 and 57.3% of the stented area exposed to low WSS for the 0.05 and 0.15 mm thicknesses respectively. The ISAR-STERO stent trial resulted in restenosis rates of 15.0 and 25.8% ($p<0.003$) for the similarly designed ACS RX Multilink stent (Guidant, IN, USA) (strut thickness 0.05 mm) and the ACS RX Multilink Duet stent (Guidant) (strut thickness 0.14 mm). The ISAR-STERO II trial resulted in restenosis rates of 17.9 and 31.4% ($p<0.001$) for the differently designed ACS RX Multilink stent (Guidant) (strut thickness 0.05 mm) and the Bx-Velocity (Bx) stent (Cordis) (strut thickness 0.14 mm). The different restenosis rates in these studies may result from different levels of altered WSS due to the different strut thicknesses. However, the threshold method of analysis in the numerical studies above does not find any significant differences in altered WSS

between stents of different strut thickness. As before with the rigid versus flexible stents, there may be no significant difference in altered WSS; however, it does seem possible that this is not the case and the method of analysis is simply not sufficient to elucidate the difference.

In a more recent study [4], CFD analyses of four commercially-available BMSs were conducted. Comparisons between two of the stents with contrasting design, the Bx stent (Cordis) and the Jostent Flex (JOMED AB), showed 58% and 57% of the stented area with low WSS respectively. Duraiswamy et al. [26] also conducted CFD analyses of three, second-generation, commercially-available BMSs: the Bx stent, the Aurora stent (Medtronic Vascular) and the NIR stent (Boston Scientific). They found 59%, 57% and 59% of the stented area with low WSS and 75% 83% and 88% of the stented area with high WSSG for the Bx, Aurora and NIR stents respectively. These previous studies depict only minor differences in the altered WSS between these stent designs. However, clinical studies have shown stent design to be linked to restenosis rates [54, 67, 103]. In light of this, it is highly probable that using threshold values of only the WSS and WSSG variables is not sufficient to fully elucidate stent-induced disturbances to the arterial WSS.

1.4 Aim and Objective

Several attempts to investigate the haemodynamics in stented arteries using CFD have been made over the last decade. Some of these works have used a method of analysis (the "threshold method") which has failed to identify significant differences in altered WSS between different stents. Therefore, the aim of this work is to develop a novel methodology to assess the haemodynamic impact of coronary stent implantation. The objective of the methodology is to fully elucidate the stent-induced

alterations to the arterial WSS. The proposed numerical prediction methodology utilises the two commonly used variables, i.e. WSS and WSSG, plus two additional WSS-based variables, the WSS angle gradient (WSSAG) and the oscillatory shear index (OSI). Each of these variables highlights a different type of disturbance to the arterial WSS which could lead to IH. Instead of using threshold values, statistical measures of the full distribution of each of these variables are calculated for a more complete analysis. To demonstrate the methodology, it is applied to three stents with contrasting features. These stents are then assessed and compared based on the level of stent-induced alteration to the WSS. It is intended that the proposed methodology can be used to identify areas of disturbed arterial haemodynamics at the design stage of future bare metal, as well as permanent and bioabsorbable drug-eluting coronary stents.

1.5 Structure of Thesis

Chapter 2 details the chronological steps in the mechanism of in-stent restenosis. Also discussed are the stimulating haemodynamic factors which encourage IH, the primary process which leads to in-stent restenosis. Chapter 3 contains basic fluid mechanics theory, presenting the mathematical description of the stresses that exist in a fluid. This background theory serves as a platform for Chapter 4 which gives the important WSS-based variables calculated in this work to assess the haemodynamic impact of a coronary stent on the artery. The chapter then concludes with a review of the recent literature in this field. The proposed methodology for stent assessment based on the level of altered WSS in the artery is presented in Chapter 5. This chapter gives the details of a novel and efficient methodology to numerically predict tissue prolapse between stent struts in the stented section of an artery and also of the transient CFD analyses conducted to simulate pulsatile blood flow through the

stented artery. The new statistical method for analysing the results is also presented in this chapter. Chapter 6 contains the results of the CFD, analysed using the proposed statistical method. This chapter contains a section for each of the WSS-based variables, followed by a section for analysis. Finally, the overall conclusions of this work and recommendations for future work are discussed in Chapter 7.

1.6 Publications

The work reported in this thesis has led to three international journal publications [87, 88, 90] and also publications in the proceedings of four international [79, 81, 83, 85] and five national bioengineering conferences [80, 82, 84, 86, 89].

1.7 Summary

Coronary stenting is now the most commonly used treatment for CAD. This work focuses on coronary stents and their main deficiency, which is restenosis. Ultimately, the goal is to develop a tool to assess any particular coronary stent based on its likelihood to develop restenosis. It is well established that stent design has a significant effect on the risk of restenosis in the treated vessel. Stent design is likely to influence the WSS of the treated artery, which would influence the restenosis rate. If the alterations to the arterial WSS created by stent implantation could be fully elucidated, it could be used to pre-clinically assess the stent. In order to develop this assessment methodology an understanding of restenosis must first be developed, or more specifically restenosis that occurs within a coronary stent known as in-stent restenosis. This is the objective of the following chapter.

CHAPTER 2

In-Stent Restenosis

2.1 Introduction

Restenosis of vascularised arteries has been the major drawback of PCI for over 30 years since its inception to treat cardiovascular disease. Restenosis can best be described as a loss of the gain that was originally achieved by the PCI, i.e. a return of the lumen of the vessel to a size resembling that prior to intervention. Restenosis is typically diagnosed using angiography where a radio-opaque dye is injected into the blood vessel while the vessel patency is examined using fluoroscopy as shown in Figure 2-1. Several different definitions of restenosis exist which are based on the extent of the re-narrowing of the vessel at angiographic follow-up. The definition of restenosis in a treated vessel can also be based on adverse clinical outcomes such as myocardial infarction or the need for target lesion revascularisation (TLR). However, the most commonly used definition of restenosis is angiographic evidence of a loss of greater than 50% of the lumen size post intervention [46]. This definition was used in the BENESTENT-I [112], STRESS [31] and BENESTENT-II [113] clinical trials to compare PTCA to implantation of the PS stent and also stent equivalency trials such as NIRVANA [3] and ASCENT [2] where the PS stent was compared to the NIR and the ACS RX Multilink stents respectively. This method of binary classification for vessel restenosis based on the 50% re-blockage threshold is likely to conceal a good deal of detail from the results of clinical trials. Hence, this method

of classification has become less popular since the introduction of DESs in the last decade. A more commonly used measure of a stent's performance in recent years is "late loss" usually defined as the lumen diameter achieved from PCI minus the lumen diameter at follow-up angiography. This method gives an absolute value for the decrease in lumen size, allowing a more informed decision on stent performance.

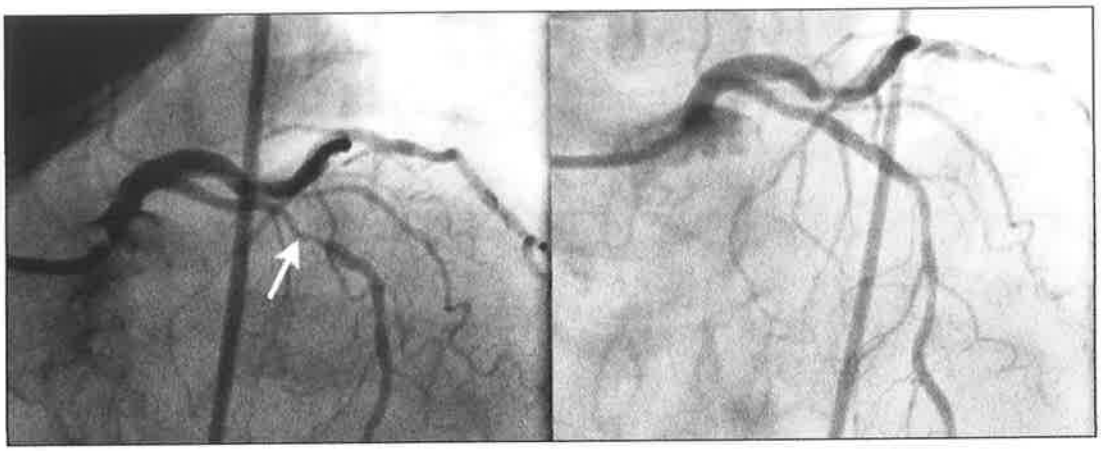

Figure 2-1: (a) Angiogram showing a stenosis (white arrow) in the left anterior descending (LAD) coronary artery and (b) the same artery following stent implantation restoring patency to the vessel [69].

As shown in Table 2-1, restenosis rates at short-term follow up have been steadily declining over the past three decades due to advances in technology and clinical procedures. Firstly, implantation of the PS stent showed improvement over PTCA [31, 112]. Second generation BMSs were then assessed by their non-inferiority to the PS stent in the stent equivalency trials [2, 3] where the majority showed a modest reduction in restenosis rates. First-generation DESs were compared to BMSs and showed a significant reduction in restenosis rates [77, 120]. In recent years, trials are now predominantly DES vs DES with restenosis rates usually below 10% for most current DESs [121, 129].

Trial (year)	Trial Design	No. of Patients	Follow up (months)	Restenosis Rate (%)
BENESTENT [112] (1994)	PS vs PTCA	520	7	22 vs 32
STRESS [31] (1994)	PS vs PTCA	410	6	32 vs 42
NIRVANA [3] (2001)	NIR vs PS	849	9	19 vs 22
ASCENT [2] (2001)	ML vs PS	529	9	16 vs 22
SIRUS [77] (2003)	SES vs BMS	1058	9	9 vs 36
TAXUS IV [120] (2005)	PES vs BMS	446	9	8 vs 27
TAXUS ATLAS [129] (2007)	Liberté PES vs Express2 PES	1862	9	9 vs 11
SPIRIT III [121] (2008)	EES vs PES	1002	12	2 vs 6

PS - Palmaz Schatz (Cordis, Johnson and Johnson, NJ, USA), PTCA - Percutaneous transluminal coronary angioplasty, NIR - NIR stent (Boston Scientific, MA, USA), ML - Multilink (Guidant, IN, USA), SES - Sirolimus-eluting stent, BMS - Bare metal stent, PES - Paclitaxel-eluting stent, EES - Everolimus-eluting stent, Liberté - Taxus Liberté stent (Boston Scientific, MA, USA), Express2 - Taxus Express2 stent (Boston Scientific, MA, USA)

Table 2-1: Selected clinical trials over the last two decades charting the decline of restenosis rates after PCI.

In-stent restenosis is caused by the growth of new tissue in the stented vessel and is categorised into four different patterns. Pattern I is known as focal, and is where the lesion is less than 10 mm in length. As shown in Figure 2-2, Pattern I is further subdivided into Classes A, B, C, and D representing articulation, margin, focal body and multifocal tissue growths respectively. Pattern II is where the tissue growth is confined within the axial limits of the stent and is known as diffuse intra-stent. Pattern III is diffuse proliferative, where the tissue extends beyond the axial limits of the stent and Pattern IV is total occlusion where the stented artery has a thrombolysis in myocardial infarction (TIMI) flow grade[1] of 0.

The biological mechanism of in-stent restenosis is different to the mechanism which results in atherosclerotic lesions. Firstly, the time course is very different between the two diseases; atherosclerotic lesions grow slowly in the arteries over a period of decades whereas in-stent restenosis typically develops within six months after intervention. As described in Chapter 1, atherosclerotic lesions result from vascular damage and a gradual build up of plaque whereas in-stent restenosis results

[1] TIMI flow grades: 0 (no flow), 1 (minimal flow), 2 (partial flow), or 3 (complete flow)

from the occurrence of thrombus deposition, inflammation, IH and negative remodelling of the artery.

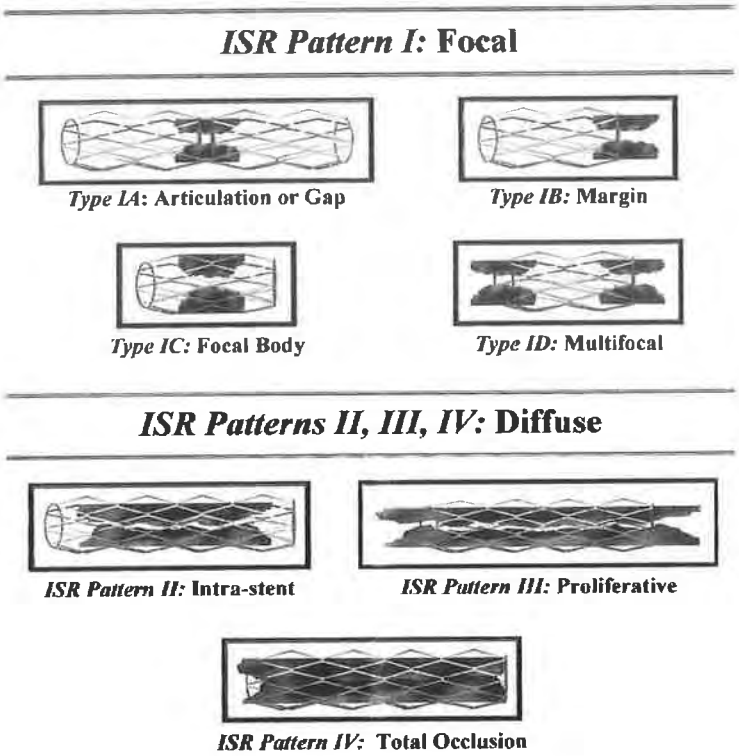

Figure 2-2: Schematic image of four patterns of restenosis. Pattern I is subdivided into four types (A-D). Patterns II - IV are classified according to the position of the in-stent restenosis in relation to the implanted stent [74].

2.2 Mechanism of Restenosis

In contrast to in-stent restenosis, up to 40% of lumen loss following PTCA is due to the acute elastic recoil of the vessel wall [102]. Another contributing factor is the chronic negative remodelling of the vessel wall [75], as the muscular part of the artery realigns to form a smaller lumen. The mechanism of in-stent restenosis is quite different to that of PTCA and can be divided into the four phases shown in Figure 2-3(a). In the first phase directly after stenting, platelets form clotting material called thrombus, which is deposited around the stent struts where the ECs have been damaged or denuded. The duration of this phase is dependent on the extent of vascular injury from the stenting procedure, with greater injury leading to prolonged

thrombus deposition [105, 109]. The second phase is inflammation as white blood cells called leucocytes adhere to the injury sites where the thrombus is forming and begin to infiltrate the tissue. The next phase is IH, which involves the migration of VSMCs from the media to the intima of the artery shown in Figure 2-3(b). The final phase is remodelling, where the muscles in the wall of the artery tighten in an effort to return the lumen diameter back to a smaller size. These four phases are discussed in more detail below.

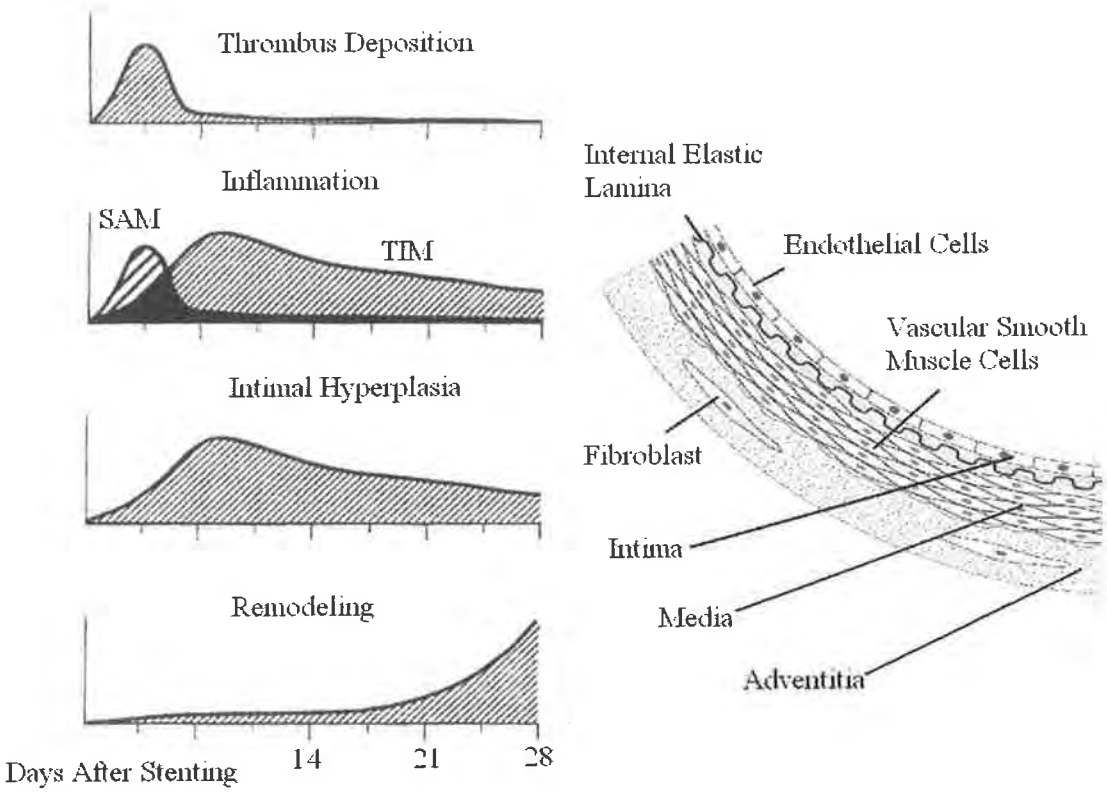

Figure 2-3: (a) Four phases of the coronary artery's pathobiological response to stent implantation and (b) the components of the artery wall [27].

2.2.1 Thrombus Deposition

Early concepts of PTCA were that the main mechanisms of lumen enlargement were compression and displacement of the atherosclerotic plaque by the inflated balloon [131, 132]. Evidence from histopathologic studies has now shown that in the majority of cases of PTCA and also stenting there is plaque splitting and endothelial

denudation, as well as some dissection of the internal elastic lamina and media [110]. These components of the artery wall are shown in Figure 2-3(b).

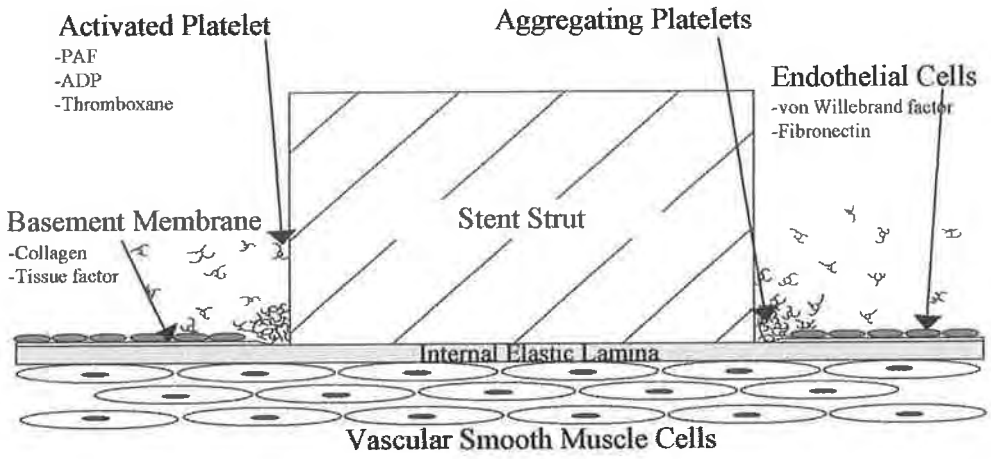

Figure 2-4: Schematic diagram of a stent strut in the hours after implantation. The ECs have been damaged and denuded exposing subendothelial components, leading to platelet activation and aggregation.

The intima of the artery consists of ECs and a layer of subendothelial connective tissue called the basement membrane. Implantation of the stent denudes ECs close to the stent struts causing blood-stream exposure to the basement membrane and also to parts of the media. ECs which are not close to the stent struts can also be denuded by the angioplasty balloon used to expand the stent [41, 104]. The trauma inflicted on the artery wall from the stenting procedure will most likely damage all ECs in that region to some extent even if they are not denuded from the wall.

Two glycoproteins called von Willebrand factor (vWf) and fibronectin which attract blood-borne platelets and help them bind together are released from damaged ECs. These glycoproteins recruit other proteins in the blood to activate platelets in the blood stream. Once activated, platelets change shape to aid aggregation (clotting) and also release granules such as platelet activating factor (PAF), adenosine

diphosphate (ADP) and thromboxane to activate more platelets and also encourage aggregation. As shown in Figure 2-4, activated platelets are transported to the injured site via the blood flow where they bind to the exposed subendothelial components using surface glycoprotein Ia/IIa receptors. In the presence of activated platelets, blood-soluble proteins synthesize into fibrin strands which bind the activated platelets together into a thrombus. The formation and deposition of thrombus begins immediately after stent implantation and is the dominant physiological response in the first seven days after implantation.

2.2.2 Inflammation

Inflammation is the immunological response to stent implantation and is the second phase of the arterial response as leucocytes are attracted to the stented region. Monocytes and lymphocytes are specific types of leucocyte designed to ingest and destroy foreign substances in the blood and tissue. In the weeks after stenting, these leucocytes are attracted to the site of the arterial injury where the thrombus has formed as shown in Figure 2-5. Activated platelets will express specific adhesion molecules on their surface such as P-selectin and glycoprotein Ib. Using these adhesion molecules, monocytes which are passing by in the blood flow will attach to the platelets using ligands on their surface. These monocytes are referred to as surface adherent monocytes (SAM) in Figure 2-3(a) above. Then, over a course of weeks these SAM will cross the platelet-fibrin thrombus to the site of endothelial injury where they will become tissue-infiltrating monocytes (TIM) or macrophages. These macrophages are usually found in the restenotic lesion near the stent struts. A linear relationship has been observed between the amount of macrophages present in the lesion and the amount of the tissue that subsequently develops from IH [105].

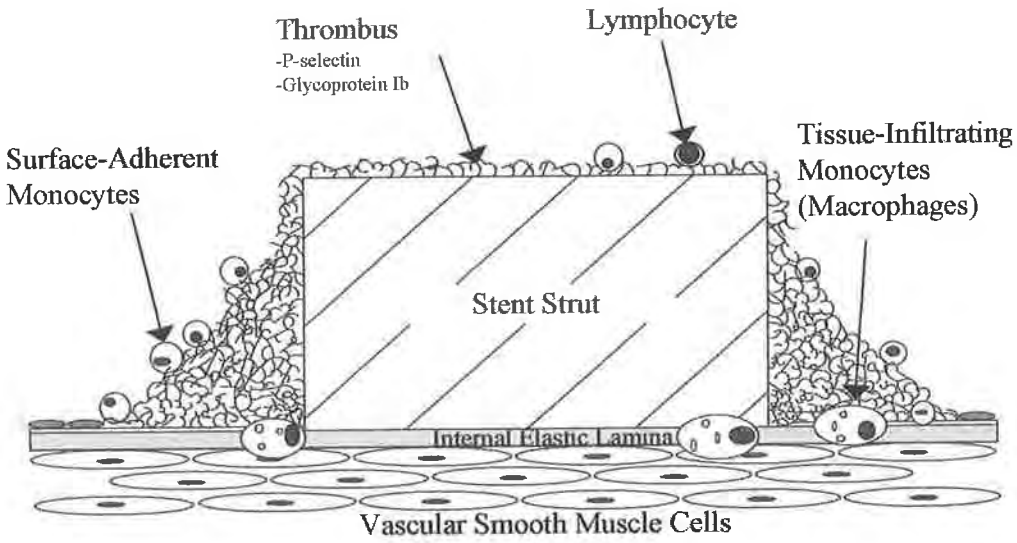

Figure 2-5: Schematic diagram of the inflammation phase of in-stent restenosis. Monocytes adhere to the injured surface and infiltrate the tissue becoming macrophages.

2.2.3 Intimal Hyperplasia

The majority of the restenotic tissue that grows after coronary stenting is comprised of VSMCs that migrate and proliferate around the stent in the IH phase of the arterial response to stenting [45, 78]. VSMCs which normally reside in the media of the artery migrate inwards through the internal elastic lamina towards the stent where they proliferate and replace the thrombus in the artery. The migration and proliferation of VSMCs has several drivers with the major drivers shown in Figure 2-6.

The IH phase really begins as soon as the stent is implanted with activated platelets releasing mitogens (substances which encourage cell proliferation) such as platelet-derived growth factor (PDGF), fibroblast growth factor (FGF) and thrombin as discussed in Section 2.2.1. The TIM discussed in Section 2.2.2 also release cytokines (signalling molecules) such as interleukin-1 and tumor necrosis factor (TNF) that stimulate the migration of VSMCs. The injured ECs are also capable of

synthesizing PDGF and FGF which encourage proliferation of the VSMCs. Finally, the VSMCs themselves which are usually contractile cells residing in the intima, when given enough stimulus from external sources (ECs, leucocytes, platelets), change from contractile to synthetic phenotype. Whilst in synthetic state the VSMC is activated and capable of producing its own mitogens such as PDGF, FGF and angiotesin II. The activated VSMC is also far more responsive to cytokines and growth factors leading to increased migration and proliferation. The cascade of events which lead to IH are briefly summarised in Figure 2-7.

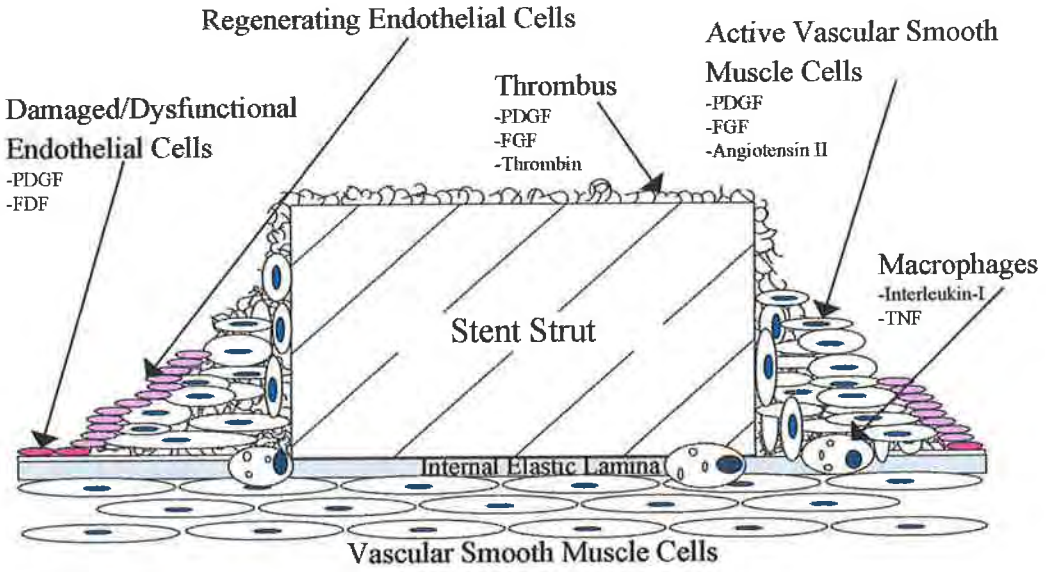

Figure 2-6: Schematic diagram of the IH phase of in-stent restenosis. Thrombus, damaged ECs, active VSMCs and macrophages are all capable of releasing cytokines which stimulate VSMC migration and proliferation.

The VSMCs, platelets and leukocytes are all held together by extracellular matrix (ECM) comprised mostly of fibroblast, which is a connective tissue rich in collagen. It is this VSMC-rich connective tissue that forms the bulk of the restenotic growth. New ECs will grow from the ECs that survive the stenting procedure. These new cells must cover the restenotic lesion and separate the stent and injury site from the blood flow in order for the arterial response and IH to cease. If the IH is

excessive, the vessel will not retain sufficient patency and a repeat revascularisation will be necessary.

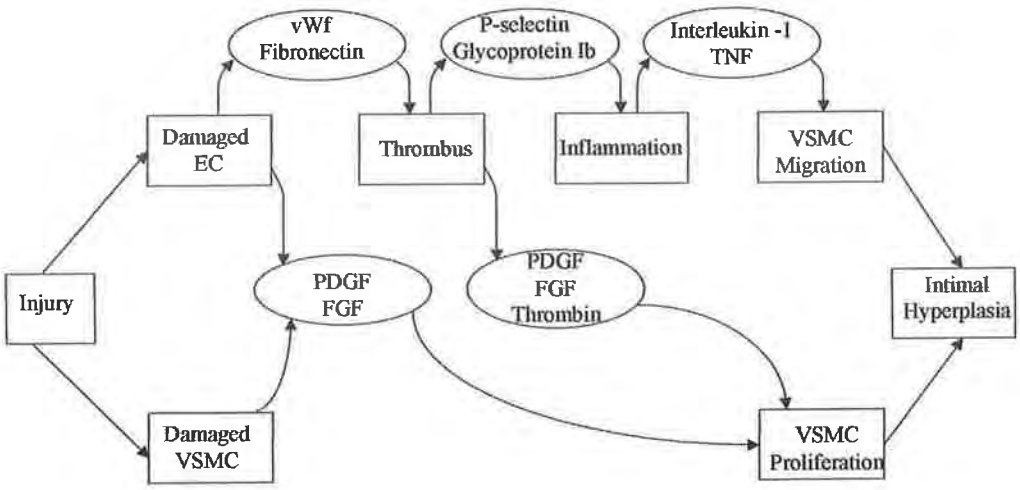

Figure 2-7: Schematic diagram of key process (square) and chemical messenger particles (oval) involved in the mechanism of IH.

2.2.4 Remodelling

The final phase in the vascular response to the stenting procedure is remodelling, defined as long term changes in vessel size. From approximately four weeks after stenting, collagen deposits in the outer layers of the artery lead to arterial shrinkage known as negative remodelling. This phase, which is one of the major causes of restenosis with PTCA, is somewhat counteracted by the presence of the stent. However, the increase in pressure on the stent can squeeze some of the artery wall through the inter-strut space creating tissue prolapse between the struts. Also, if the stent if not sufficiently rigid, negative remodelling may cause crushing or radial recoil of the stent.

2.3 Haemodynamics and Intimal Hyperplasia

The mechanism of in-stent restenosis consists of the four phases described above in chronological order. These phases are triggered and maintained by stimuli from the

stent implantation. Broadly speaking, the predominant stimuli are the presence of the stent, the injury incurred from the stenting procedure and the disturbed haemodynamics due to the presence of the stent.

The degree of injury to the ECs and underlying vessel layers has been correlated to the severity of the thrombotic reaction and amount of tissue growth from IH [103]. In light of this a poorly designed stent, or indeed a poorly inserted stent, which creates severe injury will likely result in restenosis regardless of any haemodynamic effects. In this severe-injury scenario, the damage to intimal and medial cells results in the release of large amounts of growth factors directly into the artery wall promoting excessive IH without the influence of haemodynamics. If however, the stent implantation produces a manageable degree of injury then the haemodynamics are likely to play a significant role in the recovery of the artery.

Thrombus formation immediately after stenting is heavily haemodynamically dependent. The glycoproteins vWf and fibronectin are released into the blood stream to attract platelets to the injured site. The platelets themselves are influenced by the advective forces of the flowing bloodstream [33], which indicates that haemodynamics are directly involved in the formation of thrombus. The same is true of the inflammatory cells which are known to play a significant role in IH. A direct relationship has been demonstrated between the amount of infiltrating monocytes and the volume of tissue growth from IH in rabbit models [105]. Therefore it is highly likely that haemodynamics influence restenosis through the transport of particles such as platelets, leucocytes, growth factors and cytokines to and from the artery wall. For example, an area of low or recirculating flow would be likely to

accumulate thrombotic and inflammatory particles which would encourage tissue growth from IH in that area.

The growth of a functioning layer of endothelium between the blood flow and the restenotic tissue is critical to stop the further growth of the tissue. Healthy ECs functioning under normal conditions secrete cell-growth-inhibiting substances such as prostacyclin and nitric oxide. However, the growth and behaviour of ECs is highly sensitive to arterial haemodynamics. Adverse non-physiological haemodynamics are known to cause endothelial migration, dysfunction, and increased permeability to thrombogenic and inflammatory cells. The ECs have receptors on their membranes which are capable of detecting the arterial WSS. The WSS experienced by the ECs is the major determinant in the growth and behaviour of the ECs in the stented artery and as such, is hugely important in determining the risk of restenosis posed by any particular stent. A detailed discussion of the WSS-based variables and their role in IH and restenosis will be presented in Section 4.2.

2.4 Summary

With in-stent restenosis, the growth of new tissue from the IH process is predominantly what re-blocks the artery, and if kept minimal the stenting procedure is likely to be successful. However, if the tissue growth is excessive and the artery cannot accommodate the new tissue without losing patency, a repeat procedure will be necessary.

The mechanism of in-stent restenosis consists of the phases: thrombus deposition, inflammation, IH and negative remodelling. Histopathology has shown that the IH phase is responsible for the bulk of the lesion. However, it is important to keep in mind that the severity of the thrombus and inflammation determines the

severity of the IH. After the denudation from the stenting procedure, the re-growth of a functioning layer of healthy endothelium in the stented artery is the key to the cessation of the IH cascade. WSS plays a pivotal role in both the re-growth and normal function of ECs in the artery. The effects of WSS and other related variables on endothelial re-growth and function will be discussed in full in Chapter 4. Before that it is necessary to mathematically describe the fluid viscous stress which is exerted on the artery wall by the blood flow, i.e. the WSS. This basic fluid mechanics theory is the focus of the following chapter.

CHAPTER 3

Fluid Mechanics Theory

3.1 Introduction

A fluid element may undergo four types of motion or deformation: translation, rotation, shear strain, and linear strain. Since a fluid element may be in constant motion, in fluid mechanics it is preferable to consider the motion and deformation of fluid elements in terms of rates. These are velocity (rate of translation), angular velocity (rate of rotation), shear strain rate (rate of shear strain) and linear strain rate (rate of linear strain). In order to examine these motion and deformation rates we will conduct an analysis of a fluid element which is initially cubic in shape. The dimensions of the fluid element are dx, dy, and dz in the Cartesian coordinate directions x, y and z respectively as shown in Figure 3-1.

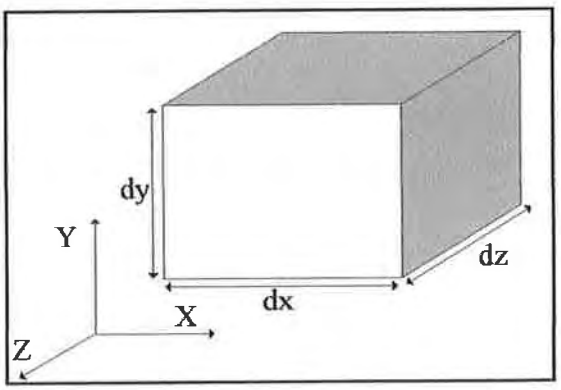

Figure 3-1: Fluid element employed for analysis of fluid motion and deformation.

3.2 Fluid Element Analysis

The relationship between the rate of deformation of a fluid element and the related stresses forms one of the fundamental building blocks of all fluid mechanics theory. The fluid stresses and how they are calculated from the deformations are critically important to the work in this thesis. With this in mind, this section examines the mathematical description of these deformations and stresses in detail.

3.2.1 Rate of Translation

The rate of translation of a fluid element is mathematically described by the velocity vector written

$$\vec{V} = u\vec{i} + v\vec{j} + w\vec{k} \tag{3-1}$$

in Cartesian coordinates, where u, v and w are the velocities in the x, y and z directions respectively. At a point in the fluid, the translations in the x, y and z directions are equal to (u dt), (v dt) and (z dt) respectively, where dt is an infinitesimally small increment of time.

3.2.2 Rate of Rotation

The rate of rotation or angular velocity at a point on the fluid element is defined as the average rotation rate of two initially perpendicular lines that intersect at that point. For simplicity consider only one two-dimensional (2D) face of the fluid element in the xy plane shown in Figure 3-2 at two instances in time, t and t + dt. At the point B in Figure 3-2 the angular rotation about the z axis is defined as the average counter clockwise rotation of the two sides BC and BA. At time t + dt, BC has rotated a counter clockwise angle $d\alpha$. BA has rotated clockwise, thus by convention its counter clockwise turn is $-d\beta$. The average rotation around the z axis

is written

$$d\Omega_z = \frac{1}{2}(d\alpha - d\beta) \tag{3-2}$$

and the rate of rotation is written

$$\frac{d\Omega_z}{dt} = \frac{1}{2}\left(\frac{d\alpha}{dt} - \frac{d\beta}{dt}\right) \tag{3-3}$$

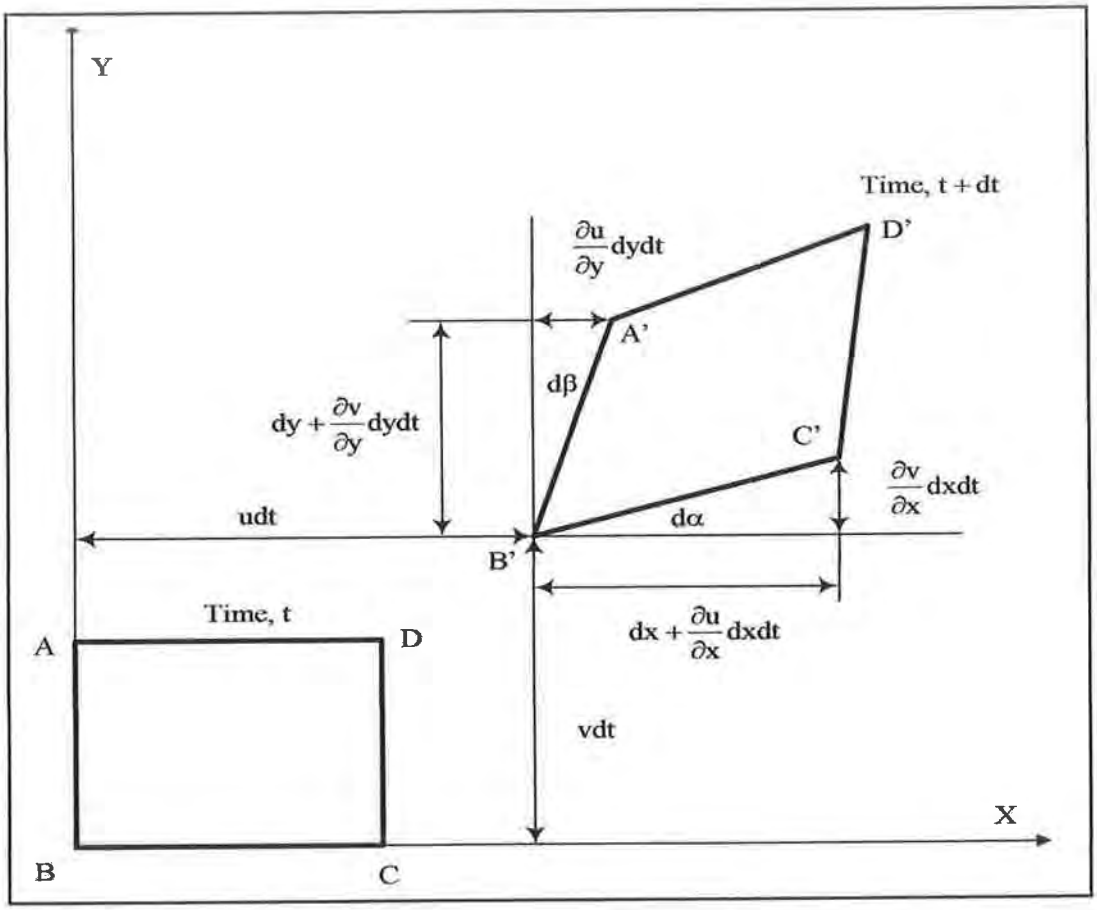

Figure 3-2: Motion and deformation of a 2D fluid element from time t to time t + dt.

The two angles in Equation (3-2) can be directly related to the velocity derivatives through the calculus limit

$$d\alpha = \lim_{dt\to 0}\left(\tan^{-1}\frac{\left(\partial v/\partial x\right)dxdt}{dx+\left(\partial u/\partial x\right)dxdt}\right)=\frac{\partial u}{\partial x}dt$$
$$d\beta = \lim_{dt\to 0}\left(\tan^{-1}\frac{\left(\partial u/\partial y\right)dydt}{dy+\left(\partial v/\partial y\right)dydt}\right)=\frac{\partial u}{\partial y}dt \qquad (3\text{-}4)$$

Substituting Equation (3-4) into Equation (3-3), the rate of rotation about the z axis is given by

$$\frac{d\Omega_z}{dt}=\frac{1}{2}\left(\frac{\partial v}{\partial x}-\frac{\partial u}{\partial y}\right) \qquad (3\text{-}5)$$

The rate of rotation around the x and y axes can be derived in the same way to produce the rate of rotation vector in Cartesian coordinates written

$$\vec{\omega}=\frac{\partial\Omega}{\partial t}=\frac{1}{2}\left(\frac{\partial w}{\partial y}-\frac{\partial v}{\partial z}\right)\vec{i}+\frac{1}{2}\left(\frac{\partial u}{\partial z}-\frac{\partial w}{\partial x}\right)\vec{j}+\frac{1}{2}\left(\frac{\partial v}{\partial x}-\frac{\partial u}{\partial y}\right)\vec{k} \qquad (3\text{-}6)$$

The factors of one-half disappear through the definition of a new quantity know as vorticity defined:

$$\vec{\varsigma}=2\vec{\omega} \qquad (3\text{-}7)$$

such that velocity and vorticity are related by

$$\vec{\varsigma}=\text{curl}\,\vec{V}=\vec{\nabla}\times\vec{V} \qquad (3\text{-}8)$$

where $\vec{\nabla}$ is the gradient operator defined as

$$\vec{i}\frac{\partial}{\partial x}+\vec{j}\frac{\partial}{\partial y}+\vec{k}\frac{\partial}{\partial z} \qquad (3\text{-}9)$$

3.2.3 Rate of Linear Strain

The linear strain rate is defined as the rate of increase of length per unit length and is also known as dilatation or extensional strain rate. Examining the horizontal side BC from Figure 3-2, the linear strain rate in the x direction is given by

$$\varepsilon_{xx} = \frac{d}{dt}\left(\frac{B'C'-BC}{BC}\right) = \frac{d}{dt}\left(\frac{\left(dx + \frac{\partial u}{\partial x}dxdt\right) - dx}{dx}\right) = \frac{\partial u}{\partial x} \tag{3-10}$$

with similar expressions for the y and z directions. The three linear strain rates are therefore

$$\varepsilon_{xx} = \frac{\partial u}{\partial x}, \varepsilon_{yy} = \frac{\partial v}{\partial y}, \varepsilon_{zz} = \frac{\partial w}{\partial z} \tag{3-11}$$

3.2.4 Rate of Shear Strain

The 2D shear strain rate is commonly defined as the average rate of decrease of the angle between two lines which are initially perpendicular in the unstrained state. Taking BA and BC in Figure 3-2 as the initial unstrained lines the shear strain occurring from time t to t + dt is

$$\chi_{xy} = \frac{1}{2}(d\alpha + d\beta) \tag{3-12}$$

and the shear strain rate is written

$$\varepsilon_{xy} = \frac{1}{2}\left(\frac{d\alpha}{dt} + \frac{d\beta}{dt}\right) = \frac{1}{2}\left(\frac{\partial v}{\partial x} + \frac{\partial u}{\partial y}\right) \tag{3-13}$$

Similarly, the other two components of the shear strain rate in the YZ and ZX Cartesian coordinate planes respectively are

$$\varepsilon_{yz} = \frac{1}{2}\left(\frac{\partial w}{\partial y} + \frac{\partial v}{\partial z}\right), \quad \varepsilon_{zx} = \frac{1}{2}\left(\frac{\partial u}{\partial z} + \frac{\partial w}{\partial x}\right) \tag{3-14}$$

and by analogy with solid mechanics the shear strain rates are symmetric, i.e. $e_{ij} = e_{ji}$ The angle under consideration A' B' C' in Figure 3-2 is by definition positive shear as the shear strain χ_{xy} is increasing.

3.2.5 Strain Rate Tensor

For the remainder of this section, only the deformation of the fluid element is important, i.e. the linear strain rate and the shear strain rate. The linear strain rate and shear strain rate can mathematically be combined into one symmetric second-order tensor called the strain rate tensor which is written

$$\vec{\vec{\varepsilon}}_{ij} = \begin{pmatrix} \varepsilon_{xx} & \varepsilon_{xy} & \varepsilon_{xz} \\ \varepsilon_{yx} & \varepsilon_{yy} & \varepsilon_{yz} \\ \varepsilon_{zx} & \varepsilon_{zy} & \varepsilon_{zz} \end{pmatrix} = \begin{pmatrix} \frac{\partial u}{\partial x} & \frac{1}{2}\left(\frac{\partial u}{\partial y} + \frac{\partial v}{\partial x}\right) & \frac{1}{2}\left(\frac{\partial u}{\partial z} + \frac{\partial w}{\partial x}\right) \\ \frac{1}{2}\left(\frac{\partial v}{\partial x} + \frac{\partial u}{\partial y}\right) & \frac{\partial v}{\partial y} & \frac{1}{2}\left(\frac{\partial v}{\partial z} + \frac{\partial w}{\partial y}\right) \\ \frac{1}{2}\left(\frac{\partial w}{\partial x} + \frac{\partial u}{\partial z}\right) & \frac{1}{2}\left(\frac{\partial w}{\partial y} + \frac{\partial v}{\partial z}\right) & \frac{\partial w}{\partial z} \end{pmatrix} \tag{3-15}$$

A property of symmetric tensors is that there exists one, and only one, set of axes where the off diagonal terms $i \neq j$ vanish. These are the principal axes, for which the strain rate tensor reduces to

$$\vec{\vec{\varepsilon}}_{ij} = \begin{pmatrix} \varepsilon_1 & 0 & 0 \\ 0 & \varepsilon_2 & 0 \\ 0 & 0 & \varepsilon_3 \end{pmatrix} \tag{3-16}$$

where $\varepsilon_1, \varepsilon_2, \varepsilon_3$ are called the principal strain rates.

3.2.6 Fluid Stress Tensor

The forces acting on a fluid element consist of body forces such as gravity and surface forces such as viscous and pressure forces. The most common body force is gravity which can be expressed as

$$\vec{F}_{Gravity} = m\vec{g} \tag{3-17}$$

where m is the mass of the fluid element and $\vec{g}$ is the gravitational acceleration vector with a magnitude of 9.81 m/s^2 at sea level. The analysis of the surface forces acting on a fluid element is more complex than that of the body forces. Firstly, a surface unlike a volume has both tangential and normal directions associated with it. Secondly, the force acting on a surface is independent of the orientation of the coordinate axis; however the description of the force in terms of coordinate components changes with axis orientation. In order to describe the surface forces acting on a fluid element, a second order stress tensor is defined as

$$\vec{\vec{\sigma}}_{ij} = \begin{pmatrix} \sigma_{xx} & \sigma_{xy} & \sigma_{xz} \\ \sigma_{yx} & \sigma_{yy} & \sigma_{yz} \\ \sigma_{zx} & \sigma_{zy} & \sigma_{zz} \end{pmatrix} \tag{3-18}$$

where σ_{xx}, σ_{yy} and σ_{zz} are called the normal stresses, composed of pressure and viscous stresses and the remaining six components are called shear stresses. Since pressure can only act normal to a surface, shear stresses are composed entirely of viscous stresses. The nine positive components of the stress tensor are illustrated in Figure 3-3.

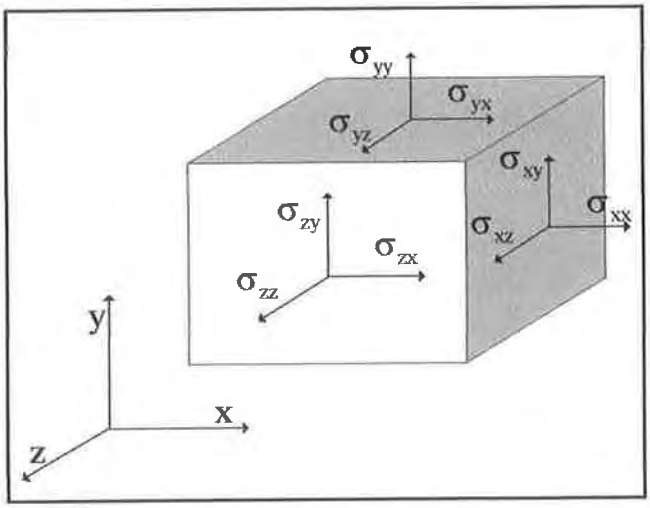

Figure 3-3: Infinitesimally small cubic fluid element with the three normal components and six shear components of the stress tensor in Cartesian coordinates.

It is convenient to use the tensor notation of Equation (3-18) when dealing with second order tensors. Tensor notation uses the indices i and j to represent directions of stresses and surface normal vectors in the chosen coordinate system. For example, in Equation (3-18), σ_{ij} represents the stress in the j direction acting on a face whose normal vector is in the i direction. In the case of the stress tensor the indices i and j are replaced by the Cartesian coordinates x, y, and z to form all nine components. The stress tensor is a symmetric tensor, i.e. $\sigma_{ij} = \sigma_{ji}$. This symmetry is required to satisfy equilibrium of moments about the three axes of the element. The counterparts of the nine stresses shown in Figure 3-3 exist on the opposing faces and are not shown. When the element is in equilibrium the counterpart stresses will be exactly equal in magnitude and opposite in direction to the stresses visible in Figure 3-3.

For a fluid at rest the only stress acting on any surface of any fluid element is static pressure which always acts inward and normal to the surface as shown in

Figure 3-4. In the case of a fluid at rest the stress tensor reduces to the static pressure tensor written

$$\vec{\vec{\sigma}}_{ij} = \begin{pmatrix} \sigma_{xx} & \sigma_{xy} & \sigma_{xz} \\ \sigma_{yx} & \sigma_{yy} & \sigma_{yz} \\ \sigma_{zx} & \sigma_{zy} & \sigma_{zz} \end{pmatrix} = \begin{pmatrix} -P & 0 & 0 \\ 0 & -P & 0 \\ 0 & 0 & -P \end{pmatrix} \tag{3-19}$$

where P is the local static pressure. When a fluid is in motion the static pressure tensor still applies; however viscous stresses may now also exist. For a fluid in motion the stress tensor can be written

$$\vec{\vec{\sigma}}_{ij} = \begin{pmatrix} \sigma_{xx} & \sigma_{xy} & \sigma_{xz} \\ \sigma_{yx} & \sigma_{yy} & \sigma_{yz} \\ \sigma_{zx} & \sigma_{zy} & \sigma_{zz} \end{pmatrix} = \begin{pmatrix} -P & 0 & 0 \\ 0 & -P & 0 \\ 0 & 0 & -P \end{pmatrix} + \begin{pmatrix} \tau_{xx} & \tau_{xy} & \tau_{xz} \\ \tau_{yx} & \tau_{yy} & \tau_{yz} \\ \tau_{zx} & \tau_{zy} & \tau_{zz} \end{pmatrix} \tag{3-20}$$

where the new tensor $\vec{\vec{\tau}}_{ij}$ is the viscous stress tensor.

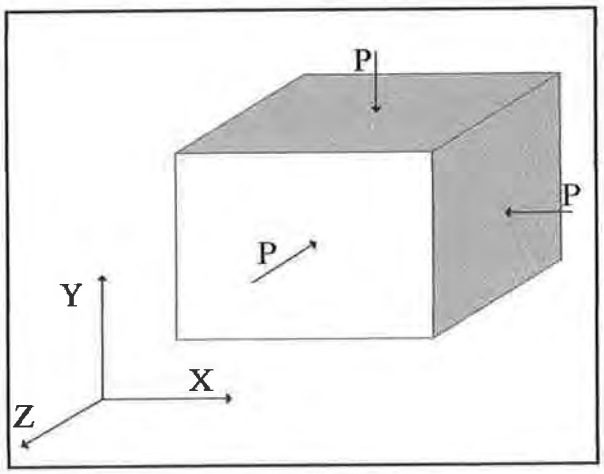

Figure 3-4: The stress on an infinitesimally small fluid element in a fluid which is at rest. The stresses reduce to static pressure which only acts inwards and normal to a surface.

3.3 Constitutive Equation for a Newtonian Fluid

Stokes [119] relates the strain rate tensor in Equation (3-15) to the stress tensor in Equation (3.19) in a deformation law through the three following three postulates:

1. The stress tensor $\vec{\vec{\sigma}}_{ij}$ is a linear function of the strain rate tensor $\vec{\vec{\varepsilon}}_{ij}$

2. The fluid is isotropic, and therefore the deformation law is independent of the coordinate axis in which it is expressed.

3. When the strain rates are zero, the deformation law must reduce to the static pressure condition which states

$$\begin{aligned} &\sigma_{xx} = \sigma_{yy} = \sigma_{zz} = -P \\ &\sigma_{ij} = 0 \text{ for } i \neq j \end{aligned} \tag{3-21}$$

Condition 2 of the deformation law requires that the principal strain axis of Equation (3-16) is exactly the same axis as the principal stress axis. On the principal axis the strain rate tensor only has the components $\varepsilon_1, \varepsilon_2$ and ε_3 making it a convenient place to begin the derivation. Letting x_1, y_1 and z_1 be the principal axis directions, the deformation law could involve at most three linear coefficients

$$\sigma_1 = -P + C_1\varepsilon_1 + C_2\varepsilon_2 + C_3\varepsilon_3 \tag{3-22}$$

The term $-P$ is added to satisfy Condition 3 of the deformation law. Also for Condition 2 to be valid, the crossflow effect of ε_2 and ε_3 must be identical, i.e. $C_2 = C_3$. Equation (3-22) can be re-written

$$\sigma_1 = -P + K\varepsilon_1 + C_2\left(\varepsilon_1 + \varepsilon_2 + \varepsilon_3\right) \tag{3-23}$$

where

$$K = C_1 - C_2 \tag{3-24}$$

and $\varepsilon_1 + \varepsilon_2 + \varepsilon_3$ is equal to $\dfrac{\partial u}{\partial x} + \dfrac{\partial v}{\partial y} + \dfrac{\partial w}{\partial z}$ from equation (3-11) and is called the divergence of the velocity $\left(\vec{\nabla}.\vec{V}\right)$ and equal to zero for incompressible flow. To find

a general deformation law, consider transforming Equation (3-23) to arbitrary axes x, y, z where the shear stresses are non zero. With respect to the principal axes x_1, y_1, z_1, let the x axis have directional cosines a_{x1}, a_{x2} and a_{x3}. These are the cosines of the angles between the three principal axes and the arbitrary x axis respectively. Similarly, let the y axis have directional cosines a_{y1}, a_{y2} and a_{y3}, and let the z axis have a_{z1}, a_{z2} and a_{z3}. For any set of directional cosines $a_{x1}^2 + a_{x2}^2 + a_{x3}^2 = 1$. The transformation rule (See Section C.3.1, p183-185 for more detail on the transformation procedure) between a normal stress or strain rate in the new arbitrary axes (x, y, z) and the principal stresses or strain rates is given by, for example

$$\begin{aligned} \sigma_{xx} &= \sigma_1 a_{x1}^2 + \sigma_2 a_{x2}^2 + \sigma_3 a_{x3}^2 \\ \varepsilon_{xx} &= \varepsilon_1 a_{x1}^2 + \varepsilon_2 a_{x2}^2 + \varepsilon_3 a_{x3}^2 \end{aligned} \tag{3-25}$$

Similarly the shear stresses and the strain rates described by the arbitrary axes are related to the principal stresses and strains by the transformation law

$$\begin{aligned} \sigma_{xy} &= \sigma_1 a_{x1} a_{y1} + \sigma_2 a_{x2} a_{y2} + \sigma_3 a_{x3} a_{y3} \\ \varepsilon_{xy} &= \varepsilon_1 a_{x1} a_{y1} + \varepsilon_2 a_{x2} a_{y2} + \varepsilon_3 a_{x3} a_{y3} \end{aligned} \tag{3-26}$$

$\sigma_1, \varepsilon_1, \sigma_2$ etc. can now be eliminated from Equation (3-25) by combining Equation (3-23) and the fact that $a_{x1}^2 + a_{x2}^2 + a_{x3}^2 = 1$. The result is

$$\sigma_{xx} = -P + K\varepsilon_{xx} + C_2 \vec{\nabla}.\vec{V} \tag{3-27}$$

with similar expressions for σ_{yy} and σ_{zz} Similarly, $\sigma_1, \varepsilon_1, \sigma_2$ etc. can be eliminated from equation (3-26) to give

$$\sigma_{xy} = K\varepsilon_{xy} \tag{3-28}$$

with similar expressions for σ_{xz} and σ_{yz}. Equations (3-27) and (3-28) can be

combined into a single general deformation law written

$$\sigma_{ij} = -P\delta_{ij} + K\varepsilon_{ij} + \delta_{ij}C_2\vec{\nabla}.\vec{V} \tag{3-29}$$

where δ_{ij} is the Kronecker delta function ($\delta_{ij} = 1$ if $i = j$ and $\delta_{ij} = 0$ if $i \neq j$). To find the first coefficient K, consider Couette flow which is flow between a stationary plate and a moving plate as shown in Figure 3-5.

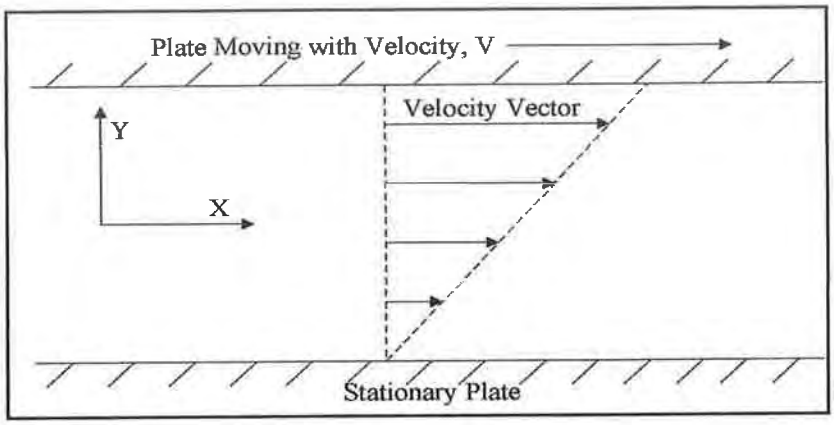

Figure 3-5: Graphical representation of 2D Couette flow in which a fluid flow is driven by a moving top plate and the fluid is held stationary at the bottom plate due to the no-slip condition.

The plate is considered infinitely long in the x direction and the flow is fully developed. The velocity vector only has an x component (u), and only varies in the y direction. With these features of Couette flow in mind, the strain rate tensor reduces to

$$\varepsilon_{xy} = \frac{1}{2}\left(\frac{\partial u}{\partial y} + \frac{\partial v}{\partial x}\right) = \frac{1}{2}\frac{\partial u}{\partial y} = \frac{1}{2}\frac{du}{dy} = \frac{1}{2}\frac{V}{H} \tag{3-30}$$

where V is the speed of the top plate and H is the vertical distance between the two plates. Experiments show that the shear stress is constant throughout the fluid and forms a linear relationship with the applied velocity, i.e.

$$\sigma_{xy} = \mu \frac{V}{H} \tag{3-31}$$

where μ is the coefficient of viscosity of a Newtonian fluid. Comparing Equations (3-30) and (3-31) yields

$$\sigma_{xy} = 2\mu\varepsilon_{xy} \tag{3-32}$$

and comparing to Equation (3-28) shows the coefficient $K = 2\mu$ The second coefficient C_2 in Equation (3-29) is independent of μ and only associated with volumetric expansion; therefore it is known as the coefficient of bulk viscosity and given the symbol λ. The general deformation law for a viscous Newtonian fluid can be written

$$\vec{\vec{\sigma}}_{ij} = -P\delta_{ij} + \mu\left(\frac{\partial u_i}{\partial x_j} + \frac{\partial u_j}{\partial x_i}\right) + \delta_{ij}\lambda\vec{\nabla}.\vec{V} \tag{3-33}$$

Stokes hypothesis [119] states that

$$\lambda = -\frac{2}{3}\mu \tag{3-34}$$

resulting in the following stress tensor for a viscous Newtonian fluid:

$$\vec{\vec{\sigma}}_{ij} = \begin{pmatrix} -P + 2\mu\frac{\partial u}{\partial x} - \frac{2}{3}\mu\vec{\nabla}.\vec{V} & \mu\left(\frac{\partial u}{\partial y} + \frac{\partial v}{\partial x}\right) & \mu\left(\frac{\partial u}{\partial z} + \frac{\partial w}{\partial x}\right) \\ \mu\left(\frac{\partial v}{\partial x} + \frac{\partial u}{\partial y}\right) & -P + 2\mu\frac{\partial v}{\partial y} - \frac{2}{3}\mu\vec{\nabla}.\vec{V} & \mu\left(\frac{\partial v}{\partial z} + \frac{\partial w}{\partial y}\right) \\ \mu\left(\frac{\partial w}{\partial x} + \frac{\partial u}{\partial z}\right) & \mu\left(\frac{\partial w}{\partial y} + \frac{\partial v}{\partial z}\right) & -P + 2\mu\frac{\partial w}{\partial z} - \frac{2}{3}\mu\vec{\nabla}.\vec{V} \end{pmatrix} \tag{3-35}$$

When a fluid is incompressible the divergence of the velocity $\left(\vec{\nabla}.\vec{V}\right)$ is zero. The viscous components of the stress tensor for an incompressible fluid are therefore given by

$$\vec{\vec{\tau}}_{ij} = \begin{pmatrix} 2\mu\frac{\partial u}{\partial x} & \mu\left(\frac{\partial u}{\partial y}+\frac{\partial v}{\partial x}\right) & \mu\left(\frac{\partial u}{\partial z}+\frac{\partial w}{\partial x}\right) \\ \mu\left(\frac{\partial v}{\partial x}+\frac{\partial u}{\partial y}\right) & 2\mu\frac{\partial v}{\partial y} & \mu\left(\frac{\partial v}{\partial z}+\frac{\partial w}{\partial y}\right) \\ \mu\left(\frac{\partial w}{\partial x}+\frac{\partial u}{\partial z}\right) & \mu\left(\frac{\partial w}{\partial y}+\frac{\partial v}{\partial z}\right) & 2\mu\frac{\partial w}{\partial z} \end{pmatrix} \quad (3\text{-}36)$$

The significance of this result is that for an incompressible Newtonian fluid, viscous normal stresses (main diagonal) and the viscous shear stresses (off diagonal) can be computed directly from the velocity gradients in the flow.

3.4 Summary

In this chapter the mathematical description of the motion and deformation of a fluid element is presented. The complete set of stresses acting on the same fluid element is then detailed followed by a famous constitutive equation for Newtonian fluids which relates the deformation to the stress. Now that viscous stresses in the fluid have been well addressed, variables are developed in the following chapter to quantify these stresses and their derivatives in the stented artery. After the variables have been introduced, an overview of their typical use in the recent literature then concludes the chapter.

CHAPTER 4

Viscous Stress Variables and CFD Modelling

4.1 Introduction

This first part of this chapter describes the variables employed in this work to fully elucidate the alterations to WSS following coronary stent implantation. The relevance of the variables is discussed with regard to the effect of high or low variable magnitudes. Complete mathematical descriptions of the variables are also presented. The second part of the chapter contains a brief literature survey of recent CFD modelling of haemodynamics in stented arteries. Some of the reviewed works employ a number of the variables predicted in this work which are described in Section 4.2. Additional variables which are not predicted in this work will be described in Section 4.3 as necessary.

4.2 Wall Shear Stress Based Variables

Most of the arterial blockage associated with in-stent restenosis is due to IH, which is the excessive growth of new tissue inside the stented segment. As discussed earlier in Chapter 2, this growth is triggered by chemical signals from sources including EC damage and dysfunction, platelet adhesion, leucocyte infiltration and VSMC signalling. Disturbed haemodynamics near the stent stimulate IH through the alteration of the natural WSS acting on both the ECs (leading to EC dysfunction) and

the subendothelial layer where ECs have been denuded (leading to disrupted EC regrowth). Disturbed haemodynamics can also stimulate IH through the increased advection of platelets and leucocytes to the artery wall. Thus, haemodynamic variables have been formulated to identify sites in the artery where IH is more likely due to these factors. This section briefly describes the four WSS-based variables used in this work to quantify the level of stent-induced alteration to the arterial WSS. Appendix C contains detailed mathematical descriptions of these variables, the numerical methodology used to calculate them and also validation procedures on devised test cases where theoretical solutions for the variables are known.

4.2.1 Wall Shear Stress

The distribution of WSS in arterial flows has been the subject of considerable research in the past decade due to its association with vascular disease. ECs subjected to elevated levels of WSS>1 N/m^2 tend to elongate and align in the direction of flow, whereas those experiencing low or oscillatory WSS<0.5 N/m^2 are circular in shape and have no preferred alignment pattern [72]. These circular cells, coupled with the low blood velocity usually present in areas of low WSS [6] lead to increased uptake of blood-borne particles to the artery wall as a result of increased permeability of the endothelial layer and increased particle residence time. Under low WSS conditions, ECs can themselves act as a catalyst for IH through, for example, the upregulation of tissue growth factors such as PDGF-A and PDGF-B [72, 130]. Numerous studies which incorporate numerical and experimental results have correlated areas of low WSS (WSS<0.5 N/m^2) with increased IH [64, 126, 134, 138].

In mathematical terms, the dot product of the unit normal vector $\vec{l}$ to a surface and the viscous stress tensor $\vec{\vec{\tau}}_{ij}$ yields the WSS vector

$$\vec{l}.\vec{\vec{\tau}}_{ij} = \vec{\tau}_w = \tau_{w,x}\vec{i} + \tau_{w,y}\vec{j} + \tau_{w,z}\vec{k} \tag{4-1}$$

where $\tau_{w,x}$, $\tau_{w,y}$ and $\tau_{w,z}$ are the Cartesian components of the WSS vector in the x, y and z directions respectively. The magnitude of the WSS vector is calculated as

$$WSS = \left(\tau_{w,x}^2 + \tau_{w,y}^2 + \tau_{w,z}^2\right)^{\frac{1}{2}} \tag{4-2}$$

4.2.2 Wall Shear Stress Gradient

Contact with the stent struts and balloon damages and denudes the ECs during stent implantation. It is important that a new layer of ECs grow in these denuded locations to form a barrier between the blood and exposed sub-endothelial layer to stop the IH cascade [17, 118]. High WSSGs are likely to affect this process as healthy ECs have been shown to migrate downstream of an area where the WSSG is above 3000 N/m^3 [22] [123]. As such, there is likely to be less EC regrowth in areas of high WSSG in the stented artery. In computational studies, sites that are susceptible to IH have been correlated with sites where the WSSG has been predicted to exceed 200 N/m^3 in an end-to-side anastomosis model [58, 92] and a rabbit iliac model [64].

The WSSG is a measure of the spatial rate of change of the WSS vector and in a local coordinate system is calculated as

$$WSSG = \left[\left(\frac{\partial \tau_m}{\partial m}\right)^2 + \left(\frac{\partial \tau_n}{\partial n}\right)^2\right]^{\frac{1}{2}} \tag{4-3}$$

where m is the WSS direction and n is the direction tangential to the arterial surface and normal to m.

4.2.3 Wall Shear Stress Angle Gradient

ECs align with the flow direction creating a selective barrier to blood borne particles such as inflammatory cells [72]. Sudden directional changes in the WSS may lead to misalignment of these barrier cells resulting in increased permeability and risk of inflammation, a precursor of IH [127]. The WSSAG has been suggested to quantify these directional changes [70]. The magnitude of the WSSAG is calculated as

$$\mathrm{WSSAG} = \left[\left(\frac{\partial \phi}{\partial m} \right)^2 + \left(\frac{\partial \phi}{\partial n} \right)^2 \right]^{\frac{1}{2}} \tag{4-4}$$

where ϕ is the angular difference between of the time-averaged WSS vector at the node of interest $\vec{\tau}_o$ and corresponding vector at the neighbour node $\vec{\tau}_n$ and is computed as

$$\phi = \pm \mathrm{Cos}^{-1} \left(\frac{\vec{\tau}_o . \vec{\tau}_n}{|\vec{\tau}_o| |\vec{\tau}_n|} \right), \quad -\pi < \phi < \pi \tag{4-5}$$

for each of the neighbour nodes At the node of interest the value of ϕ is set to zero and the WSSAG is calculated. The WSSAG is mesh dependent at points of boundary layer separation and reattachment in the flow, with values tending towards infinity as the mesh spacing reduces to zero. To ensure only relevant WSSAG values are considered, an upper limit of 300 rad/mm is set on the variable. This approximately corresponds to the WSSAG magnitude created by the maximum angular difference possible between two WSS vectors (π) acting on two small (~ 10μm) adjacent ECs.

4.2.4 Oscillatory Shear Index

The OSI was originally proposed to evaluate regions of low oscillatory WSS in carotid arteries [56]. Regions of high OSI have been shown to be at greater risk of

arterial narrowing from lesion development [138]. Endothelial permeability to blood-borne particles is also shown to be increased with higher OSI [43] along with increased production of the gene endothelin-1 mRNA which increases cell proliferation [71]. It is therefore likely that sites of high OSI will be at an increased risk of IH in the stented artery. Although some regions of the coronary tree such as the left anterior descending (LAD) artery may exhibit some natural flow reversal over the cardiac cycle [91] the presence of a stent has been shown to greatly enhance the amount of OSI in certain parts of the artery [5, 99]. The OSI is calculated as

$$OSI = 1 - \frac{\left| \int_0^T \vec{\tau}_w dt \right|}{\int_0^T |\vec{\tau}_w| dt} \tag{4-6}$$

where T is the period of the cardiac cycle. The range of this variable is from 0 for unidirectional flow, to a maximum of 1 in areas of highly-altered fully-oscillatory WSS.

4.3 CFD Modelling of Haemodynamics in Stented Arteries

4.3.1 Introduction

This section contains a review of the recent literature published on CFD modelling of the haemodynamics in stented arteries. The ultimate goal of these reviewed CFD analyses is to provide reasons why some stents or stent locations are more prone to restenosis and IH than others. Restenosis rates have been shown to vary from one BMS design to another [2, 3, 53, 54, 93, 135]. IH has also been shown to be more prominent in certain locations in the stented artery [34, 36, 64, 74, 134]. Specific value ranges of the variables discussed in Section 4.2 are believed to encourage IH. Therefore, some investigators predict these variables and quantitatively assess

locations in the stented artery that fall inside the threshold of the "IH range". They may also qualitatively identify predicted features of the flow such as recirculation zones, separation and reattachment points to identify locations where IH may be accelerated.

Lead Author	Year	Reynolds No.	Wormersley No.	Timestep (ms)	Period (s)	Mesh nodes (n), elements (e)
Chen [16]	2009	-	-	-	-	-
Duraiswamy [26]	2009	130 (avg.)	2.80	8.57	0.86	640,008 e
Balossino [4]	2008	105 (avg.)	2.87	-	0.52	160,000 n
Duraiswamy [25]	2008	130 (avg.)	2.80	8.57	0.86	640,008 e
Banerjee [5]	2007	800 (peak)	2.32	0.1-1.0	0.80	650,000 e
Faik [29]	2007	240 (avg.)	2.80	-	0.80	192,000 e
LaDisa [59]	2006	105 (avg.)	2.91	8.00	0.54	500,000 n
Rajamohan [99]	2006	800 (peak)	2.32	0.1-1.0	0.80	650,000 e
He [42]	2005	50 - 240	5.00	8.57	0.86	279,083 e
LaDisa [62]	2005	105 (avg.)	2.91	8.00	0.54	250,000 n
LaDisa [63]	2005	105 (avg.)	2.91	8.00	0.54	250,000 n
LaDisa [64]	2005	105 (avg.)	2.91	8.00	0.54	-
Seo [111]	2004	200 (avg.)	2.80	-	-	99,492 n
Frank [33]	2002	-	-	7.81	-	-
Berry [7]	2000	-	-	-	-	-

Table 4-1: A list of the publications that are reviewed in this chapter. These publications all involve CFD modelling of blood flow through a stented coronary artery.

The research in this field is generally of a comparative nature. Some studies will compare two or more similar stent designs with a well defined difference in the model, for example comparing straight and curved arteries, different stent sizing or Newtonian versus non-Newtonian blood flow. In contrast, other studies investigate the effects of the stent design itself and compare different stents under the same modelling conditions. All of the work reviewed in this section is summarised in Table 4-1.

4.3.2 CFD Modelling

In one study, LaDisa et al. hypothesised that axial stent strut angle influences WSS and WSSG in the stented artery [62]. Their models consisted of stents deployed at

1.2 to 1 stent to artery ratio at lengths of 16 mm (ideal) and progressively foreshortened models of 14 mm and 12 mm lengths as shown in Figure 4-1(a). Thresholds for low WSS and high WSSG were set at 0.5 N/m^2 and 200 N/m^3 respectively at mean blood flow velocity. The main findings were that although the total area exposed to low WSS reduces with progressive foreshortening with 117 mm^2, 111 mm^2 and 96.8 mm^2, when normalised by the stented area there is an increase in normalised area exposed to low WSS with values of 0.71, 0.77 and 0.78 for the 16 mm, 14 mm and 12 mm lengths respectively. There was no significant difference in normalised area exposed to high WSSG with values of 0.54, 0.50 and 0.54 for the same three lengths respectively. However, the maximum WSSG increased with progressive foreshortening with values of 248 N/m^3, 293 N/m^3 and 395 N/m^3, again for the same three lengths respectively. Another finding was that under mean flow conditions the percentage of inter-strut area exposed to low WSS was greatest in the proximal area regardless of stent length or strut orientation. This study demonstrates that progressive strut misalignment with the flow direction increases normalised arterial wall area exposed to low WSS and elevates WSSG. The intuitive observation from this result is that stent struts should be aligned with the flow to reduce these effects. From an analysis perspective, it is interesting to note that the maximum WSSG has increased by almost 60% from the 16 mm stent to the 12 mm stent yet the normalised area with WSSG>200 N/m^3 is 0.54 for the two stents. This indicates that the distribution of the WSSG may not be fully elucidated by the threshold method.

Figure 4-1: (A) Three models of a stented coronary artery which are different lengths due to foreshortening from LaDisa et al. [62]. (B) Model of a stented coronary artery from Rajamohan et al. [99].

The geometric model in Figure 4-1(b) was used by Rajamohan et al. [99] and Banerjee at al. [5] in a joint study to compare the effect of developing versus developed flow in a stented coronary artery. Developing flow was simulated by imposing a transient plug flow at the inlet of the CFD model and was representative of flow through a stent deployed at the origin of a branched artery [99]. Developed flow was simulated with a transient parabolic velocity profile at the inlet [5]. This model represented flow through a stent implanted at a downstream region of a coronary artery. The velocity profiles near the entrance and exit are shown in Figure 4-2(a) and (b) respectively. The profiles are given at four different times for developed flow and at t = 2.0 s for developing flow which is the time of peak inlet velocity. For developed flow, a near parabolic velocity profile is observed with the peak velocity at the centre for all flow rates. For developing flow the peak velocity occurs close to the artery wall, near the entrance and exit. There is an 83% and 37% increase in the near wall velocity gradient at the inlet and outlet respectively from developed to developing hyperaemic flow of 200 ml/min at time = 2.0 s. The higher near wall velocity gradient at the inlet for developing flow accounts for the higher WSS magnitude of 53 N/m^2 predicted on the first strut intersection compared with the magnitude of 29 N/m^2 on the first strut intersection with developed flow.

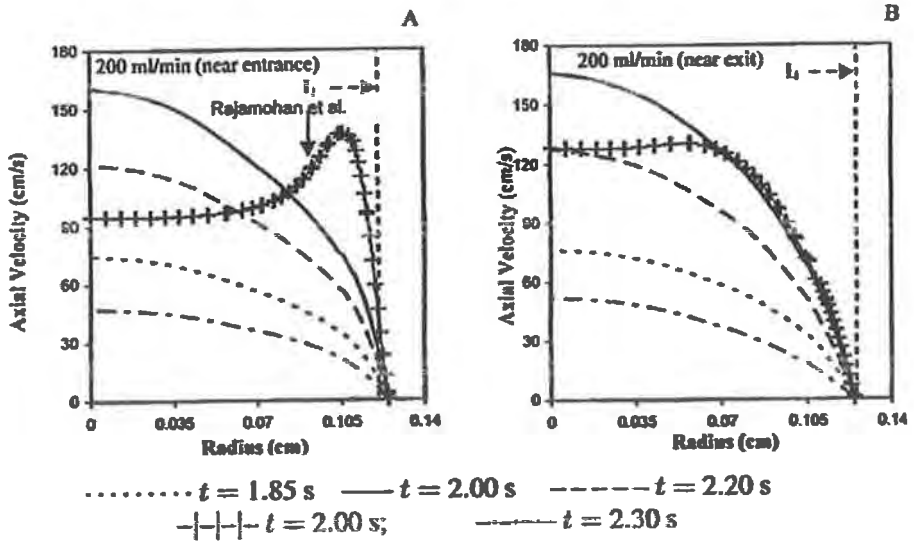

Figure 4-2: Velocity profiles from the centreline (0 cm) to the top of the stent wire (0.13 cm) at the (A) first and (B) last stent strut intersection for developing flow from Rajamohan et al. [99] and for developed flow from Banerjee et al. [5].

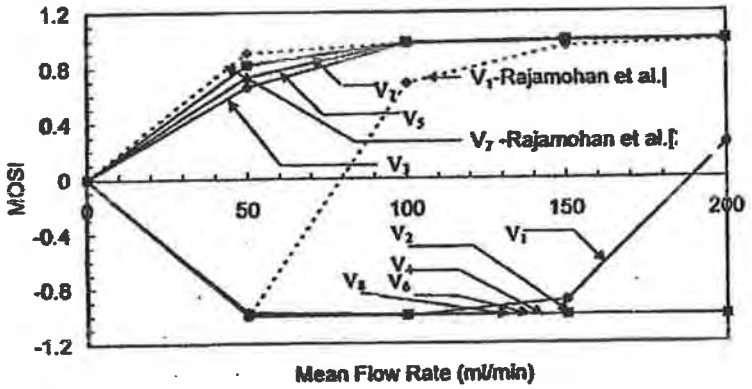

Figure 4-3: The MOSI for vertices V1 - V8 from the inlet to outlet respectively for flow rates 50, 100, 150 and 200 ml/min for developing flow from Rajamohan et al. [99]. Vertices V1 and V7 are also shown for developed flow from Banerjee et al. [5].

To further analyse the flow, the modified oscillatory shear index (MOSI) written

$$\mathrm{MOSI} = 1 - \frac{\int_0^T \vec{\tau}_w \, dt}{\int_0^T \left| \vec{\tau}_w \right| dt} \tag{4-7}$$

is plotted upstream and downstream of the four strut intersections which are shown

in Figure 4-1(b). These vertices are labelled V1-V8 from inlet to outlet respectively. For developed flow, MOSI values of nearly +1 and -1 are observed at the upstream and downstream of each strut intersection respectively for all flow rates as shown in Figure 4-3. This demonstrates that there is negative WSS at the downstream of each intersection (V2, V4, V6 and V8) and positive WSS at the upstream of each strut intersection (V3, V5 and V7) except near the entrance, where there is negative WSS for 50, 100 and 150 ml/min flow rates. These negative MOSI values signify recirculation zones downstream of each strut intersection for all flow rates and upstream of the first strut intersection for 50 ml/min with developing flow and with 50, 100 and 150 ml/min for developed flow. These studies have also shown that when compared with developed flow, maximum recirculation length and height downstream of strut intersections for developing flow are 100% and 50% higher respectively. These two studies highlight the significant impact of a stent's location in the artery on the local haemodynamic environment.

LaDisa et al. [61] investigated the haemodynamic effect of the stent deployment ratio, number of struts, strut thickness and strut width. One finding was that reducing strut thickness from 0.096 mm to 0.056 mm reduced the stented area exposed to low WSS from 2.4% to 0.3%, and reduced the stented area exposed to high WSSG from 38% to 32%. Keeping the strut thickness constant at 0.096 mm and reducing the width from 0.329 mm to 0.197 mm did not make significant differences with low WSS (2.4 vs 2.7%) and high WSSG (38 vs 37%) respectively. Maintaining constant strut width (0.197 mm) and thickness (0.096) and increasing from four struts to eight had an effect on the area of low WSS increasing it from 2.7% to 8.5% but the area of high WSSG remained the same for both at 37%. The most significant result of the study was produced by keeping the stent number (4), thickness (0.096

mm) and width (0.329 mm) constant and increasing the stent to artery deployment ratio from 1.1:1 to 1.2:1. This increased the area of low WSS from 2.4 to 25% but only increased the area of high WSSG from 38 to 39%.

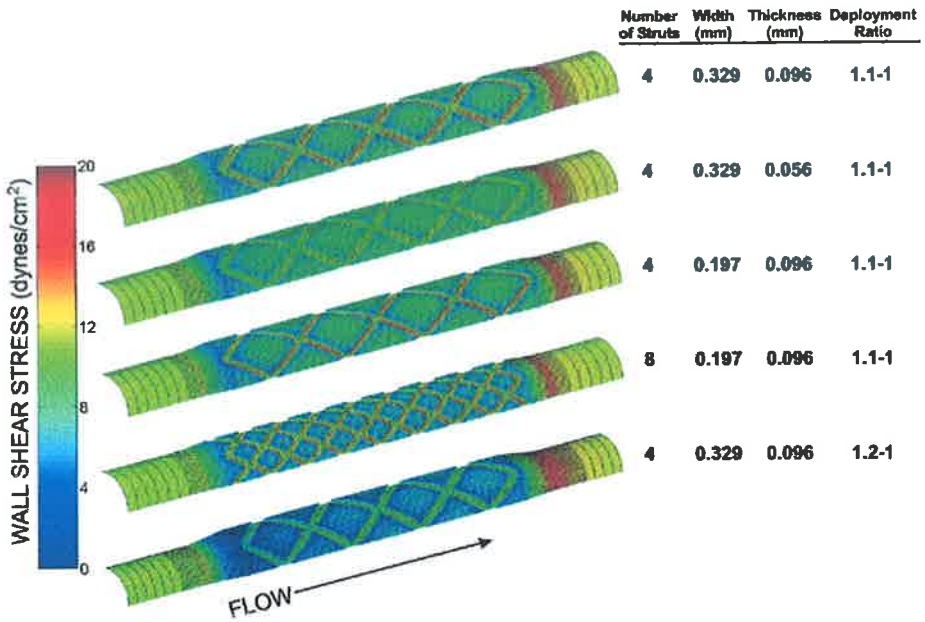

Figure 4-4: WSS contour plot from the results of a study by LaDisa et al. [61] examining the effect of deployment ratio, number of struts, strut thickness and strut width. WSS values given in Dynes/cm^2, where 1 N/m^2 = 10 Dynes/cm^2.

This study demonstrates the importance of modelling the stented artery as accurately as possible with regard to stent geometry and deployment ratio in particular, which has been shown to have a dramatic effect on the WSS result as shown in the contour plot in Figure 4-4. The study shows only minor differences in WSS and WSSG when comparing stents with a different number of struts, strut thickness and strut width. In light of the fact strut thickness [53, 93] and configuration [2, 3, 54, 67] affect the restenosis rate associated with the stent, it again seems plausible that this threshold method may have missed some of the detail of the altered WSS associated with these stents.

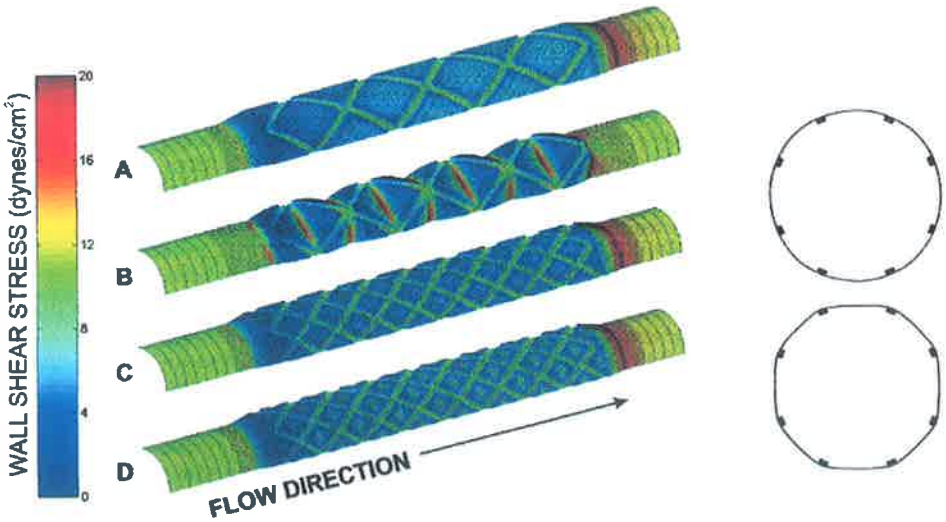

Figure 4-5: WSS Contour plot from the results of a study by LaDisa et al. [63] examining the effect of vascular deformation and number of struts. WSS values given in Dynes/cm^2, where 1 N/m^2 = 10 Dynes/cm^2.

Many investigators use a simplified circular arterial cross section when modelling the arterial wall [5, 29, 60, 62, 99]. LaDisa et al. have examined the effect of circumferential vascular deformation on a CFD model of the stented artery [63]. The models with circumferential vascular deformation were created simply by joining the vertices of the stent struts to make a polygonal shape as shown in Figure 4-5. Four-strutted and eight-strutted stents were compared in arteries of circular and polygonal cross section. The major finding was that the maximum WSSG was 221 N/m^3 with a circular cross section and 706 N/m^3 with a polygonal cross section of the artery with the four-strutted stents. The total area exposed to low WSS summed over six points in time in the cardiac cycle was 419.5 mm^2 and 437.2 mm^2 for four struts and 126.0 mm^2 and 117.4 mm^2 for eight struts with circular and polygonal cross sections respectively. The total area exposed to high WSSG summed over the same six points in time was 76.8 mm^2 and 100 mm^2 for four struts and 76.4 mm^2 and 89.2 mm^2 for eight struts with circular and polygonal cross sections respectively.

The results demonstrate that when vascular deformation is taken into consideration, having fewer struts leads to increased areas of low WSS and elevated WSSG. From a modelling perspective, these results show that simplifying the arterial cross section to a circular shape can introduce significant error in the results, particularly with regard to WSSG. Furthermore, major differences are evident between the WSS distributions of the circular and polygonal arterial cross sections with the four-strutted stent as shown in Figure 4-6. This is not sufficiently highlighted by the threshold method of WSS analysis which simply shows a 4% increase in area the exposed to low WSS.

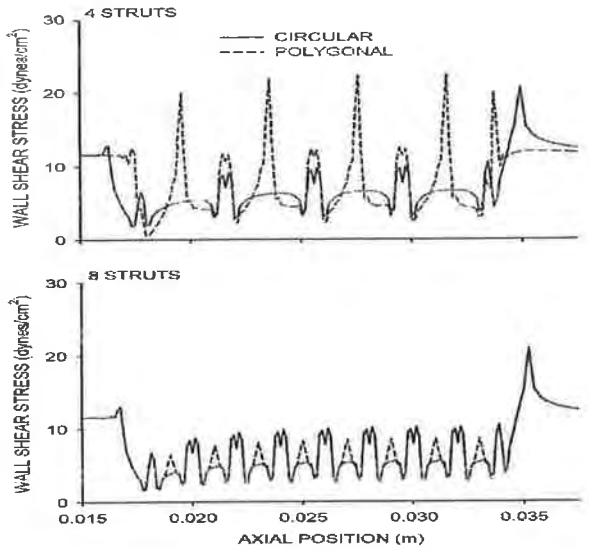

Figure 4-6: Axial plots demonstrating the influence of stent-induced vascular prolapse on WSS in an artery implanted with a four-strutted stent [63]. WSS values given in Dynes/cm^2, where 1 N/m^2 = 10 Dynes/cm^2.

The majority of the coronary arteries have some degree of curvature. Atherosclerotic lesions and IH are more prominent on the inner or myocardial curve of the artery [117, 134]. It has been demonstrated that the velocity profile tends to skew to the pericardial (outer) surface in curved arteries [98, 111]. Wentzel et al. demonstrated that implantation of a stent may cause straightening of the coronary artery segment where the stent is deployed [133]. This straightening of the artery

causes an increase in curvature of over 100% at the entrance and exit of the stented region. LaDisa et al. have attempted to quantify this effect on the WSS [59]. Two models were created and are shown in Figure 4-7, an artery stented with a flexible stent that conforms to the 20.3 mm radius of curvature of the artery and another stented with an inflexible stent which straightens the artery similar to that reported by Wentzel et al. [133]. The total area exposed to low WSS was similar for the two models with 29.0 mm^2 and 99.1 mm^2 for the flexible stent at peak and mean flow respectively and 24.4 mm^2 and 103.7 mm^2 for the inflexible stent at peak and mean flow respectively. The most interesting finding from this study was the WSS values which were time averaged over the cardiac cycle. These WSS values were examined in the centre of the first proximal and last distal diamond along the pericardial and myocardial luminal surfaces as shown in Table 4-2. Both models show very low WSS on the myocardial surface at the proximal end. The inflexible stent has high values of WSS on the proximal pericardial surface and the distal myocardial surface due to the reorientation of velocity profile as blood enters and leaves the region, respectively. The flexible stent allowed gradual transition from artery to stent and hence the velocity profile maintained its modest skewing toward the pericardial surface resulting in higher WSS values on that surface along the length of the stent. Previous work has shown that for a straight vessel implanted with a similar stent and conditions the time-averaged WSS has a value of 0.83 N/m^2 along the entire length of the stent [62]. The lower WSS values predicted on the myocardial surface and shown in Table 4-2, may account for the higher tissue growth in this region, particularly in the proximal region of the stent where the WSS is low regardless of stent flexibility. From the perspective of analysing the results, more conclusions can be drawn from the values of the time-averaged WSS at four locations on each stent

model than from the threshold analysis above which doesn't definitively distinguish between the stents.

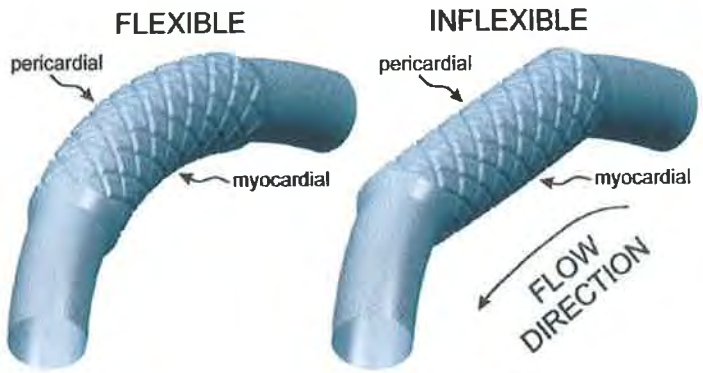

Figure 4-7: "Flexible" and "inflexible" models of a stented artery from LaDisa et al. [59].

Time-averaged	Proximal		Distal	
WSS [N/m²]	Pericardial	Myocardial	Pericardial	Myocardial
Flexible	0.89	0.49	1.15	0.89
Inflexible	1.17	0.43	0.83	1.26

Table 4-2: Values of time-averaged WSS in the centre of the first proximal and last distal diamond on the pericardial and myocardial surfaces for the "flexible" and "inflexible" models of a stented coronary artery from LaDisa et al. [59].

Chen et al. have examined the effect of stent undersizing on endothelial WSS and WSSG, as well as OSI [16]. Three CFD models were created with stent undersizing of 5%, 10% and 20%. As shown in Figure 4-8, the presence of the stent struts decreases the WSS and increases the WSSG along the arterial wall with the 5% undersized stent. The presence of the stent wires becomes less significant with the 10% undersized case as the WSS and WSSG get closer to the non-stented values. This trend is continued with the 20% undersized case with the WSS and WSSG approaching the non-stented value further (not shown).

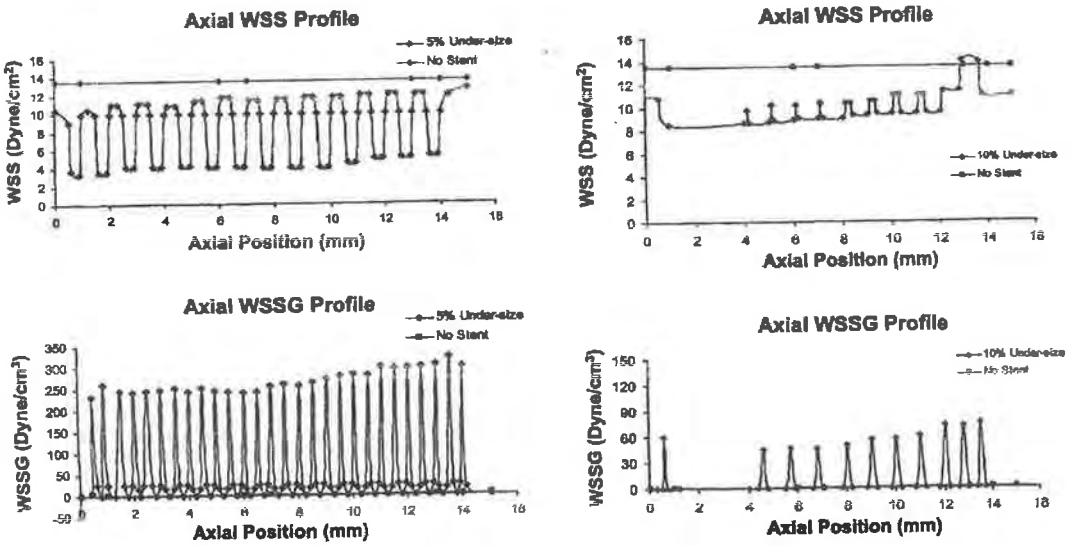

Figure 4-8: The effects of 5% and 10% stent undersizing on the axial WSS and WSSG from Chen et al. [16]. WSS values given in Dynes/cm^2, where 1 N/m^2 = 10 Dynes/cm^2.

The results also include von Mises stress distribution in the arterial wall for 10% and 20% oversized cases, but no CFD results are given for the oversized cases. Whilst the results show that undersizing the stent could increase the WSS and reduce the WSSG, in practice stent oversizing to ensure maximum patency is more common [67].

Seo et al. created models to investigate flow disturbances in 2D straight and curved vessels with Newtonian and non-Newtonian flow [111]. Their main finding with time-dependent flow is that regions of flow disturbance periodically increase and decrease in size. The primary impact of the non-Newtonian properties of the blood is to reduce the size of the flow separation downstream of the stent by approximately 8%.

Faik et al. have conducted time-dependent 3D simulations of a stented artery to study the characteristics of blood flow and shear rate [29]. The results show significant secondary flow in an annulus region near the artery wall as well as low

shear rates on the artery wall near the struts and high shear rates on the tips of the struts.

He et al. have conducted a parametric comparison of strut design patterns which are illustrated in Figure 4-9 [42]. The near-strut region of the artery wall is usually denuded of most ECs during the stenting procedure and it is possible that the major influence of the blood flow on new tissue growth is through transport of particles to the artery wall. The inter-strut region is likely to retain most of the WSS sensitive ECs during stenting, provided they have not been damaged by the balloon. It is therefore important to quantify WSS and also flow separation in the inter-strut region, as both can influence tissue growth through IH. To this end, the flow separation parameter (FSP) was introduced by He et al. [42] and is written

$$\varphi = \frac{T_s}{T} \tag{4-8}$$

where T_s is the amount of time the flow is separated and T is the duration of the cardiac cycle. Flow separation is defined by He et al. [42] as occurring when the angle between the WSS vector and the mean flow direction is greater than 90°. The FSP has also been modified for low flow conditions to account for the natural WSS oscillation as follows:

$$\varphi = \frac{T_P \varphi_{Pos} + T_N \varphi_{Neg}}{T} \tag{4-9}$$

where φ_{Pos} is the separation parameter during the time of forward mainstream flow T_p, φ_{Neg} is the separation parameter during the time of reverse mainstream flow T_N, and T is the total time of the flow cycle ($T = T_P + T_N$). Blood was modelled as a homogeneous Newtonian incompressible fluid. The model had rigid wall boundaries

and a sinusoidal input velocity. A significant finding was that within the narrow band of model (b) in Figure 4-9 the mean axial WSS was very low at approximately 0.2 N/m^2, and the mean traverse WSS (normal to the axial direction) was approximately 30% higher than that of model (a). Increasing the axial distance between the struts, h, to 3.6 mm increased the degree to which axial WSS was restored between the struts in model (c) and reduced the traverse WSS by ~40%. Increasing the axial strut length, f, did not significantly increase axial or decrease traverse WSS. One of the most significant recommendations of this study was that the longitudinal distance between adjacent rows of struts should be maximised to restore WSS values between the struts. This has the effect of decreasing the FSP between the struts as shown in Figure 4-10 below.

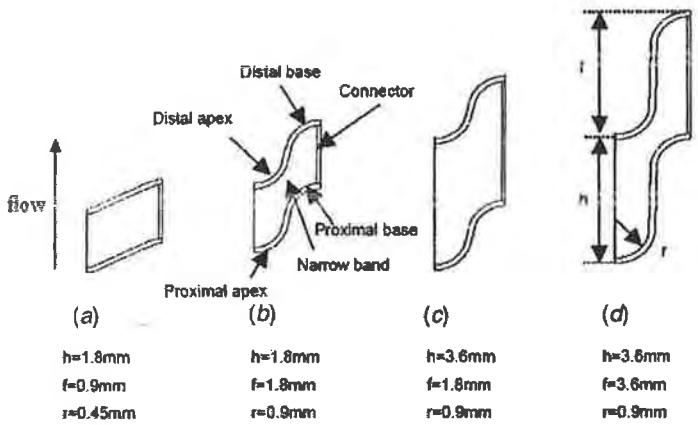

Figure 4-9: Stent strut configurations studied by He et al. in a parametric comparison of strut design patterns [42]. The parameters are r, the strut radius, h, the axial distance between the struts and f, the axial strut length.

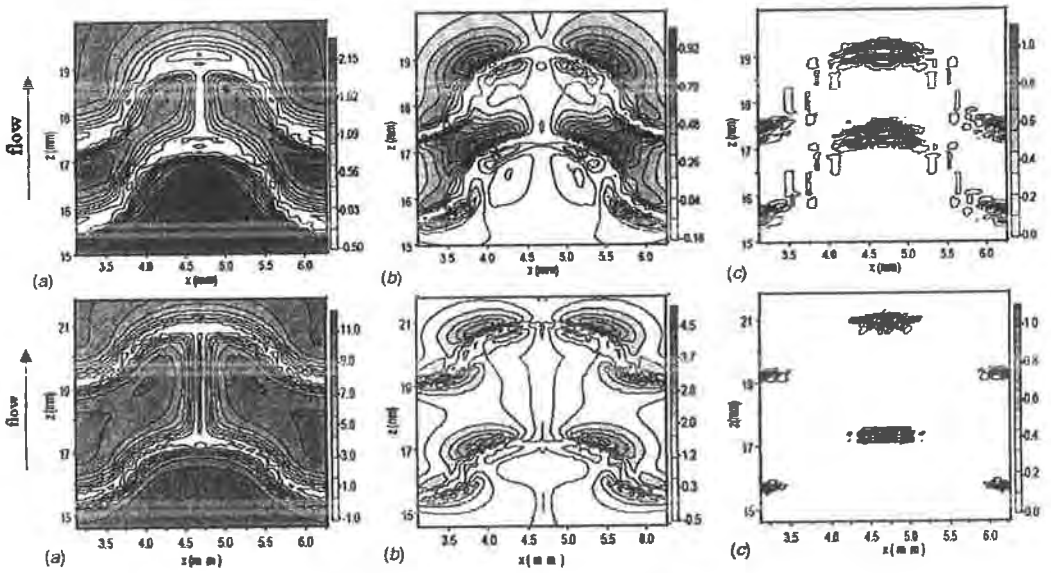

Figure 4-10: (a) Axial WSS (b) traverse WSS and (c) FSP for two different stent strut configurations from He et al. [42]. WSS values given in Dynes/cm^2, where 1 N/m^2 = 10 Dynes/cm^2.

Frank et al. [33] conducted an *in vitro* platelet adhesion experiment in conjunction with a 2D CFD analysis to determine the effect of stent strut spacing on WSS, the FSP and platelet deposition. The lowest platelet deposition occurred at the shortest spacing of 2.5H (2.5 x strut height) with approximately double the platelet deposition at strut spacing of 4H and 7H as shown in Figure 4-11. Figure 4-12 shows the WSS was low and reversed in direction from the main flow for 2.5H and 4H spacing and only restored between the two struts for the largest strut spacing. The FSP was one everywhere between the two struts for the smallest spacing and had a value of zero for the majority of the space between the struts for the largest spacing as shown in Figure 4-13. As the spacing increased, there was flow reattachment between the struts which reduced the FSP. However, this reattachment transported platelets into the region between the two struts. This is an undesirable result as platelet accumulation around the stent struts is likely to increase the volume of IH. On the other hand, the ECs are more likely to be functional and prevent IH with the

larger spacing since the WSS has been restored. It can also be seen from Figure 4-11 and Figure 4-12 that there is increased platelet deposition whether the WSS is low (4H spacing) or high (7H spacing). These results are consistent with the conclusions of Berry et al. that flow reattachment occurs after a strut spacing of six diameters for a circular strut [7].

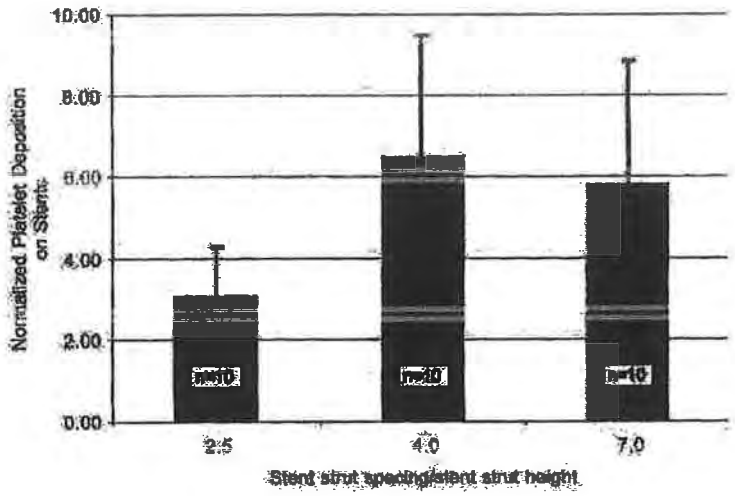

Figure 4-11: Inter-strut platelet deposition for three different ratios of stent strut spacing to stent strut height.

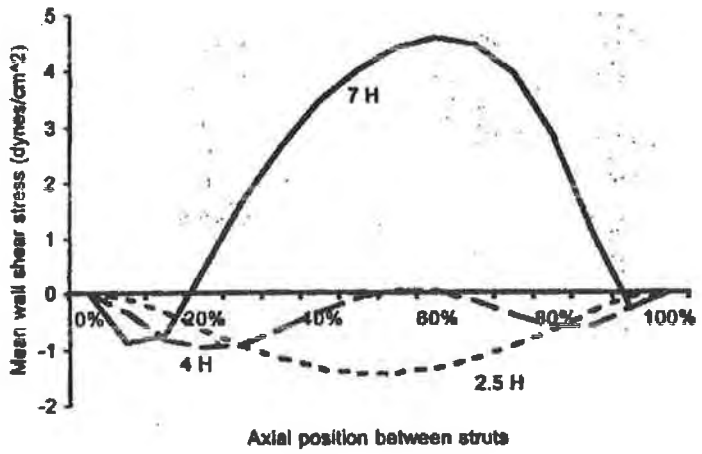

Figure 4-12: Mean inter-strut WSS values for three different ratios of stent strut spacing to stent strut height. WSS values given in Dynes/cm^2, where 1 N/m^2 = 10 Dynes/cm^2.

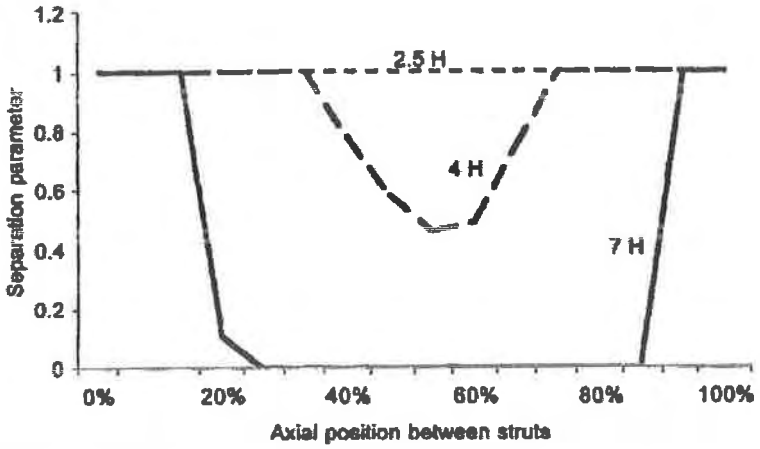

Figure 4-13: Inter-strut FSP values for three different ratios of stent strut spacing to stent strut height.

Duraiswamy et al. extended this work to four commercially available stents [26]. They created models of single units of the Wallstent (Boston Scientific), the Bx stent, Aurora stent and the NIR stent. The stents were modelled as single unit cells on a flat rigid surface and the computational domain had a sinusoidal input velocity with a frequency of 1.1 Hz. The main results are listed in Table 4-3 below. The time-averaged WSS was lowest for the Wallstent with a value of 0.29 N/m^2 and similar for the other three with values of 0.50, 0.53 and 0.58 N/m^2 for the Aurora, NIR and Bx stents respectively. The Wallstent had over 90% and 100% of its stented area with low WSS and high WSSG respectively for over 50% of the cardiac cycle. These are significantly poorer haemodynamic characteristics produced by the Wallstent compared to the other three. However, the low WSS threshold does not significantly distinguish between the Aurora, NIR and Bx stents, with the high WSSG threshold slightly favouring the Bx stent. Another significant finding from this study was the percentage stented area with FSP > 0.5 for over 50% of the cardiac cycle. The Bx stent had 20.4% which is relatively high compared to 5.5%, 5.2% and 0.6% for the Aurora, NIR and Wallstent stents respectively. This finding is explained by a coinciding *in vitro*/CFD study [25] detailed below.

Stent	Wallstent	Bx	Aurora	NIR
TAWSS [N/m^2]	0.29	0.58	0.50	0.53
WSS < 0.5 N/m^2 (>50%T) [%]	90.5	59.3	57.1	58.7
WSSG > 200 N/m^3 (>50%T) [%]	100.0	75.0	82.8	87.9
FSP > 0.5 (>50%T) [%]	0.6	20.4	5.5	5.2

Table 4-3: Indices of mean time-averaged WSS and normalised stented area with WSS below 0.5 N/m^2, WSSG above 200 N/m^3 and FSP above 0.5 for greater than 50% of the cardiac cycle, T, for the Wallstent, Bx, Aurora and NIR stents from Duraiswamy et al. [26].

The *in vitro* model of a repeating unit of the Wallstent, Bx, Aurora and NIR stents from Duraiswamy [25] examined platelet deposition inside the stent unit. Further CFD analyses were also used to examine the streamlines of the flow in the near wall region of the strut unit. The CFD methodology was the same as that in the previous CFD study of the WSS, WSSG and FSP [26]. The main finding was that there were regions of constant flow separation distal and proximal to the struts P (proximal) and D (distal) respectively as shown in Figure 4-14. These constant separation regions exhibited very low platelet deposition. Figure 4-15 shows the platelet deposition was highest downstream of the recirculation regions; this is likely due to advection towards the artery wall in this region. The streamlines also revealed complex helically recirculating flow patterns near the S-shaped axial connector of the Bx stent which is shown in Figure 4-16. This would explain the high FSP values associated with this stent in the previous CFD study [26]. Interestingly, Duraiswamy [24] has shown that platelet deposition to be quite high in this connector region even though the WSS is low. The helical flow patterns are likely to transport and trap the particles in this region. It has therefore been shown that platelet deposition can be high in areas of high [33] and low [24, 33] WSS with the biggest risk factor for high platelet deposition being streamlines of flow toward the wall and complex recirculating flow patterns [25].

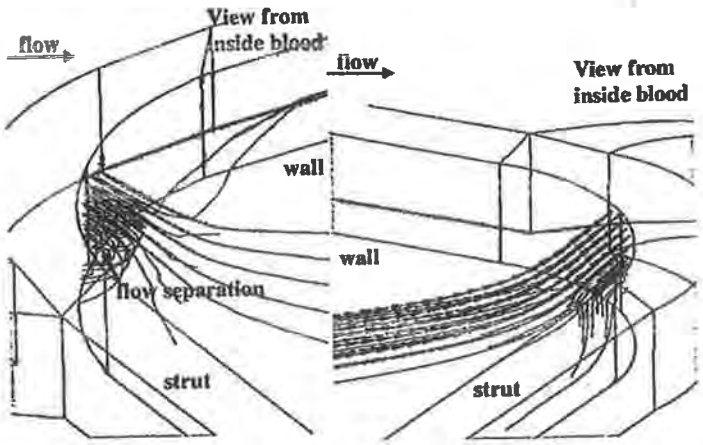

Figure 4-14: Flow separation distal to strut P and proximal to strut D with the Bx stent from Duraiswamy et al. [25].

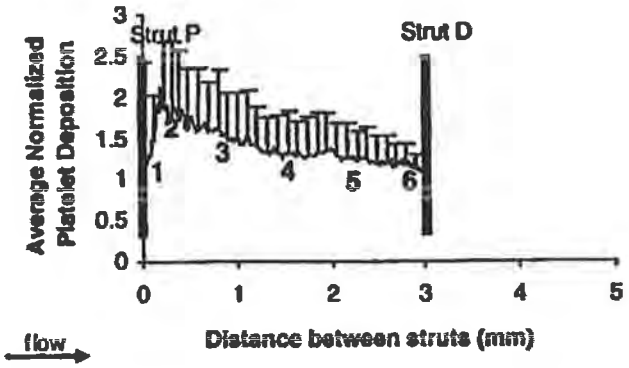

Figure 4-15: Platelet deposition between the stent struts of the Bx stent from Duraiswamy et al. [25]. There is low platelet deposition distal to strut P and proximal to strut D where the flow separation occurs as shown in Figure 4-14.

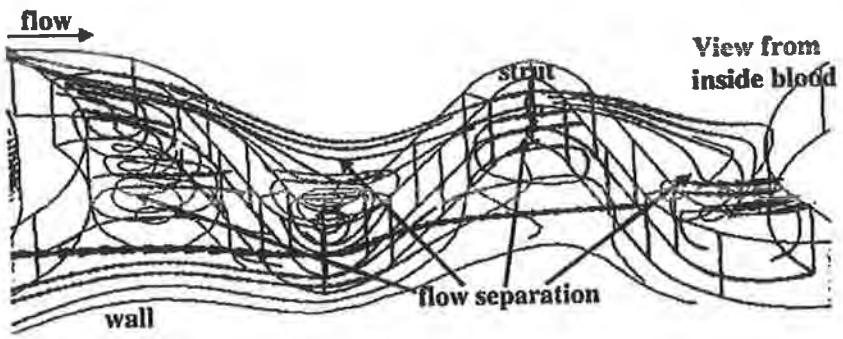

Figure 4-16: Instantaneous streamlines near the S-shaped axial connector of the Bx stent showing complex helically recirculating flow patterns.

Balossino et al. [4] have also compared four commercially available stent designs. In this paper, stents A, B, C and D correspond to the Bx stent, Jostent Flex, Sorin Carbostent (Sorin Biomedica, Saluggia, Italy) and PS stent respectively. They used finite element analysis (FEA) to model the expansion of a single unit of each stent into separate arteries containing idealised plaques. The rigid shape of deformed stent, artery and plaque was then used to define the boundaries of the CFD domain. A canine blood flow velocity waveform [63] was applied at the inlet. The most interesting result was that there was not significant variation in the results between the different stent models as shown in Figure 4-17. The time-averaged value of percentage of vessel area below 0.5 N/m^2 was 57.8% for stent A and 57.3% for stent B. They also demonstrated that the highest WSS exists on the stent struts throughout the cardiac cycle. Thicker struts were also shown to slightly decrease the area subjected to low WSS<0.5 N/m^2 over the cardiac cycle from 60.6% to 57.3%. A disadvantage of this study was the only parameters used to differentiate between the stents were low and maximum WSS.

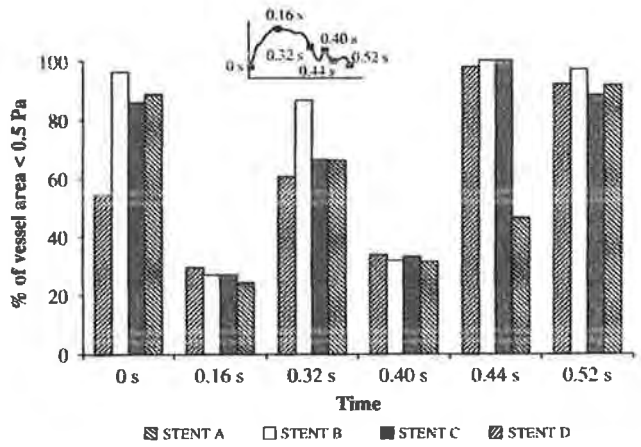

Figure 4-17: Histograms of the percentage of vascular wall surface with WSS values lower than 0.5 N/m² for the four stents at six time intervals from Balossino et al. [4]. Stents A, B, C and D correspond to the Bx stent, Jostent Flex, Sorin Carbostent and PS stent respectively.

4.3.3 Conclusions

A large amount of information has been provided from LaDisa et al. regarding the effects of realistic features in the model of a stented artery, including stent deployment ratio, vascular deformation and curvature. The combined efforts of Banerjee et al. [5] and Rajahmon et al. [99] demonstrated the importance of applying boundary conditions that match the arterial location to be modelled, as the difference between developed and developing flow is quite substantial in relation to the effect on the WSS. Seo et al. have shown that even in large vessels (>3 mm) the non-Newtonian effects of the blood are important when a stent is present in the vessel. With regard to the geometric influence of the stent, He et al. have demonstrated that increasing the distance between the struts restores the WSS and reduces the recirculation in the inter-strut region. However, Frank et al. showed that restoring the WSS also increases the platelet deposition in this region.

Some of the reviewed studies have shown evidence of stent-induced haemodynamic disturbance such as dramatic changes in: maximum WSSG values [62, 63], plots of WSS [63] and time-averaged WSS values [59] between different stents. Other studies [4, 26, 61] have examined different stent designs which have different *in vivo* restenosis rates, suggesting different levels of altered WSS. Yet, the majority of results from these studies (summarised in Table 4-4) have shown only minor differences between the stents using the threshold method of analysis. These results strengthen the argument that a more complete method of analysis is necessary to fully elucidate the stent-induced alterations to the arterial WSS.

Study Design	Model	WSS<0.5N/m²	WSSG>200N/m³
The effects of stent foreshortening. LaDisa et al. [62]	16 mm stent	71.0%	54.0%
	14 mm stent	77.0%	50.0%
	12 mm stent	78.0%	54.0%
The effects of stent design. LaDisa et al. [61]	Stent thickness 0.096 mm	2.4%	38.0%
	Stent thickness 0.056 mm	0.3%	32.0%
	Stent width 0.329 mm	2.4%	38.0%
	Stent width 0.197 mm	2.7%	37.0%
	Stent with 4 struts	2.7%	37.0%
	Stent with 8 struts	8.5%	37.0%
	Stent deployment ratio 1.1:1	2.4%	38.0%
	Stent deployment ratio 1.2:1	25.0%	39.0%
The effects of stent design and vascular deformation. LaDisa et al. [63]	Stent with 4 struts (Circular artery)	419.5 mm²	76.8 mm²
	Stent with 4 struts (Polygonal artery)	437.2 mm²	100.0 mm²
	Stent with 8 struts (Circular artery)	126.0 mm²	76.4 mm²
	Stent with 8 struts (Polygonal artery)	117.4 mm²	89.2 mm²
The effects of stent flexibility. LaDisa et al. [59]	Flexible stent (peak flow)	29.1 mm²	-
	Inflexible stent (peak flow)	24.4 mm²	-
	Flexible stent (mean flow)	99.1 mm²	-
	Inflexible stent (mean flow)	103.7 mm²	-
The effects of stent design. Duraiswamy et al. [26]	Wallstent	90.5%	100.0%
	Bx stent	59.3%	75.0%
	Aurora stent	57.1%	82.8%
	NIR stent	58.7%	87.9%
The effects of stent design. Balossino et al. [4]	Bx stent	57.8%	-
	Jostent Flex	57.3%	-
	Strut thickness 0.05 mm	60.6%	-
	Strut thickness 0.15 mm	57.3%	-

Table 4-4: Brief summary of the results from recent publications which use the threshold method to analyse the haemodynamic effect of stent implantation.

4.4 Summary

This chapter outlines the relevance and mathematical descriptions of the WSS-based variables employed in this work to quantify the altered WSS in the stented artery. The use of some of these variables is examined in the literature review contained in the second half of this chapter. Particular focus is placed on work where these variables are analysed using the threshold method of analysis, which is shown to do little to distinguish between alterations to the WSS induced by different stents. The

CHAPTER 6

Results

6.1 Introduction

This chapter contains the main body of results obtained from the numerical prediction of the haemodynamics in a stented coronary artery. In these results, numerical predictions are produced for the three different stents: PS, GR-II and Bx, each implanted separately in the LAD coronary artery. The first two sections contain the results of a mesh convergence study and timestep convergence study, conducted to ensure sufficient accuracy of the computational model. The results from the transient numerical analysis of the three stents above are then presented in Section 6.4. This main section of the results is divided into four subsections, one for each of the WSS-based variables: WSS, WSSG, WSSAG and OSI.

6.2 Mesh Convergence Study

As discussed in the previous chapter, the computational domains are discretised using an unstructured mesh topology for the PS, GR-II and Bx stents. A mesh convergence study is conducted for all stents to ensure the results are independent of the computational mesh density. The steady-state CFD analysis employed in each mesh convergence study is the same as that described in Section 5.3.4. Results are considered mesh converged when the difference in the RMS value of WSS between successive mesh densities is less than 1% along sample lines in the domain. Two sample lines are chosen for each stent and their locations are shown in Figure 6-1 for

the PS, GR-II and Bx stents. The mesh density is varied by changing the maximum allowable element edge length on the stent struts between 35 and 20 μm. Elements on the struts have a minimum allowable edge length of 1 μm to allow adequate resolution of any complex geometric features. Elements in the centre of the artery have a maximum edge length of 200 μm. Three meshes are created for both the PS and GR-II stents and two meshes are created for the Bx stent. The details of the meshes are given in Table 6-1. Table 6-2 contains the results of the mesh convergence study and shows that mesh convergence as defined above is achieved between Mesh 1 and 2 for both the PS and GR-II stents. However, to ensure the similar results between Mesh 1 and 2 are not a symptom of too small an increase in mesh density, a third, denser mesh is created for both stents. Again, there is no significant change in the results between Mesh 2 and 3 for either stent and so mesh convergence has been achieved. The numerical analysis is therefore conducted on Mesh 3 for both the PS and GR-II stents. The Bx stent required Mesh 1 to be quite dense in order to resolve the geometry of the stent. Mesh 2, which is significantly bigger than Mesh 1, produced no significant change in results and therefore mesh convergence has been achieved for the Bx stent model and the numerical analysis is conducted on Mesh 2. Generally in a CFD analysis a very coarse mesh is used initially, with mesh convergence apparent as the results converge after several mesh refinements. This approach is not possible here as the initial mesh needs to be quite refined for adequate resolution of the stent and artery wall. However, the evidence from the mesh convergence study suggests that any further mesh refinement would not produce any significant change in the results and therefore the mesh resolution is sufficient. Plots of the WSS along the sample lines used in the mesh convergence study are shown in Figure 6-2 and Figure 6-3 for the PS stent. Figure 6-4 shows

images of the mesh chosen (Mesh 3) for the numerical analysis of the PS stent. The same results are shown in Figure 6-5 through to Figure 6-10 for the GR-II and Bx stents respectively. Mesh convergence is achieved with 4,551,484, 3,038,536 and 5,840,890 elements for the PS, GR-II and Bx stents respectively.

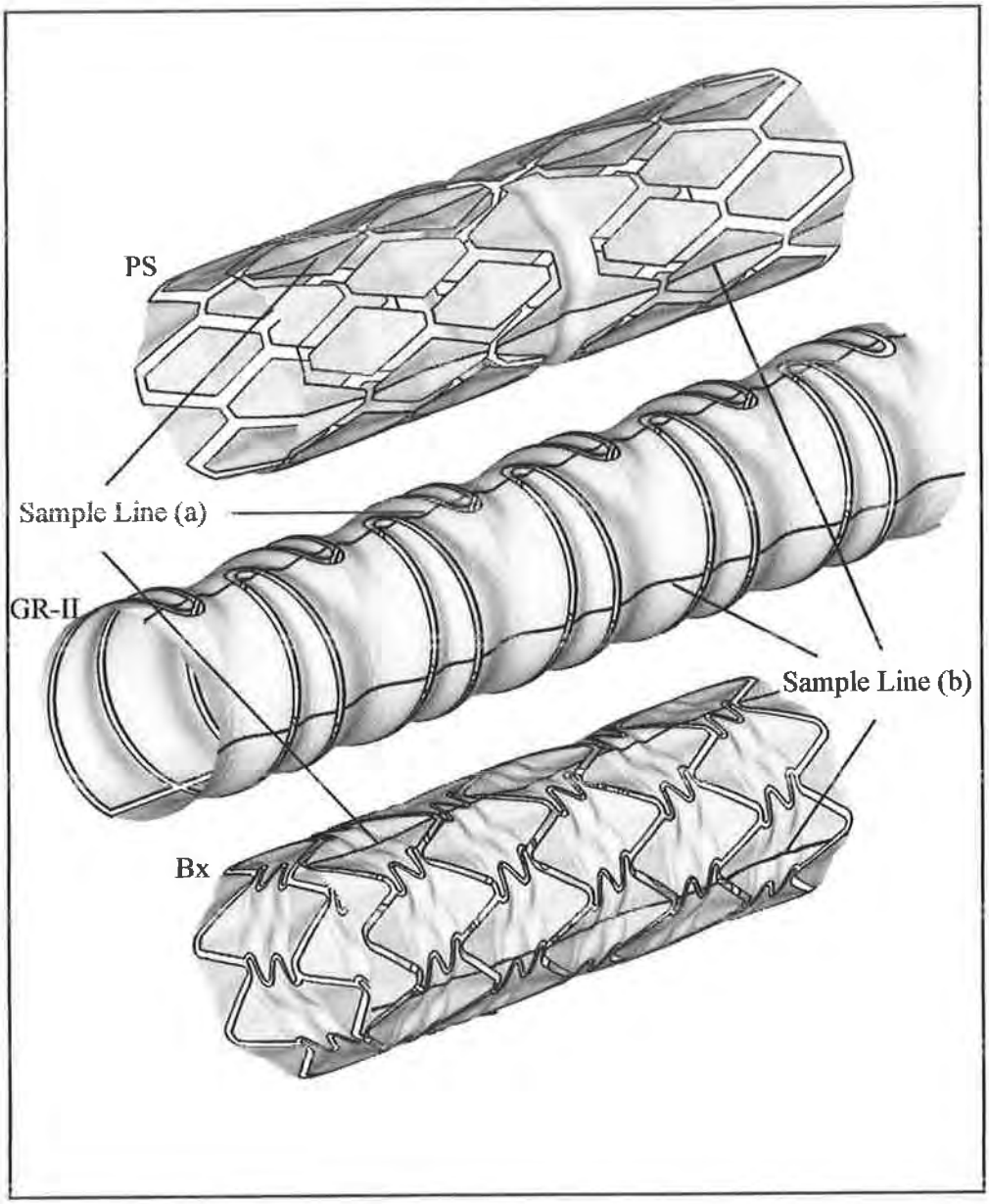

Figure 6-1: Sample lines (a) and (b) used in the mesh convergence study of the PS (top), GR-II (middle) and Bx (bottom) stent models.

Mesh		PS	GR-II	Bx
1	nodes	515,925	435,456	918,714
	elements	2,741,719	2,238,670	4,865,169
2	nodes	778,825	493,947	1,100,608
	elements	4,149,976	2,548,027	5,840,890
3	nodes	854,154	592,033	-
	elements	4,551,484	3,038,536	-

Table 6-1: Mesh densities of the PS, GR-II and Bx stent models used in the mesh convergence study.

Stent	Sample Line	Mesh	WSS (RMS) [N/m²]	% Difference
PS	a	1	0.9381	-
		2	0.9469	0.9
		3	0.9498	0.3
	b	1	1.0141	-
		2	1.0170	0.3
		3	1.0206	0.4
GR-II	a	1	0.6926	-
		2	0.6932	0.1
		3	0.6947	0.2
	b	1	0.7292	-
		2	0.7311	0.3
		3	0.7295	-0.2
Bx	a	1	0.5421	-
		2	0.5429	0.1
	b	1	0.5957	-
		2	0.5932	-0.4

Table 6-2: Results of the mesh convergence study for the PS, GR-II and Bx stent models.

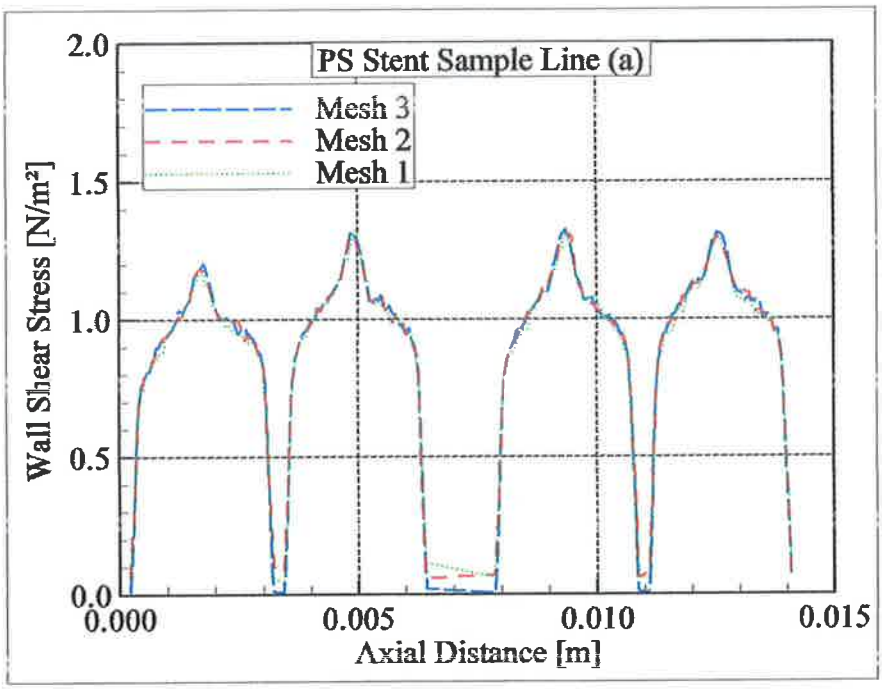

Figure 6-2: Plot of the WSS versus axial distance along sample line (a) of the PS stent model for three different mesh densities.

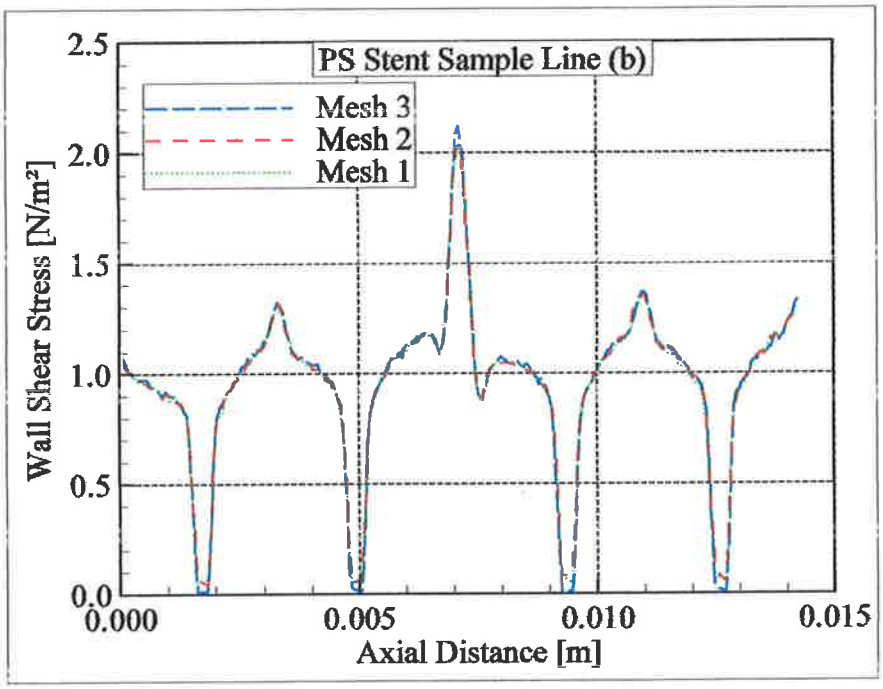

Figure 6-3: Plot of the WSS versus axial distance along sample line (b) of the PS stent model for three different mesh densities.

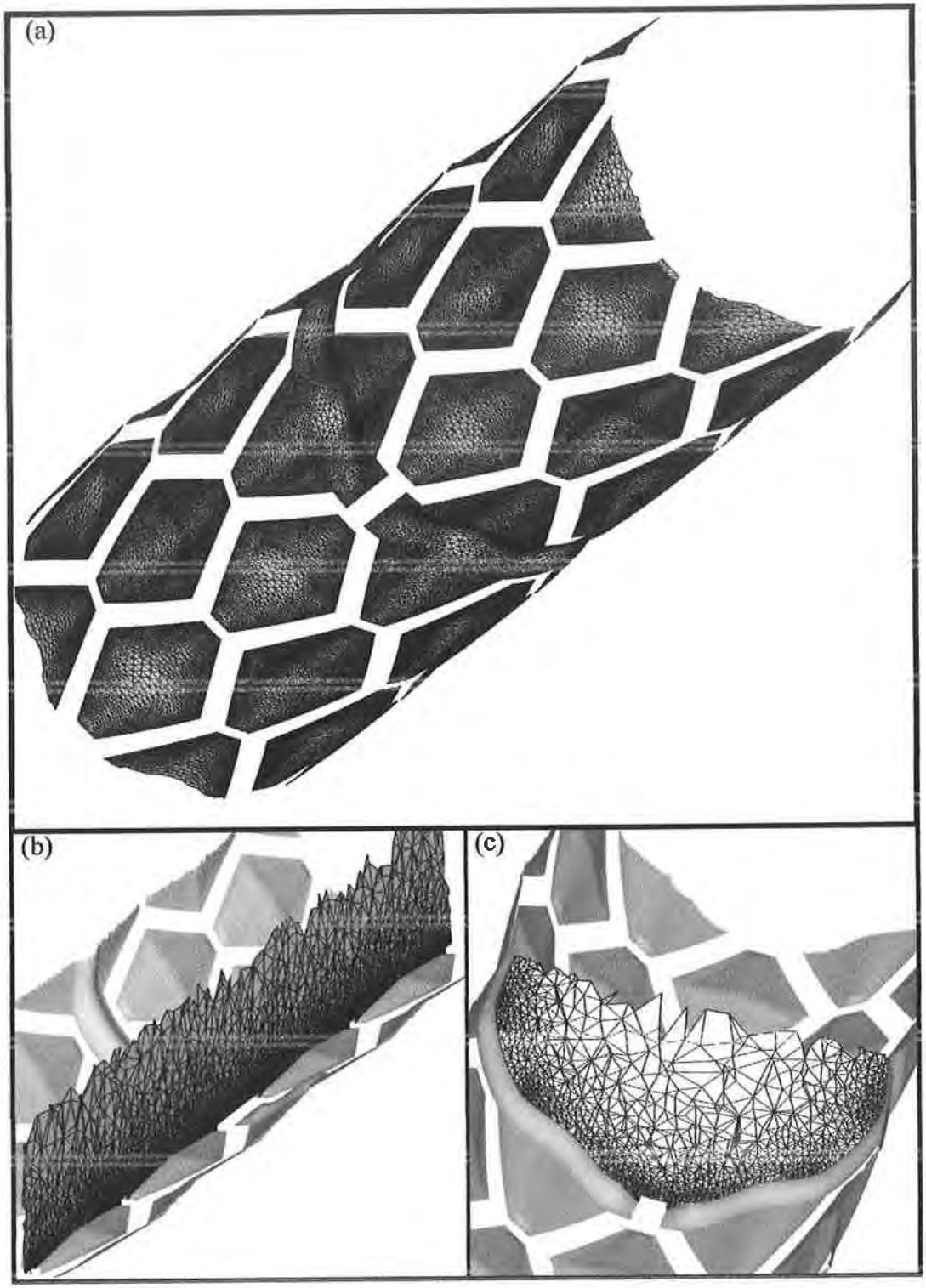

Figure 6-4: Mesh used (Mesh 3) in the numerical analysis of the PS stent model. The plots show (a) the surface mesh on the artery wall with (b) axial and (c) radial slices of the volume mesh.

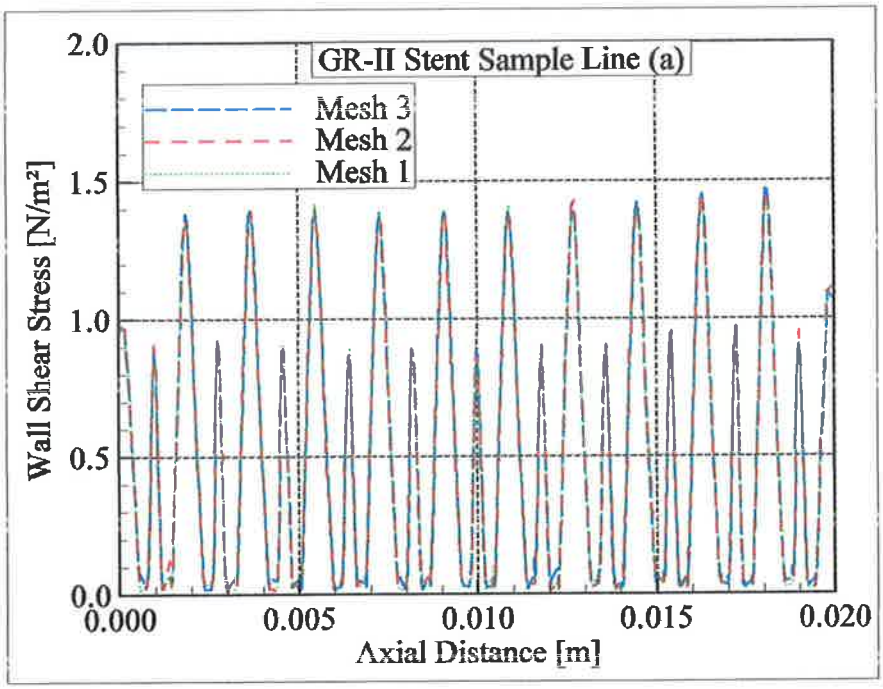

Figure 6-5: Plot of the WSS versus axial distance along sample line (a) of the GR-II stent model for three different mesh densities.

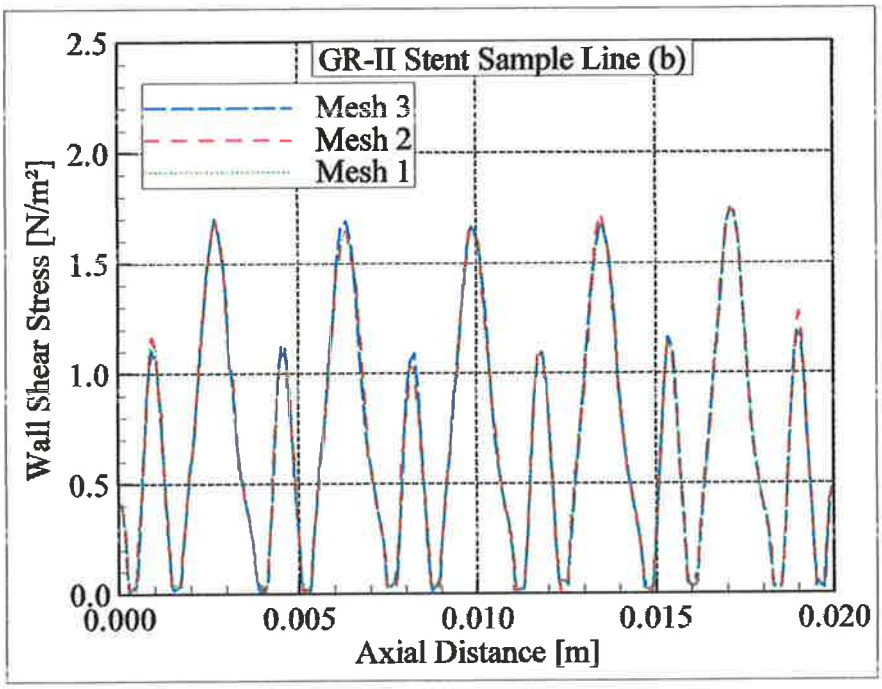

Figure 6-6: Plot of the WSS versus axial distance along sample line (b) of the GR-II stent model for three different mesh densities.

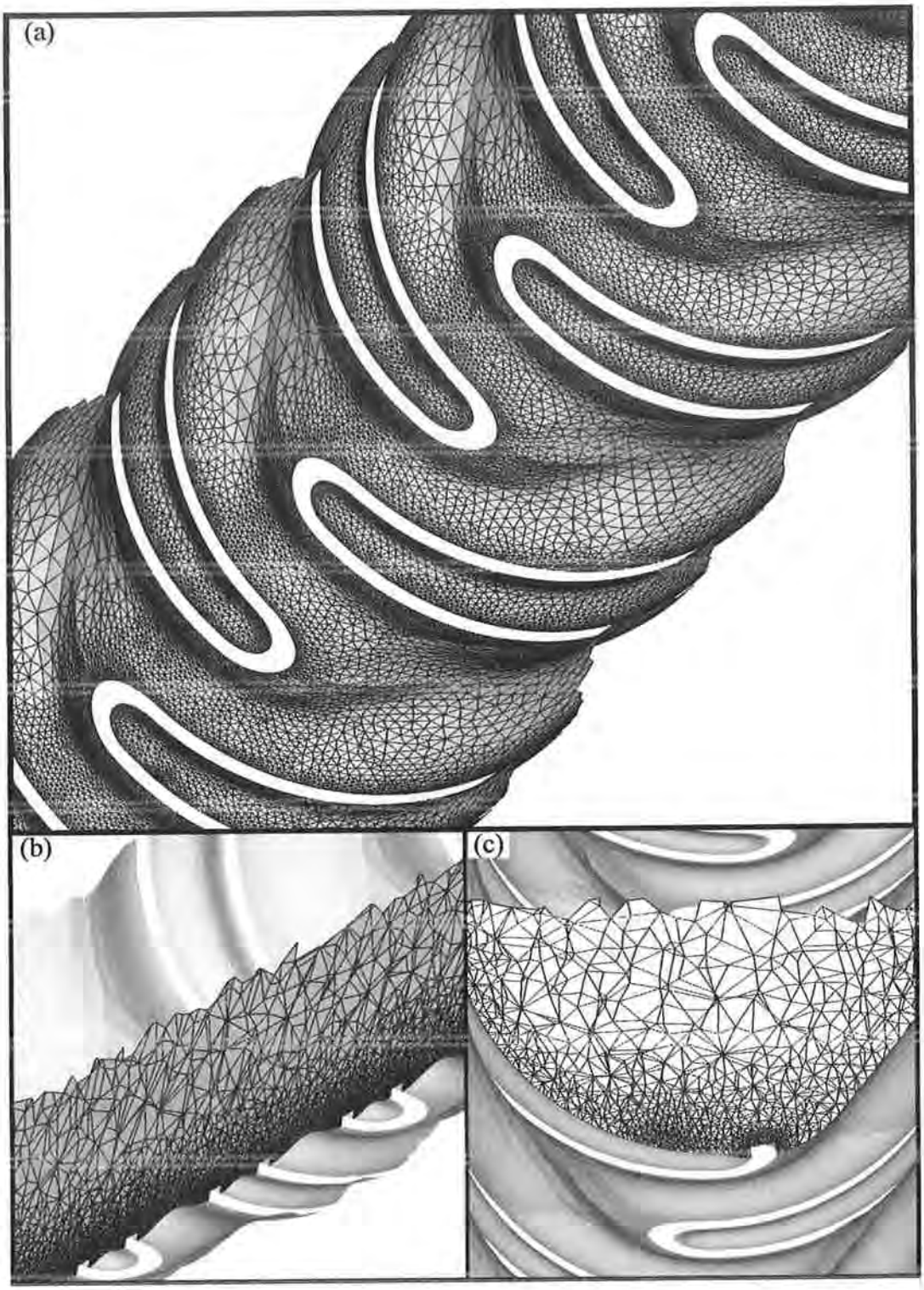

Figure 6-7: Mesh used (Mesh 3) in the numerical analysis of the GR-II stent model. The plots show (a) the surface mesh on the artery wall with (b) axial and (c) radial slices of the volume mesh.

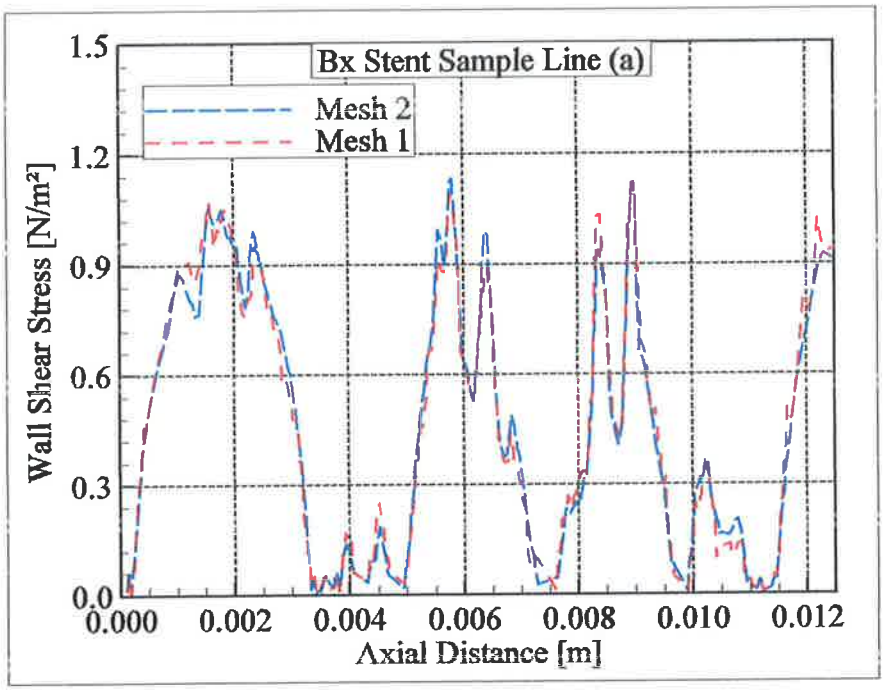

Figure 6-8: Plot of the WSS versus axial distance along sample line (a) of the Bx stent model for two different mesh densities.

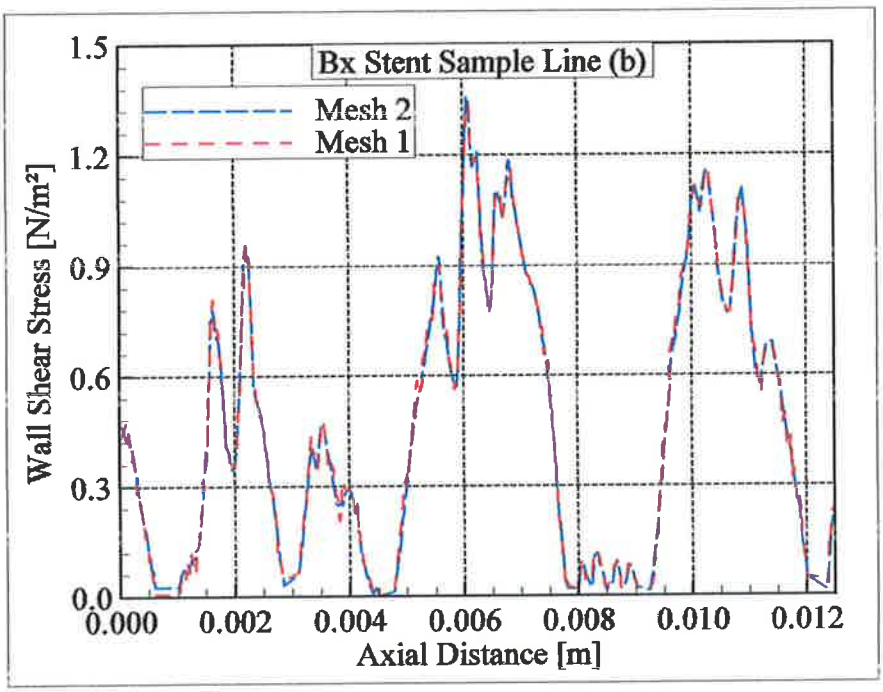

Figure 6-9: Plot of the WSS versus axial distance along sample line (b) of the Bx stent model for two different mesh densities.

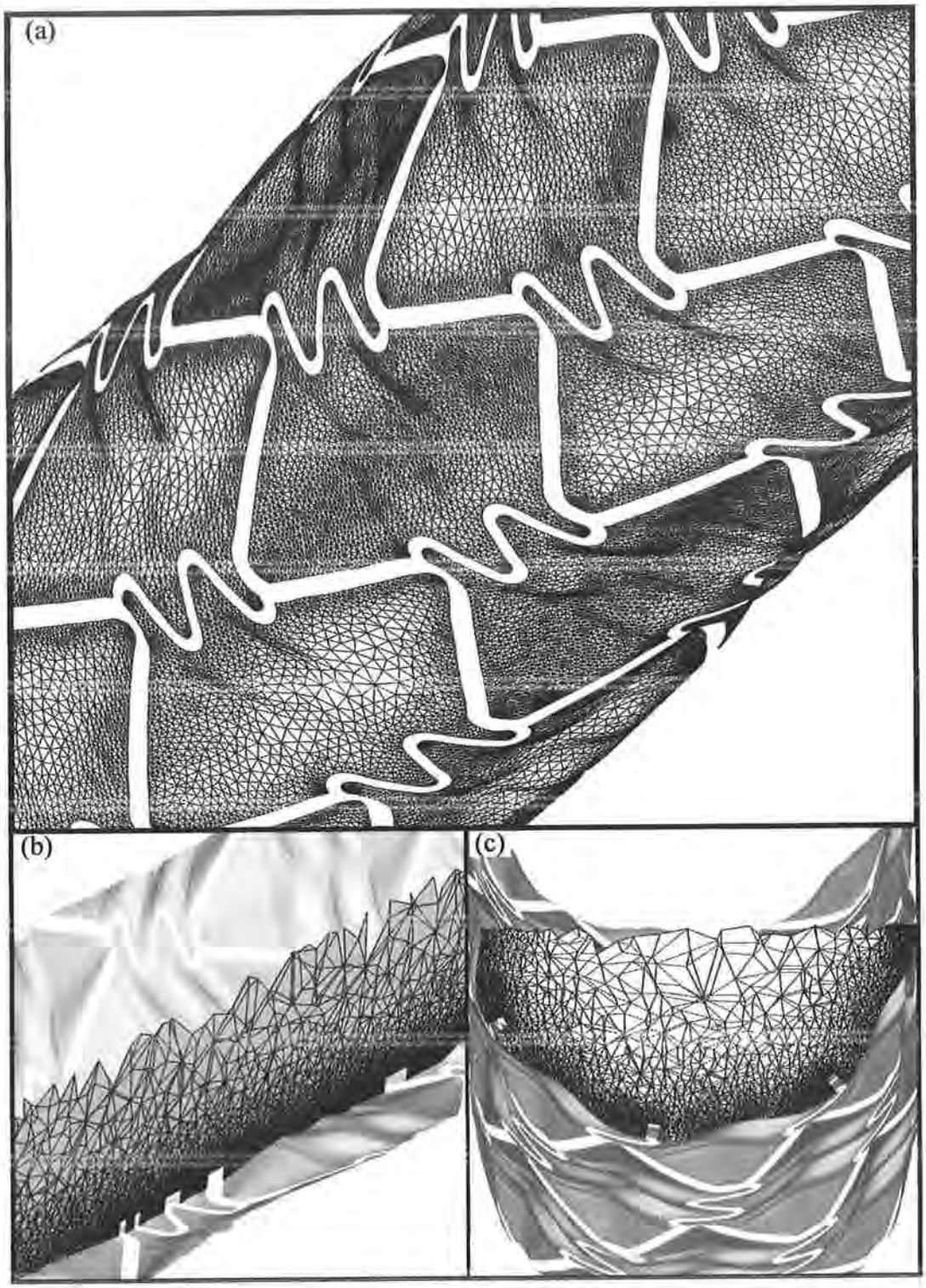

Figure 6-10: Mesh used (Mesh 2) in the numerical analysis of the Bx stent model. The plots show (a) the surface mesh on the artery wall with (b) axial and (c) radial slices of the volume mesh

6.3 Timestep Convergence Study

The transient numerical simulation is performed over the 0.8 s duration of the cardiac cycle. Three consecutive cycles are simulated to ensure that the results were periodically similar. Almost identical results were obtained from Cycles 2 and 3, and hence results are taken from Cycle 3 for all simulations. Solutions are obtained by dividing the simulation time into steps (timesteps) where the flow field is predicted at the end of each one. The timestep chosen should be sufficiently small to ensure that any further reduction in size would not produce a significant change in the results. A timestep convergence study is conduced to examine the effect of the timestep on the time-averaged WSS along sample lines in the domain. Since the transient boundary conditions are the same for all stents, it is only necessary to conduct the timestep convergence study on one of the stent models. The GR-II model is chosen for the study as it has the most abrupt changes in WSS. As shown in Table 6-3, simulations are conducted using timesteps of 50, 25 and 12.5 ms, corresponding to 16, 32 and 64 timesteps per cardiac cycle respectively. Temporal convergence of the results is achieved between the last two simulations within 0.5%. The timestep of 12.5 ms is therefore used in the numerical analyses. Plots of the WSS are shown in Figure 6-11 and Figure 6-12 along the two sample lines for the simulations conducted with the three different timesteps.

Stent	Sample Line	Timestep (ms)	WSS (RMS) [N/m²]	% Difference
GR-II	a	50	0.7421	-
		25	0.7083	-4.6
		12.5	0.7049	-0.5
	b	50	0.7737	-
		25	0.7412	-4.2
		12.5	0.7376	-0.5

Table 6-3: Results of the timestep convergence study conducted on the GR-II stent model.

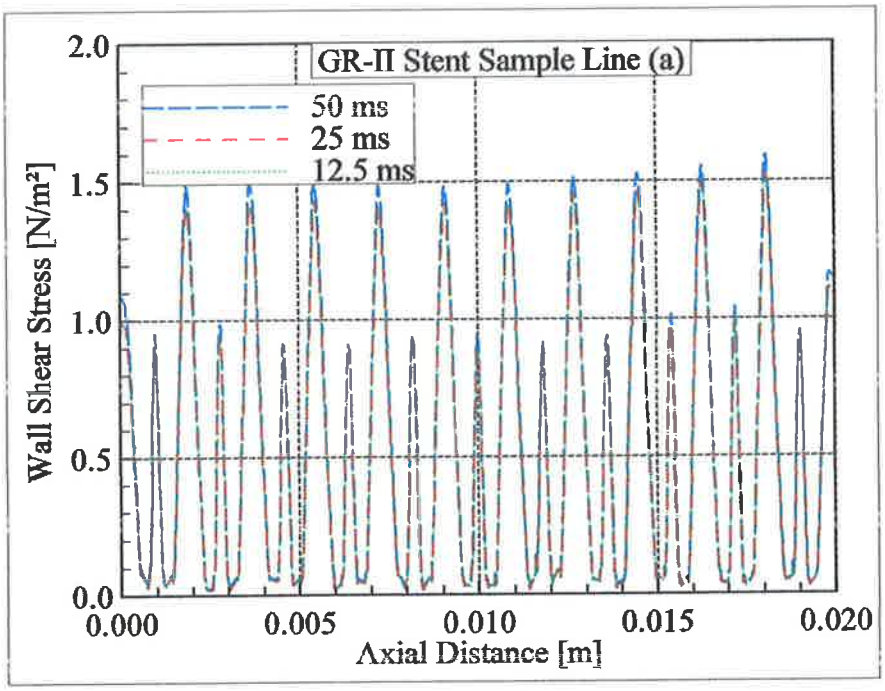

Figure 6-11: Plot of the WSS versus axial distance along sample line (a) of the GR-II stent model for three transient simulations with different timesteps.

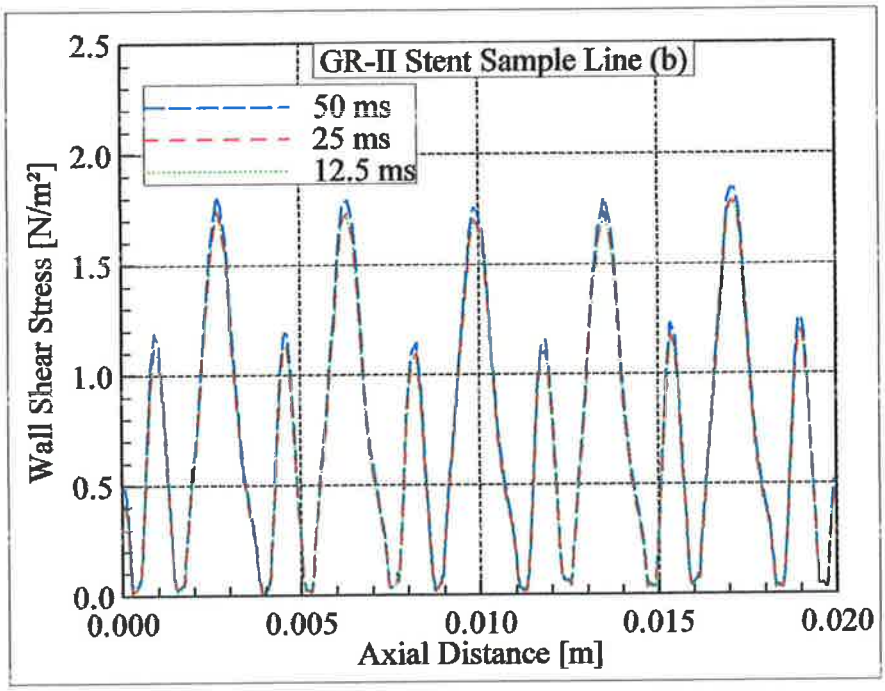

Figure 6-12: Plot of the WSS versus axial distance along sample line (b) of the GR-II stent model for three transient simulations with different timesteps.

6.4 Results of the Numerical Analysis

In this section, the CFD results are presented for the models of the LAD artery implanted separately with the three different stents. The next four subsections contain the results for the calculated WSS, WSSG, WSSAG and OSI variables respectively. The results are displayed in histogram form for each variable. The histograms display the amount of arterial tissue area contained between specific intervals of each element-face-averaged variable. The area in the histograms is normalised by the total area analysed which is the tissue area confined within the axial limits of the stent. Colour and line contour plots as well as vector plots are also provided for each variable to help visualise and explain the predicted variables. The distribution of the four variables is also quantified by the statistical measures given in each subsection.

6.4.1 Wall Shear Stress

The distribution of the WSS is presented in Figure 6-13, Figure 6-14 and Figure 6-15 for the PS, GR-II and Bx stents respectively with the statistical measures given in Table 6-4. Figure 6-16 shows contour plots of the WSS over the entire stented area for all three stents while Figure 6-17 shows the WSS near a strut of each stent with overlaid velocity vectors.

Mean WSS values are similar for the PS and GR-II stents with values of 0.760 N/m² and 0.764 N/m² respectively. The mean is substantially lower for the Bx stent with a value of 0.522 N/m². These WSS values are 25 - 50% lower than those expected for an unstented 3.2 mm artery under similar flow conditions (~1.0 N/m²). The results therefore predict that insertion of these stents reduces the WSS on the artery wall. Figure 6-16 shows that WSS values are reduced below 1.0 N/m² in large

areas around all stent struts. This is a similar result to previous studies [61, 62]. Large areas of low WSS are visible on the proximal and distal sides of the GR-II struts in Figure 6-16, due to low flow velocity in this region shown in Figure 6-17. The thicker struts of the Bx stent create large near-strut low WSS regions. In particular, these regions occur around the S-connectors where there is significantly retarded flow as shown in Figure 6-17. These low WSS regions with the Bx stent are much larger than those produced for the similarly shaped PS stent.

The standard deviation of the WSS is highest for the GR-II stent, and the relatively low kurtosis reveals this is not due to extreme values but rather a wider spread of WSS values in the artery. This is due to the high WSS values at the peaks of the prolapse and lower values in the troughs around the GR-II stent struts as shown in Figure 6-16. The GR-II stent allows more tissue to prolapse into the artery than the other stents. The higher standard deviation quantifies a haemodynamic effect of the larger volume of prolapsing tissue with the GR-II stent. The 63% higher value of kurtosis for the PS stent compared to the GR-II stent indicates that the PS mean WSS value represents a larger portion of the artery compared to the similar GR-II mean value. This is because the higher PS kurtosis value means that the standard deviation is influenced more so by small areas of tissue where the value of the WSS deviates greatly from the mean. Figure 6-16 shows these areas of tissue at the peaks of the prolapsing tissue at the articulation site. The thinner struts of the PS stent have lead to a more uniform distribution of WSS in each of the closed cells in comparison to the wider spread of values in the closed cells of the Bx stent. This haemodynamic effect, which is attributable to the contrasting stent geometries, is captured by the different kurtosis values for the PS and Bx stents. Conditions are more favourable in the artery implanted with the GR-II stent compared to the PS

stent, with the worst WSS values created by implantation of the Bx stent. Comparing the stents gives PS to Bx (d = -0.703), PS to GR-II (d = 0.010) and GR-II to Bx (d = -0.613). This puts the stents in order from best to worst as GR-II, PS and Bx.

The commonly used threshold method of analysis shows that the PS stent has 22.4% of arterial tissue exposed to WSS<0.5 N/m^2 compared with 32.3% for the GR-II stent and 49.5% for the Bx stent. For the WSS, the threshold method does not rank the stents in agreement with the proposed methodology because the areas of high WSS are not taken into account by the threshold method. The proposed method also provides a far greater level of detail from the histograms and statistical measures about the distribution of the WSS in each stented artery.

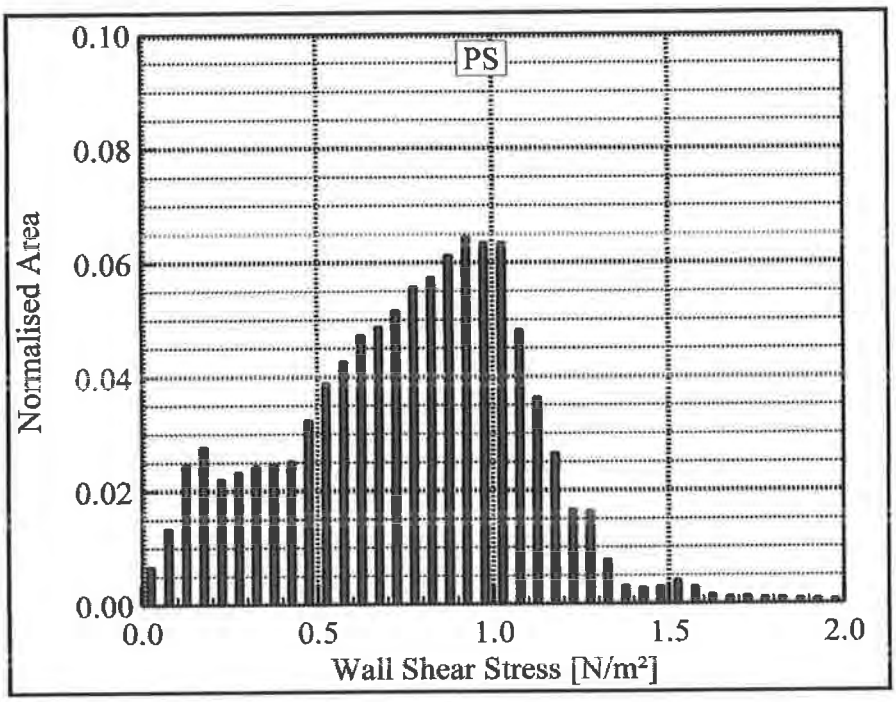

Figure 6-13: Distribution of WSS for the PS stent. The bars represent the amount of normalized area with WSS values bounded by the tick marks on the abscissa. Bin widths are 0.05 N/m^2.

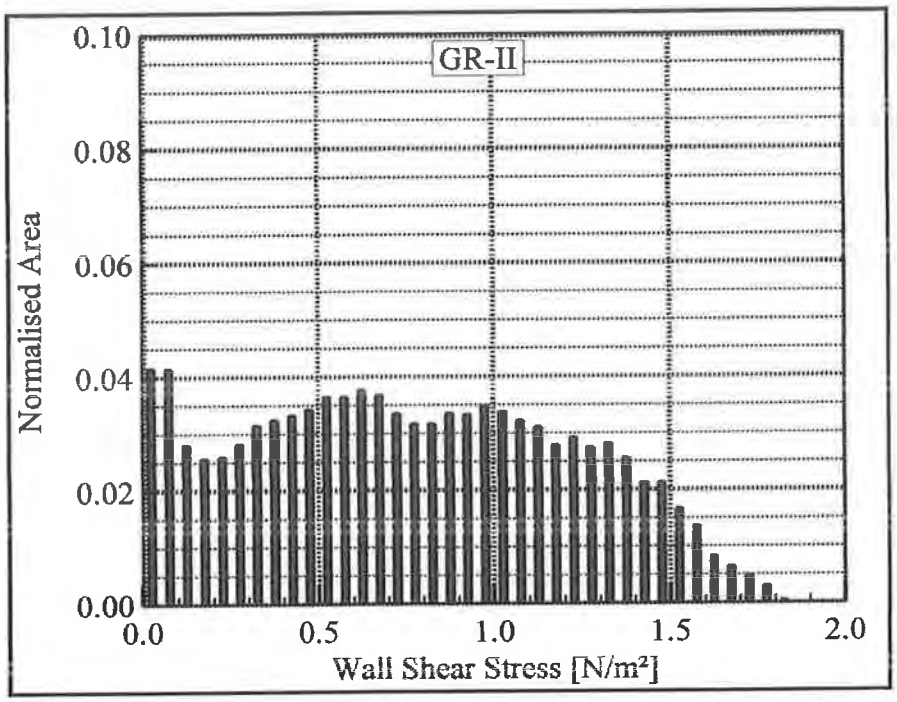

Figure 6-14: Distribution of WSS for the GR-II stent. The bars represent the amount of normalized area with WSS values bounded by the tick marks on the abscissa. Bin widths are 0.05 N/m^2.

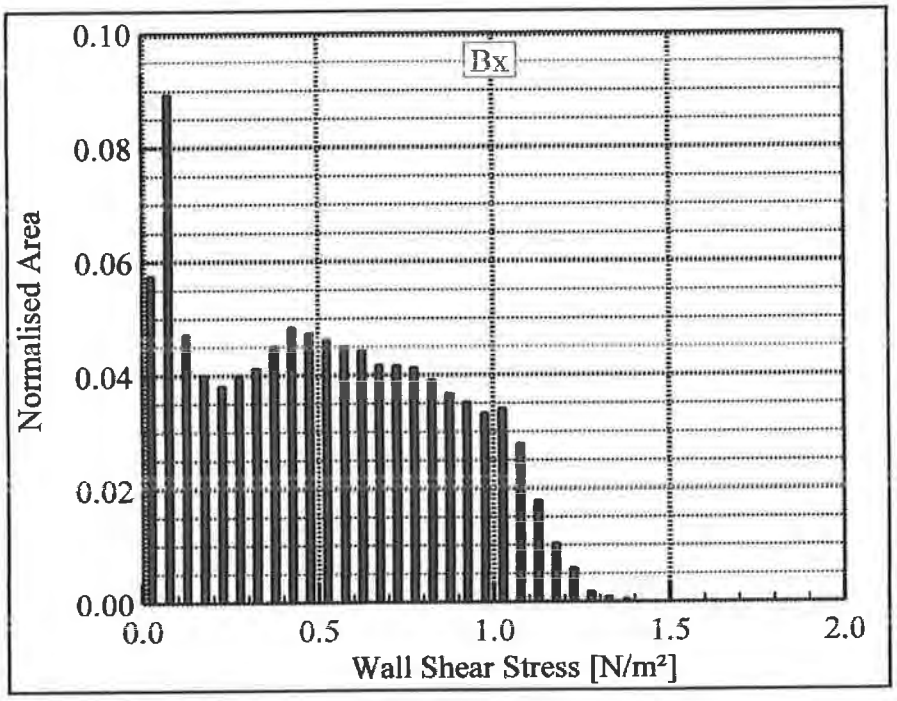

Figure 6-15: Distribution of WSS for the Bx stent. The bars represent the amount of normalized area with WSS values bounded by the tick marks on the abscissa. Bin widths are 0.05 N/m^2.

Stent	Mean [N/m²]	Standard Deviation [N/m²]	Kurtosis
PS	0.760	0.341	3.262
GR-II	0.764	0.454	1.999
Bx	0.522	0.336	1.925

Table 6-4: The statistical measures of the WSS for the PS, GR-II and Bx stents.

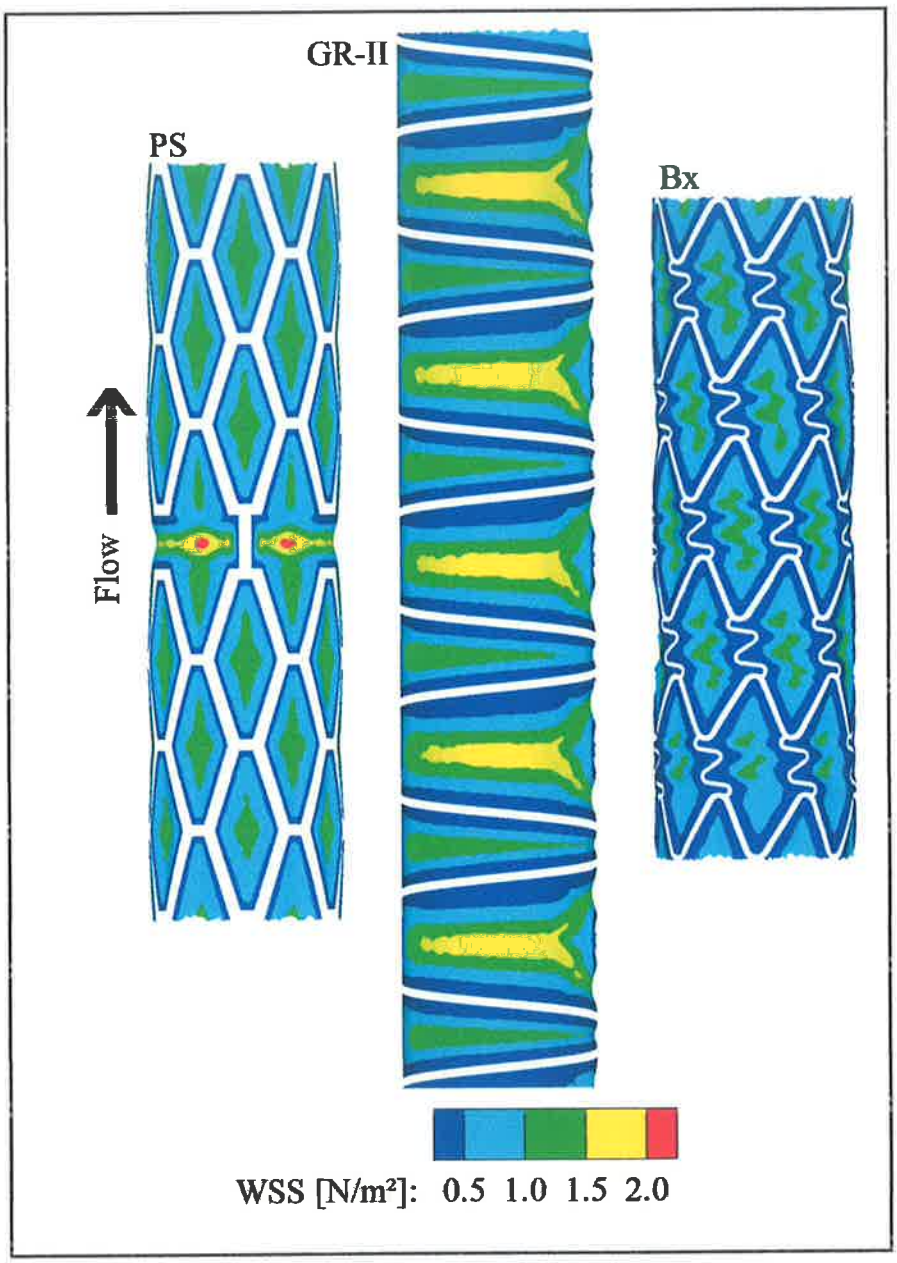

Figure 6-16: Contour plots of WSS for the PS, GR-II and Bx stents.

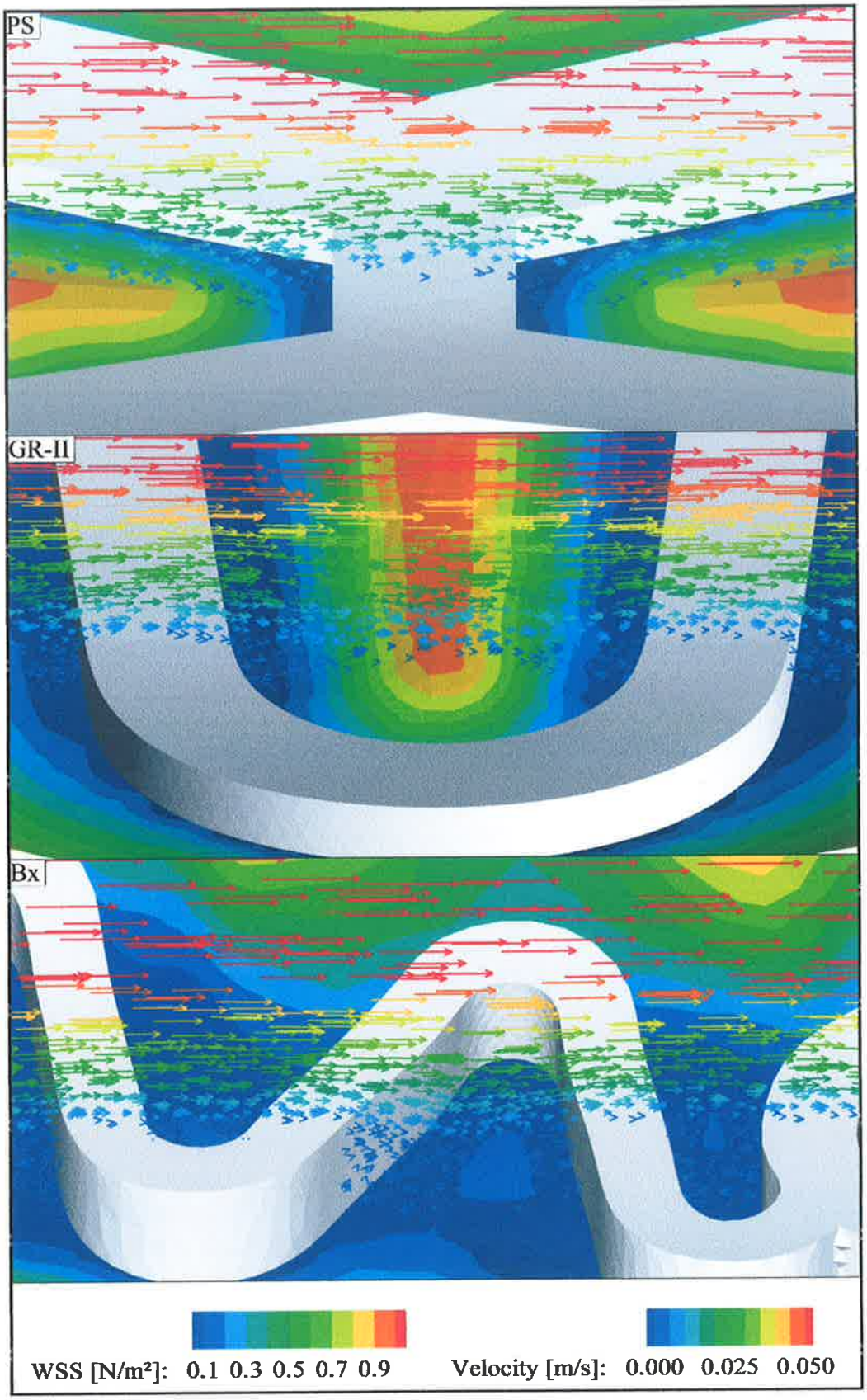

Figure 6-17: Detailed contour plots of the WSS on the artery near the struts of the PS, GR-II and Bx stents. Velocity vectors are also shown on a 2D plane crossing over the struts.

6.4.2 Wall Shear Stress Gradient

The distribution of the WSSG is shown in Figure 6-18, Figure 6-19 and Figure 6-20 for the PS, GR-II and Bx stents respectively with the statistical measures given in Table 6-6. Figure 6-21 shows a colour contour plot of WSSG for the entire stented region of the PS, Bx and GR-II stents, while Figure 6-22 shows colour contour plots of WSSG with overlaid line contour plots of WSS in the near-strut regions of all three stents.

The mean WSSG value for the GR-II stent is 73% higher than that for the PS stent and 55% higher than that for the Bx stent. As shown in Figure 6-22, with the GR-II stent the WSS values quickly increase in the axial direction from the low values at the struts. This creates the large WSSGs visible between the struts and quantified by the large mean value. The mean WSSG value for the Bx stent is 12% higher than that for the PS stent. Contributing to this higher value are the regions of WSSG>2000 N/m^3 on the uneven prolapse near the S-connectors of the Bx stent shown in Figure 6-21 caused by the sudden changes in WSS shown in Figure 6-22. The PS stent has much more favourable WSSG in the inter-strut region as shown in Figure 6-22 but is impaired by the high WSSG at the articulation site visible in Figure 6-21.

The results show the highest standard deviation and lowest kurtosis for the GR-II stent indicating a wider spread of WSSG values. This signifies large spatial fluctuations in the WSSG acting on the arterial tissue. Figure 6-21 illustrates this effect, with large regions of high WSSG (>2000 N/m^3) on the proximal and distal side of the smallest inter-strut regions and low WSSG (<500 N/m^3) in the middle of the largest inter-strut regions of the GR-II stent. The standard deviation is 24%

higher for the PS stent when compared to the Bx stent. However, the higher kurtosis value for the PS stent indicates that the standard deviation is influenced by small areas of tissue with very high WSSG values (>2000 N/m³). In contrast the Bx stent has larger areas with high WSSG values of 1000 - 2000 N/m³ as shown in the histograms of Figure 6-18 and Figure 6-20 and the contour plot in Figure 6-21. This demonstrates how the histograms, statistical measures and contour plots compliment each other to reveal the detail of the variable distributions produced by the different stent designs. Comparing the stents gives PS to Bx (d = 0.159), PS to GR-II (d = 0.837) and GR-II to Bx (d = -0.764). This puts the stents in order from best to worst as PS, Bx and GR-II.

Comparing the stents using the threshold method of analysis, the PS stent exposes 99.5% of the arterial tissue to WSSG>200 N/m^3 compared with 98.9% with the GR-II stent and 98.9% with the Bx stent. These results are very similar, and fail to distinguish between the stents. The results of extending the threshold method to examine the effect of using different threshold values are shown in Table 6-5. These results show that threshold values of 500 N/m³ and 1000 N/m³ rank the stents from best to worst as PS, Bx and GR-II in accordance with the proposed method. The threshold of 2000 N/m³ still ranks the GR-II the worst but ranks the Bx stent ahead of the PS. These higher thresholds are better at ranking the stents than the commonly used 200 N/m³. However, the problem of which threshold value to choose is highlighted by the change in ranking between PS and Bx stents for the value of 2000 N/m³.

Stent	Area > 200 N/m³	Area > 500 N/m³	Area > 1000 N/m³	Area > 2000 N/m³
PS	99.5	77.3	21.5	9.5
GR-II	98.9	91.9	74.4	29.3
Bx	98.9	85.3	43.4	7.5

Table 6-5: Areas of stented artery above different threshold values of WSSG.

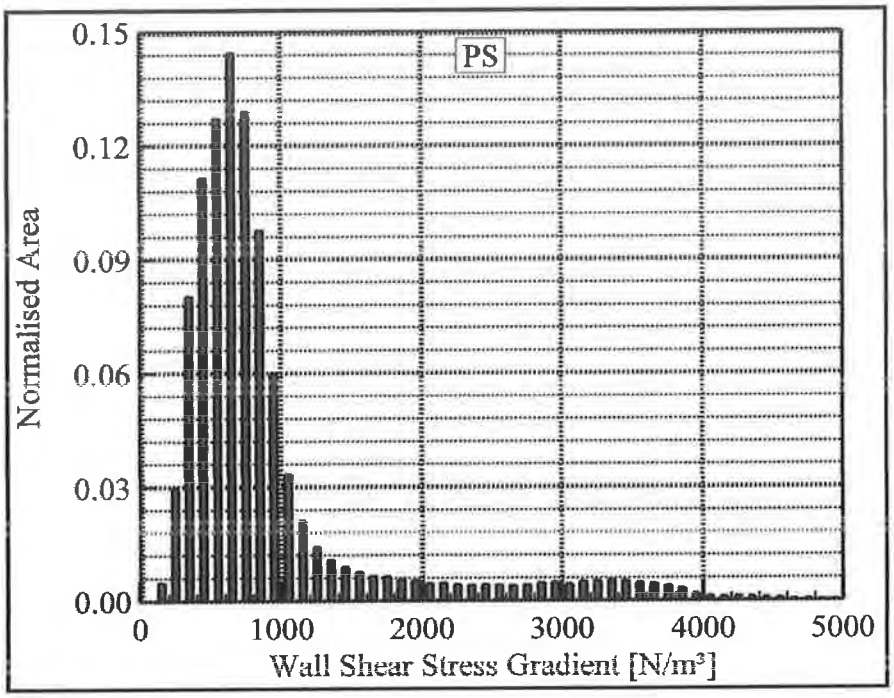

Figure 6-18: Distribution of WSSG for the PS stent. The bars represent the amount of normalized area with WSS values bounded by the tick marks on the abscissa. Bin widths are 100 N/m³.

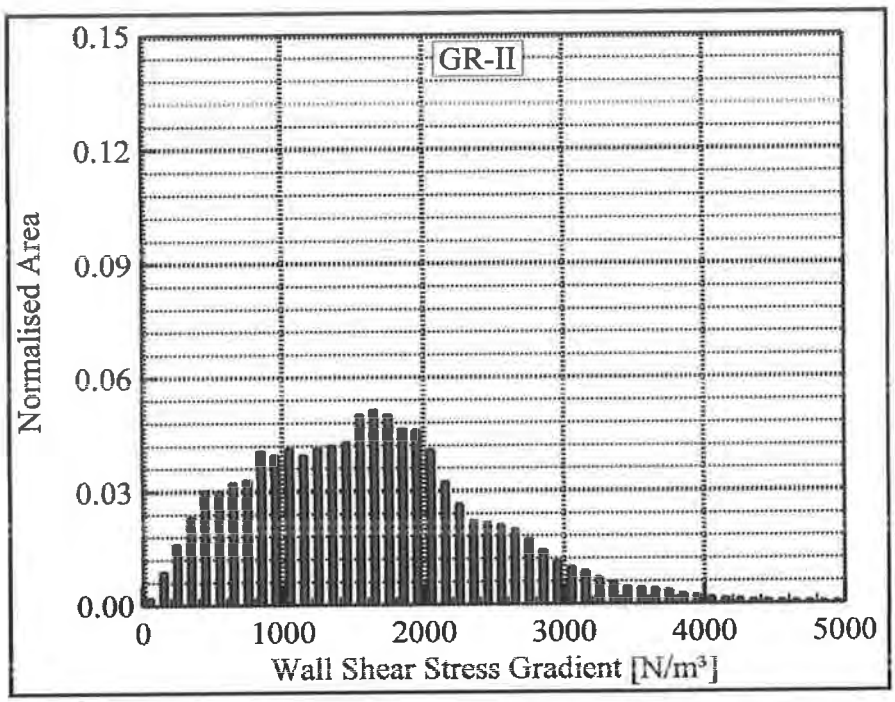

Figure 6-19: Distribution of WSSG for the GR-II stent. The bars represent the amount of normalized area with WSS values bounded by the tick marks on the abscissa. Bin widths are 100 N/m^3.

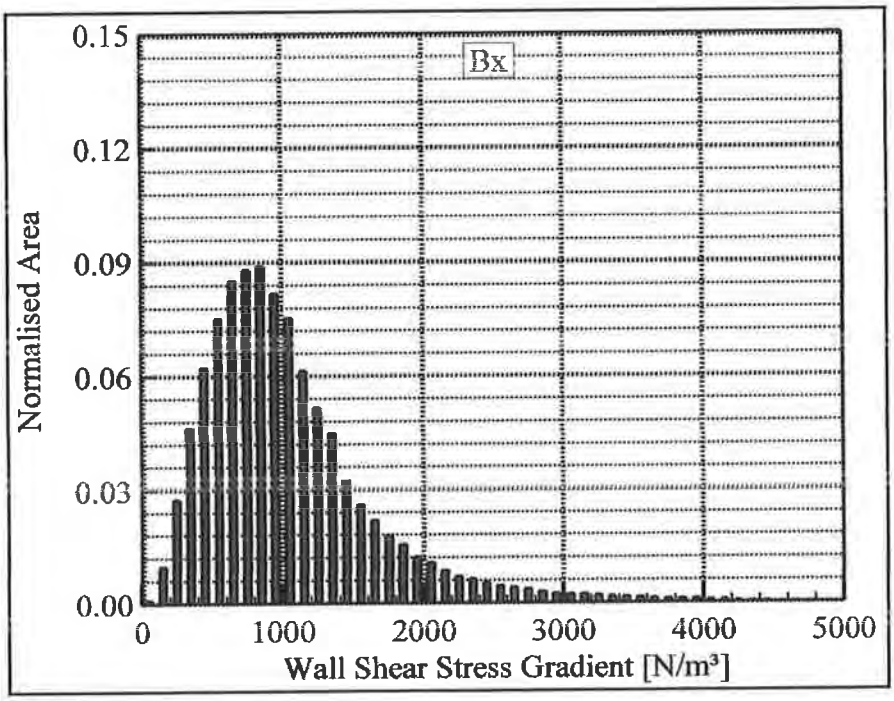

Figure 6-20: Distribution of WSSG for the Bx stent. The bars represent the amount of normalized area with WSS values bounded by the tick marks on the abscissa. Bin widths are 100 N/m^3.

Stent	Mean [N/m^3]	Standard Deviation [N/m^3]	Kurtosis
PS	938.8	783.3	8.9
GR-II	1626.9	858.4	3.9
Bx	1051.6	631.4	8.0

Table 6-6: The statistical measures of the WSSG for the PS, GR-II and Bx stents.

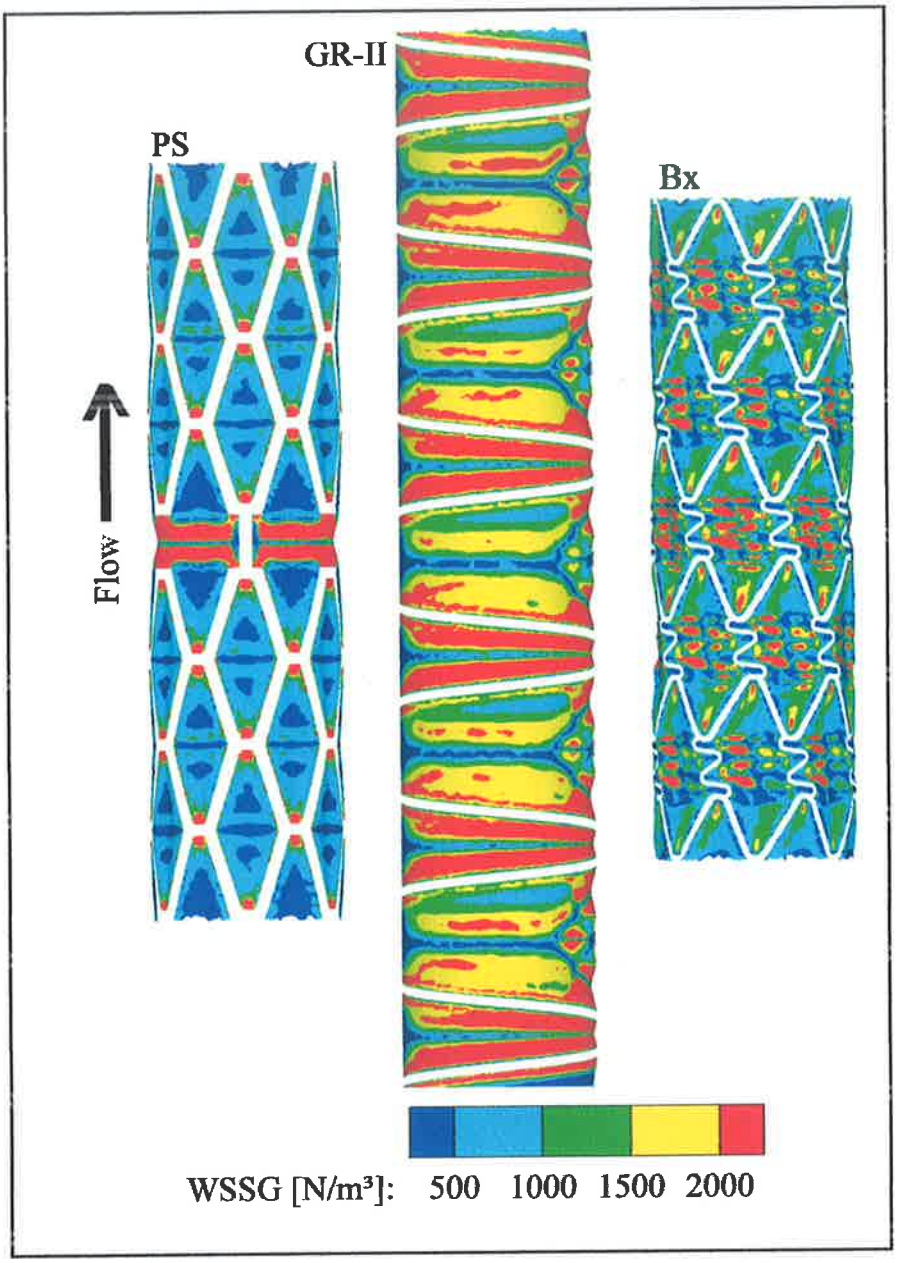

Figure 6-21: Contour plots of WSSG for the PS, GR-II and Bx stents.

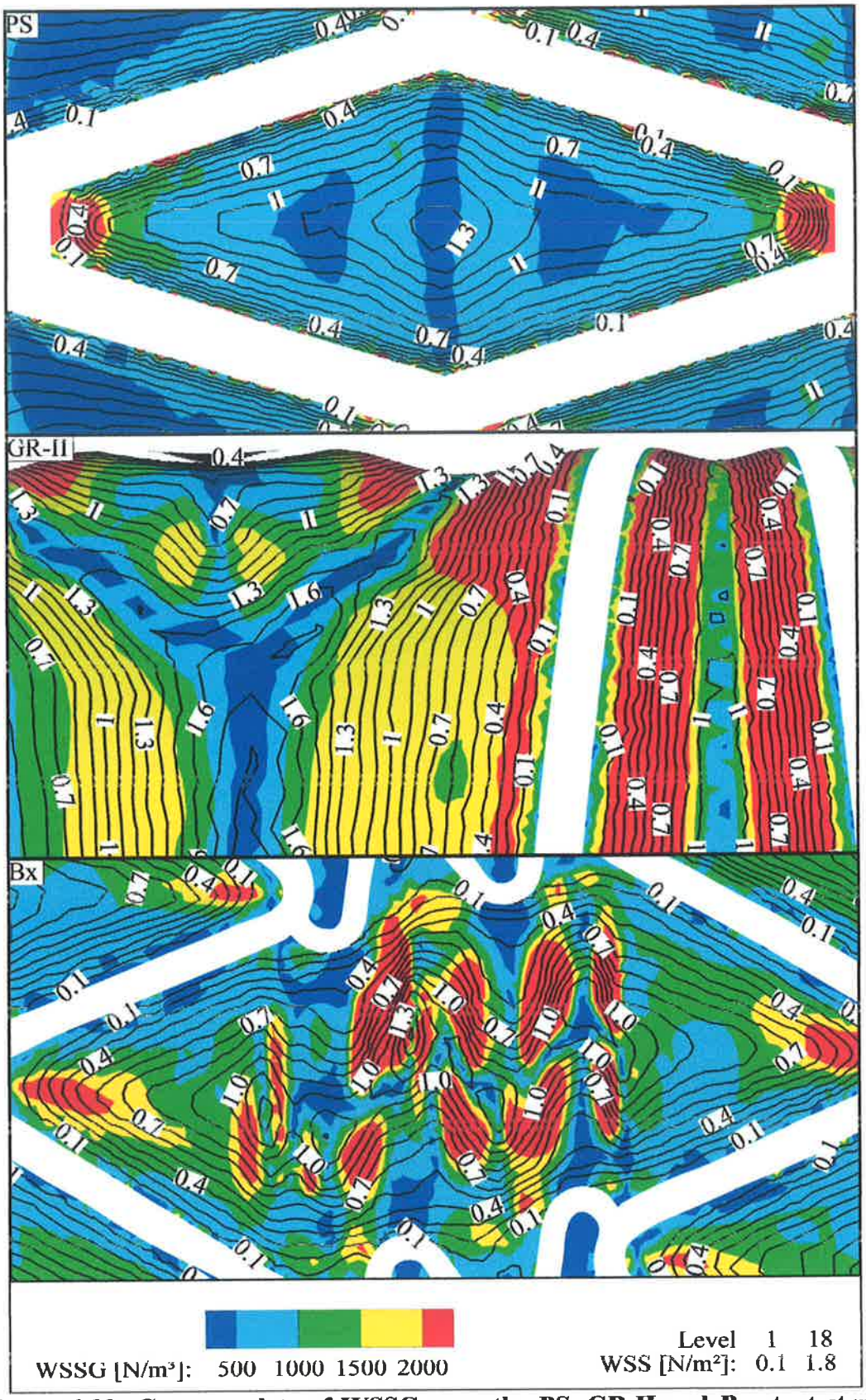

Figure 6-22: Contour plots of WSSG near the PS, GR-II and Bx stent struts with overlaid line contour plots of WSS (labelled by magnitude [N/m²]).

6.4.3 Wall Shear Stress Angle Gradient

The distribution of the WSSAG is presented for the PS, GR-II and Bx stents in Figure 6-23, Figure 6-25 and Figure 6-27 respectively using semi-log plots to ensure that the trend of the data is identifiable and in Figure 6-24, Figure 6-26 and Figure 6-28 respectively using log-log plots to ensure that all of the analysed area is visible on the plot. Statistical measures are provided in Table 6-7. Figure 6-29 shows a colour contour plot of WSSAG for the entire stented region of the PS, Bx and GR-II stents, while Figure 6-30 shows more detailed colour contour plots of the WSSAG with overlaid WSS vectors in the near-strut regions of all three stents.

The PS stent has the best result with the lowest mean WSSAG value of 2.405 rad/mm. This is followed by the GR-II stent with 4.260 rad/mm and finally the Bx stent with 5.009 rad/mm indicating that implantation of this stent leads to the greatest alteration to the WSS direction. The log-log histograms show that all stents have a small amount of area (approximately 0.03%) in the 100-200 rad/mm histogram range and the GR-II and Bx have very small amounts of area (approximately 0.001%) in the 200-300 rad/mm range. Figure 6-29 shows that the regions of highest WSSAG are immediately proximal and distal to the stent struts that traverse the flow with the PS and GR-II stents. This is caused by the flow separation and recirculation in these regions evident from the directions of the WSS vectors shown in Figure 6-30. The WSS vectors in Figure 6-30 also suggest highly disturbed flow around the S-connectors of the Bx stent which is consistent with previous work [26]. This flow disturbance has created large WSSAG values in this region which contribute to this stent having the largest mean value.

The GR-II has the highest standard deviation and lowest kurtosis indicating a lot of areas where the WSSAG values are high; these are notable near all the GR-II struts in Figure 6-29. Large areas of low WSSAG are evident in between the struts of the PS stent with values peaking near the small portions of the struts that traverse the flow. These small areas with very high WSSAG values shown in Figure 6-30 lead to the very high kurtosis value for the PS stent. The standard deviation and kurtosis for the Bx stent are both roughly in between the other two quantifying the very high localised WSSAG values around the S-connectors and also the high WSSAG values over the entire stented region as shown in Figure 6-29. Comparing the stents gives PS to Bx ($d = 0.338$), PS to GR-II ($d = 0.213$) and GR-II to Bx ($d = 0.082$). This puts the stents in order from best to worst as PS, GR-II and Bx.

To the author's knowledge no upper threshold has ever been defined in the literature for the WSSAG, such that an artery with WSSAG values above this threshold can be considered to be at an elevated risk for IH. Indeed, the author considers this to be the first time this variable has been predicted in a model of a stented artery. The results show that the performance of the stents with regard to this variable can easily be evaluated using the analysis technique employed in this work.

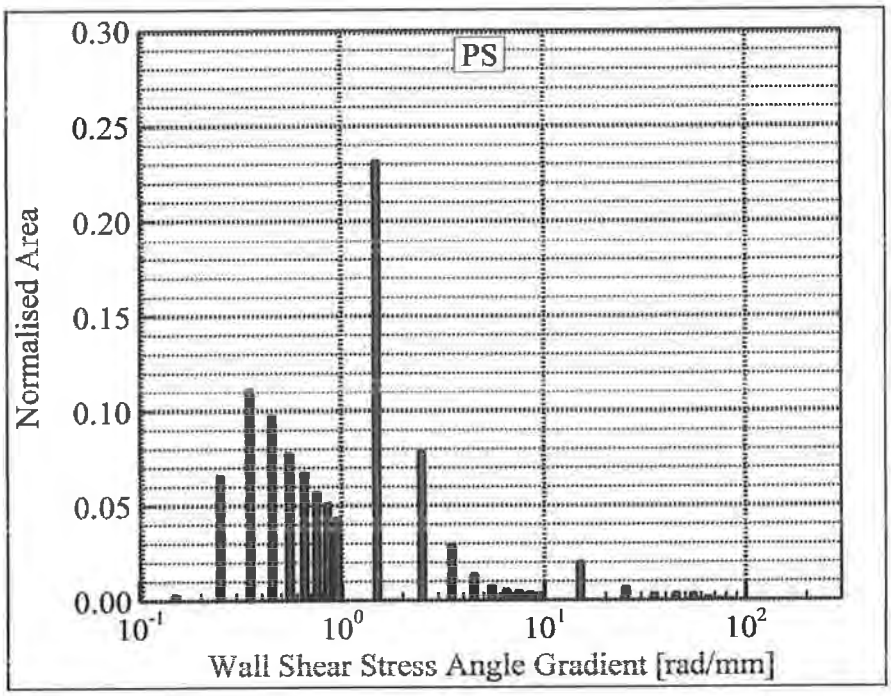

Figure 6-23: Distribution of the WSSAG for the PS stent. The bars represent the amount of normalised area with WSSAG values bounded by the tick marks on the abscissa. Bin widths are distributed logarithmically.

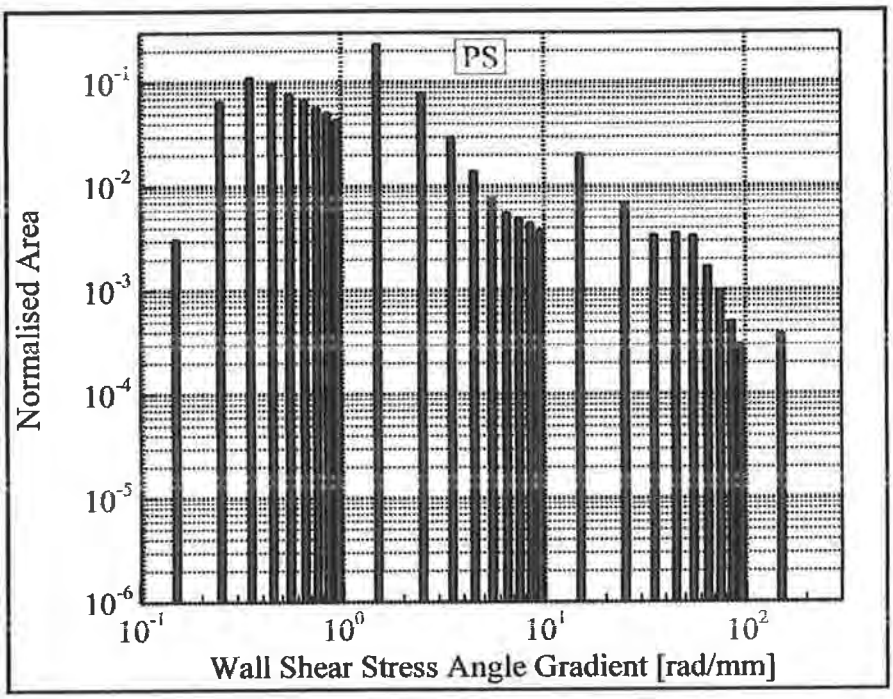

Figure 6-24: Distribution of the WSSAG for the PS stent on a log-log plot provided to display all of the arterial area analysed.

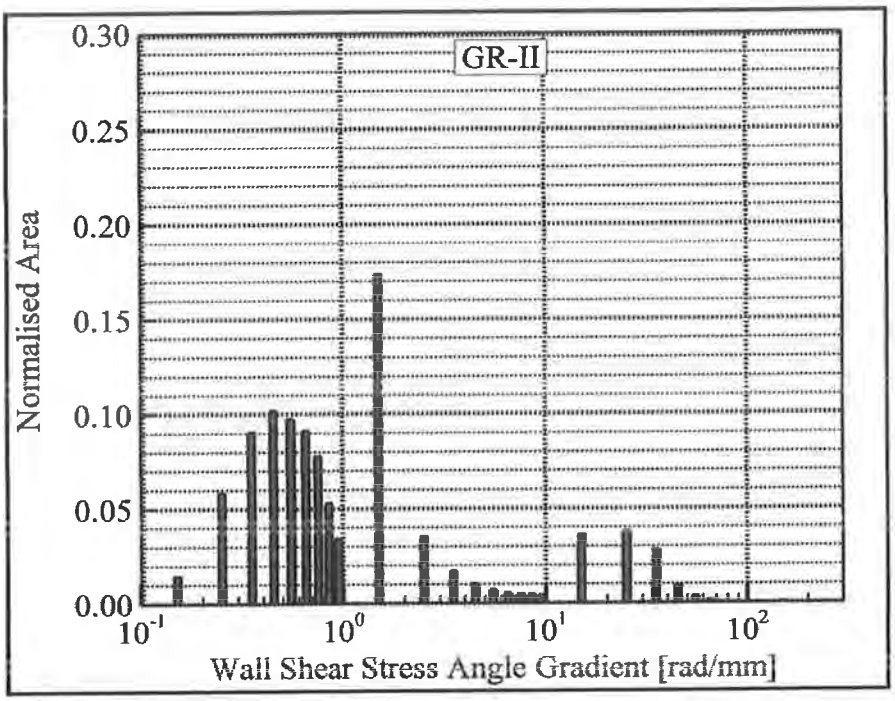

Figure 6-25: Distribution of the WSSAG for the GR-II stent. The bars represent the amount of normalised area with WSSAG values bounded by the tick marks on the abscissa. Bin widths are distributed logarithmically.

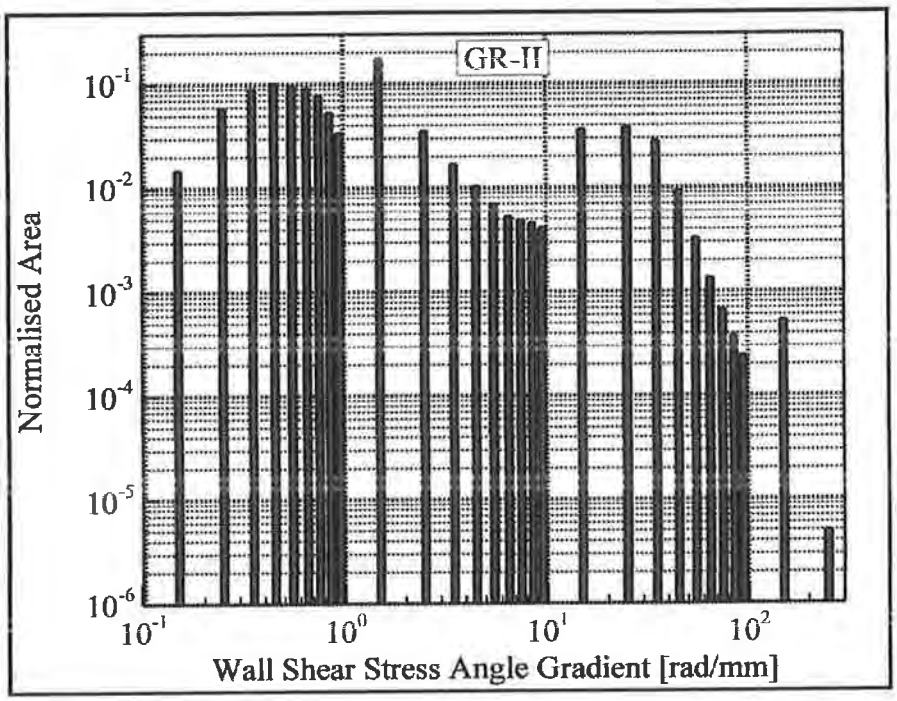

Figure 6-26: Distribution of the WSSAG for the GR-II stent on a log-log plot provided to display all of the arterial area analysed.

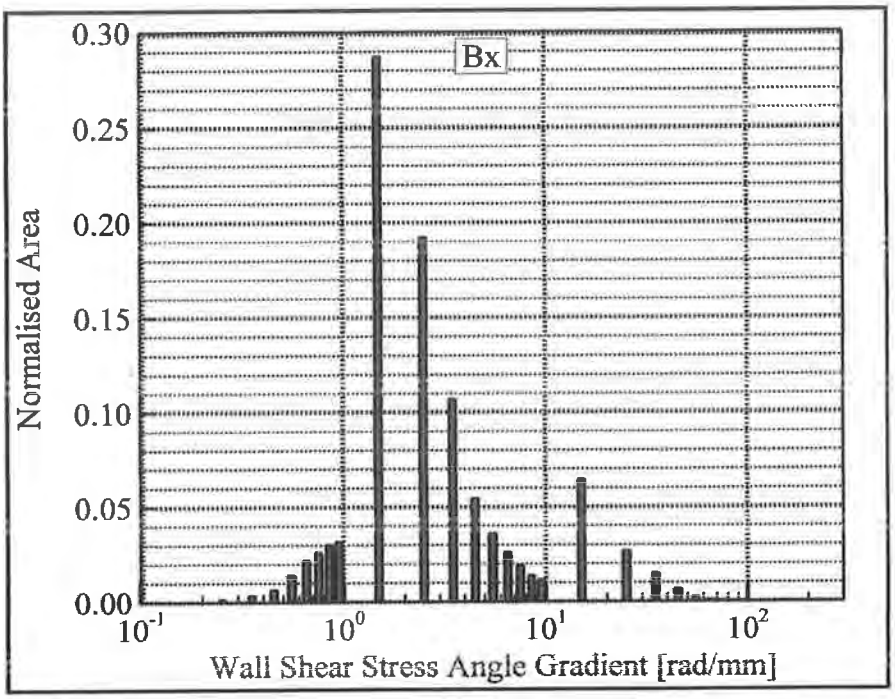

Figure 6-27: Distribution of the WSSAG for the Bx stent. The bars represent the amount of normalised area with WSSAG values bounded by the tick marks on the abscissa. Bin widths are distributed logarithmically.

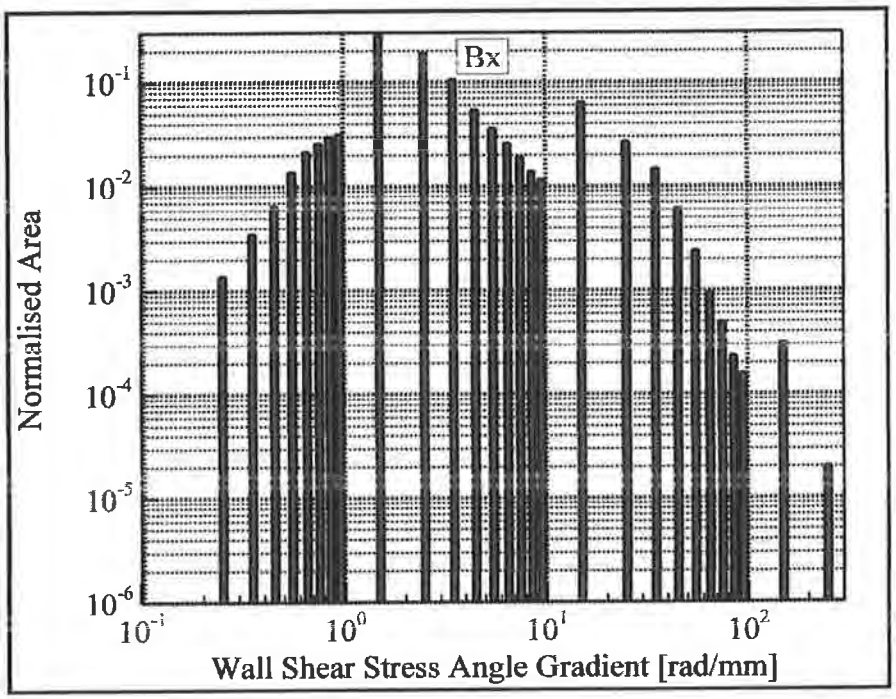

Figure 6-28: Distribution of the WSSAG for the Bx stent on a log-log plot provided to display all of the arterial area analysed.

Stent	Mean [rad/mm]	Standard Deviation [rad/mm]	Kurtosis
PS	2.405	7.176	82.818
GR-II	4.260	10.041	27.853
Bx	5.009	8.199	52.332

Table 6-7: The statistical measures of the WSSAG for the PS, GR-II and Bx stents.

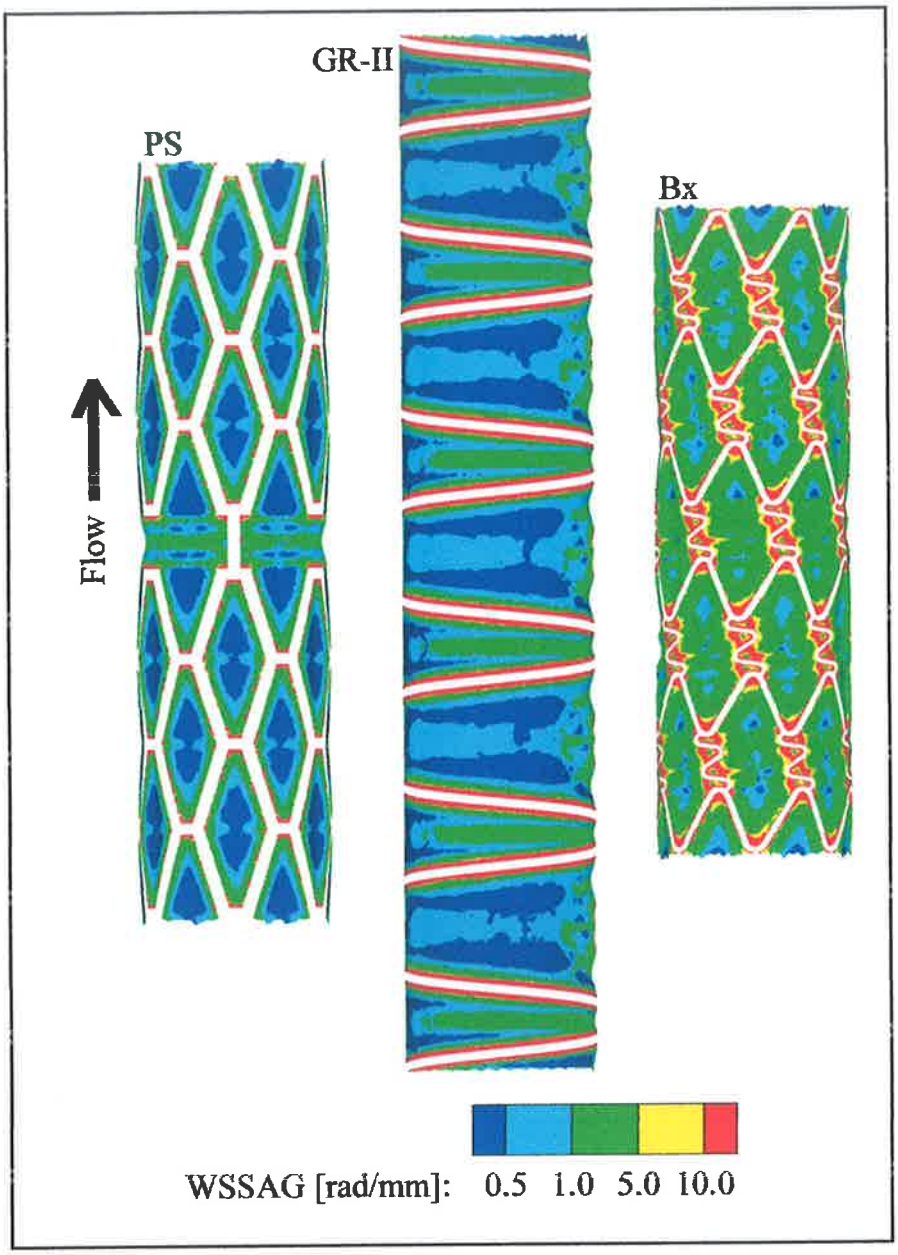

Figure 6-29: Contour plots of WSSAG for the PS, GR-II and Bx stents.

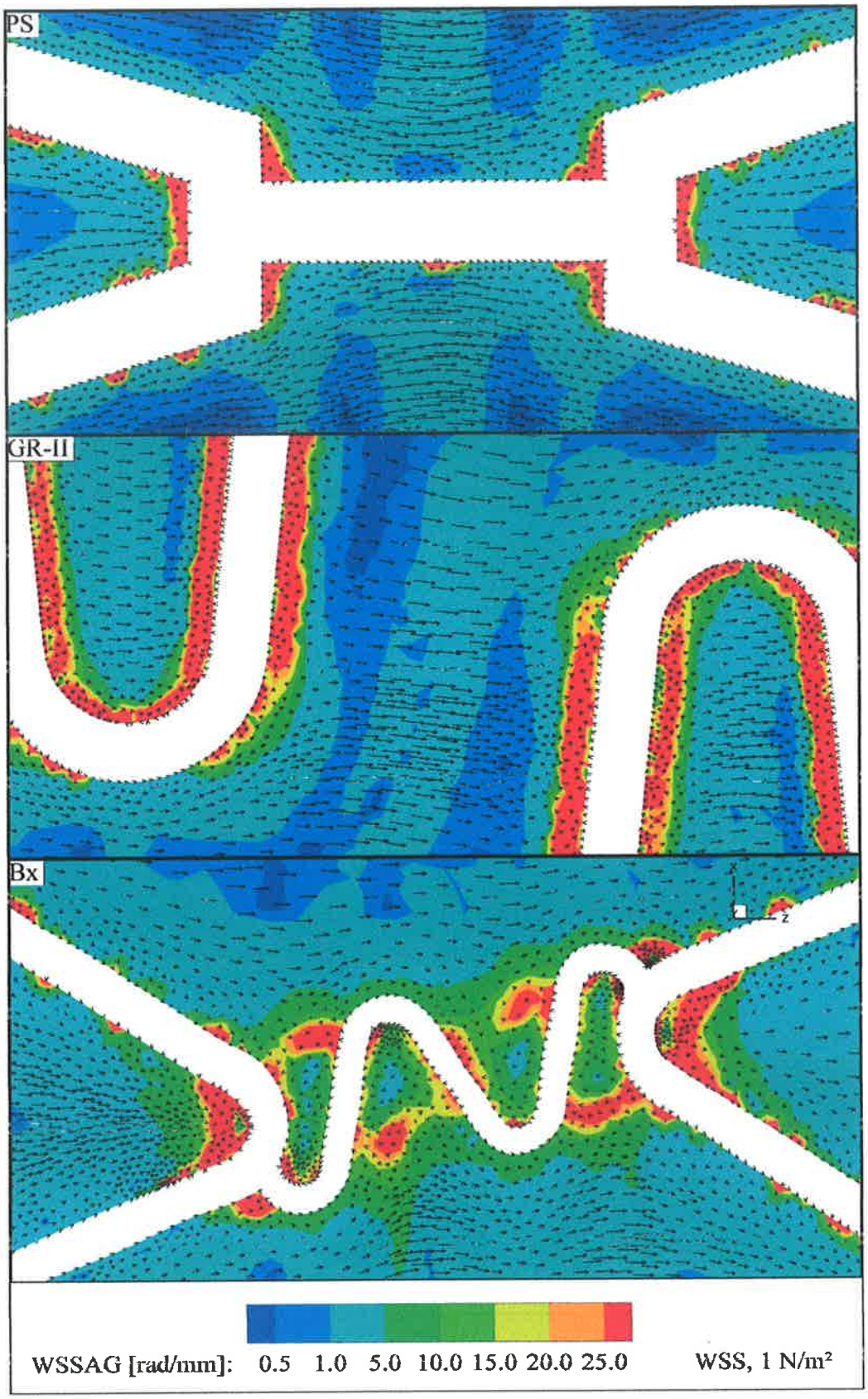

Figure 6-30: Detailed contour plot of the WSSAG in the near-strut regions of the PS, GR-II and Bx stents with the WSS vectors overlaid.

6.4.4 Oscillatory Shear Index

The distribution of the OSI is presented for the PS, GR-II and Bx stents in Figure 6-31, Figure 6-33 and Figure 6-35 respectively using semi-log plots to ensure that the trend of the data is identifiable and in Figure 6-32, Figure 6-34 and Figure 6-36 respectively on log-log plots to ensure that all of the analysed area is visible on the plot. Statistical measures are provided in Table 6-8. Figure 6-37 shows a contour plot of OSI for the entire stented region of the PS, Bx and GR-II stents, while Figure 6-38 shows line contour plots of the higher OSI values with overlaid time-averaged and instantaneous WSS direction arrows in the near-strut regions of all three stents.

Implantation of the Bx stent creates the greatest transient variation in the WSS direction as the mean of the OSI is 30% and 54% higher than that for the GR-II and PS stents respectively. Since the range of the OSI is from 0 to 1, the mean values of OSI in the arteries for the three stents are relatively very low and as such, the differences in the distributions may be viewed as insignificant. However, the OSI quantifies transient directional changes in flow direction which may only be significant for IH in specific small areas of the artery which could amplify the significance of these small differences. The log-log plots show small areas in the 0.4 - 0.5 range of OSI for the PS stent and small areas in the 0.5 - 0.6 range for the GR-II and Bx stents. This indicates regions where there are highly transient directional changes in the WSS vector. Figure 6-38 graphically shows how these high values arise in the near-strut regions of the stents as the instantaneous WSS direction continually changes over the cardiac cycle. However, since the inlet flow is unidirectional, most of the stented artery has low values (<0.05) of OSI as shown in Figure 6-37.

Comparatively the PS stent has the lowest standard deviation with the highest kurtosis indicating that for the majority of the artery the WSSAG values are close to the mean value with localised high spots near the traversing struts. Compared to the PS stent larger amounts of area exist around the GR-II stent wires with high OSI values indicated by the much lower kurtosis and higher standard deviation values. However, the Bx stent has the highest standard deviation and lowest kurtosis of the three stents indicating larger areas where the WSSAG values deviate from the mean compared to the other stents. These higher values are visible near the S-connectors and in large portions of the inter-strut regions, particularly in the proximal part of the stent. Comparing the stents gives PS to Bx ($d = 0.620$), PS to GR-II ($d = 0.315$) and GR-II to Bx ($d = 0.380$). This puts the stents in order from best to worst as PS, GR-II and Bx.

Although this variable has been predicted before in stented arteries [5, 99], no threshold has ever been suggested such that an artery with OSI values above this threshold can be considered to be at an elevated risk for IH. However, as with the WSSAG, the results show that the performance of the stents with regard to the OSI can again be evaluated using the analysis technique employed in this work.

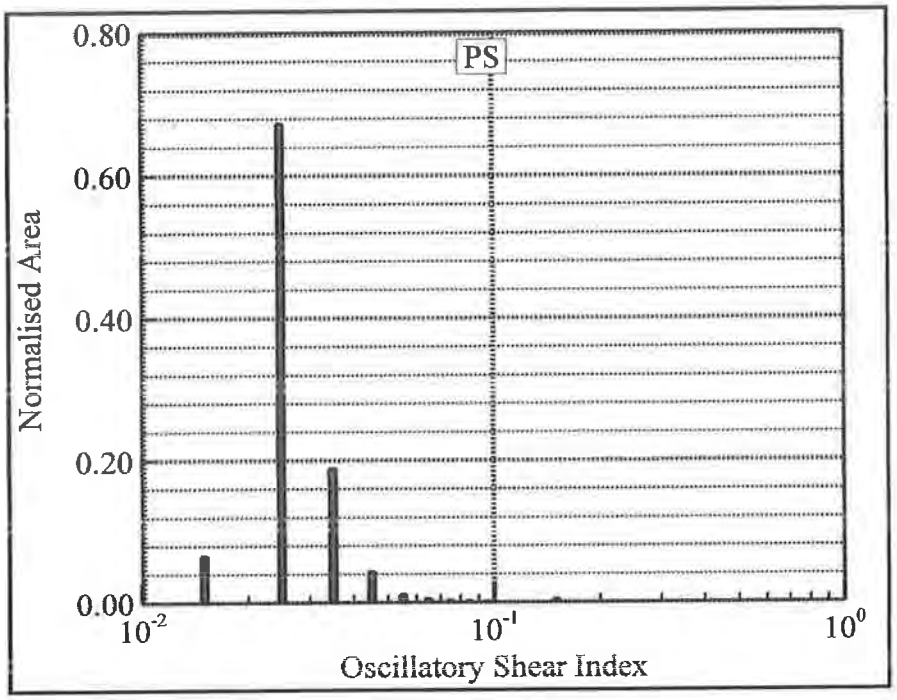

Figure 6-31: Distribution of the OSI for the PS stent. The bars represent the amount of normalised area with OSI values bounded by the tick marks on the abscissa. Bin widths are distributed logarithmically.

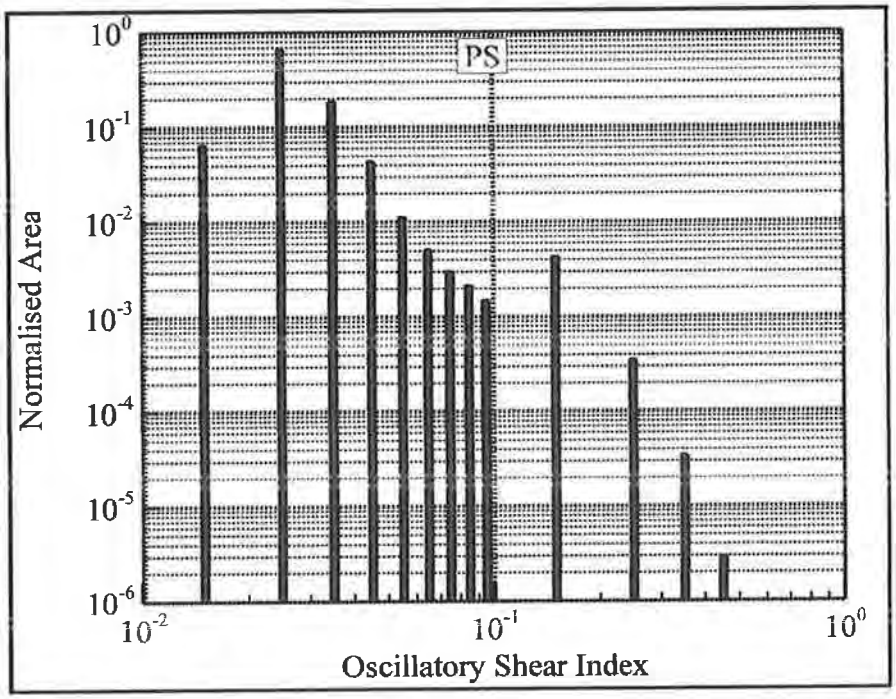

Figure 6-32: Additional log-log plot of the distribution of the OSI for the PS stent provided to display all of the arterial area analysed.

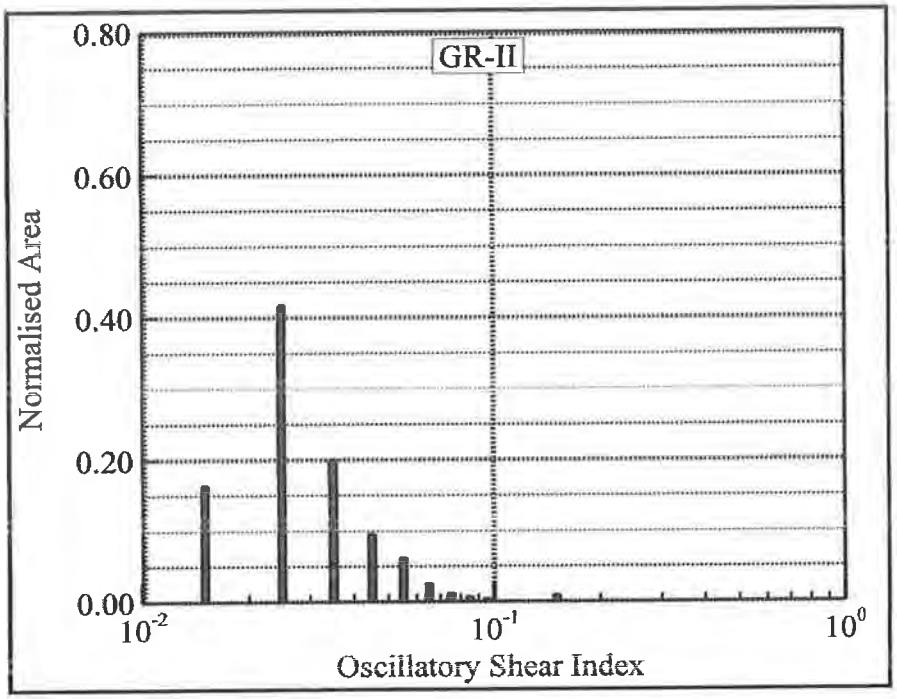

Figure 6-33: Distribution of the OSI for the GR-II stent. The bars represent the amount of normalised area with OSI values bounded by the tick marks on the abscissa. Bin widths are distributed logarithmically.

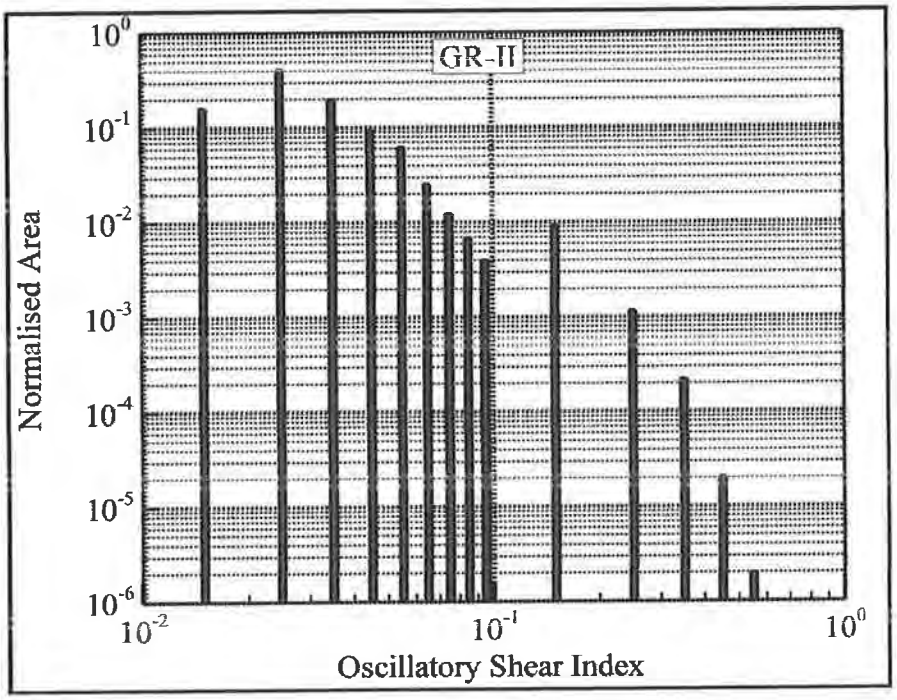

Figure 6-34: Additional log-log plot of the distribution of the OSI for the GR-II stent provided to display all of the arterial area analysed

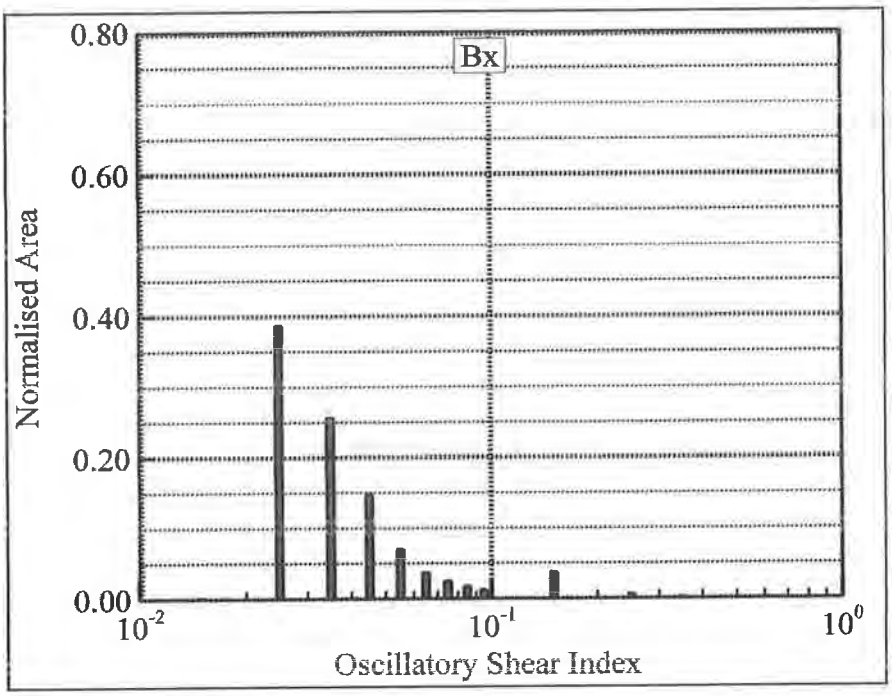

Figure 6-35: Distribution of the OSI for the Bx stent. The bars represent the amount of normalised area with OSI values bounded by the tick marks on the abscissa. Bin widths are distributed logarithmically.

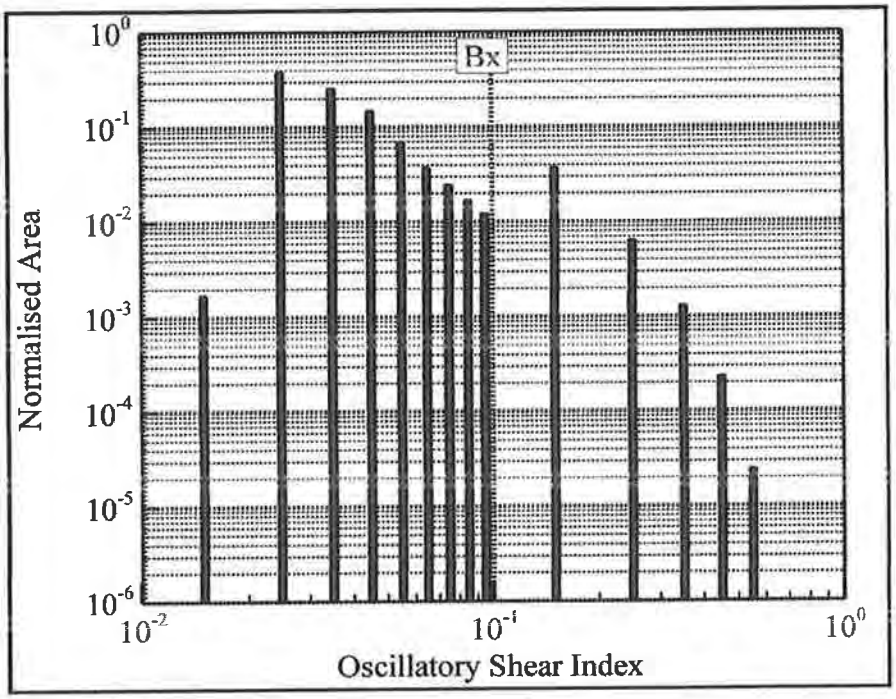

Figure 6-36: Additional log-log plot of the distribution of the OSI for the Bx stent provided to display all of the arterial area analysed.

Stent	Mean	Standard Deviation	Kurtosis
PS	0.028	0.012	94.604
GR-II	0.033	0.019	47.763
Bx	0.043	0.032	31.938

Table 6-8: The statistical measures of the OSI for the PS, GR-II and Bx stents.

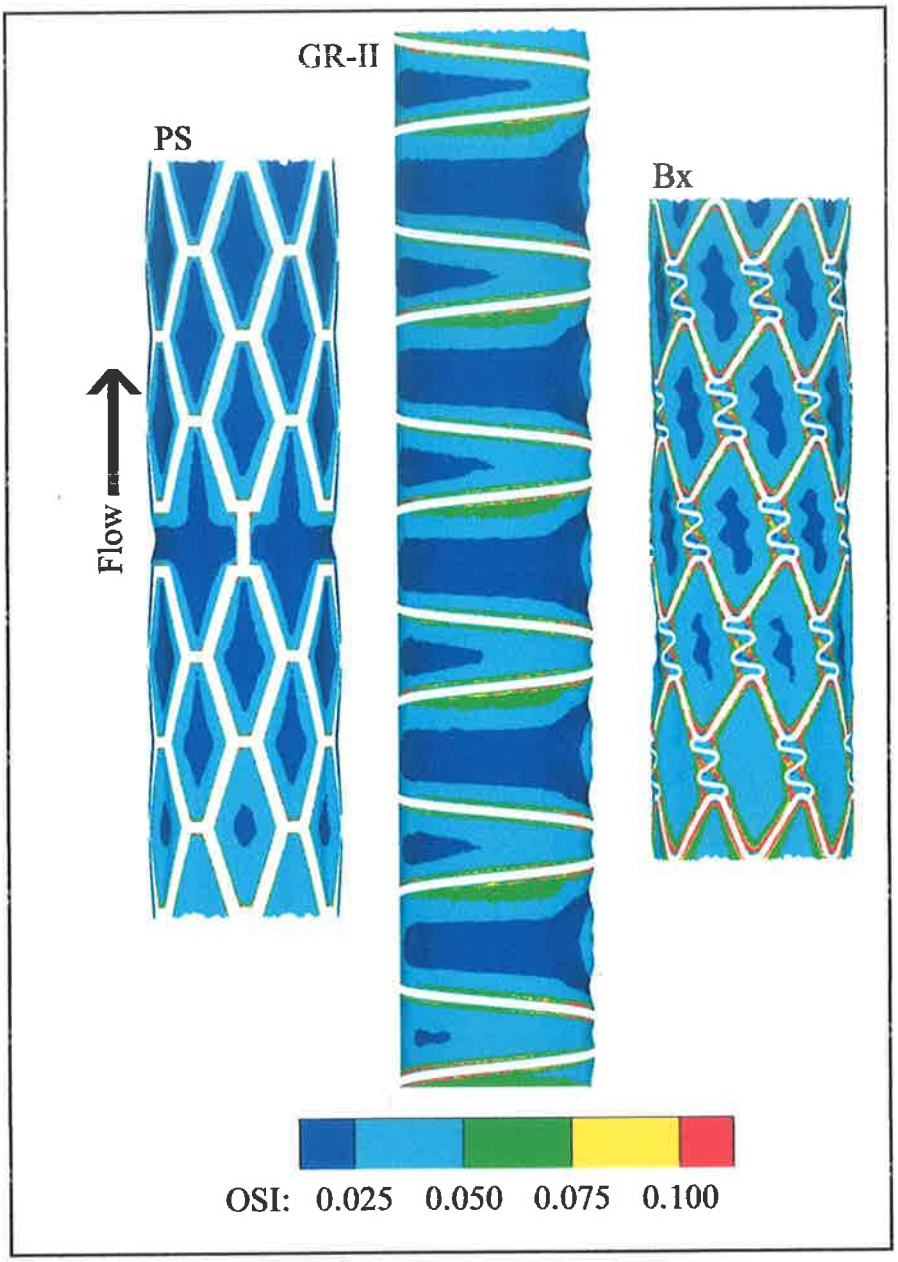

Figure 6-37: Contour plots of the OSI for the PS, GR-II and Bx stents.

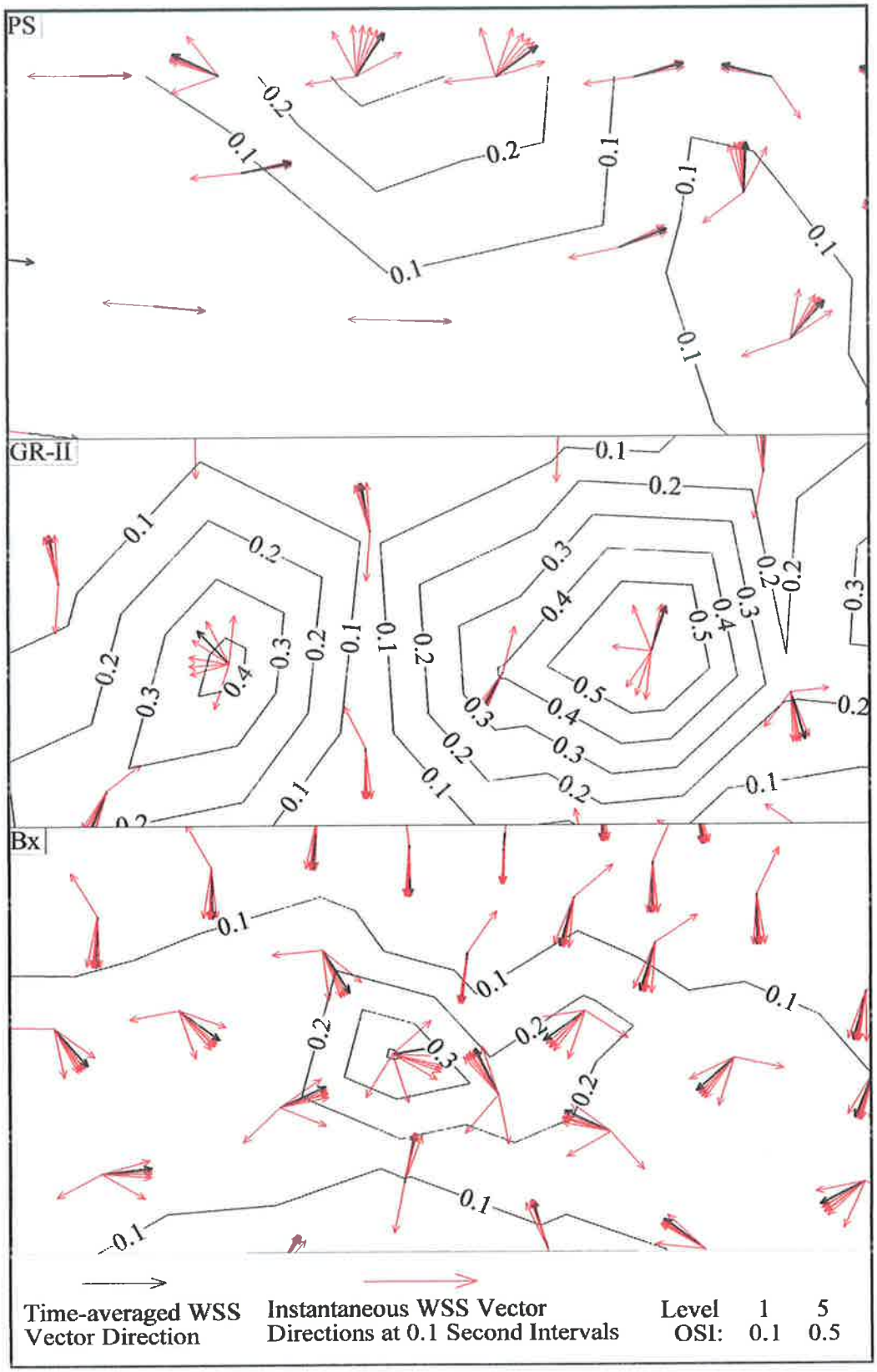

Figure 6-38: Line contour plots of the OSI in the near-strut region for the PS, GR-II and Bx stents. The plots are overlaid by arrows representing the time-averaged WSS direction (Black) and the instantaneous WSS direction (Red) at 0.1 s intervals over the cardiac cycle.

6.5 Analysis of Results

The results have favoured the PS as the implanted stent which creates the least alteration to the WSS in the artery. The WSSG and WSSAG variables rank the PS stent the best. The OSI also favours the PS stent; however the magnitudes of the mean OSI values are quite small for the stents. Nevertheless, the histograms and contour plots do show that the GR-II and Bx stents create higher magnitudes of OSI around the stent struts compared to the PS stent. The WSS, WSSAG and OSI variables rank the GR-II ahead of the Bx stent, with the only exception to the trend being the WSSG where the GR-II ranks the lowest. Overall, the methodology indicates the stents perform haemodynamically in the order of PS, GR-II and finally Bx.

Using the threshold method, the WSS variable identifies the PS as the best stent, followed by the GR-II and the Bx stents whereas the WSSG variable yields inconclusive results using the 200 N/m^3 threshold value. In this case, the threshold method has managed to distinguish between the stents using one variable, but does not rank them in agreement with the proposed methodology. Also, the threshold method does not quantify the complex haemodynamic disturbances that are identified in these results. Furthermore, the threshold method has been proven inadequate to distinguish between stents in previous studies [4, 26, 61-63], where the proposed method may have proved more successful.

Examples of how this method of analysis improves upon the threshold method can be found in each of the WSS-based variables. Figure 6-17 shows that the WSS varies quickly from low values at the stent struts to higher values on the prolapsing tissue with the PS and GR-II stents. The WSS is also shown to be quite

low due to the disturbed haemodynamics around the S-connector of the Bx stent. These effects are captured qualitatively by the distribution plots and also quantitatively by the statistical measures. Figure 6-22 shows the complex WSS distribution around the struts for all three stents leading to the creation of localised high values of WSSG. The statistical measures and distribution plots show that the GR-II creates large areas of high WSSG whereas the other two stents create smaller local regions of high WSSG. This analysis of WSS and WSSG is far more detailed and beneficial towards the improvement of future stent design than simply measuring the area above or below a certain threshold. Figure 6-30 shows how the WSS vectors quickly change direction due to the uneven prolapse near the Bx stent struts, leading to high WSSAG in this area. High WSSAG are also visible proximal and distal to the traversing struts of the PS and GR-II stents which may well lead to increased IH. Figure 6-38 shows regions of high OSI in the near-strut regions for the three stents as the WSS direction changes with time. This could also have an undesirable effect on ECs and lead to IH, and as such is also an important consideration for stent design. These haemodynamic effects are not identified by the use of the threshold method and such features could easily have been overlooked in the aforementioned previous studies.

6.6 Summary

This chapter contains the main body of results from this work. Firstly, the results of the mesh convergence study are presented where it is shown that refinements to the mesh do not lead to any significant changes in results. The timestep for the analyses is then chosen based on the results of the timestep convergence study. The results from the numerical predictions of the haemodynamics are then presented for an artery implanted separately with a PS, GR-II and Bx stent. The results are presented

in a variable-by-variable format with each variable analysed using a proposed technique utilising distribution graphs and statistical measures. Where possible, this analysis technique is compared to a threshold analysis technique found throughout the literature. The results are finally analysed together in the last section with some key points highlighted pertaining to the merits of the proposed method of analysis.

CHAPTER 7

Conclusion

7.1 Discussion

In this work, a new methodology is proposed to fully elucidate the disturbance to arterial WSS induced by stent deployment. Four variables are employed in the methodology, each of which highlights a different type of alteration to the arterial WSS which could lead to IH development. The proposed method of analysing the WSS-based variables provides a clear qualitative and quantitative assessment of each variable distribution making it possible to accurately assess the haemodynamic impact of an implanted stent.

Three stents are analysed and their clinical performance is available from the results of several clinical trials which are summarised in Table 7-1. The most commonly used method of comparison of BMS *in vivo* performance is angiographic restenosis rates, defined as percentage of patients with >50% renarrowing of the target vessel at follow up. The PS and GR-II stents were directly compared in a trial consisting of 755 patients with de novo lesions [67]. Restenosis rates were found to be statistically significant ($p<0.001$) between the two stents with values of 47.3% and 20.6% for the GR-II and PS stents respectively. A possible factor in the poor GR-II result is the "clamshell" deployment which is likely to cause more arterial damage than for the slotted-tube type stents such as the PS. "Infrequent optimal GR-II size selection" was also noted in the study which would likely contribute to poor

stent performance. The PS stent has also been involved in the stent equivalency trials ASCENT [2] and NIRVANA [3] and had restenosis rates of 22.1% and 22.4% respectively. There were similar criteria for inclusion in these three trials such as native vessel diameter of greater than 3 mm, de novo lesions, and similar study end points. The Bx stent had a restenosis rate of 31.4% in the ISAR-STEREO-II [93] which had patients with de novo and restenotic lesions, but similar vessel diameter and trial end points. The Bx stent also had a restenosis rate of 23.4% in the control arm of the RAVAL DES trial [114] where inclusion criteria were a de novo lesion with native vessel diameter between 2.5 and 3.5 mm. These different restenosis rates between ISAR-STERO-II and RAVAL for the Bx highlight the fact that results from different clinical trials cannot be used to directly compare stents.

Trial (year)	Trial Design	No. of Patients	Follow up (months)	Restenosis Rate (%)
Lanskey et al. [67] (2000)	GR-II vs PS	755	12	47.3 vs 20.6
NIRVANA [3] (2001)	NIR vs PS	849	9	19.3 vs 22.4
ASCENT [2] (2001)	ML vs PS	529	9	16.0 vs 22.1
RAVEL DES [114] (2002)	SES vs Bx	283	6	0.0 vs 23.4
ISAR-STERO II [93] (2003)	ML vs Bx	611	6	17.9 vs 31.4
PS - Palmaz Schatz (Cordis, Johnson and Johnson, NJ, USA), NIR - NIR stent (Boston Scientific, MA, USA), ML - Multilink (Guidant, CA, USA), SES - Sirolimus-eluting stent.				

Table 7-1: Angiographic restenosis rates for the PS, GR-II and Bx stents from five clinical trials.

The CFD results rank the stents (best to worst) for WSS as follows: GR-II, PS, Bx (Cohen's d: -0.01, -0.613), for WSSG: PS, Bx, GR-II (d: 0.159, 0.764), for WSSAG: PS GR-II Bx (d: 0.213, 0.082), and for OSI: PS, GR-II, Bx (d: 0.315, 0.380). The Bx stent had the worst haemodynamic impact on the artery even though it is a second generation BMS. Also from the CFD results, the GR-II stent performed worse than the PS stent haemodynamically. The GR-II stent also performed worse than the PS stent in the clinical trial [67]. However, it would have to be concluded

that other influential factors were also to blame for the stents poor clinical performance as it had such a severe restenosis rate.

Limitations of the methodology employed in this work include the assumptions of fully-developed laminar flow, a rigid stent and arterial wall, and the omission of a stenotic plaque. Whilst the depth of tissue prolapse is based on FEA data [97], the shape of the protruding tissue is a further limitation as it is idealised and based entirely on the geometry of the stent. Curvature and taper of the artery have also been omitted in the analysis for simplicity. The outlet boundary condition of a fixed static pressure is a limitation creating a non-physiological transient pressure in the CFD model. However, this outlet boundary condition is the standard practice for modelling of pulsatile flow in arteries [4, 5, 7, 33, 59, 62, 63, 99]. With this boundary condition, the CFD software calculates the necessary inlet pressure to drive the flow. The velocity which is specified at the inlet should therefore maintain reasonable physiological accuracy in the computational domain.

This work demonstrates the advantages of a new method developed to fully elucidate the alterations to the arterial WSS following coronary stent implantation. The previously used threshold method overlooks some of the important haemodynamic features identified by the method of analysis proposed in this thesis. The detailed alterations to the WSS identified in Chapter 6 demonstrate that the threshold method is insufficient to fully elucidate the alterations to the WSS in a stented artery. The aim of this work is to develop a novel methodology to assess the haemodynamic impact of coronary stent implantation by elucidating the stent-induced alterations to the WSS. The multivariable approach coupled with the histograms and statistical measures employed in the proposed methodology have

been shown to elucidate the altered WSS in the stented artery to a high level of detail, thus allowing the stents to be assessed accordingly based on their haemodynamic impact on the artery. As such, this method of stent assessment should assist in stent design in the future and is applicable to bare metal, drug-eluting and any future stents that alter the WSS in the artery after implantation.

7.2 Future Work and Recommendations

This thesis sets out a concise methodology to evaluate the alterations to WSS created by an implanted stent. This methodology can be improved however by incorporating additional facets to investigate other important features in the environment of the stented artery.

An FEA of the stent deployment can provide valuable information about the related stresses induced in the artery wall [4, 65]. The analysis should also produce an accurate geometric model of the deformed artery wall and stent which could be used to generate the computational domain for the CFD analysis. The geometry of the stented artery may also be generated on a patient-specific basis using combined angiographic and intravascular-ultrasound techniques [133] or high resolution computerised tomography scans [10]. Combining these models with the stent assessment technique presented in this work may be very useful to pre clinically assess the haemodynamic impact of a particular stent for a specific patient or lesion. It would also be useful to use these models to assess stents that have been directly compared in animal models or clinical trials to relate the stent's haemodynamic performance to its clinical performance.

In the past decade DESs have become popular in interventional cardiology as a result of lower restenosis rates compared to BMSs. The first DESs had permanent

synthetic polymer coating materials which gradually released the drug into the artery. Recently these permanent polymers have been replaced by biocompatible polymers to reduce thrombus formation. Currently, research is focused on bioabsorbable polymers and stents. Modelling of drug diffusion and stent absorption would therefore be useful additions to help explain the performance of these future stents. However, combining these additional modelling techniques with the haemodynamics modelling is not trivial. In this work, haemodynamics are evaluated immediately after stent implantation. Subsequent to this instant in time, thrombus forms and IH develops over a period of weeks to months changing the geometry of the stented artery and thus, the haemodynamics. This creates challenges for modelling of haemodynamics coincidentally with drug release and stent absorption which occur over these "week to month" timescales.

The task of ranking a stent based on the results predicted in this work is not trivial. Considerable effort has gone into reducing the results sufficiently to easily identify the best stent with regard to each variable. Even so, it is difficult to say which of the four WSS-based variables is the most important with regard to IH and so each is assigned equal significance. While there is a sizeable amount of research on the arterial effect of low WSS, much less is known about the effects of WSSG, WSSAG and OSI in the stented artery making it difficult to assign the appropriate significance to each. This problem is exacerbated as results from FEA, and models of drug elution and stent absorption are added to the CFD results. This large volume of results data is appropriate to reflect the huge and complex cascade of events triggered by actual stent implantation *in vivo*. However, the main challenge for the future of modelling this complex environment is the management and interpretation of all this predicted data. Experimentation is needed to identify the predicted

variables that are the most responsible for adverse effects in the stented artery. Stents or stent features could then be ranked accordingly from prediction of these variables by the computational model.

APPENDIX A

ANSYS CFX Software Theory

A.1 Introduction

CFD is a computer-based tool which is now regarded as the "third" technique for the solution of fluid-flow problems, complementing, but not replacing, the well-established approaches of theory and experiment. It is a relatively new branch of fluid mechanics and finds its niche in predicting fluid flows that are difficult or impossible to analyse using theory and are complex, time consuming, or expensive to measure experimentally.

ANSYS CFX 12.0 is the commercial CFD software employed in this work. The software uses a vertex-centred finite volume scheme with implicit time stepping to solve the governing equations of fluid dynamics and hence predict the flow-field variables. In any CFD analysis, the first step is to create the desired geometry of the flow domain to be modelled; this forms the computational domain. In ANSYS CFX 12.0 the computational domain is then discretised into an unstructured computational mesh comprised of tetrahedral, hexahedral and/or wedge elements. Boundary conditions are then imposed on all external bounding surfaces of the domain. A discretised form of the governing equations of fluid dynamics is then solved subject to these boundary conditions using an implicit time-stepping technique.

A.2 Mesh Generation

ANSYS CFX 12.0 uses a vertex-centred finite volume method. With the finite volume method, the computational domain is divided into a set of much smaller non-overlapping sub-domains called elements which constitute the mesh. Meshes may be structured which have an ordered design or unstructured which have a random or chaotic design. In this work, unstructured meshes are generated in ANSYS Workbench 12.0 using the advancing front method. With this method, elements are progressively added to the domain starting from the boundaries. This results in the propagation of several fronts into the domain which form a boundary between meshed and unmeshed regions. The mesh generation is complete when these advancing fronts meet at a point somewhere near the centre of the domain. Nodes are located at the vertices of the unstructured elements and all flow-field variables are stored at these nodes. This mesh is used to solve the governing flow equations which are given in the next section.

A.3 Governing Flow Equations

The governing equations of fluid mechanics which are solved in this work are the continuity and three momentum equations given in equations (A-1) and (A-2) to (A-4) respectively. The equations are in partial differential form and are written in a 3D Cartesian coordinate system as

$$\frac{\partial \rho}{\partial t} + \vec{\nabla}.\left(\rho \vec{V}\right) = 0 \qquad \text{(A-1)}$$

$$\frac{\partial (\rho u)}{\partial t} + \vec{\nabla}.\left(\rho u \vec{V}\right) = -\frac{\partial P}{\partial x} + \frac{\partial}{\partial x}\left(\tau_{xx}\right) + \frac{\partial}{\partial y}\left(\tau_{yx}\right) + \frac{\partial}{\partial z}\left(\tau_{zx}\right) \qquad \text{(A-2)}$$

$$\frac{\partial(\rho v)}{\partial t}+\vec{\nabla}.\left(\rho v\vec{V}\right)=-\frac{\partial P}{\partial y}+\frac{\partial}{\partial x}\left(\tau_{xy}\right)+\frac{\partial}{\partial y}\left(\tau_{yy}\right)+\frac{\partial}{\partial z}\left(\tau_{zy}\right) \qquad \text{(A-3)}$$

$$\frac{\partial(\rho w)}{\partial t}+\vec{\nabla}.\left(\rho w\vec{V}\right)=-\frac{\partial P}{\partial z}+\frac{\partial}{\partial x}\left(\tau_{xz}\right)+\frac{\partial}{\partial y}\left(\tau_{yz}\right)+\frac{\partial}{\partial z}\left(\tau_{zz}\right) \qquad \text{(A-4)}$$

where ρ is the fluid density, P is the static pressure, $\vec{V}$ is the velocity vector with components u, v and w in the Cartesian x, y and z directions respectively, and τ_{ij} is the viscous stress acting in the j direction on a face normal to the i direction. These equations are referred to as the hydrodynamic equations and can be integrated over a control volume such as the one shown in Figure A-1 below.

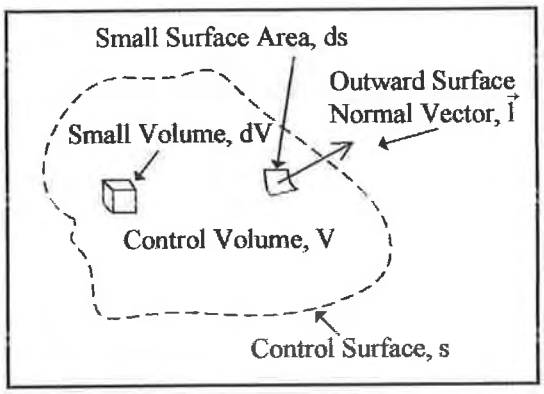

Figure A-1: Control volume V bounded by control surface s. Flow quantities can be integrated over a control volume by summation over all the small volumes dV. The flux of quantities across the control surface s can be integrated by summation over all the small surface areas ds.

Gauss' divergence theorem is applied to convert some volume integrals to surface integrals and is written for the velocity as

$$\int_V\left(\vec{\nabla}\cdot\vec{V}\right)dV=\int_s\left(\vec{V}\cdot\vec{I}\right)ds \qquad \text{(A-5)}$$

where dV is an infinitesimally small volume integrated over the entire control volume V, and $\vec{I}$ is the outward normal vector of the infinitesimally small surface element ds integrated over the control surface s as shown in Figure A-1. The

resulting continuity equation in integral form is

$$\frac{d}{dt}\int_V \rho dV + \int_s \left(\rho \vec{V}.\vec{l}\right) ds = 0 \qquad \text{(A-6)}$$

the x momentum equation is

$$\frac{d}{dt}\int_V (\rho u) dV + \int_s \left(\rho u \vec{V}.\vec{l}\right) ds = \int_s \left(-P\vec{l}.\vec{i} + \tau_{xx}\vec{l}.\vec{i} + \tau_{yx}\vec{l}.\vec{j} + \tau_{zx}\vec{l}.\vec{k}\right) ds \qquad \text{(A-7)}$$

the y momentum equation is

$$\frac{d}{dt}\int_V (\rho v) dV + \int_s \left(\rho v \vec{V}.\vec{l}\right) ds = \int_s \left(-P\vec{l}.\vec{j} + \tau_{xy}\vec{l}.\vec{i} + \tau_{yy}\vec{l}.\vec{j} + \tau_{zy}\vec{l}.\vec{k}\right) ds \qquad \text{(A-8)}$$

and the z momentum equation is

$$\frac{d}{dt}\int_V (\rho w) dV + \int_s \left(\rho w \vec{V}.\vec{l}\right) ds = \int_s \left(-P\vec{l}.\vec{k} + \tau_{xz}\vec{l}.\vec{i} + \tau_{yz}\vec{l}.\vec{j} + \tau_{zz}\vec{l}.\vec{k}\right) ds \qquad \text{(A-9)}$$

where $\vec{i}, \vec{j}$ and $\vec{k}$ are unit vectors in the Cartesian x, y and z directions respectively. The terms differentiated with respect to t are the transient terms and represent the rate of change of mass and momentum inside the control volume with respect to time. The terms on the left which are integrated with respect to s are the advection terms and represent the net transfer of mass and momentum across the surface of the control volume. The terms on the right hand side of the momentum equations are the pressure and diffusion terms which represent the stresses acting on the surface of the control volume. The first step in solving these equations numerically is to approximate the terms in the equations using discrete functions. The discrete functions used are dependent on the numerical method employed and also the level of accuracy required. As outlined below, the finite volume method is used in this work and the discrete functions are second order accurate in both space and time.

A.4 Finite Volume Method

Analytical solutions to the governing equations of fluid mechanics exist for only the simplest of flows under ideal conditions. To obtain solutions for real flows a numerical approach must be adopted whereby the governing flow equations are replaced by algebraic approximations which may be solved using a numerical method. With the finite volume method, discrete forms of the governing equations are solved over finite control volumes in the domain. These control volumes are generated from the unstructured mesh as described in the next section.

A.4.1 Generation of Finite Control Volumes

The numerical scheme employed in ANSYS Workbench 12.0, involves generating finite control volumes from the mesh, a 2D example of which is shown in Figure A-2.

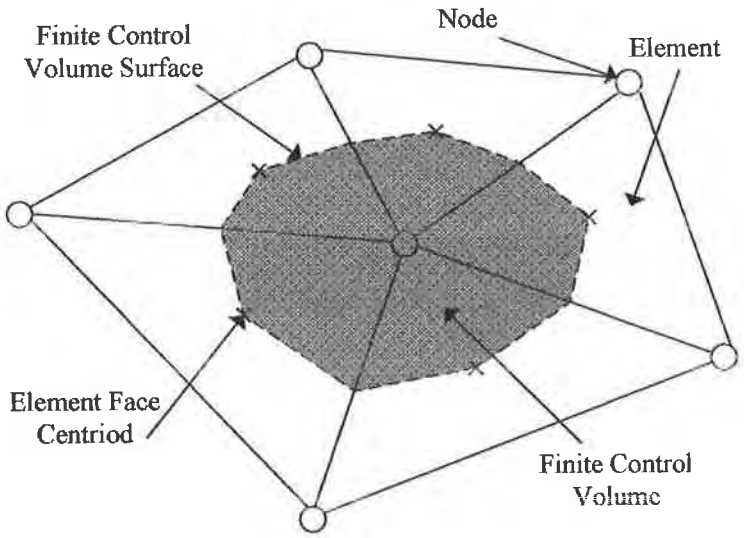

Figure A-2: Typical 2D mesh elements. The control volume is constructed around each mesh node using the median-dual discretisation scheme.

In the figure above, each node is surrounded by a set of surfaces which comprise the control volume. The control volume is constructed around each mesh node using the median-dual discretisation scheme. The boundary of the control volume is defined

by lines joining the centres of the element edges with the element centroids surrounding the node, as shown in Figure A-2.

A.4.2 The Discretised Equations

The governing equations in integral form are applied to each finite control volume such that the relevant quantity (mass or momentum) is conserved in a discrete sense for each. Considering an isolated 2D mesh element for simplicity, such as the one shown in Figure A-3, the surface fluxes of the continuous equations must be discretely represented at the three integration points to complete the conversion of the continuous equations into their discrete forms.

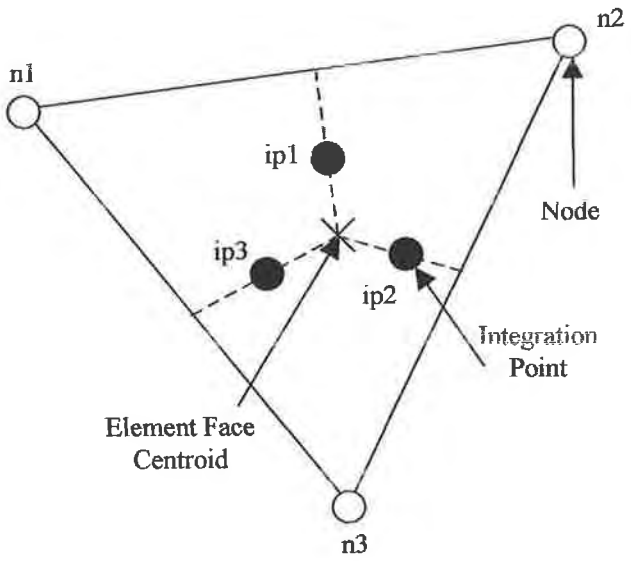

Figure A-3: An isolated triangular 2D mesh element with nodes (n1, n2 and n3) and integration points (ip1, ip2 and ip3) shown.

The integration points, ipn, are located at the centre of each boundary segment surrounding the control volume as shown in Figure A-3. Using a second-order-accurate backward Euler scheme in time the discrete form of the integral equations for a node are written implicitly as the continuity equation

$$\frac{V}{\Delta t}\left(\frac{3}{2}(\rho)-2(\rho)^{\circ}+\frac{1}{2}(\rho)^{\infty}\right)+\sum_{i=1}^{ip}\left(\rho\vec{V}.\vec{l}\right)_i=0 \qquad \text{(A-10)}$$

the x momentum equation

$$\frac{V}{\Delta t}\left(\frac{3}{2}(\rho u)-2(\rho u)^{\circ}+\frac{1}{2}(\rho u)^{\infty}\right)+\sum_{i=1}^{ip}\left(\rho u\vec{V}.\vec{l}\right)_i=\sum_{i=1}^{ip}(Pl_x)_i+\sum_{i=1}^{ip}\left(\tau_{xx}l_x+\tau_{yx}l_y+\tau_{zx}l_z\right)_i$$

(A-11)

the y momentum equation

$$\frac{V}{\Delta t}\left(\frac{3}{2}(\rho v)-2(\rho v)^{\circ}+\frac{1}{2}(\rho v)^{\infty}\right)+\sum_{i=1}^{ip}\left(\rho v\vec{V}.\vec{l}\right)_i=\sum_{i=1}^{ip}(Pl_y)_i+\sum_{i=1}^{ip}\left(\tau_{xy}l_x+\tau_{yy}l_y+\tau_{zy}l_z\right)_i$$

(A-12)

and the z momentum equation

$$\frac{V}{\Delta t}\left(\frac{3}{2}(\rho w)-2(\rho w)^{\circ}+\frac{1}{2}(\rho w)^{\infty}\right)+\sum_{i=1}^{ip}\left(\rho w\vec{V}.\vec{l}\right)_i=\sum_{i=1}^{ip}(Pl_z)_i+\sum_{i=1}^{ip}\left(\tau_{xz}l_x+\tau_{yz}l_y+\tau_{zz}l_z\right)_i$$

(A-13)

where the summation is over all the ip integration points of the finite control volume, l_x, l_y and l_z are the components of the surface area normal vector in the Cartesian x, y and z directions respectively, Δt is the timestep, the superscript $^{\circ}$ refers to the solution from the last timestep, and $^{\infty}$ refers to the solution from the timestep before that.

The viscous stress terms on the right hand side of the discretised momentum equations (A.11) to (A.13) are calculated as follows

$$\begin{bmatrix} \tau_{xx} & \tau_{xy} & \tau_{xz} \\ \tau_{yx} & \tau_{yy} & \tau_{yz} \\ \tau_{zx} & \tau_{zy} & \tau_{zz} \end{bmatrix} = \begin{bmatrix} \left(2\mu\frac{\partial u}{\partial x} - \frac{2}{3}\mu\vec{\nabla}\cdot\vec{V}\right) & \mu\left(\frac{\partial u}{\partial y} + \frac{\partial v}{\partial x}\right) & \mu\left(\frac{\partial u}{\partial z} + \frac{\partial w}{\partial x}\right) \\ \mu\left(\frac{\partial v}{\partial x} + \frac{\partial u}{\partial y}\right) & \left(2\mu\frac{\partial v}{\partial y} - \frac{2}{3}\mu\vec{\nabla}\cdot\vec{V}\right) & \mu\left(\frac{\partial v}{\partial z} + \frac{\partial w}{\partial y}\right) \\ \mu\left(\frac{\partial w}{\partial x} + \frac{\partial u}{\partial z}\right) & \mu\left(\frac{\partial w}{\partial y} + \frac{\partial v}{\partial z}\right) & \left(2\mu\frac{\partial w}{\partial z} - \frac{2}{3}\mu\vec{\nabla}\cdot\vec{V}\right) \end{bmatrix}$$

(A-14)

where the variables are as before.

For compressible flow, the continuity and momentum equations must be augmented by the energy equation and also an equation of state in order to close the set. However, for the incompressible flow in this work the density ρ is specified, reducing the unknowns to four dependant variables P, u, v, and w contained within four equations. Hence, the set of equations is closed and the solver can calculate P, u, v and w values for each mesh node.

A.4.3 Methods of Interpolation

The majority of the terms in Equations (A.10) to (A.13) are evaluated at the integration points. Therefore the variation of the variable within the element must be calculated via interpolation. The handling of this interpolation is dependant on the term involved. The pressure and diffusion terms on the right hand side of momentum Equations (A.11) to (A.13) require tri-linear interpolation of pressure and velocity using finite element shape functions, the details of which can be found elsewhere [100]. The advection term on the left hand side of the momentum equations in general form is

$$\sum_{i=1}^{ip}\left(\rho\phi\vec{V}.\vec{I}\right)_i \qquad \text{(A-15)}$$

where ϕ is the transported variable. The value of ϕ at an integration point is related to the nodal values of ϕ using

$$\phi_{ip} = \phi_{up} + \beta \vec{\nabla}\phi \cdot \vec{r} \tag{A-16}$$

where ϕ_{up} is the variable value at the upwind node, $\vec{r}$ is the directional vector from the upwind node to the integration point, $\vec{\nabla}\phi$ is calculated from the adjacent nodal gradients and β is a blend factor specified from between 0 and 1.

A.5 Solution Strategy

A.5.1 Steady-State Analysis

Starting with user-specified initial conditions, the discretised equations above are solved implicitly at each timestep subject to the applied boundary conditions. The solution is marched through time until the transience of the variables in the domain reduces to near-zero values. This implicit time-marching approach is widely used in modern CFD and usually provides good numerical stability and faster convergence to the steady-state solution than explicit approaches. For steady-state problems the timestep behaves like an 'acceleration parameter', to guide the approximate solutions in a physically based manner to a steady-state solution. The discretised governing equations are advanced in time using a timestep that is calculated automatically from a prescribed stability criterion [101].

A.5.2 Transient Analysis

In a transient simulation, the total time for the simulation is divided into timesteps equal to

$$\Delta t = \frac{T}{p} \tag{A-17}$$

where T is the time duration and p is the number of timesteps. The governing equations are then solved at each timestep to produce the transient flow-field variables.

A.5.3 The Coupled System of Equations

Segregated solvers employ a solution strategy where the momentum equations are first solved using a guessed value for pressure, and then a pressure-correction equation is obtained. A corrected value for pressure is then calculated which is subsequently used to solve the momentum equations again, with this cycle repeated until convergence is achieved. This approach typically results in a large number of iterations due to its "guess-and-correct" nature. ANSYS CFX 12.0 on the other hand uses a coupled solver which solves the hydrodynamic equations for P, u, v and w as a single system. In solving these equations, the first of two numerically intensive steps is to linearise the equation set into matrix form for each node i written as

$$\sum_{k=1}^{n} a_k^i \phi_k^i = b^i \tag{A-18}$$

where ϕ is the solution matrix, b is the right hand side of known values at the node i from the previous timesteps, a is the matrix of equation coefficients (also known) and the summation is over the n neighbouring nodes to the node i. For the 3D mass-momentum equation set, the left hand side terms of this equation for each neighbouring node are a 4x4 matrix and a 4x1 vector expressed as

$$a_k^i = \begin{bmatrix} a_{uu} & a_{uv} & a_{uw} & a_{uP} \\ a_{vu} & a_{vv} & a_{vw} & a_{vP} \\ a_{wu} & a_{wv} & a_{ww} & a_{wP} \\ a_{Pu} & a_{Pv} & a_{Pw} & a_{PP} \end{bmatrix}_k^i \tag{A-19}$$

and

$$\phi_k^i = \begin{bmatrix} u \\ v \\ w \\ P \end{bmatrix}_k^i \tag{A-20}$$

and the right hand side contains known values from previous timesteps at the node itself and is written

$$b^i = \begin{bmatrix} b_u \\ b_v \\ b_w \\ b_P \end{bmatrix}^i \tag{A-21}$$

The advantages of a coupled pressure-velocity approach are robustness, efficiency and simplicity. The principle drawback is the high storage space needed for all of the coefficients.

In the second numerically intensive solution step, ANSYS CFX 12.0 uses a multigrid-accelerated incomplete lower-upper factorisation technique for solving the discrete system of linearised equations. In a steady-state simulation the linearised equations are solved only once at each timestep. For a transient analysis this step is performed multiple times at each timestep as the exact solution of the equations is approached during the course of several iterations. The linearised system of discrete equations described above can be written in the general matrix form

$$A\phi = b \tag{A-22}$$

where A is the coefficient matrix, ϕ the solution vector and b is the right hand side. The above equation can be solved iteratively by starting with an approximate solution ϕ^n that is to be improved by a correction ϕ' to yield a better solution, ϕ^{n+1}, i.e.

$$\phi^{n+1} = \phi^n + \phi' \tag{A-23}$$

where $\phi'$is the solution of

$$A\phi' = r^n \tag{A-24}$$

with r^n, the residual vector, obtained from

$$r^n = b - A\phi^n \tag{A-25}$$

The raw residuals are then normalized for the purpose of solution monitoring. For each solution variable, ϕ, the normalized residual is given in general by

$$\overline{r}_\phi = \frac{r_\phi}{a\Delta\phi} \tag{A-26}$$

where r_ϕ is the raw residual control volume imbalance, a is representative of the control volume coefficient, and $\Delta\phi$ is a representative value of the variable in the domain. Solution convergence must be achieved for a steady-state and for each timestep of the transient simulation. The residual is a measure of the local imbalance of each conservative control volume equation and is the most important measure of solution convergence as it relates directly to whether the equations have been solved.

A.6 Summary

This appendix outlines the theory behind the operation of ANSYS CFX 12.0 software. Firstly, a description of how the geometry of the flow domain is discretised

into an unstructured mesh is provided. The general form of the governing equations of fluid dynamics are then given, followed by a summary of how these equations are converted into integral equations for use in this numerical method. The equations must then be replaced by algebraic approximations in the discretisation procedure. These discretised equations are then applied to finite control volumes in the discretised flow domain. The equations are then solved using a vertex-centred finite volume scheme with implicit time stepping to obtain the variables P, u, v and w.

APPENDIX B

ANSYS CFX Software Validation

B.1 Introduction

This appendix contains analysis of the unconfined laminar incompressible flow over a sharp flat plate. Such a flow will have a viscous effect near the plate surface and will display inviscid characteristics far from the plate. There are currently three techniques in place to study such unconfined flows: (1) numerical solutions (CFD), (2) experimentation and (3) boundary layer theory. The purpose of this appendix is to compare boundary layer theory to CFD results obtained from the ANSYS CFX 12.0 software in order to validate the functionality and accuracy of the software.

B.2 Boundary Layer Theory

Consider the flat plate shown in the Figure B-1 where the flowing fluid approaches the plate with constant axial velocity U. Fluid particles that make contact with the plate will stick to it, which reduces their velocity to zero. This effect, known as the "no-slip" condition, leads to the development of a boundary layer close to the plate as the stationary particles retard their neighbours above. Inside the boundary layer the fluid velocity gradually increases from zero at the plate surface to 99% of the free-stream velocity at some vertical distance from the plate. This vertical distance is called the boundary layer thickness δ. In general the boundary layer begins as

laminar at the leading edge of the plate. An indication as to the laminar or turbulent nature of the flow is provided by the ratio of inertial to viscous forces in the fluid called the Reynolds number which is given by

$$Re_x = \frac{\rho U x}{\mu} \tag{B-1}$$

where ρ is the fluid density, μ is the fluid dynamic viscosity and x is the axial distance along the plate, with x = 0 at the leading edge. As Re_x increases linearly with x, disturbances in the flow begin to grow and the laminar boundary layer eventually becomes turbulent. For smooth polished plates the transition may be delayed until $Re_x \approx 3,000,000$. However, for typical commercial surfaces a more realistic value for transition is $Re_x \approx 500,000$.

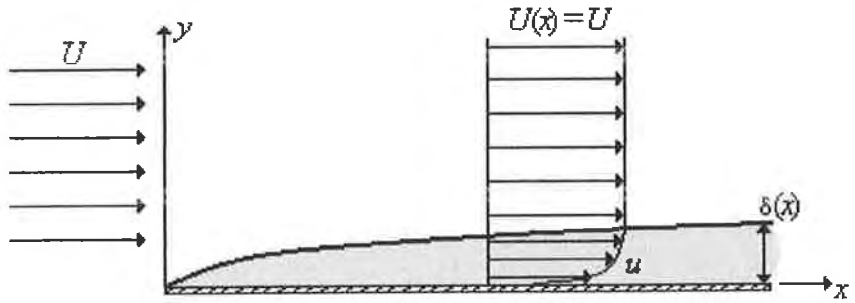

Figure B-1: Schematic diagram of the laminar boundary layer with high Reynolds number ($Re_x >> 1$) flow over a flat plate.

Certain approximations can be made for flow inside a boundary layer, which reduce the governing equations of fluid dynamics to what are known as the boundary layer equations. To derive the boundary layer equations, consider 2D steady incompressible flow in the x-direction as in the Figure B-1 above. The complete equations of motion consist of the continuity and x and y momentum equations

$$\frac{\partial u}{\partial x}+\frac{\partial v}{\partial y}=0$$
$$\rho\left(u\frac{\partial u}{\partial x}+v\frac{\partial u}{\partial y}\right)=-\frac{\partial P}{\partial x}+\mu\left(\frac{\partial^2 u}{\partial x^2}+\frac{\partial^2 u}{\partial y^2}\right) \quad \text{(B-2)}$$
$$\rho\left(u\frac{\partial v}{\partial x}+v\frac{\partial v}{\partial y}\right)=-\frac{\partial P}{\partial y}+\mu\left(\frac{\partial^2 v}{\partial x^2}+\frac{\partial^2 v}{\partial y^2}\right)$$

where P is pressure, x and y are spatial coordinates in the plate surface axial and vertical directions respectively as shown in Figure B-1, and u and v are the x and y components of the fluid velocity vector respectively. Ludwig Prandtl developed boundary layer theory in 1904 to mathematically describe the thin region of fluid near solid boundaries where viscous forces are dominant [96]. Prandtl deduced that the shear layer must be very thin ($\delta << L$) if the Reynolds number is large ($Re_x >> 1$) where L is the axial length of the plate. An integral analysis of the boundary layer reveals that a large Reynolds number creates the following strong inequalities:

$$Re_x >> 1,\ \delta << L,\ v << u,\ \frac{\partial u}{\partial x} << \frac{\partial u}{\partial y},\ \frac{\partial v}{\partial x} << \frac{\partial v}{\partial y}$$

Using these inequalities, Prandtl reduced the governing equations above to two boundary-layer equations written

$$\frac{\partial u}{\partial x}+\frac{\partial v}{\partial y}=0$$
$$u\frac{\partial u}{\partial x}+v\frac{\partial u}{\partial y}=-\frac{1}{\rho}\frac{\partial P}{\partial x}+\nu\frac{\partial^2 u}{\partial y^2} \quad \text{(B-3)}$$

where ν is the fluid kinematic viscosity. One implication of these equations is that the vertical pressure gradient is negligible, i.e.

$$\frac{\partial P}{\partial y}\approx 0,\ P=P(x)$$

The axial pressure gradient in the boundary layer is therefore equal to the axial

pressure gradient in the inviscid free stream which can be calculated from Bernoulli's equation in differential form as

$$\frac{\partial P}{\partial x} = \frac{dP}{dx} = -\rho U \frac{dU}{dx} \tag{B-4}$$

Assuming that the free-stream velocity and hence the pressure is constant over the flat plate, the boundary layer equations can be solved exactly for the u and v velocity components in a laminar flow. These boundary layer equations were first solved numerically by H. Blasius, a student of Prandtl, in 1908 [8]. Blasius showed that the non-dimensional axial velocity u* is a function f of a single composite dimensionless variable η written

$$u^* = \frac{u}{U} = f'(\eta) \tag{B-5}$$

where the dash denotes differentiation and

$$\eta = y\sqrt{\frac{U}{\nu x}} \tag{B-6}$$

Following substitution of Equation (B-5) into the boundary layer Equations (B-3) and much manipulation the two boundary layer equations can be reduced to a single third-order nonlinear ordinary differential equation for f written

$$f''' + \frac{1}{2} f f'' = 0 \tag{B-7}$$

which can be solved by a numerical integration technique. Subsequently from the continuity equation the non-dimensional vertical velocity v* is obtained as follows

$$v^* = \frac{v}{U} = \frac{1}{2}\sqrt{\frac{\nu}{Ux}}\left(\eta f' - f\right) \tag{B-8}$$

The Blasius solution for u* and v* is shown in Table B-1 below. From fluid particle

analysis theory (Chapter 3) the 2D viscous stress exerted on the flat plate at any point reduces to a vector with shear and normal components in the x and y directions respectively written

$$\vec{\tau}_w = \tau_{yx}\vec{i} + \tau_{yy}\vec{j} = \mu\left(\frac{\partial v}{\partial x} + \frac{\partial u}{\partial y}\right)\vec{i} + 2\mu\frac{\partial v}{\partial y}\vec{j} \tag{B-9}$$

where all of the derivatives are calculated at the surface. However, on the surface of the flat plate the no slip condition implies that $\frac{\partial u}{\partial x} = \frac{\partial v}{\partial x} = 0$ and thus, from the continuity equation $\left(\frac{\partial u}{\partial x} + \frac{\partial v}{\partial y}\right) = 0$, it follows that $\frac{\partial v}{\partial y} = 0$. Hence, in this location the viscous stress vector only has a shear stress component which is called the WSS and is written

$$\vec{\tau}_w = \mu\frac{du}{dy}\vec{i} \tag{B-10}$$

where $\frac{du}{dy}$ is the axial velocity gradient in the vertical direction at the surface of the flat plate. The WSS can therefore be calculated from the Blasius solution as

$$\vec{\tau}_w = \left|\vec{\tau}_w\right| = \mu\left.\frac{du}{dy}\right|_{y=0} = \frac{\mu U f''(0)}{\sqrt{2\nu x/U}} \tag{B-11}$$

or can also be expressed in terms of the non-dimensional skin friction coefficient

$$C_f = \frac{2\tau_w}{\rho U^2} = \frac{0.664}{\sqrt{Re_x}} \tag{B-12}$$

The boundary layer thickness for laminar flow can also be calculated from the Blasius solution where u* = 0.99 and is

$$\delta = \frac{5x}{\sqrt{Re_x}} \tag{B-13}$$

where the terms are as before. This boundary layer theory will be used to assess the accuracy of the CFD results. The methodology of the CFD analysis is contained in the following section.

η	f	u*	v*	η	f	u*	v*
0.0	0.0000	0.0000	0.0000	1.8	0.5295	0.5748	0.0007
0.1	0.0017	0.0332	0.0000	2.0	0.6500	0.6298	0.0008
0.2	0.0066	0.0664	0.0000	2.2	0.7812	0.6813	0.0010
0.3	0.0149	0.0996	0.0000	2.4	0.9223	0.7290	0.0011
0.4	0.0266	0.1328	0.0000	2.6	1.0725	0.7725	0.0013
0.5	0.0415	0.1659	0.0001	2.8	1.2310	0.8115	0.0014
0.6	0.0597	0.1989	0.0001	3.0	1.3968	0.8460	0.0016
0.8	0.1061	0.2647	0.0001	3.5	1.8377	0.9130	0.0019
1.0	0.1656	0.3298	0.0002	4.0	2.3057	0.9555	0.0021
1.2	0.2380	0.3938	0.0003	4.5	2.7901	0.9795	0.0022
1.4	0.3230	0.4563	0.0004	5.0	3.2833	0.9915	0.0023

Table B-1: Blasius solution for the non-dimensional axial u* and vertical v* velocity components for a laminar boundary layer with high Reynolds number ($Re_x >> 1$) flow over a flat plate.

B.3 Numerical Simulation of Flat Plate Boundary Layer Flow

The first step in the 2D simulation of laminar flow over a flat plate is to generate the computational domain. The computational domain is created by first generating a 3D solid model; this is necessary as the software requires 3D volumes to execute the finite volume technique. This geometry is then discretised into elements to form the computational domain. The governing equations of fluid dynamics are then solved subject to applied boundary conditions to produce the relevant flow-field variables.

B.3.1 Computational Domain

The dimensions of the computational domain are 1.100 m by 1.581 m by 0.0001 m in the axial, vertical and traverse directions respectively. These dimensions are chosen to facilitate simulation of a 1 m long flat plate preceded by a 0.1 m long free-

slip region, a domain height 1000 times the height of the boundary layer at the end of the plate, $\delta_{x=L}$, and a domain thickness comparable with the smallest element edge length in the mesh. The domain is then discretised into a one-element-thick mesh of unstructured wedge and hexahedral elements. To establish mesh independence four meshes are created in total which are numbered one to four and consecutively increase in element density. For each mesh, the boundary layer region $0 \le x \le L$, $0 \le y \le \delta_{x=L}$ is meshed with equally spaced hexahedral elements and the inviscid region is meshed with unstructured wedge elements. The element vertical edge length in the boundary layer region is specified as a fraction of the boundary layer thickness at the end of the plate, $\delta_{x=L}$. A simulation is performed with each mesh and results are considered mesh converged when the percentage difference ψ_m in the RMS of the variables between successive mesh densities is less than 1% along a sample line. The calculation for ψ_m is

$$\psi_m = \frac{\sqrt{\frac{1}{N}\sum_{i=1}^{N}\left(\Phi_i^{m+1}\right)^2} - \sqrt{\frac{1}{N}\sum_{i=1}^{N}\left(\Phi_i^{m}\right)^2}}{\sqrt{\frac{1}{N}\sum_{i=1}^{N}\left(\Phi_i^{m}\right)^2}} \times 100 \qquad \text{(B-14)}$$

where N is the number of data points on the sample line to which Φ values have been interpolated from the mesh m, in a similar fashion to the methodology set out in Section 5.4. The mesh details are given in Table B-2 and the final mesh used for simulation of laminar flow over a flat plate is shown in Figure B-2.

Mesh Number	Element Edge Length in Boundary Layer Region (mm)	Number of Elements	Number of Nodes
1	0.6324	2,924	4,834
2	0.4743	4,649	8,334
3	0.3162	6,360	11,820
4	0.1581	8,619	16,460

Table B-2: Details of the four computational meshes created in the mesh convergence study for the simulation of a laminar boundary layer with high Reynolds number ($Re_x >> 1$) flow over a flat plate.

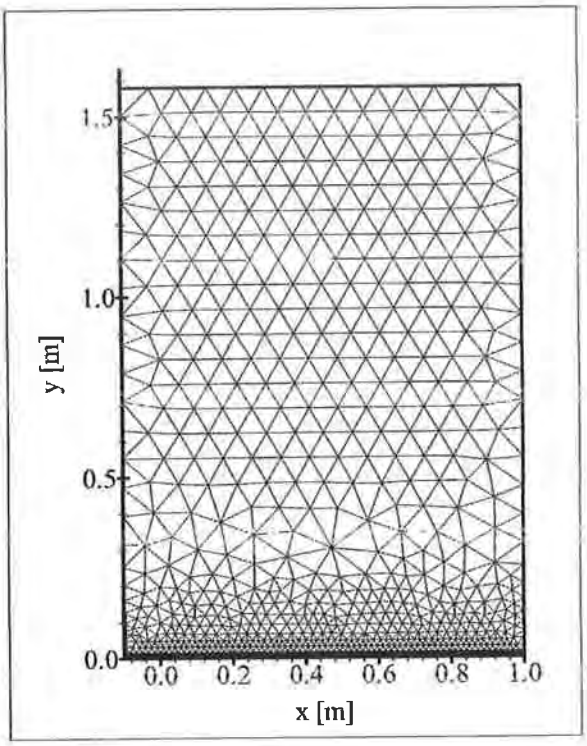

Figure B-2: Mesh 4 for the simulation of a laminar boundary layer with high Reynolds number ($Re_x >> 1$) flow over a flat plate. This mesh consists of 8,619 wedge and hexahedral elements.

B.3.2 Boundary Conditions

As shown in Figure B-3, inlet, outlet, opening, symmetry, free-slip and no-slip wall boundary conditions are applied on the external boundaries of the computational domain to simulate laminar flow over a flat plate. A constant axial velocity of 0.3333 m/s is applied at the inlet corresponding to a Reynolds number of 100,000 at the end of the plate, i.e. $Re_{x=L} = 100{,}000$. The static pressure at the outlet is set equal to the reference pressure of 1 Atm. The streamwise pressure gradient is set to zero at the

top of the domain (opening type boundary condition) to model inviscid flow conditions. Symmetry boundary conditions are placed on the two largest faces and the no-slip boundary condition is applied at the surface representing the flat plate. A 0.1 m free-slip region is placed before the beginning of the flat plate to reduce possible error from the inlet boundary condition.

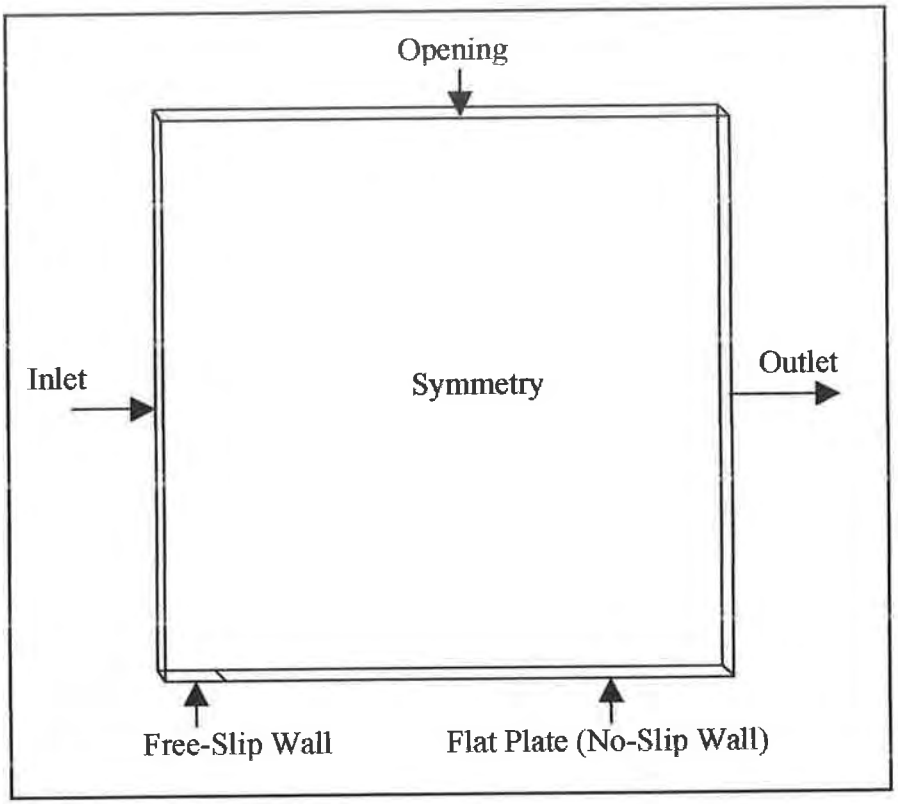

Figure B-3: A schematic diagram of the computational domain and applied boundary conditions for the simulation of laminar flow over a flat plate.

B.3.3 CFD Analysis

Steady-state CFD simulations are conducted to simulate incompressible steady laminar flow over a flat plate for each mesh. The properties of the fluid in the domain are approximately those of human blood with a constant density of $1050\ \mathrm{kg/m^3}$ and a dynamic viscosity of $0.0035\ \mathrm{kg/m \cdot s}$. The continuity and momentum equations are solved by the commercial software package ANSYS CFX 12.0 in a Cartesian coordinate system using a vertex-centred finite volume scheme

with implicit time stepping. At each timestep the convergence criterion employed is a 10^{-6} reduction in the maximum residuals of the discretised equations.

B.3.4 Post-Processing

Four sample lines are created in the flow field, one at the surface of the flat plate running the axial distance of the plate (1 m) to monitor the WSS. The other three sample lines are vertical lines positioned at axial locations of 0.25 m, 0.50 m and 0.75 m along the plate. These lines are the theoretical boundary layer thickness δ in height at each axial location. Due to the structured mesh topology in the boundary layer, variable values can be taken at the evenly spaced boundaries between the elements.

B.4 Results

The results of the mesh convergence study are given in Table B-3. Overall, the results are very well converged between meshes 3 and 4, with all variables converged to within 1%. The change in skin friction coefficient values shows the most uniform decrease with increasing mesh density.

Non-dimensional axial (u*) and vertical (v*) velocity profiles are compared to the Blasius solution for the three axial locations (0.25 m, 0.50 m, 0.75 m) in Figures B-4, B-5, B-7, B-8, B-10, and B-11. Meshes 3 and 4 compare very well with the Blasius solution for all axial locations. There is slight disagreement with the top of the u* velocity profile and the Blasius curve for all locations. This is due to a 1-2% velocity overshoot at the top of the boundary layer as the displaced fluid is forced to accelerate. This result is consistent with previously published work [14]. The velocity vectors are plotted to a height δ at each axial sampling location for

visualisation of the growth of the boundary layer thickness in the axial direction and are shown in Figures B-6, B-9 and B-12. The skin friction coefficient shown in Figure B-13 displays good agreement between the mesh converged results and the theoretical solution for the majority of the plate. However, there is some inaccuracy at the leading edge of the plate; present even for the densest mesh (mesh 4). It may be possible to improve upon these results by compacting the elements in the axial direction around the leading edge of the plate; a meshing strategy previously used by Hirsch [44]. On the basis of these results, the validation of the CFD software is complete. The software has been proven to produce accurate results for incompressible laminar flow over a flat plate.

Variable	% Change Between Meshes 1 and 2	% Change Between Meshes 2 and 3	% Change Between Meshes 3 and 4
u* at 0.25 m	-0.72	-1.35	0.16
v* at 0.25 m	-1.34	-2.61	0.17
u* at 0.50 m	-0.39	-0.13	-0.15
v* at 0.50 m	-0.58	-0.27	-0.22
u* at 0.75 m	-0.27	-0.75	0.13
v* at 0.75 m	-0.36	-1.42	0.27
0.5 Log C_f	0.10	0.04	0.02

Table B-3: Variation of the non-dimensional axial (u*) and vertical (v*) velocity profiles, and skin friction coefficient (C_f) between the four meshes which consecutively increase in element density.

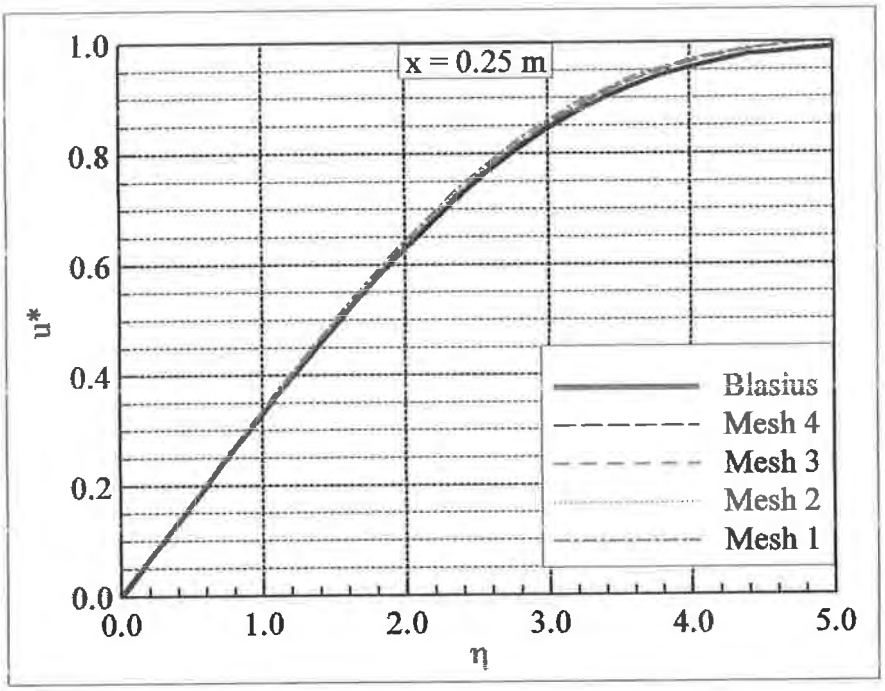

Figure B-4: Non-dimensional axial velocity profiles from the mesh convergence study. The predicted profiles are from axially one-quarter way along the plate (x = 0.25m) and are compared to the exact Blasius solution.

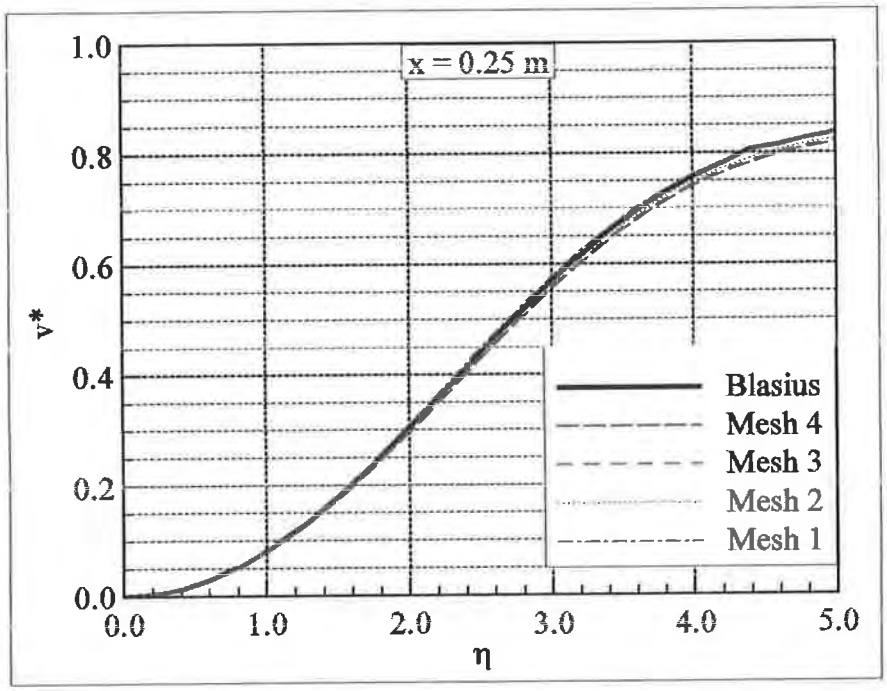

Figure B-5: Non-dimensional vertical velocity profiles from the mesh convergence study. The predicted profiles are from axially one-quarter way along the plate (x = 0.25m) and are compared to the exact Blasius solution.

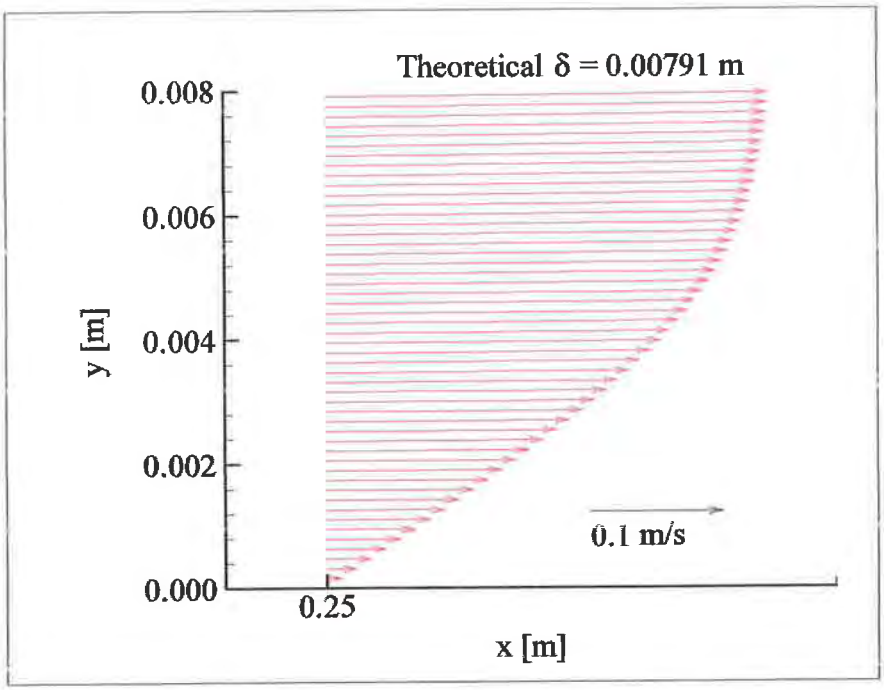

Figure B-6: Velocity vectors near the plate for the finest mesh (8,619 elements). The vectors are plotted at an axial distance of 0.25 m along the plate and to a height δ of 0.00791 m vertically.

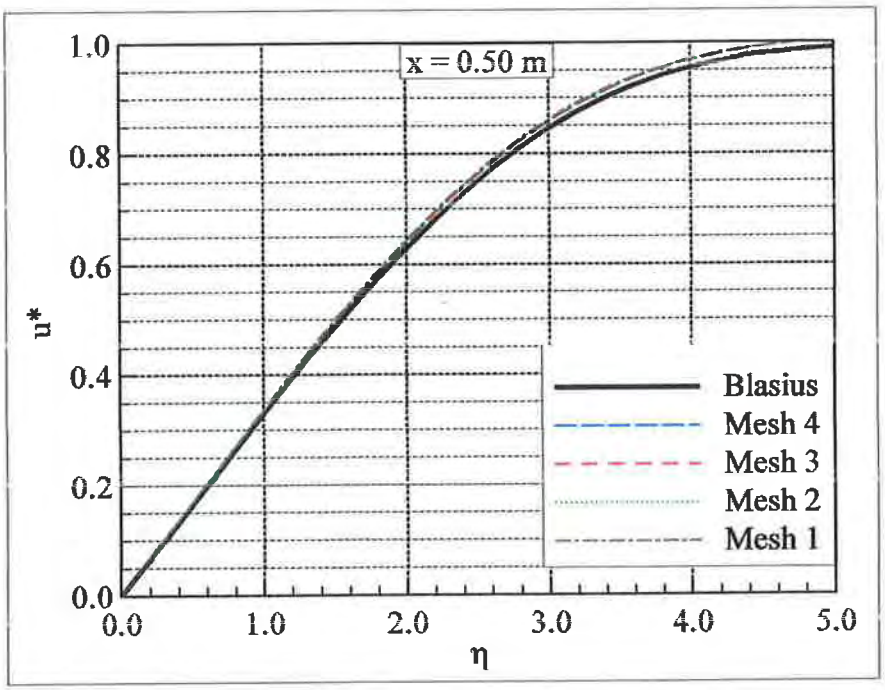

Figure B-7: Non-dimensional axial velocity profiles from the mesh convergence study. The predicted profiles are from axially halfway along the plate (x = 0.5 m) and are compared to the exact Blasius solution.

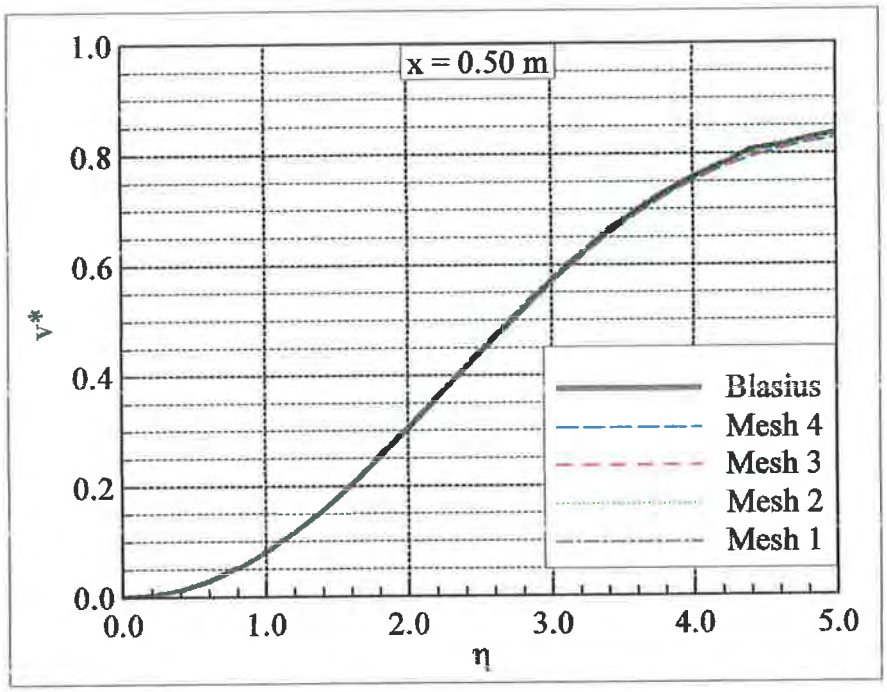

Figure B-8: Non-dimensional vertical velocity profiles from the mesh convergence study. The predicted profiles are from axially halfway along the plate (x = 0.5 m) and are compared to the exact Blasius solution.

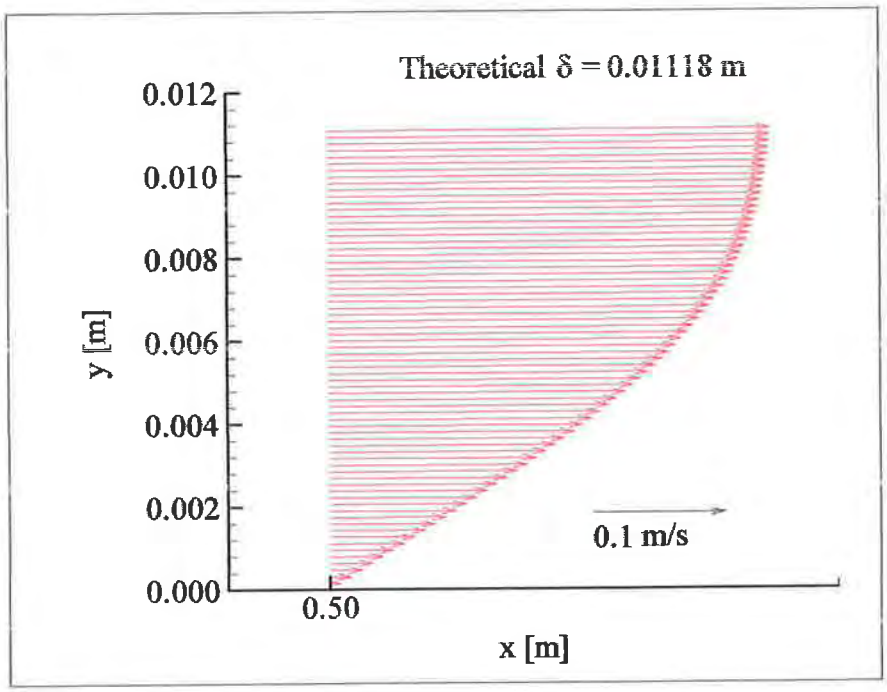

Figure B-9: Velocity vectors near the plate for the finest mesh (8,619 elements). The vectors are plotted at an axial distance of 0.50 m along the plate and to a height δ of 0.01118 m vertically.

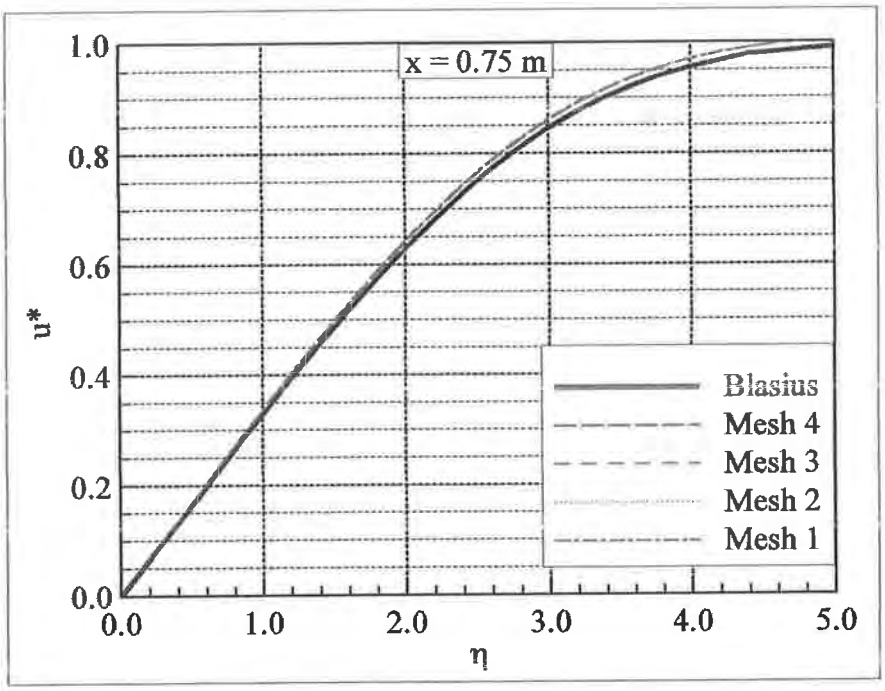

Figure B-10: Non-dimensional axial velocity profiles from the mesh convergence study. The predicted profiles are from axially three-quarter way along the plate (x = 0.75 m) and are compared to the exact Blasius solution.

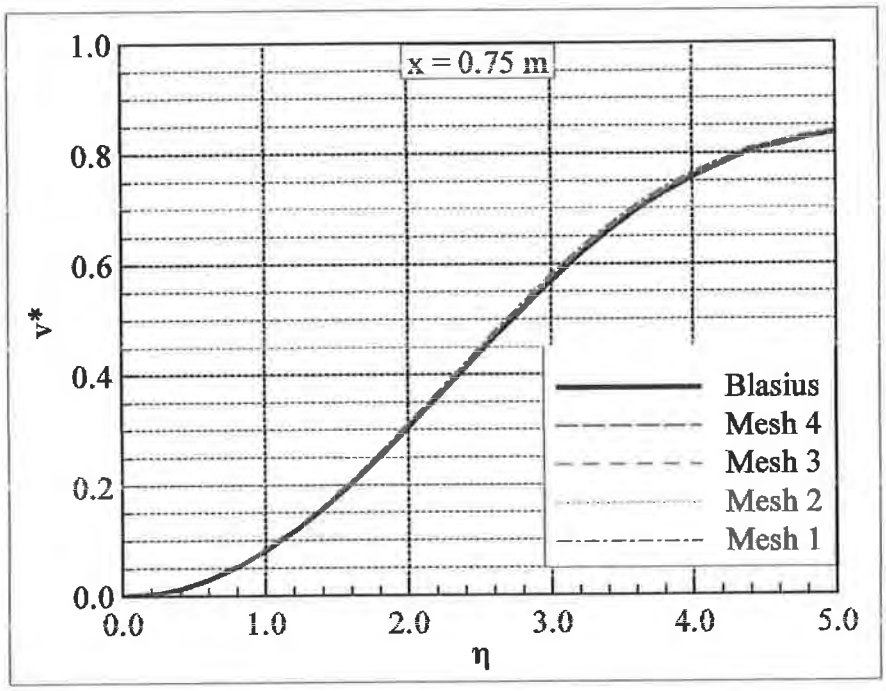

Figure B-11: Non-dimensional vertical velocity profiles from the mesh convergence study. The predicted profiles are from axially three-quarter way along the plate (x = 0.75 m) and are compared to the exact Blasius solution.

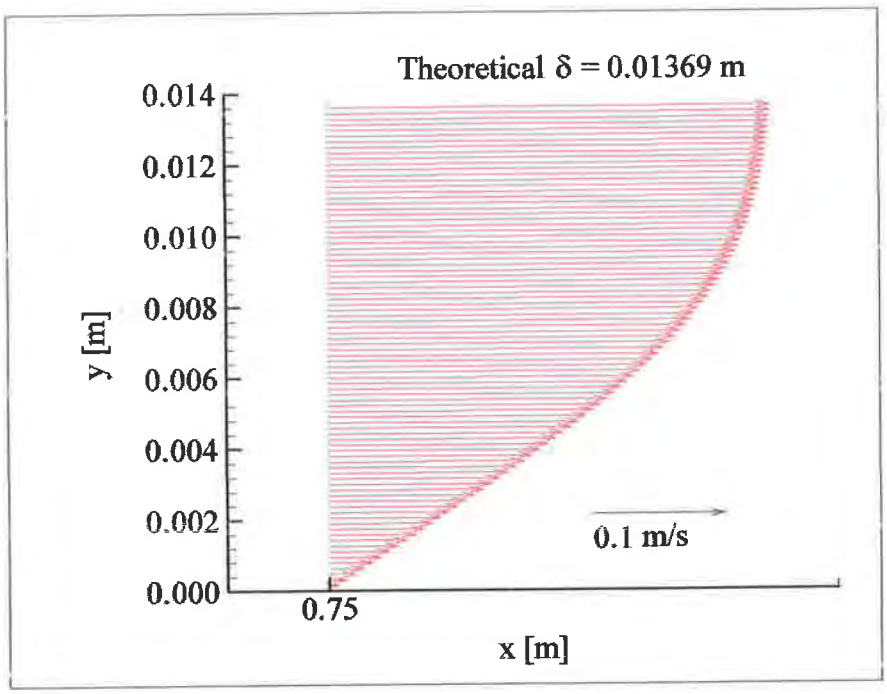

Figure B-12: Velocity vectors near the plate for the finest mesh (8,619 elements). The vectors are plotted at an axial distance of 0.75 m along the plate and to a height δ of 0.01369 m vertically.

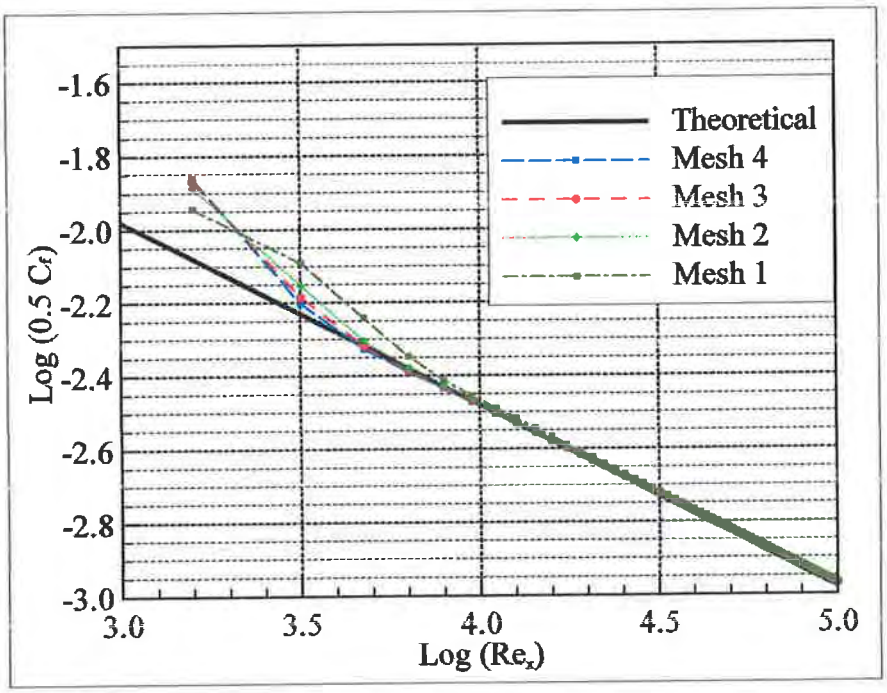

Figure B-13: Variation of the skin friction coefficient with the Reynolds number along the flat plate. The predicted values are compared to the exact Blasius solution.

B.5 Summary

The purpose of this appendix is to validate the ANSYS CFX 12.0 software. This has been achieved through the successful prediction of the laminar flow over a flat plate. The results clearly show that the software can accurately predict the exact theoretical solution. The mesh convergence study also gives a good indication of the level of computational expense necessary to predict the viscous WSS at the artery wall for these flow conditions.

APPENDIX C

Calculation of the WSS-Based Variables

C.1 Introduction

The mathematical description and relevance of the WSS-based variables employed in this work are presented in Chapter 4. This appendix describes the numerical methodology used to calculate these WSS-based variables at the nodes on all surfaces representing the arterial tissue. Test cases are devised and sample calculations provided to demonstrate how the variables are computed. Theoretical solutions are calculated where possible and compared to the computed solutions for validation.

C.2 Wall Shear Stress

The WSS is a vector calculated by ANSYS CFX 12.0 on all bounding walls of the computational domain where the no-slip condition is imposed. All of the WSS-based variables use the components of the WSS vector; hence this is the first variable to be calculated. This section contains a description of the numerical methodology employed to calculate the WSS, followed by a demonstration of the calculation at sample nodes for two different test cases. Finally, to supplement the WSS validation from Appendix B, the theoretical solution is also calculated at these sample nodes and compared to the predicted values.

C.2.1 Numerical Methodology

The three Cartesian components of the WSS vector are $\tau_{w,x}$, $\tau_{w,y}$ and $\tau_{w,z}$ in the x, y and z directions respectively. These components are calculated directly by ANSYS CFX 12.0 as follows

$$\vec{\tau}_w = \vec{l} \cdot \vec{\vec{\tau}}_{ij} = \tau_{w,x}\vec{i} + \tau_{w,y}\vec{j} + \tau_{w,z}\vec{k} \tag{C-1}$$

where

$$\vec{l} = l_x\vec{i} + l_y\vec{j} + l_z\vec{k} \tag{C-2}$$

and l_x, l_y and l_z are the Cartesian components of the surface normal vector in the x, y and z directions respectively, and the viscous stress tensor $\vec{\vec{\tau}}_{ij}$ for an incompressible Newtonian fluid is

$$\vec{\vec{\tau}}_{ij} = \begin{pmatrix} \tau_{xx} & \tau_{xy} & \tau_{xz} \\ \tau_{yx} & \tau_{yy} & \tau_{yz} \\ \tau_{zx} & \tau_{zy} & \tau_{zz} \end{pmatrix} = \begin{pmatrix} 2\mu\dfrac{\partial u}{\partial x} & \mu\left(\dfrac{\partial u}{\partial y}+\dfrac{\partial v}{\partial x}\right) & \mu\left(\dfrac{\partial u}{\partial z}+\dfrac{\partial w}{\partial x}\right) \\ \mu\left(\dfrac{\partial v}{\partial x}+\dfrac{\partial u}{\partial y}\right) & 2\mu\dfrac{\partial v}{\partial y} & \mu\left(\dfrac{\partial v}{\partial z}+\dfrac{\partial w}{\partial y}\right) \\ \mu\left(\dfrac{\partial w}{\partial x}+\dfrac{\partial u}{\partial z}\right) & \mu\left(\dfrac{\partial w}{\partial y}+\dfrac{\partial v}{\partial z}\right) & 2\mu\dfrac{\partial w}{\partial z} \end{pmatrix} \tag{C-3}$$

To demonstrate the calculation, consider the 2D element face inclined at an angle θ to the horizontal x-axis and with a surface normal vector $\vec{l}$ shown in Figure C-1. The components of the WSS vector are calculated by summing the stresses in each direction on an area ratio basis as

$$\vec{\tau}_w = \tau_{w,x}\vec{i} + \tau_{w,y}\vec{j} = \left[\left(\tau_{xx}\frac{A_x}{A}\right)+\left(\tau_{yx}\frac{A_y}{A}\right)\right]\vec{i} + \left[\left(\tau_{xy}\frac{A_x}{A}\right)+\left(\tau_{yy}\frac{A_y}{A}\right)\right]\vec{j} \tag{C-4}$$

where A is the surface area of the element face, A_x and A_y are the projected areas of the element face in the x and y coordinate directions respectively, and τ_{ij} is the

component of the viscous stress tensor acting on the i face in the j direction. For the element in Figure C-1, the area ratios can be replaced by the Cartesian components of the surface normal vector through the relations

$$-\frac{A_x}{A} = l_x, \quad \frac{A_y}{A} = l_y$$

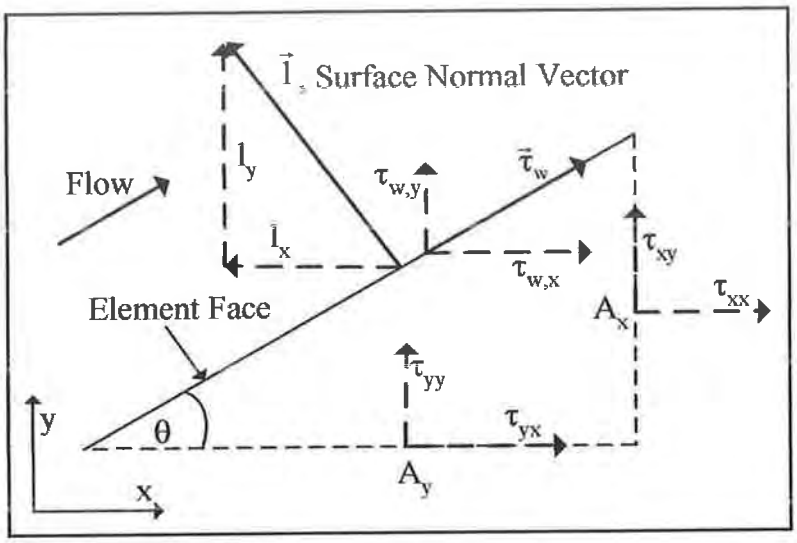

Figure C-1: Schematic diagram of a 2D element face inclined at an angle θ to the horizontal with a surface normal vector $\vec{l}$ and an area A. The element face has projected areas A_x and A_y in the Cartesian x and y directions respectively.

It is common in CFD to compute element face areas from the cross product of coordinate vectors on the face of the element to create an area vector. The area ratios above can therefore be positive or negative depending on the orientation of the face. The relations above can be extended to three dimensions to show that

$$\pm\frac{A_z}{A} = l_z$$

Hence, the three components of the WSS vector are calculated as

$$\tau_{w,x} = (l_x)\left[2\mu\frac{\partial u}{\partial x}\right] + (l_y)\left[\mu\left(\frac{\partial v}{\partial x} + \frac{\partial u}{\partial y}\right)\right] + (l_z)\left[\mu\left(\frac{\partial w}{\partial x} + \frac{\partial u}{\partial z}\right)\right]$$
$$\tau_{w,y} = (l_x)\left[\mu\left(\frac{\partial u}{\partial y} + \frac{\partial v}{\partial x}\right)\right] + (l_y)\left[2\mu\frac{\partial v}{\partial y}\right] + (l_z)\left[\mu\left(\frac{\partial w}{\partial y} + \frac{\partial v}{\partial z}\right)\right] \quad \text{(C-5)}$$
$$\tau_{w,z} = (l_x)\left[\mu\left(\frac{\partial u}{\partial z} + \frac{\partial w}{\partial x}\right)\right] + (l_y)\left[\mu\left(\frac{\partial v}{\partial z} + \frac{\partial w}{\partial y}\right)\right] + (l_z)\left[2\mu\frac{\partial w}{\partial z}\right]$$

and the magnitude of the WSS is calculated as

$$WSS = \sqrt{\tau_{w,x}^2 + \tau_{w,y}^2 + \tau_{w,z}^2} \quad \text{(C-6)}$$

For a transient simulation, the magnitude of the WSS is calculated at each timestep and then the time-averaged WSS is calculated by numerical integration of the magnitudes over the duration of the transient cycle using the trapezoidal rule written

$$WSS = \frac{1}{T}\int_0^T \frac{T}{2(p-1)}\left[WSS_0 + 2\left(WSS_1 + WSS_2 + .. + WSS_{p-1}\right) + WSS_p\right] \quad \text{(C-7)}$$

where T is the period of the transient cycle and p is the number of timesteps. The above methodology is demonstrated in the next section at a sample node on the flat plate test case.

C.2.2 Flat Plate Test Case

The results from the steady-state analysis of laminar flow over a flat plate presented in Appendix B are used here to demonstrate the WSS calculation. The results are taken from a sample node of Mesh 4, approximately halfway along the plate at an axial distance of 0.5079 m from the leading edge as shown in Figure C-2.

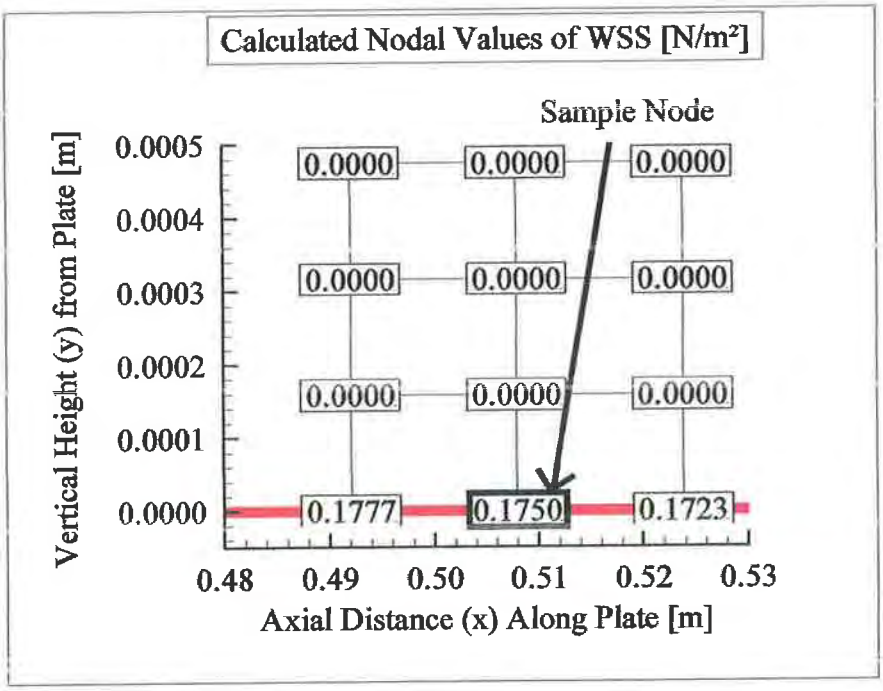

Figure C-2: The location of the sample node taken from Mesh 4 of the flat plate test case which is described in Appendix B. The WSS values are plotted at the nodes.

Variable values from the node located at this point are taken directly from the CFX solution and are as follows:

$$\frac{\partial u}{\partial x} = -0.0076\ s^{-1},\ \frac{\partial u}{\partial y} = 49.9735\ s^{-1},\ \frac{\partial v}{\partial x} = 0.0000\ s^{-1},\ \frac{\partial v}{\partial y} = 0.0086\ s^{-1}$$

$$l_x = 0.0000,\ l_y = 1.0000,\ \mu = 0.0035\ kg/m \cdot s,$$

$$\tau_{w,x} = 0.1750\ N/m^2,\quad \tau_{w,y} = 0.0000\ N/m^2$$

$$WSS = \sqrt{0.1750^2 + 0.0000^2} = 0.1750\ N/m^2$$

Putting the appropriate values into Equation 3-5 above yields

$$\tau_{w,x} = (1)\left[(0.0035)(0.0000 + 49.9735)\right] = 0.1749\ N/m^2$$

$$\tau_{w,y} = (1)[(2)(0.0035)(0.0086)] = 0.0001\ N/m^2$$

$$WSS = \sqrt{0.1749^2 + 0.0001^2} = 0.1749\ N/m^2$$

The result for the WSS components obtained from substituting the velocity gradients and normal vector components into Equation (C-5) are quite similar to the results obtained from the software as expected. The slight difference exists because the

velocity gradients at the wall in the results file (given above) are copied from the adjacent interior node and therefore cannot be relied upon to give the exact stress computed at the wall by the solver. However, the sample calculation is close enough to the software output to prove that this is the method of calculation for the WSS.

A transient simulation is also conducted on the flat plate test case to demonstrate and validate the time-averaging calculation. Instead of having a constant inlet velocity of 0.3333 m/s, the transient simulation has a time-dependent inlet velocity of

$$V_{Inlet} = 0.3333 + 0.0033\left[\sin\left(7.85398\right)\left(t\right)\right] \text{ m/s}$$

The magnitude of the velocity is represented by a sinusoidal wave with a period of 0.8 seconds and amplitude of 0.0033 m/s. Over the period of the transient cycle the magnitude of this inlet velocity will only change by 1% of the steady-state inlet velocity which is 0.3333 m/s. If the time-averaging methodology and calculation is accurate then there should be very little discrepancy between the time-averaged and steady-state variables. The simulation is run for ten cycles of 0.8 seconds with a timestep of 0.1 seconds and the variables are integrated over the final cycle. The time-averaged WSS is calculated from the transient results for the flat plate test case as

$$WSS = \frac{1}{0.8}\left[\frac{0.8}{(2)(8)}\begin{pmatrix}0.1850+(2)(0.1902\\+0.1866+0.1762\\+0.1651+0.1598\\+0.1635+0.1739)\\+0.1849\end{pmatrix}\right] = 0.1750 \text{ N/m}^2$$

which matches the steady-state result extremely well indicating that the time-averaging procedure is performed correctly.

C.2.3 Inclined Flat Plate Test Case

To demonstrate the WSS calculation further, a second steady-state test case is conducted using an inclined flat plate. The WSS vector should have two Cartesian components $\tau_{w,x}$ and $\tau_{w,y}$ acting on the surface of the plate. The geometry is the exact same as the previous flat plate test case except that now the plate is inclined upwards at an angle of 30° to the horizontal. The meshing parameters are the same as those used to create Mesh 4 in the previous test case. The results from the simulation are used to demonstrate the WSS calculation at a sample node approximately halfway along the plate at an axial distance of 0.5 m from the leading edge as shown in Figure C-3.

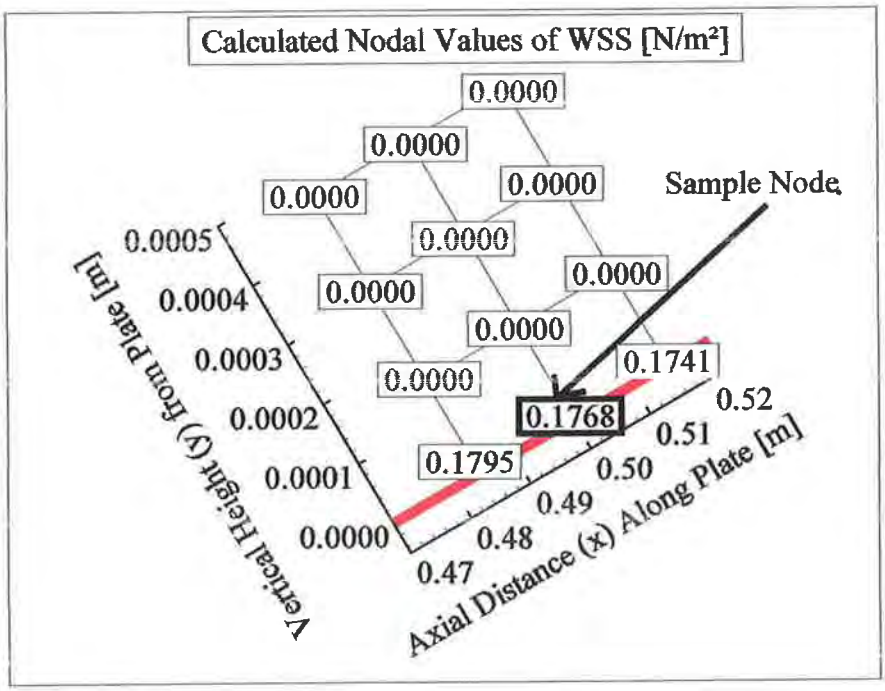

Figure C-3: The location of the sample node on the second test case which is the flat plate inclined upwards at an angle of 30° to the horizontal. WSS values are plotted at the nodes.

Variable values from the node located at this point are taken directly from the CFX solution and are as follows:

$$\frac{\partial u}{\partial x} = -21.8676 \text{ s}^{-1},\ \frac{\partial u}{\partial y} = 37.8624 \text{ s}^{-1},\ \frac{\partial v}{\partial x} = -12.6302 \text{ s}^{-1},\ \frac{\partial v}{\partial y} = 21.8684 \text{ s}^{-1}$$

$l_x = -0.5000,\ l_y = 0.8660,\ \mu = 0.0035 \text{ kg/m} \cdot \text{s},$

$\tau_{w,x} = 0.1531 \text{ N/m}^2,\ \tau_{w,y} = 0.0884 \text{ N/m}^2$

$$\text{WSS} = \sqrt{0.1531^2 + 0.0884^2} = 0.1768 \text{ N/m}^2$$

Putting the appropriate values into Equation (C-5) above yields

$$\tau_{w,x} = (-0.5)[(2)(0.0035)(-21.8676)] + (0.866)[(0.0035)(-12.6302 + 37.8624)]$$
$$= 0.1530 \text{ N/m}^2$$
$$\tau_{w,y} = (-0.5)[(0.0035)(37.8624 + (-12.6302))] + (0.866)[(2)(0.0035)(21.8684)]$$
$$= 0.0884 \text{ N/m}^2$$
$$\text{WSS} = \sqrt{0.1530^2 + 0.0884^2} = 0.1767 \text{ N/m}^2$$

The WSS components from the sample calculation are again slightly different to those outputted from the software. This is again due to the velocity gradients being slightly different to those used in the actual computation.

C.2.4 Validation

The accuracy of the software has been validated through comparison of the computed steady-state WSS results to those from the exact Blasius solution in Appendix B. This section contains a more detailed analysis of the theoretical and predicted values of WSS at the sample nodes for both test cases. The WSS from the Blasius solution for laminar flow over a flat plate is

$$\text{WSS} = \frac{(0.332)(\rho)^{\frac{1}{2}}(\mu)^{\frac{1}{2}}(U)^{\frac{3}{2}}}{x^{\frac{1}{2}}} \qquad \text{(C-8)}$$

where x is the axial distance along the plate, ρ is the fluid density and U is the free-stream velocity. Equation (C-8) is equally applicable to both the horizontal and inclined flat plate test cases as the effect of gravity is neglected in both cases. For the horizontal flat plate test case the results from the Blasius solution and the software

are

$$WSS_{Blasius} = \frac{(0.332)(1050)^{\frac{1}{2}}(0.0035)^{\frac{1}{2}}(0.3333)^{\frac{3}{2}}}{0.5079^{\frac{1}{2}}} = 0.1718 \text{ N/m}^2$$

$$WSS_{Predicted} = \sqrt{0.1750^2 + 0.0000^2} = 0.1750 \text{ N/m}^2$$

respectively, and for the inclined flat plate test case are

$$WSS_{Blasius} = \frac{(0.332)(1050)^{\frac{1}{2}}(0.0035)^{\frac{1}{2}}(0.3333)^{\frac{3}{2}}}{0.5000^{\frac{1}{2}}} = 0.1732 \text{ N/m}^2$$

$$WSS_{Predicted} = \sqrt{0.1530^2 + 0.0884^2} = 0.1767 \text{ N/m}^2$$

respectively. In both cases the software has computed a WSS result approximately 2% greater than the Blasius solution. This is attributable to the assumption of free-stream velocity at the top of the boundary layer with the Blasius solution. In reality there is usually velocity overshoot at the top of the boundary layer due to the displacement of fluid. As shown from the results of several simulations in Figure C-4, the overshoot ranges from between 1 - 5% depending on the Reynolds number, which is consistent with previous work [44].

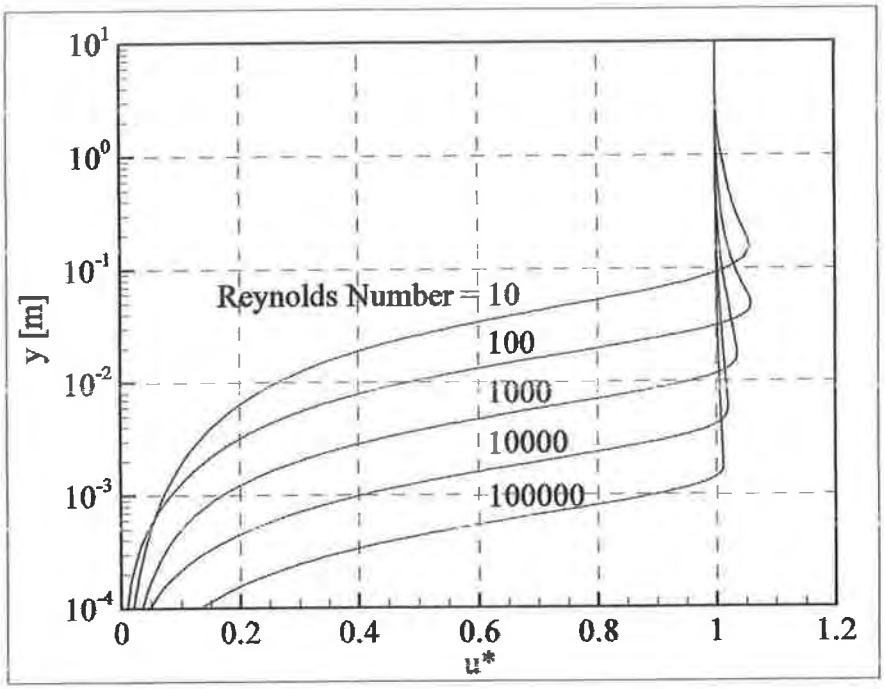

Figure C-4: Plot of the non-dimensional axial velocity (u*) versus height above the plate (y) for several simulations of laminar flow over a flat plate with different Reynolds numbers (Re_L). Mesh 4 from Appendix B is used in all cases.

In both flat plate test cases the Reynolds number (Re_L) is 100000 and the velocity overshoot is approximately 2%. This would cause slightly larger velocity gradients in the boundary layer than those predicted from the Blasius solution. This overshoot is the most likely cause of the overestimated WSS because from the results of Appendix B the variables are mesh converged to within a small fraction of a percent (0.02%) which does not suggest a significant discretisation error. In any case, the present section supports the validation from Appendix B that the software can calculate the WSS with a reasonably good degree of accuracy.

C.2.5 Script

The following is the Python script for calculating the time-averaged WSS

```
import TecUtil
import TecVals
from numpy import*
def TP_TAWSS():
        dt = 0.0125
        TecUtil.DataSetAddVar("Time-Averaged Wall Shear Stress",None)
        novar1 = TecUtil.DataSetGetNumVars()
        info = TecUtil.ZoneGetInfo(1)
        node = range (1, info[0]+1)
        numzones = TecUtil.DataSetGetNumZones()
        zones = range(2,numzones)
        WSSvarnum = TecUtil.VarGetNumByName("Wall Shear Stress [Pa]")
        WSSemparr = ([])
        for i in node:
                WSST1 = TecUtil.DataValueGetByZoneVar(1, WSSvarnum, i)
                WSSTn = TecUtil.DataValueGetByZoneVar(numzones, WSSvarnum, i)
                for j in zones:
                        WSSTj = TecUtil.DataValueGetByZoneVar(j, WSSvarnum, i)
                        WSSemparr.extend([WSSTj])
                WSSTjsum = sum(WSSemparr)
                WSSTrap = (WSST1 + WSSTn)*(dt/2) + WSSTjsum*dt
                TAWSS = (1/0.8)*WSSTrap
                TecUtil.DataValueSetByZoneVar(1,novar1,i,TAWSS)
                WSSemparr = ([])
```

C.3 Wall Shear Stress Gradient

This section contains the methodology employed to calculate the WSSG, which is the spatial gradient of the WSS vector. Sample calculations are performed on both the horizontal and inclined flat plate test cases that were used in the previous section. Finally, a validation of the calculation is conducted through comparison with theoretical results obtained from the Blasius solution.

C.3.1 Numerical Methodology

At any point, the spatial gradient of a scalar is a vector pointing in the direction of the greatest change of the scalar, with a magnitude equal to the greatest change of the scalar. However, the spatial gradient of a vector results in a nine component tensor, representing the rate of change of each of the three components of the vector in each of the three orthogonal coordinate directions. In a Cartesian coordinate system, the WSSG is obtained by calculating the spatial gradient of the WSS vector as follows

$$\vec{\nabla}\vec{\tau}_w = \left(\frac{\partial}{\partial x}\vec{i} + \frac{\partial}{\partial y}\vec{j} + \frac{\partial}{\partial z}\vec{k}\right)\left(\tau_{w,x}\vec{i} + \tau_{w,y}\vec{j} + \tau_{w,z}\vec{k}\right) = \begin{pmatrix} \frac{\partial \tau_{w,x}}{\partial x} & \frac{\partial \tau_{w,x}}{\partial y} & \frac{\partial \tau_{w,x}}{\partial z} \\ \frac{\partial \tau_{w,y}}{\partial x} & \frac{\partial \tau_{w,y}}{\partial y} & \frac{\partial \tau_{w,y}}{\partial z} \\ \frac{\partial \tau_{w,z}}{\partial x} & \frac{\partial \tau_{w,z}}{\partial y} & \frac{\partial \tau_{w,z}}{\partial z} \end{pmatrix} \quad \text{(C-9)}$$

In order to compute this tensor at any node on a computational mesh, the components of the WSS vector $\tau_{w,x}, \tau_{w,y}$ and $\tau_{w,z}$ are considered one at a time. Letting Φ represent any of the WSS vector components, then the change of that component $\Delta\Phi$ and the change in the Cartesian coordinates Δx, Δy and Δz between the node of interest and any neighbour node are input to the general equation

$$\frac{\partial \Phi}{\partial x}\Delta x + \frac{\partial \Phi}{\partial y}\Delta y + \frac{\partial \Phi}{\partial z}\Delta z = \Delta\Phi \quad \text{(C-10)}$$

A similar equation is constructed for each neighbouring node to the node of interest. These equations are then combined into a matrix to compute the gradient of the WSS vector component. For example, a node surrounded by four neighbouring nodes numbered from one to four would have the following matrix equation for the solution of $\partial\tau_{w,x}/\partial x$, $\partial\tau_{w,x}/\partial y$ and $\partial\tau_{w,x}/\partial z$:

$$\begin{bmatrix} \frac{\partial \tau_{w,x}}{\partial x}\Delta x_1 & \frac{\partial \tau_{w,x}}{\partial y}\Delta y_1 & \frac{\partial \tau_{w,x}}{\partial z}\Delta z_1 \\ \frac{\partial \tau_{w,x}}{\partial x}\Delta x_2 & \frac{\partial \tau_{w,x}}{\partial y}\Delta y_2 & \frac{\partial \tau_{w,x}}{\partial z}\Delta z_2 \\ \frac{\partial \tau_{w,x}}{\partial x}\Delta x_3 & \frac{\partial \tau_{w,x}}{\partial y}\Delta y_3 & \frac{\partial \tau_{w,x}}{\partial z}\Delta z_3 \\ \frac{\partial \tau_{w,x}}{\partial x}\Delta x_4 & \frac{\partial \tau_{w,x}}{\partial y}\Delta y_4 & \frac{\partial \tau_{w,x}}{\partial z}\Delta z_4 \end{bmatrix} = \begin{bmatrix} \Delta\tau_{x_1} \\ \Delta\tau_{x_2} \\ \Delta\tau_{x_3} \\ \Delta\tau_{x_4} \end{bmatrix} \quad \text{or}$$

$$\begin{bmatrix} \Delta x_1 & \Delta y_1 & \Delta z_1 \\ \Delta x_2 & \Delta y_2 & \Delta z_2 \\ \Delta x_3 & \Delta y_3 & \Delta z_3 \\ \Delta x_4 & \Delta y_4 & \Delta z_4 \end{bmatrix} \cdot \begin{bmatrix} \frac{\partial \tau_{w,x}}{\partial x} \\ \frac{\partial \tau_{w,x}}{\partial y} \\ \frac{\partial \tau_{w,x}}{\partial z} \end{bmatrix} = \begin{bmatrix} \Delta\tau_{x_1} \\ \Delta\tau_{x_2} \\ \Delta\tau_{x_3} \\ \Delta\tau_{x_4} \end{bmatrix}$$

which can be written as

$$A \cdot x = B \tag{C-11}$$

The solution vector x can now be found by multiplying both sides of Equation (C-11) by the inverse of matrix A. This is achieved using least squares regression with singular value decomposition (SVD). The first step is to decompose the matrix A into

$$A = U \cdot s \cdot V^T \tag{C-12}$$

where the matrices U and V are orthogonal such that

$$U^T \cdot U = V^T \cdot V = 1 \tag{C-13}$$

and s is a matrix with diagonal elements only. The inverse of A can then be expressed as

$$A^{-1} = V \cdot [1/s] \cdot U^T \tag{C-14}$$

So, the solution vector x is obtained as follows

$$x = V \cdot [1/s] \cdot U^T \cdot B \tag{C-15}$$

In practice, for this application there will usually be three unknowns which are the three Cartesian components of the spatial derivative. However, there may be less, equal or more equations than unknowns depending on the number of neighbouring nodes. This calculation is conducted using Tecplot which uses a cluster of neighbouring nodes in the calculation. All nodes connected to the node of interest as well as all the nodes connected to these connected nodes are included in the calculation. The components of matrix A and matrix B in Equation (C-11) are assigned weighting factors based on their proximity to the node of interest. This method is known as moving least squares regression. The SVD procedure above is robust in that it will invert the matrix A as much as it can be inverted and give the best possible answer for the gradient that the data can produce. This procedure is performed for $\tau_{w,x}$, $\tau_{w,y}$ and $\tau_{w,z}$ to calculate the nine tensor components of Equation (C-9)

In order to obtain the relevant components of the WSSG which act on the ECs, the tensor in Equation (C-9) must be transformed from a global Cartesian coordinate system to a local coordinate system at each node. The local coordinate system is defined as m - the WSS direction, l - the surface normal direction, and n - tangential to the surface and normal to m. Directional vectors are defined as follows

$$\begin{aligned}
\vec{m} &= m_1\vec{i} + m_2\vec{j} + m_3\vec{k} = \tau_{w,x}\vec{i} + \tau_{w,y}\vec{j} + \tau_{w,z}\vec{k} \\
\vec{l} &= l_1\vec{i} + l_2\vec{j} + l_3\vec{k} = l_x\vec{i} + l_y\vec{j} + l_z\vec{k} \\
\vec{n} &= n_1\vec{i} + n_2\vec{j} + n_3\vec{k} \\
&= \vec{m} \times \vec{l} = (m_2l_3 - m_3l_2)\vec{i} + (m_3l_1 - m_1l_3)\vec{j} + (m_1l_2 - m_2l_1)\vec{k}
\end{aligned} \tag{C-16}$$

The $\vec{\nabla}\vec{\tau}_w$ tensor with respect to the Cartesian xyz coordinate system can be

transformed to the local mnl coordinate system by a standard component wise tensor transformation written in suffix notation as

$$\frac{\partial \tau_{w,i}}{\partial s_j} = a_{ik} a_{jl} \frac{\partial \tau_{w,k}}{\partial x_l} \tag{C-17}$$

where s_1, s_2 and s_3 denote the m, n and l directions respectively, and x_1, x_2 and x_3 denote the x, y and z directions respectively. The left hand side of Equation (C-17) represents the gradients in the mnl coordinate system whilst the right hand side represents the xyz coordinate system multiplied by two directional cosines. In the suffix notation above the letters i and j are both fixed at 1 to create the first of the nine tensor components in the mnl coordinate system. Letters k and l are then separately replaced by 1, 2 and 3 consecutively to form a total of nine different combinations from the right hand side of Equation (C-17) which are summed to form the equation for the first of the nine transformed tensor components. Letters i and j are then replaced by 1 and 2 respectively and the process repeated to form the second transformed tensor component and so on. The terms a_{ik} and a_{jl} represent the cosines of the angles between the two directions in question. These cosines can be found from the vectors that point in these directions. The cosine of the angle between any two vectors $\vec{a}$ and $\vec{b}$ can be calculated as

$$a_{ab} = \frac{\vec{a}.\vec{b}}{|\vec{a}||\vec{b}|} \tag{C-18}$$

The resultant tensor for the local coordinate system is written

$$\vec{\nabla}\vec{\tau}_w = \begin{pmatrix} \frac{\partial \tau_{w,m}}{\partial m} & \frac{\partial \tau_{w,m}}{\partial n} & \frac{\partial \tau_{w,m}}{\partial l} \\ \frac{\partial \tau_{w,n}}{\partial m} & \frac{\partial \tau_{w,n}}{\partial n} & \frac{\partial \tau_{w,n}}{\partial l} \\ \frac{\partial \tau_{w,l}}{\partial m} & \frac{\partial \tau_{w,l}}{\partial n} & \frac{\partial \tau_{w,l}}{\partial l} \end{pmatrix} \tag{C-19}$$

The choice of mnl coordinate system describes the $\vec{\nabla}\vec{\tau}_w$ tensor in terms of surface normal and tangential direction. Only the tangential components of the tensor have aggravating effects on the EC. Specifically,

$$\vec{\nabla}\vec{\tau}_w = \begin{pmatrix} \frac{\partial \tau_{w,m}}{\partial m} & \frac{\partial \tau_{w,m}}{\partial n} \\ \frac{\partial \tau_{w,n}}{\partial m} & \frac{\partial \tau_{w,n}}{\partial n} \end{pmatrix} \tag{C-20}$$

The diagonal components $\partial\tau_{w,m}/\partial m$ and $\partial\tau_{w,n}/\partial n$ generate intracellular tension which causes widening and shrinking of the intracellular gaps. The off-diagonal components $\partial\tau_{w,m}/\partial n$ and $\partial\tau_{w,n}/\partial m$ cause relative movement of adjacent cells. Lei et al. [68] suggested those creating intracellular tension are the most important with regard to IH. With this in mind, a scalar combination of these normal components is calculated as the WSSG, i.e.

$$\text{WSSG} = \sqrt{\left(\frac{\partial \tau_{w,m}}{\partial m}\right)^2 + \left(\frac{\partial \tau_{w,n}}{\partial n}\right)^2} \tag{C-21}$$

In the following section, the horizontal and inclined flat plate test cases are used again to demonstrate the steady-state calculation of this variable. Transient results are also obtained for the horizontal flat plate test case to demonstrate the WSSG time-averaging procedure.

C.3.2 Flat Plate Test Case

The flat plate test case from the previous section is now used to provide the simplest demonstration of the methodology above. The methodology from the previous section is implemented using Tecplot software. Nodal values are output from the software at the same location on the flat plate as before (axial distance of 0.5079 m from the leading edge) and also from the two closest neighbour nodes to this point on the surface of the plate which are shown in Figure C-5. All the relevant variables output from Tecplot are shown in Table C-1.

Node	Axial Distance [m]	$\tau_{w,x}$ [N/m^2]	l_y	$\partial\tau_{w,x}/\partial x$ [N/m^3]	$\partial\tau_{w,m}/\partial m$ [N/m^3]	WSSG [N/m^3]
Left	0.4921	0.1723	1	-0.1776	-0.1776	0.1776
Sample	0.5079	0.1750	1	-0.1695	-0.1695	0.1695
Right	0.5238	0.1777	1	-0.1620	-0.1620	0.1620

Table C-1: Values of the relevant variables taken directly from Tecplot at the sample node shown in Figure C-5 and its two neighbour nodes for the horizontal flat plate test case.

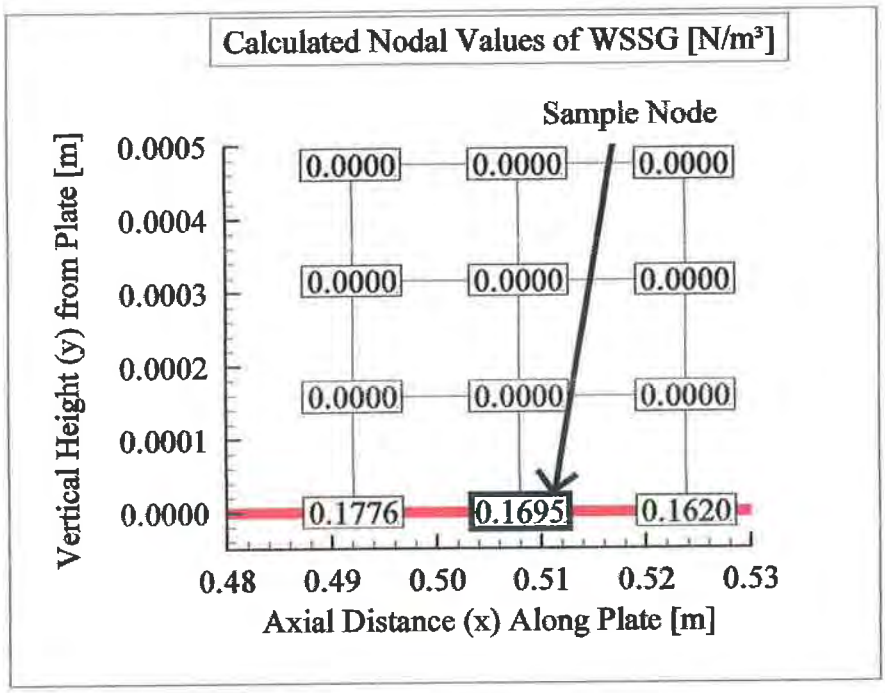

Figure C-5: The location of the sample node taken from Mesh 4 of the flat plate test case which is described in Appendix B. The WSSG values are plotted at the nodes.

For the purposes of this sample calculation, only the two closest neighbouring nodes are considered which demonstrates the calculation to a reasonable degree of accuracy without excessive data manipulation. Using Equation (C-10) with the information in Table C-1 above, the matrix equation for the gradient of $\tau_{w,x}$ is

$$\begin{pmatrix} -0.0026 \\ 0.0027 \end{pmatrix} = \begin{pmatrix} (0.0159)\partial\tau_{w,x}/\partial x + (0)\partial\tau_{w,x}/\partial y + (0)\partial\tau_{w,x}/\partial z \\ (-0.0159)\partial\tau_{w,x}/\partial x + (0)\partial\tau_{w,x}/\partial y + (0)\partial\tau_{w,x}/\partial z \end{pmatrix}$$

for the centre node using data from its two closest neighbours (Left and Right). Applying SVD to solve for the gradients returns

$$x = \begin{bmatrix} \partial\tau_{w,x}/\partial x \\ \partial\tau_{w,x}/\partial y \\ \partial\tau_{w,x}/\partial z \end{bmatrix} = \begin{bmatrix} -1 & 0 & 0 \\ 0 & 1 & 0 \\ 0 & 0 & 0 \end{bmatrix} \cdot \begin{bmatrix} 44.4721 & 0 & 0 \\ 0 & 0 & 0 \\ 0 & 0 & 0 \end{bmatrix} \cdot \begin{bmatrix} -0.7071 & 0.7071 & 0 \\ 0.7071 & 0.7071 & 0 \\ 0 & 0 & 0 \end{bmatrix} \cdot \begin{bmatrix} -0.0026 \\ 0.0027 \\ 0 \end{bmatrix} = \begin{bmatrix} -0.1667 \\ 0 \\ 0 \end{bmatrix}$$

The same method is used to calculate the gradient of $\tau w_{,y}$ in all directions which equal zero in this test case. The mnl coordinate system is then defined as

$$\vec{m} = 0.1750\vec{i} + 0\vec{j} + 0\vec{k}$$
$$\vec{l} = 0\vec{i} + 1\vec{j} + 0\vec{k}$$
$$\vec{n} = \vec{m} \times \vec{l} = 0\vec{i} + 0\vec{j} + 0.1750\vec{k}$$

In order to change the WSSG from Cartesian xyz components into local mnl components, the cosines of the nine angles between the components of the Cartesian coordinate system and the components of the local coordinate system must be found. In this case only three of the cosines at the node of interest are important and are calculated as

$$a_{mx} = \frac{\vec{m}.\vec{x}}{|\vec{m}||\vec{x}|} = \frac{m_1x_1 + m_2x_2 + m_3x_3}{\left(\sqrt{m_1^2 + m_2^2 + m_3^2}\right)\left(\sqrt{x_1^2 + x_2^2 + x_3^2}\right)} = \frac{(0.1750)(1) + 0 + 0}{(0.1750)(1)} = 1$$

$$a_{nz} = \frac{\vec{n}.\vec{z}}{|\vec{n}||\vec{z}|} = \frac{n_1z_1 + n_2z_2 + n_3z_3}{\left(\sqrt{n_1^2 + n_2^2 + n_3^2}\right)\left(\sqrt{z_1^2 + z_2^2 + z_3^2}\right)} = \frac{0 + 0 + (0.1750)(1)}{(0.1750)(1)} = 1$$

$$a_{ly} = \frac{\vec{l}.\vec{y}}{|\vec{l}||\vec{y}|} = \frac{l_1y_1 + l_2y_2 + l_3y_3}{\left(\sqrt{l_1^2 + l_2^2 + l_3^2}\right)\left(\sqrt{y_1^2 + y_2^2 + y_3^2}\right)} = \frac{0 + (1)(1) + 0}{(1)(1)} = 1$$

The WSSG components can now be calculated in the local coordinate system. The only non-zero component is $\partial\tau_{w,m}/\partial m$ and is calculated as

$$\frac{\partial \tau_{w,m}}{\partial m} = a_{mx}a_{mx}\frac{\partial \tau_{w,x}}{\partial x} + a_{mx}a_{my}\frac{\partial \tau_{w,x}}{\partial y} + a_{mx}a_{mz}\frac{\partial \tau_{w,x}}{\partial z} + a_{my}a_{mx}\frac{\partial \tau_{w,y}}{\partial x} + a_{my}a_{my}\frac{\partial \tau_{w,y}}{\partial y}$$
$$+ a_{my}a_{mz}\frac{\partial \tau_{w,y}}{\partial z} + a_{mz}a_{mx}\frac{\partial \tau_{w,z}}{\partial x} + a_{mz}a_{my}\frac{\partial \tau_{w,z}}{\partial y} + a_{mz}a_{mz}\frac{\partial \tau_{w,z}}{\partial z}$$
$$= (1)(1)(-0.1667) + 0 + ...0 = -0.1667 \text{ N/m}^3$$

Finally, the WSSG is calculated as a scalar combination of the two most important components

$$\text{WSSG} = \sqrt{\left(\frac{\partial \tau_{w,m}}{\partial m}\right)^2 + \left(\frac{\partial \tau_{w,n}}{\partial n}\right)^2} = \sqrt{(-0.1667)^2 + (0)^2} = 0.1667 \text{ N/m}^3$$

There is approximately a 1.7% difference between the result above and the result outputted by the software. The difference arises as the calculation above only considers the closest two nodes and assigns them equal weight in the calculation whereas the actual calculation uses a cluster with a proximity-related weighting function as discussed earlier.

The time-averaged WSSG is calculated from the transient results for the sample node on the flat plate test case as

$$\text{WSSG} = \frac{1}{0.8}\left[\frac{0.8}{(2)(8)}\begin{pmatrix} 0.1718 + (2)(0.1735 \\ +0.1726 + 0.1696 \\ +0.1662 + 0.1646 \\ +0.1656 + 0.1687) \\ +0.1720 \end{pmatrix}\right] = 0.1691 \text{ N/m}^3$$

which is very close to the steady-state result outputted by the software and given in Table C-1, indicating that the time-averaging technique is again accurate and calculated correctly.

C.3.3 Inclined Flat Plate Test Case

The inclined flat plate test case is now utilised to demonstrate the WSSG calculation

when there are WSS vector components acting in two directions. The node of interest and two neighbour nodes are shown in Figure C-6 and the relevant data is provided in Table C-2. Again only the two closest neighbouring nodes will be used in the sample calculation. Using the data in Table C-2, the matrix equation for the calculation of the gradient of $\tau_{w,x}$ at the centre node is

$$\begin{pmatrix} 0.0024 \\ -0.0023 \end{pmatrix} = \begin{pmatrix} (-0.0135)\partial\tau_{w,x}/\partial x + (-0.0078)\partial\tau_{w,x}/\partial y + (0.0000)\partial\tau_{w,x}/\partial z \\ (0.0135)\partial\tau_{w,x}/\partial x + (0.0078)\partial\tau_{w,x}/\partial y + (0.0000)\partial\tau_{w,x}/\partial z \end{pmatrix}$$

and solving this equation returns

$$\partial\tau_{w,x}/\partial x = -0.1333, \quad \partial\tau_{w,x}/\partial y = -0.0770, \quad \partial\tau_{w,x}/\partial z = 0.0000$$

Similarly, the matrix equation for the gradient of $\tau_{w,y}$ is

$$\begin{pmatrix} 0.0014 \\ -0.0014 \end{pmatrix} = \begin{pmatrix} (-0.0135)\partial\tau_{w,y}/\partial x + (-0.0078)\partial\tau_{w,y}/\partial y + (0.0000)\partial\tau_{w,y}/\partial z \\ (0.0135)\partial\tau_{w,y}/\partial x + (0.0078)\partial\tau_{w,y}/\partial y + (0.0000)\partial\tau_{w,y}/\partial z \end{pmatrix}$$

and solving this equation returns the values

$$\partial\tau_{w,y}/\partial x = -0.0777, \quad \partial\tau_{w,y}/\partial y = -0.0449, \quad \partial\tau_{w,y}/\partial z = 0.0000$$

For the purpose of demonstration these are again approximate answers, as only the two closest neighbouring nodes are considered.

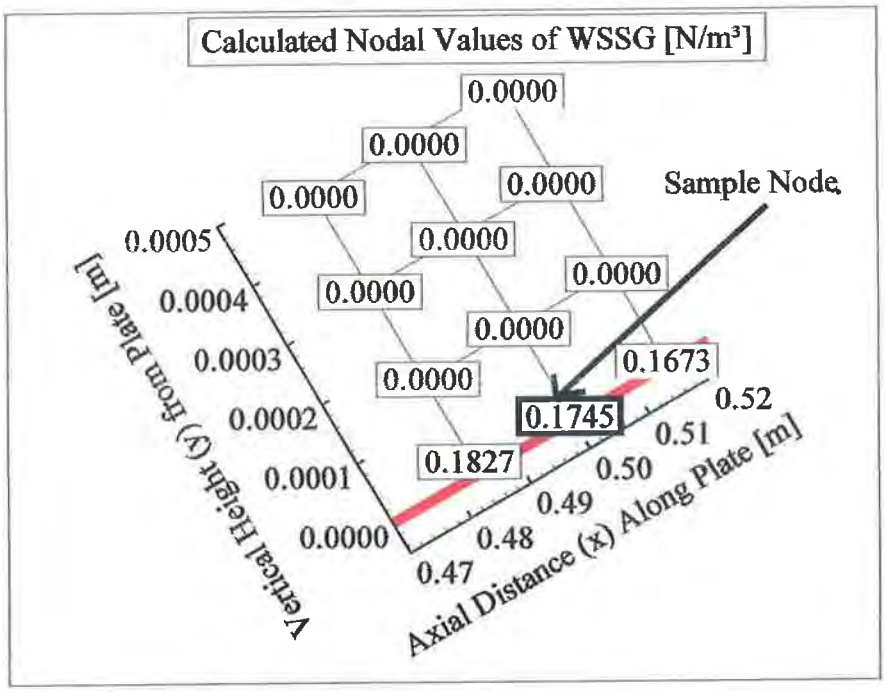

Figure C-6: The location of the sample node on the inclined flat plate test case. WSSG values are plotted at the nodes.

Node	x [m]	y [m]	Axial Distance [m]	$\tau_{w,x}$ [N/m^2]	$\tau_{w,y}$ [N/m^2]	l_x	l_y
Left	0.4195	0.2422	0.4844	0.1555	0.0898	0.866	0.5
Sample	0.4330	0.2500	0.5000	0.1531	0.0884	0.866	0.5
Right	0.4465	0.2578	0.5156	0.1508	0.0870	0.866	0.5

Node	$\partial\tau_{w,x}/\partial x$ [N/m^3]	$\partial\tau_{w,x}/\partial y$ [N/m^3]	$\partial\tau_{w,y}/\partial x$ [N/m^3]	$\partial\tau_{w,y}/\partial y$ [N/m^3]	$\partial\tau_{w,m}/\partial m$ [N/m^3]	WSSG [N/m^3]
Left	-0.1370	-0.0791	-0.0791	-0.0457	-0.1827	0.1827
Sample	-0.1309	-0.0756	-0.0756	-0.0436	-0.1745	0.1745
Right	-0.1255	-0.0724	-0.0724	-0.0418	-0.1673	0.1673

Table C-2: Values of the relevant variables taken directly from Tecplot at the sample node shown in Figure C-6 and its two neighbour nodes for the inclined flat plate test case.

The vectors defining the local coordinate system at the node of interest are

$$\vec{m} = 0.1531\vec{i} + 0.0884\vec{j} + 0.0000\vec{k}$$

$$\vec{l} = -0.5000\vec{i} + 0.8660\vec{j} + 0.0000\vec{k}$$

$$\vec{n} = 0.0000\vec{i} + 0.0000\vec{j} + 0.1768\vec{k}$$

The non-zero directional cosines at this location are

$$a_{mx} = 0.866,\ a_{my} = 0.5,\ a_{nz} = 1,\ a_{lx} = -0.5,\ a_{ly} = 0.866$$

The WSSG component $\partial\tau_{w,m}/\partial m$ is then calculated as

$$\frac{\partial\tau_{w,m}}{\partial m} = (0.866)(0.866)(-0.1333) + (0.866)(0.5)(-0.0770) + (0.5)(0.866)(-0.0777) + (0.5)(0.5)(-0.0449) = -0.1782\ \text{N/m}^3$$

and the WSSG magnitude is calculated as

$$\text{WSSG} = \sqrt{\left(\frac{\partial\tau_{w,m}}{\partial m}\right)^2 + \left(\frac{\partial\tau_{w,n}}{\partial n}\right)^2} = \sqrt{(-0.1782)^2 + (0)^2} = 0.1782\ \text{N/m}^3$$

There is approximately a 2.1% difference between the result above and the result outputted by the software. The difference again arises as the calculation above only considers the closest two neighbour nodes as discussed earlier

C.3.4 Validation

The formula for theoretical WSS calculated from the Blasius solution earlier in Equation (C-8) can be differentiated with respect to the axial distance along the plate x to give an expression for the 1D gradient of the WSS on the flat plate written

$$\text{WSSG}_{\text{Blasius}} = \left| \frac{(-0.5)(0.332)(\rho)^{\frac{1}{2}}(\mu)^{\frac{1}{2}}(U)^{\frac{3}{2}}}{x^{\frac{3}{2}}} \right| \qquad \text{(C-22)}$$

where the symbols are the same as before. For the horizontal flat plate test case, the theoretical and predicted values are

$$WSSG_{Blasius} = \left| \frac{(-0.5)(0.332)(1050)^{\frac{1}{2}}(0.0035)^{\frac{1}{2}}(0.3333)^{\frac{3}{2}}}{0.5079^{\frac{3}{2}}} \right| = 0.1692 \text{ N/m}^3$$

$$WSSG_{Predicted} = \sqrt{-0.1695^2 + 0.0000^2} = 0.1695 \text{ N/m}^3$$

and for the inclined plate test case

$$WSSG_{Blasius} = \left| \frac{(-0.5)(0.332)(1050)^{\frac{1}{2}}(0.0035)^{\frac{1}{2}}(0.3333)^{\frac{3}{2}}}{0.5000^{\frac{3}{2}}} \right| = 0.1732 \text{ N/m}^3$$

$$WSSG_{Predicted} = \sqrt{-0.1745^2 + 0.0000^2} = 0.1745 \text{ N/m}^3$$

The percentage difference in both cases is less than 1%. These results prove that the methodology functions correctly and calculates the WSSG to a high degree of accuracy for these test cases.

C.3.5 Script

The following is the Tecplot script used to calculate the instantaneous WSSG at each timestep.

```
$!ALTERDATA  EQUATION = '{m1} = {WallShearX}'
$!ALTERDATA  EQUATION = '{m2} = {WallShearY}'
$!ALTERDATA  EQUATION = '{m3} = {WallShearZ}'
$!ALTERDATA  EQUATION = '{l1} = {X Grid K Unit Normal}'
$!ALTERDATA  EQUATION = '{l2} = {Y Grid K Unit Normal}'
$!ALTERDATA  EQUATION = '{l3} = {Z Grid K Unit Normal}'
$!ALTERDATA  EQUATION = '{n1} =  {m2}*{l3} - {l2}*{m3} '
$!ALTERDATA  EQUATION = '{n2} = {m3}*{l1} - {m1}*{l3} '
$!ALTERDATA  EQUATION = '{n3} =  {m1}*{l2} - {l1}*{m2}'
$!ALTERDATA  EQUATION = '{mx} = {m1} / sqrt( {m1}**2 + {m2}**2 + {m3}**2 )'
$!ALTERDATA  EQUATION = '{my} = {m2} / sqrt( {m1}**2 + {m2}**2 + {m3}**2 )'
$!ALTERDATA  EQUATION = '{mz} = {m3} / sqrt( {m1}**2 + {m2}**2 + {m3}**2 )'
$!ALTERDATA  EQUATION = '{nx} = {n1} / sqrt( {n1}**2 + {n2}**2 + {n3}**2 )'
$!ALTERDATA  EQUATION = '{ny} = {n2} / sqrt( {n1}**2 + {n2}**2 + {n3}**2 )'
$!ALTERDATA  EQUATION = '{nz} = {n3} / sqrt( {n1}**2 + {n2}**2 + {n3}**2 )'
$!ALTERDATA  EQUATION = '{lx} = {l1} / sqrt( {l1}**2 + {l2}**2 + {l3}**2 ) '
$!ALTERDATA  EQUATION = '{ly} =  {l2} / sqrt( {l1}**2 + {l2}**2 + {l3}**2 ) '
$!ALTERDATA  EQUATION = '[108] =  {l3} / sqrt( {l1}**2 + {l2}**2 + {l3}**2 ) '
$!ALTERDATA  EQUATION = '{MM} = {mx}*{mx}*{XX} + {mx}*{my}*{XY} +
                        {mx}*{mz}*{XZ} + {my}*{mx}*{YX} + {my}*{my}*{YY} +
                        {my}*{mz}*{YZ} + {mz}*{mx}*{ZX} + {mz}*{my}*{ZY} +
                        {mz}*{mz}*{ZZ}'
```

```
$!ALTERDATA  EQUATION = '{NN} = {nx}*{nx}*{XX} + {nx}*{ny}*{XY} +
                         {nx}*{nz}*{XZ} + {ny}*{nx}*{YX} + {ny}*{ny}*{YY} +
                         {ny}*{nz}*{YZ} + {nz}*{nx}*{ZX} + {nz}*{ny}*{ZY} +
                         {nz}*{nz}*{ZZ}'
$!ALTERDATA  EQUATION = '{LL} = {lx}*{lx}*{XX} + {lx}*{ly}*{XY} + {lx}*[108]*{XZ}+
                         {ly}*{lx}*{YX} + {ly}*{ly}*{YY} + {ly}*[108]*{YZ} +
                         [108]*{lx}*{ZX} + [108]*{ly}*{ZY} + [108]*[108]*{ZZ}'
$!ALTERDATA  EQUATION = '{Wall Shear Stress [Pa]} = sqrt({WallShearX}**2 +
                         {WallShearY}**2 + {WallShearZ}**2)'
$!ALTERDATA  EQUATION = '{Wall Shear Stress Gradient [Pa/m]} = sqrt( {MM}**2 +
                         {NN}**2 )'
```

The time-averaged WSSG is then calculated with the following Python script

```
import TecUtil
import TecVals
from numpy import*
def TP_TAWSSG():
        dt = 0.0125
        TecUtil.DataSetAddVar("Time-Averaged Wall Shear Stress Gradient",None)
        novar2 = TecUtil.DataSetGetNumVars()
        info = TecUtil.ZoneGetInfo(1)
        node = range (1, info[0]+1)
        numzones = TecUtil.DataSetGetNumZones()
        zones = range(2,numzones)
        WSSGvarnum = TecUtil.VarGetNumByName("Wall Shear Stress Gradient [Pa/m]")
        WSSGemparr = ([])
        for i in node:
                WSSGT1 = TecUtil.DataValueGetByZoneVar(1, WSSGvarnum, i)
                WSSGTn = TecUtil.DataValueGetByZoneVar(numzones, WSSGvarnum, i)
                for j in zones:
                        WSSGTj = TecUtil.DataValueGetByZoneVar(j, WSSGvarnum, i)
                        WSSGemparr.extend([WSSGTj])
                WSSGTjsum = sum(WSSGemparr)
                WSSGTrap = (WSSGT1 + WSSGTn)*(dt/2) + WSSGTjsum*dt
                WSSAGTrap = (WSSAGT1 + WSSAGTn)*(dt/2) + WSSAGTjsum*dt
                TAWSSG = (1/0.8)*WSSGTrap
                TecUtil.DataValueSetByZoneVar(1,novar2,i,TAWSSG)
                WSSGemparr = ([])
```

C.4 Wall Shear Stress Angle Gradient

The purpose of the WSSAG variable is to quantify the change in WSS direction between neighbouring nodes. As explained in the following section, two variables previously employed in this role [48, 70] have been limited due to the methodology behind their calculation. An improved numerical methodology is presented here for the calculation of the WSSAG that overcomes these limitations. A sample calculation is conducted on a bended duct test case and the variable values are

validated through some simple geometric calculations.

C.4.1 Numerical Methodology

Hyun et al. [48] suggested the wall shear stress angle deviation (WSSAD) to quantify the change in WSS direction between neighbouring nodes. The WSSAD is calculated as the mean angle between the WSS vector at the node of interest $\vec{\tau}_o$ and the WSS vectors at the surrounding nodes $\vec{\tau}_n$ written

$$\text{WSSAD} = \frac{\sum_{i=1}^{n}\left(\text{Cos}^{-1}\left(\frac{\vec{\tau}_o.\vec{\tau}_n}{|\vec{\tau}_o|.|\vec{\tau}_n|}\right)\right)_i}{n} \qquad \text{(C-23)}$$

where n is the number of surrounding nodes. The limitation of this variable is that the magnitude of the WSSAD converges towards zero as the mesh spacing becomes smaller. This mesh-dependent behaviour of the WSSAD suggests that this variable should only be used to compare models with very similar mesh spacing. Subsequently, Longest and Kleinstreuer [70] suggested the WSSAG as a mesh-independent parameter. The first step in calculating the WSSAG for the node of interest is to compute a scalar field of relative WSS angle deviations for each surrounding node as

$$\phi = \text{Cos}^{-1}\left(\frac{\vec{\tau}_o.\vec{\tau}_n}{|\vec{\tau}_o|.|\vec{\tau}_n|}\right) \qquad \text{(C-24)}$$

where the terms are as before. The WSSAG is then calculated at the node of interest as

$$\overrightarrow{\text{WSSAG}} = \vec{\nabla}\phi = \frac{\partial\phi}{\partial x}\vec{i} + \frac{\partial\phi}{\partial y}\vec{j} + \frac{\partial\phi}{\partial z}\vec{k} \qquad \text{(C-25)}$$

This definition of the WSSAG eliminates the mesh dependence that exists with the

WSSAD through the use of the gradient operator. However, the use of the inverse cosine function is a limitation of the methodology of Longest and Kleinstreuer because no account is made for the clockwise or anticlockwise nature of the angle ϕ. To demonstrate this limitation, consider the set of three adjacent nodes shown in Figure C-7. The WSS vectors to the left and right of the central node are 20° anticlockwise and clockwise to the central WSS vector respectively. It is intuitive that the WSSAG at the central node should be 20°/m based on this information.

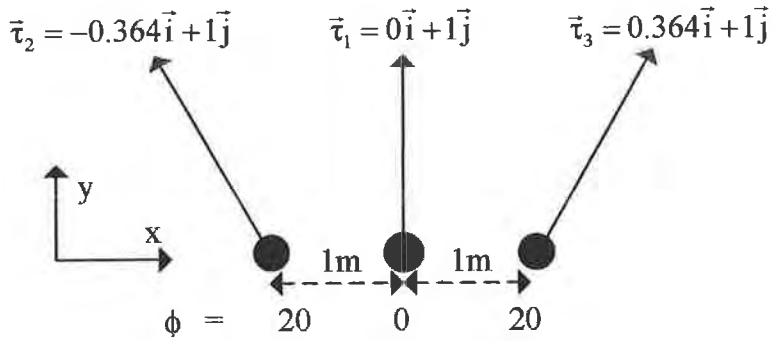

Figure C-7: Set of three adjacent nodes with WSS vectors. The inverse cosine function returns the absolute value of the smallest angle between the vectors.

Using the inverse cos function to compute the angular difference the matrix equation for the WSSAG at the central node of Figure C-7 is

$$\begin{pmatrix} 20 \\ 20 \end{pmatrix} = \begin{pmatrix} 1\dfrac{\partial\phi}{\partial x} + 0\dfrac{\partial\phi}{\partial y} \\ -1\dfrac{\partial\phi}{\partial x} + 0\dfrac{\partial\phi}{\partial y} \end{pmatrix}$$

and solving this equation yields $\partial\phi/\partial x = 0$ and $\partial\phi/\partial y = 0$ which is incorrect and highlights the limitation of this methodology. The immediately apparent solution to this problem is to use the absolute value of the distances between the nodes, so the above equation would be

$$\begin{pmatrix} 20 \\ 20 \end{pmatrix} = \begin{pmatrix} 1\dfrac{\partial\phi}{\partial x} + 0\dfrac{\partial\phi}{\partial y} \\ 1\dfrac{\partial\phi}{\partial x} + 0\dfrac{\partial\phi}{\partial y} \end{pmatrix}$$

which would yield the correct result. However, this approach fails however when there are positive and negative values in the same right hand side of the matrix equation. For example if the nodes of Figure C-7 were positioned such that the matrix equation was

$$\begin{pmatrix} 20 \\ 20 \end{pmatrix} = \begin{pmatrix} 2\dfrac{\partial\phi}{\partial x} - 3\dfrac{\partial\phi}{\partial y} \\ -\dfrac{\partial\phi}{\partial x} + 5\dfrac{\partial\phi}{\partial y} \end{pmatrix}$$

simply taking the absolute values for all the distances on the right hand side of the equation would not return the correct result. The left hand side of the equation must take the clockwise or anticlockwise nature of the angle into account to get the correct result for the WSSAG components $\partial\phi/\partial x$ and $\partial\phi/\partial y$. An improved definition for the WSSAG is presented in this work to address this limitation. The clockwise or anticlockwise nature of the angle between the central WSS vector and its neighbour vectors is determined and included in the calculation. In this calculation the relative WSS angle deviation for each surrounding node is calculated as

$$\phi = \frac{I}{|I|}\mathrm{Cos}^{-1}\left(\frac{\vec{\tau}_o \cdot \vec{\tau}_n}{|\vec{\tau}_o| \cdot |\vec{\tau}_n|}\right) \qquad \text{(C-26)}$$

where $\vec{\tau}_o$ is the time-averaged WSS vector at the node of interest and $\vec{\tau}_n$ the time-averaged WSS vectors at the surrounding nodes, and the indicator function I is defined as

$$I = \vec{l}.(\vec{\tau}_o \times \vec{\tau}_n) \tag{C-27}$$

where $\vec{l}$ is the surface normal vector. If I is positive the WSS vector at the neighbour node is an anticlockwise angle from the vector at the node of interest, and if I is negative the angle is clockwise. This computed angular difference is then assigned to each neighbour node. The next step is to compute the distances between the node of interest and the neighbouring nodes. Computing these distances in the Cartesian xyz coordinate system would produce three unknowns to be calculated in order to obtain the WSSAG vector, namely $\partial\phi/\partial x$, $\partial\phi/\partial y$ and $\partial\phi/\partial z$. However, if these distances are computed in the local mnl coordinate system, the problem reduces to two unknowns, $\partial\phi/\partial m$ and $\partial\phi/\partial n$, since only the tangential components are important for EC alignment. Hence, the coordinates of the nodes are transformed from the Cartesian xyz coordinate system to a local mnl coordinate system as shown in Figure C-8, by a standard vector component transformation detailed below.

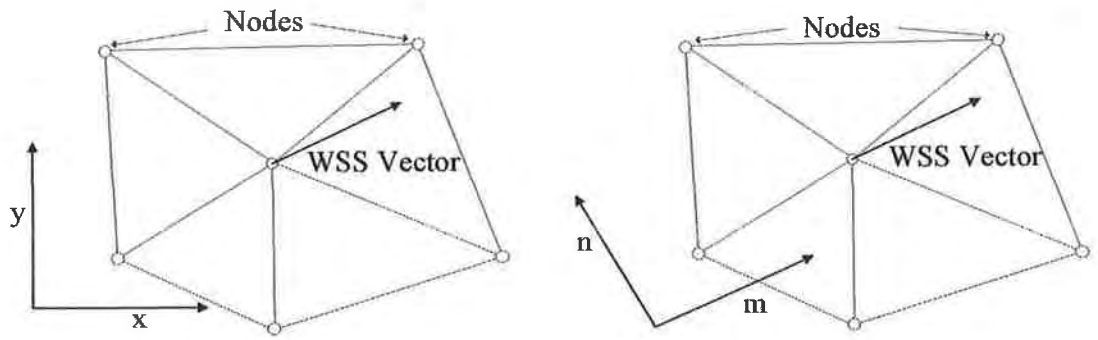

Figure C-8(a): WSS vector described in a Cartesian coordinate system and (b) WSS vector described in a local coordinate system.

The Cartesian coordinates at each nodal location are defined by the vector

$$\vec{C} = x\vec{i} + y\vec{j} + z\vec{k} \tag{C-28}$$

and the local coordinates defined by the vector

$$\vec{L} = m\vec{q} + n\vec{p} + l\vec{r} \tag{C-29}$$

are related to $\vec{C}$ by

$$\begin{aligned} m &= a_{mx}x + a_{my}y + a_{mz}z \\ n &= a_{nx}x + a_{ny}y + a_{nz}z \\ l &= a_{lx}x + a_{ly}y + a_{lz}z \end{aligned} \tag{C-30}$$

where $\vec{p}$, $\vec{q}$ and $\vec{r}$ are unit vectors in the m, n and l directions respectively and the directional cosines between the axes are calculated as before. The local coordinate system shown in the figure above can now be used to find the distance in the m coordinate direction between two adjacent nodes. The same is true of the n and l directions. With the local coordinate system set up, SVD is employed as before to find the components of the WSSAG vector. When the correct angle is assigned to all neighbouring nodes the WSSAG vector is calculated for the node of interest as

$$\overrightarrow{WSSAG} = \frac{\partial\phi}{\partial m}\vec{p} + \frac{\partial\phi}{\partial n}\vec{q} + \frac{\partial\phi}{\partial l}\vec{r} \tag{C-31}$$

Since only the tangential components are important for EC alignment the magnitude of the WSSAG is then calculated as

$$WSSAG = \sqrt{\left(\frac{\partial\phi}{\partial m}\right)^2 + \left(\frac{\partial\phi}{\partial n}\right)^2} \tag{C-32}$$

Since the WSSAG is calculated from the time-averaged WSS vectors there are no further time-averaging calculations required. The WSSAG calculation is performed

in Tecplot with user implemented python scripts. The scripts are necessary as the above calculation must be performed on a node-by-node basis, a task impossible inside the normal graphical user interface of Tecplot.

C.4.2 Bended Duct Test Case

A model of flow through a rectangular duct that bends clockwise through 90° is created as a test case for the WSSAG variable and is shown in Figure C-9. This model is discretised with five evenly spaced layers of 2D extruded elements across the 1 mm thickness of the duct. The mesh spacing is controlled by fixing the maximum element edge length to 0.1 mm everywhere. The mesh consists of 469,794 nodes and 778,155 elements. A constant velocity of 0.1 m/s is applied at the inlet, a static pressure equal to the reference pressure of 1 Atm. is applied at the outlet, and the no-slip boundary condition is applied at all other boundaries which represent the walls of the duct. The fluid approximately represents blood as before with a density of 1050 kg/m^3 and a dynamic viscosity of 0.0035 kg/m.s.

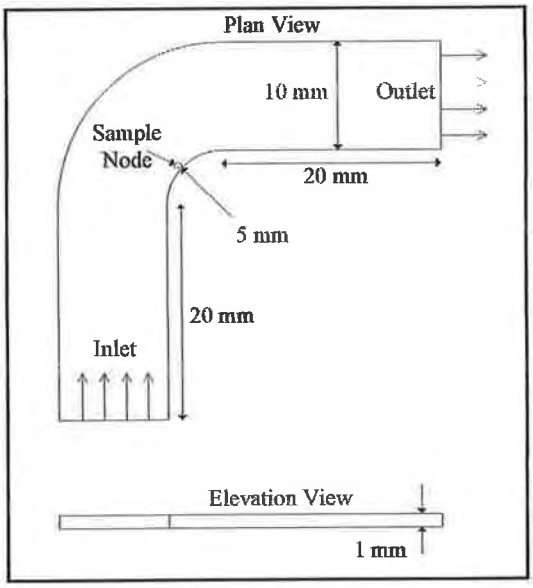

Figure C-9: Schematic of a rectangular duct model which bends clockwise through 90°. This model is used for the sample calculation of the WSSAG variable.

The sample calculation is performed at a node near the inner curve of the bend test case which is shown in Figure C-9 and Figure C-10 below. The sample node is surrounded by six neighbour nodes and all relevant variable values are presented in Table C-3. Initially, an indicator function is calculated for each surrounding node to determine the sign of the angular difference. For this test case the surface normal vector on the 2D surface analysed is $\vec{l} = 0\vec{i} + 0\vec{j} - \vec{k}$ at all node locations, hence for the node (a) below, the indicator function is calculated as

$$\begin{aligned} I &= \vec{l}.(\vec{\tau}_o \times \vec{\tau}_n) \\ &= (l_x)\left[(\tau_{o,y})(\tau_{n,z}) - (\tau_{o,z})(\tau_{n,y})\right] + (l_y)\left[(\tau_{o,z})(\tau_{n,x}) - (\tau_{o,x})(\tau_{n,z})\right] \\ &\quad + (l_z)\left[(\tau_{o,x})(\tau_{n,y}) - (\tau_{o,y})(\tau_{n,x})\right] \\ &= 0 + 0 + (-1)[(1.6151)(1.5415) - (1.3712)(1.9370)] \\ &= -0.1663 \end{aligned}$$

The angular difference for node (a) is then calculated as

$$\begin{aligned} \phi &= \frac{-0.1663}{|-0.1663|}\,\mathrm{Cos}^{-1}\left(\frac{(1.6151)(1.9370) + (1.3712)(1.5415)}{\left(\sqrt{1.6151^2 + 1.3712^2}\right)\left(\sqrt{1.9370^2 + 1.5415^2}\right)}\right) \\ &= -0.0317 \text{ rad} \end{aligned}$$

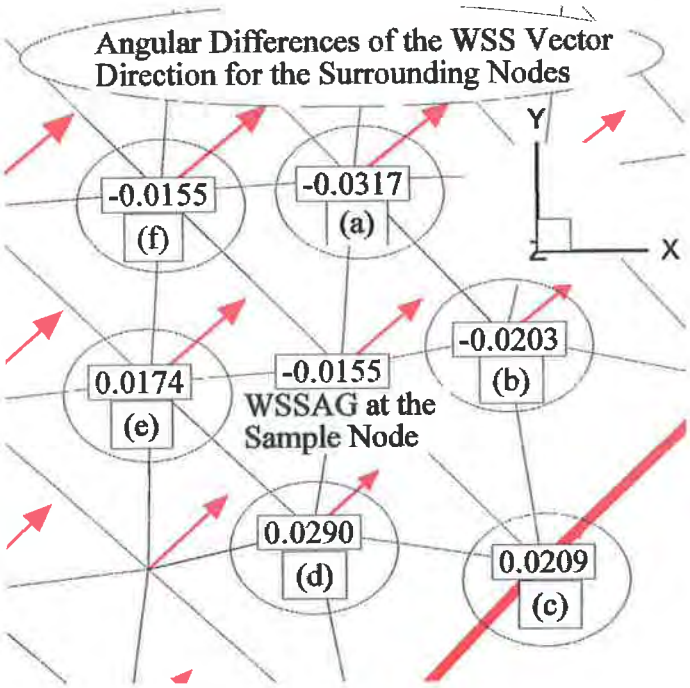

Figure C-10: The sample node at the inner curve of the bend test case. The value of the WSSAG is given at the sample node which is surrounded by six neighbour nodes (circled) where the WSS angular differences are given.

The other angular differences are calculated in the same way and are given in Table C-3. The mnl coordinate system is now defined at the node of interest as

$$\vec{m} = 1.6151\vec{i} + 1.3712\vec{j} + 0\vec{k}$$

$$\vec{l} = 0\vec{i} + 0\vec{j} - 1\vec{k}$$

$$\vec{n} = \vec{m} \times \vec{l} = -1.3712\vec{i} + 1.6151\vec{j} + 0\vec{k}$$

Node	x [mm]	y [mm]	$\tau_{w,x}$ [N/m^2]	$\tau_{w,y}$ [N/m^2]	$\Delta\phi$ [rad]
Sample	-3.7196	3.7196	1.6151	1.3712	0.0000
(a)	-3.7078	3.8944	1.9370	1.5415	-0.0317
(b)	-3.5679	3.7475	1.3568	1.1053	-0.0203
(c)	-3.5355	3.5355	0.8530	0.7542	0.0209
(d)	-3.7475	3.5679	1.3266	1.1941	0.0290
(e)	-3.8944	3.7078	1.8904	1.6623	0.0174
(f)	-3.8838	3.8838	2.1126	1.7380	-0.0155

Table C-3: Information taken directly from the bend test case at the sample node and all of its six neighbouring nodes labelled from (a) to (f).

Node	x [mm]	y [mm]	m [mm]	n [mm]
Sample	-3.7196	3.7196	-0.4281	5.2429
(a)	-3.7078	3.8944	-0.3060	5.3684
(b)	-3.5679	3.7475	-0.2944	5.1659
(c)	-3.5355	3.5355	-0.4069	4.9834
(d)	-3.7475	3.5679	-0.5476	5.1452
(e)	-3.8944	3.7078	-0.5690	5.3469
(f)	-3.8838	3.8838	-0.4470	5.4743
	Δx [mm]	Δy [mm]	Δm [mm]	Δn [mm]
(a)	-0.0118	-0.1748	-0.1221	-0.1255
(b)	-0.1517	-0.0279	-0.1337	0.0770
(c)	-0.1841	0.1841	-0.0212	0.2595
(d)	0.0279	0.1517	0.1195	0.0977
(e)	0.1748	0.0118	0.1409	-0.1040
(f)	0.1642	-0.1642	0.0189	-0.2314

Table C-4: Components of the position vectors $\vec{C}$ and $\vec{L}$ and the distances between the nodes in the x, y, m and n directions as calculated from the position vectors.

The non-zero cosines between the two axes are

$$a_{mx} = \frac{m_1x_1 + m_2x_2 + m_3x_3}{\left(\sqrt{m_1^2 + m_2^2 + m_3^2}\right)\left(\sqrt{x_1^2 + x_2^2 + x_3^2}\right)} = \frac{(1.6151)(1)}{\sqrt{(1.6151)^2 + (1.3712)^2}\sqrt{(1)^2}} = 0.7623$$

$$a_{my} = \frac{m_1y_1 + m_2y_2 + m_3y_3}{\left(\sqrt{m_1^2 + m_2^2 + m_3^2}\right)\left(\sqrt{y_1^2 + y_2^2 + y_3^2}\right)} = \frac{(1.3712)(1)}{\sqrt{(1.6151)^2 + (1.3712)^2}\sqrt{(1)^2}} = 0.6472$$

$$a_{nx} = \frac{n_1x_1 + n_2x_2 + n_3x_3}{\left(\sqrt{n_1^2 + n_2^2 + n_3^2}\right)\left(\sqrt{x_1^2 + x_2^2 + x_3^2}\right)} = \frac{(-1.3712)(1)}{\sqrt{(-1.3712)^2 + (1.6508)^2}\sqrt{(1)^2}} = -0.6472$$

$$a_{ny} = \frac{n_1y_1 + n_2y_2 + n_3y_3}{\left(\sqrt{n_1^2 + n_2^2 + n_3^2}\right)\left(\sqrt{y_1^2 + y_2^2 + y_3^2}\right)} = \frac{(1.6151)(1)}{\sqrt{(-1.3712)^2 + (1.6508)^2}\sqrt{(1)^2}} = 0.7623$$

$$a_{lz} = \frac{l_1z_1 + l_2z_2 + l_3z_3}{\left(\sqrt{l_1^2 + l_2^2 + l_3^2}\right)\left(\sqrt{z_1^2 + z_2^2 + z_3^2}\right)} = \frac{(-1)(1)}{\sqrt{(-1)^2}\sqrt{(1)^2}} = -1$$

The Cartesian coordinates at the node of interest and also at each surrounding node are then rotated to the local mnl coordinate system. The transformation for the node of interest is

$$m = 0.7623(-3.7196) + 0.6472(3.7196) = -0.4281$$
$$n = -0.6472(-3.7196) + 0.7623(3.7196) = 5.2429$$

The components of the coordinate vectors for the surrounding nodes are calculated in the same way and presented in Table C-4. The difference between coordinate vector components Δm between nodes is now the distance between the nodes in the m direction. Similarly Δn is the distance between the nodes in the n direction. For the node of interest, the spatial gradient of the local angular differences results is calculated from the equation

$$\begin{pmatrix} -0.0317 \\ -0.0203 \\ 0.0209 \\ 0.0290 \\ 0.0174 \\ -0.0155 \end{pmatrix} = \begin{pmatrix} -0.1221\dfrac{\partial\phi}{\partial m} & -0.1255\dfrac{\partial\phi}{\partial n} \\ 0.1337\dfrac{\partial\phi}{\partial m} & 0.0770\dfrac{\partial\phi}{\partial n} \\ -0.0212\dfrac{\partial\phi}{\partial m} & 0.2595\dfrac{\partial\phi}{\partial n} \\ 0.1195\dfrac{\partial\phi}{\partial m} & 0.0977\dfrac{\partial\phi}{\partial n} \\ 0.1409\dfrac{\partial\phi}{\partial m} & -0.1040\dfrac{\partial\phi}{\partial n} \\ 0.0189\dfrac{\partial\phi}{\partial m} & -0.2314\dfrac{\partial\phi}{\partial n} \end{pmatrix}$$

where the solution to this matrix equation is

$$\frac{\partial\phi}{\partial m} = -0.1836 \text{ rad/mm}, \quad \frac{\partial\phi}{\partial n} = -0.0852 \text{ rad/mm}$$

and finally the magnitude of the WSSAG is calculated as

$$\sqrt{\left(\frac{\partial\phi}{\partial m}\right)^2 + \left(\frac{\partial\phi}{\partial n}\right)^2} = \sqrt{-0.1836^2 + -0.0852^2} = 0.2024 \text{ rad/mm}$$

C.4.3 Validation

In order to validate the calculation, a value for the WSSAG can be estimated for the

sample node. At the inner radius of the bend the WSS vectors must turn through an angle of 90° or 1.5708 radians over a distance of

$$\frac{2\pi r}{4} = \frac{2\pi(5)}{4} = 7.8540 \text{ mm}$$

which would create a WSSAG of

$$\frac{1.5708}{7.8540} = 0.2000 \text{ rad/mm}$$

There is a 2.4% difference between this theoretical value and the calculated value above. A similar test can be carried out on sample node adjacent to the outer radius where the WSSAG is calculated (results not shown) as

$$\sqrt{\left(\frac{\partial\phi}{\partial m}\right)^2 + \left(\frac{\partial\phi}{\partial n}\right)^2} = \sqrt{-0.0668^2 + 0.0162^2} = 0.0687 \text{ rad/mm}$$

and the theoretical value is

$$1.5708 \Big/ \frac{2\pi(15)}{4} = 0.0666 \text{ rad/mm}$$

giving a 3.2% difference between estimated and predicted results. The difference can be attributed to only considering distances and angular changes in a perfect arc around the bend in the estimated value. The actual solution uses a cluster of nodes from the surrounding node locations which would likely result in the slightly different answer. However, this difference is small enough to indicate that the WSSAG is being calculated correctly.

C.4.4 Script

The following Python script calculates the instantaneous WSSAG

```
import TecUtil
import TecVals
from numpy import*
nodeConnectionMap = {}
def addNodeToNodeConnectionMap(node, connectedNodes):
    if node in nodeConnectionMap:
        nodeList = nodeConnectionMap[node]
    else:
        nodeConnectionMap[node] = []
        nodeList = nodeConnectionMap[node]
    for curNode in connectedNodes:
        if curNode not in nodeList:
            nodeList.append(curNode)
def createNodeConnectionMap():
    nodeMap = TecUtil.DataNodeGetRef(1)
    results = TecUtil.ZoneGetInfo(1)
    numElements = results[1]
    numCorners = results[2]
    assert numCorners==3
    for element in range(1, numElements+1):
        node1 = TecUtil.DataNodeGetByRef(nodeMap, element, 1)
        node2 = TecUtil.DataNodeGetByRef(nodeMap, element, 2)
        node3 = TecUtil.DataNodeGetByRef(nodeMap, element, 3)
        addNodeToNodeConnectionMap(node1, [node2, node3])
        addNodeToNodeConnectionMap(node2, [node1, node3])
        addNodeToNodeConnectionMap(node3, [node1, node2])
def TP_GetConnectedNodes():
    createNodeConnectionMap()
    results = TecUtil.ZoneGetInfo(1)
    nzones = TecUtil.DataSetGetNumZones()
    nodes = range(1, results[0]+1)
    zones = range(1, 2)
    count = 0
    TecUtil.DataSetAddVar("Wall Shear Stress Angle Gradient",None)
    novar = TecUtil.DataSetGetNumVars()
    for z in zones:
      for i in nodes:
        connectedNodes = nodeConnectionMap[i]
        b = len(connectedNodes)
        neighbours = range(0, b)
        X = TecUtil.DataValueGetByZoneVar(z,1,i)
        Y = TecUtil.DataValueGetByZoneVar(z,2,i)
        Z1 = TecUtil.DataValueGetByZoneVar(z,3,i)
        WSSX = TecUtil.DataValueGetByZoneVar(z,4,i)
        WSSY = TecUtil.DataValueGetByZoneVar(z,5,i)
        WSSZ = TecUtil.DataValueGetByZoneVar(z,6,i)
        L1 = TecUtil.DataValueGetByZoneVar(z,7,i)
        L2 = TecUtil.DataValueGetByZoneVar(z,8,i)
        L3 = TecUtil.DataValueGetByZoneVar(z,9,i)
        N1 =  WSSY*L3 - L2*WSSZ
        N2 =  WSSZ*L1 - WSSX*L3
        N3 =  WSSX*L2 - L1*WSSY
        MX = WSSX / sqrt( WSSX**2 + WSSY**2 + WSSZ**2)
        MY = WSSY / sqrt( WSSX**2 + WSSY**2 + WSSZ**2)
        MZ = WSSZ / sqrt( WSSX**2 + WSSY**2 + WSSZ**2)
```

```
NX = N1 / sqrt( N1**2 + N2**2 + N3**2)
NY = N2 / sqrt( N1**2 + N2**2 + N3**2)
NZ = N3 / sqrt( N1**2 + N2**2 + N3**2)
LX = L1 / sqrt( L1**2 + L2**2 + L3**2)
LY = L2 / sqrt( L1**2 + L2**2 + L3**2)
LZ = L3 / sqrt( L1**2 + L2**2 + L3**2)
COM = MX*X + MY*Y + MZ*Z1
CON = NX*X + NY*Y + NZ*Z1
COL = LX*X + LY*Y + LZ*Z1
A = []
B = []
for j in neighbours:
   x = TecUtil.DataValueGetByZoneVar(z,1,connectedNodes[j])
   y = TecUtil.DataValueGetByZoneVar(z,2,connectedNodes[j])
   z1 = TecUtil.DataValueGetByZoneVar(z,3,connectedNodes[j])
   ncom = MX*x + MY*y + MZ*z1
   ncon = NX*x + NY*y + NZ*z1
   ncol = LX*x + LY*y + LZ*z1
   nwsx = TecUtil.DataValueGetByZoneVar(z,4,connectedNodes[j])
   nwsy = TecUtil.DataValueGetByZoneVar(z,5,connectedNodes[j])
   nwsz = TecUtil.DataValueGetByZoneVar(z,6,connectedNodes[j])
   nnx = TecUtil.DataValueGetByZoneVar(z,7,connectedNodes[j])
   nny = TecUtil.DataValueGetByZoneVar(z,8,connectedNodes[j])
   nnz = TecUtil.DataValueGetByZoneVar(z,9,connectedNodes[j])
   CA = (WSSY*nwsz-WSSZ*nwsy)
   CB = (WSSZ*nwsx-WSSX*nwsz)
   CC = (WSSX*nwsy-WSSY*nwsx)
   Dot = nnx*CA + nny*CB + nnz*CC
   dm = (ncom-COM)
   dn = (ncon-CON)
   dl = (ncol-COL)
   Angle =
arccos((WSSX*nwsx+WSSY*nwsy+WSSZ*nwsz)/((sqrt(WSSX**2+WSSY**2+WSSZ**2))*(sqrt(
nwsx**2+nwsy**2+nwsz**2)))))
   if Dot > 0:
            Angle = -Angle
   A.append([ dm, dn ])
   B.append([Angle])
A = matrix(A)
B = matrix(B)
U, s, V = linalg.svd(A, 0, 1)
s1 = 1/s[0]
s2 = 1/s[1]
W = ([[s1,0],[0,s2]])
W = matrix(W)
T1 = sqrt ((W[0,0])**2)
T2 = sqrt ((W[1,1])**2)
if T1 > 100000000:
   W[0,0] = 0
if T2 > 100000000:
   W[1,1] = 0
X = V.T*W*U.T*B
X = array(X)
X1 = ((X[0][0]))
X2 = ((X[1][0]))
WSSAG = (sqrt(X1**2 + X2**2)) / 1000
if WSSAG > 300:
   WSSAG = 300
   count = count + 1
TecUtil.DataValueSetByZoneVar(z,novar,i,WSSAG)
```

The following Python script calculates the time-averaged WSSAG

```
import TecUtil
import TecVals
from numpy import*
def TP_TAWSSAG():
        dt = 0.0125
        TecUtil.DataSetAddVar("Wall Shear Stress Angle Gradient",None)
        novar3 = TecUtil.DataSetGetNumVars()
        info = TecUtil.ZoneGetInfo(1)
        node = range (1, info[0]+1)
        numzones = TecUtil.DataSetGetNumZones()
        zones = range(2,numzones)
        WSSAGvarnum = TecUtil.VarGetNumByName("Wall Shear Stress Angle Gradient")
        WSSAGemparr = ([])
        for i in node:
                WSSAGT1 = TecUtil.DataValueGetByZoneVar(1, WSSAGvarnum, i)
                WSSAGTn = TecUtil.DataValueGetByZoneVar(numzones, WSSAGvarnum, i)
                for j in zones:
                        WSSAGTj = TecUtil.DataValueGetByZoneVar(j, WSSAGvarnum, i)
                        WSSAGemparr.extend([WSSAGTj])
                WSSAGTjsum = sum(WSSAGemparr)
                WSSAGTrap = (WSSAGT1 + WSSAGTn)*(dt/2) + WSSAGTjsum*dt
                TAWSSAG = (1/0.8)*WSSAGTrap
                TecUtil.DataValueSetByZoneVar(1,novar3,i,TAWSSAG)
                WSSAGemparr = ([])
```

C.5 Oscillatory Shear Index

The final WSS-based variable is the OSI. As usual, the following section contains the numerical methodology behind the calculation of the variable. This is followed by two sample calculations on the flat plate test case. One calculation is performed for unidirectional flow and the other for fully oscillatory flow. In the absence of any theoretical solutions for this variable, the ability to distinguish between these types of flow will also serve as a validation for the calculation of the variable.

C.5.1 Numerical Methodology

Cyclic departure of the WSS vector from its predominant direction indicates flow disruption over time and is measured using the OSI calculated as follows

$$OSI = 1 - \frac{\left| \int_0^T \vec{\tau}_w dt \right|}{\int_0^T |\vec{\tau}_w| dt} \tag{C-33}$$

The numerator in Equation (C-33) is the magnitude of the summation of the components of the WSS vector and can be expanded as

$$\left| \int_0^T \vec{\tau}_w dt \right| = \left[\left(\int_0^T \tau_{w,x} dt \right)^2 + \left(\int_0^T \tau_{w,y} dt \right)^2 + \left(\int_0^T \tau_{w,z} dt \right)^2 \right]^{\frac{1}{2}} \tag{C-34}$$

The denominator of Equation (C-33) is the summation of the magnitudes of the WSS vectors and can be expanded as

$$\int_0^T |\vec{\tau}_w| dt = \int_0^T \left[\left(\tau_{w,x} \right)^2 + \left(\tau_{w,y} \right)^2 + \left(\tau_{w,z} \right)^2 \right]^{\frac{1}{2}} dt \tag{C-35}$$

To find the correct value of the magnitude of the time-averaged WSS vector and the time-averaged magnitude of the WSS vectors, Equations (C-34) and (C-35) must be divided by T, the time duration, respectively. Since this operation is performed in the numerator and denominator of Equation (C-33) it is excluded from the calculation of the OSI. All summations are performed using the trapezoidal method as before. The OSI calculation is performed in Tecplot with user implemented python scripts. The scripts are necessary in this case to manipulate the large arrays of data involved in the calculation.

C.5.2 Flat Plat Test Case and Validation

To demonstrate the calculation, the transient flat plate test case described in Section C.2.1 will be examined. The magnitude of the inlet velocity has a small time-dependent oscillation and is given by

$$V_{Inlet} = 0.3333 + 0.0033\left[\sin\left(7.85398\right)\left(t\right)\right] \text{ m/s}$$

In this case the WSS is completely unidirectional and the summary of WSS values is shown in Table C-5. Again, results are taken from the sample node approximately halfway along the plate at an axial distance of 0.5079 m from the leading edge as shown in Figure C-2. The integral summations are calculated as

$$\left|\int_0^T \vec{\tau}_w dt\right| = \left[\left[\frac{0.8}{(2)(8)}\begin{pmatrix}0.1850+(2)(0.1902\\+0.1866+0.1762\\+0.1651+0.1598\\+0.1635+0.1739)\\+0.1849\end{pmatrix}\right]^2\right]^{\frac{1}{2}} = 0.1400 \text{ N/m}^2$$

and

$$\int_0^T \left|\vec{\tau}_w\right| dt = \left[\left[\frac{0.8}{(2)(8)}\begin{pmatrix}0.1850+(2)(0.1902\\+0.1866+0.1762\\+0.1651+0.1598\\+0.1635+0.1739)\\+0.1849\end{pmatrix}\right]^2\right]^{\frac{1}{2}} = 0.1400 \text{ N/m}^2$$

and the OSI is calculated as

$$\text{OSI} = 1 - \frac{0.1400}{0.1400} = 0$$

as expected for this unidirectional flow

Timestep	$\tau_{w,x}$ [N/m^2]	WSS [N/m^2]
1	0.1850	0.1850
2	0.1902	0.1902
3	0.1866	0.1866
4	0.1762	0.1762
5	0.1651	0.1651
6	0.1598	0.1598
7	0.1635	0.1635
8	0.1739	0.1739
9	0.1849	0.1849
Integral Summation	0.1400	0.1400

Table C-5: The components and magnitudes of the WSS at the sample node on the horizontal flat plate test case for unidirectional flow.

To demonstrate the opposite scenario the same test case and sample node are used but this time the inlet velocity is fully oscillatory and is given by

$$V_{Inlet} = 0.3333\left[\sin\left(7.85398\right)\left(t\right)\right] \text{ m/s}$$

This represents a sinusoidal wave with a period of 0.8 seconds and amplitude of 0.3333 m/s. As in the previous case, the simulation is run for ten cycles of 0.8 seconds with a timestep of 0.1 seconds and the variables are integrated over the final cycle. The results for the components and magnitudes of WSS at each timestep are given in Table C-6 below. The integral summations are calculated as

$$\left|\int_0^T \bar{\tau}_w dt\right| = \left[\left[\frac{0.8}{(2)(8)}\begin{pmatrix}1.2209+(2)(1.8677\\+1.4197+0.1360\\-1.2298-1.8766\\-1.4280+0.1439)\\+1.2211\end{pmatrix}\right]^2\right]^{\frac{1}{2}} = 0.0034 \text{ N/m}^2$$

and

$$\int_0^T |\vec{\tau}_w| dt = \left[\left[\frac{0.8}{(2)(8)} \begin{pmatrix} 1.2209 + (2)(1.8677 \\ +1.4197 + 0.1360 \\ +1.2298 + 1.8766 \\ +1.4280 + 0.1439) \\ +1.2211 \end{pmatrix}^2 \right]^{\frac{1}{2}} \right] = 0.9323 \text{ N/m}^2$$

and the OSI is calculated as

$$OSI = 1 - \frac{0.0034}{0.9323} = 0.9964$$

which is as expected for the fully oscillatory WSS produced by the oscillatory inlet velocity.

Timestep	$\tau_{w,x}$ [N/m^2]	WSS [N/m^2]
1	1.2209	1.2209
2	1.8677	1.8677
3	1.4197	1.4197
4	0.1360	0.1360
5	-1.2298	1.2298
6	-1.8766	1.8766
7	-1.4280	1.4280
8	-0.1439	0.1439
9	1.2211	1.2211
Integral Summation	0.0034	0.9323

Table C-6: The components and magnitudes of the WSS at the sample node on the horizontal flat plate test case for fully oscillatory flow.

C.5.3 Script

The following Python script calculates the OSI

```
import TecUtil
import TecVals
from numpy import*
def TP_TAWSS():
        dt = 0.0125
        TecUtil.DataSetAddVar("Oscillatory Shear Index",None)
        novar4 = TecUtil.DataSetGetNumVars()
        info = TecUtil.ZoneGetInfo(1)
        node = range (1, info[0]+1)
        numzones = TecUtil.DataSetGetNumZones()
        zones = range(2,numzones)
        WSSvarnum = TecUtil.VarGetNumByName("Wall Shear Stress [Pa]")
        WSSXvarnum = TecUtil.VarGetNumByName("WallShearX")
        WSSYvarnum = TecUtil.VarGetNumByName("WallShearY")
```

```
WSSZvarnum = TecUtil.VarGetNumByName("WallShearZ")
WSSemparr = ([])
WSSXemparr = ([])
WSSYemparr = ([])
WSSZemparr = ([])
for i in node:
        WSST1 = TecUtil.DataValueGetByZoneVar(1, WSSvarnum, i)
        WSSTn = TecUtil.DataValueGetByZoneVar(numzones, WSSvarnum, i)
        WSSXT1 = TecUtil.DataValueGetByZoneVar(1, WSSXvarnum, i)
        WSSXTn = TecUtil.DataValueGetByZoneVar(numzones, WSSXvarnum, i)
        WSSYT1 = TecUtil.DataValueGetByZoneVar(1, WSSYvarnum, i)
        WSSYTn = TecUtil.DataValueGetByZoneVar(numzones, WSSYvarnum, i)
        WSSZT1 = TecUtil.DataValueGetByZoneVar(1, WSSZvarnum, i)
        WSSZTn = TecUtil.DataValueGetByZoneVar(numzones, WSSZvarnum, i)
        for j in zones:
                WSSTj = TecUtil.DataValueGetByZoneVar(j, WSSvarnum, i)
                WSSemparr.extend([WSSTj])
                WSSXTj = TecUtil.DataValueGetByZoneVar(j, WSSXvarnum, i)
                WSSXemparr.extend([WSSXTj])
                WSSYTj = TecUtil.DataValueGetByZoneVar(j, WSSYvarnum, i)
                WSSYemparr.extend([WSSYTj])
                WSSZTj = TecUtil.DataValueGetByZoneVar(j, WSSZvarnum, i)
                WSSZemparr.extend([WSSZTj])
        WSSTjsum = sum(WSSemparr)
        WSSXTjsum = sum(WSSXemparr)
        WSSYTjsum = sum(WSSYemparr)
        WSSZTjsum = sum(WSSZemparr)
        WSSTrap = (WSST1 + WSSTn)*(dt/2) + WSSTjsum*dt
        WSSXTrap = (WSSXT1 + WSSXTn)*(dt/2) + WSSXTjsum*dt
        WSSYTrap = (WSSYT1 + WSSYTn)*(dt/2) + WSSYTjsum*dt
        WSSZTrap = (WSSZT1 + WSSZTn)*(dt/2) + WSSZTjsum*dt
        TAWSS = (1/0.8)*WSSTrap
        MAGTAWSSV = sqrt( (WSSXTrap)**2 + (WSSYTrap)**2 + (WSSZTrap)**2 )
        OSI = 1-(MAGTAWSSV / WSSTrap)
        WSSemparr = ([])
        TecUtil.DataValueSetByZoneVar(1,novar4,i,OSI)
        WSSXemparr = ([])
        WSSYemparr = ([])
        WSSZemparr = ([])
```

C.6 Summary

The purpose of this appendix is to firstly describe the methodology employed in the calculation of the WSS-based variables. Sample calculations are then shown for each variable to demonstrate how it is actually computed by ANSYS CFX, Tecplot and/or the user implemented codes. Finally, a validation step is performed to ensure that the variable values are accurate thus demonstrating that the variables are being calculated as expected.

BIBLIOGRAPHY

[1] Allender, S., P. Scarborough, V. Peto, M. Raymer, J. Leal, R. Luengo-Fernandez and A. Gray, European cardiovascular disease statistics, *European Heart Network* (2008).

[2] Baim, D.S., D.E. Cutlip, M. Midei, T.J. Linnemeier, T. Schreiber, D. Cox, D. Kereiakes, J.J. Popma, L. Robertson, R. Prince, A.J. Lansky, K.K.L. Ho and R.E. Kuntz, Final results of a randomized trial comparing the MULTI-LINK stent with the Palmaz-Schatz stent for narrowings in native coronary arteries, *The American Journal of Cardiology* **87** (2001), 157-162.

[3] Baim, D.S., D.E. Cutlip, C.D. O'Shaughnessy, J.B. Hermiller, D.J. Kereiakes, A. Giambartolomei, S. Katz, A.J. Lansky, M. Fitzpatrick, J.J. Popma, K.K.L. Ho, M.B. Leon and R.E. Kuntz, Final results of a randomized trial comparing the NIR stent to the Palmaz-Schatz stent for narrowings in native coronary arteries, *The American Journal of Cardiology* **87** (2001), 152-156.

[4] Balossino, R., F. Gervaso, F. Migliavacca and G. Dubini, Effects of different stent designs on local hemodynamics in stented arteries, *Journal of Biomechanics* **41** (2008), 1053-1061.

[5] Banerjee, R.K., S.B. Devarakonda, D. Rajamohan and L.H. Back, Developed pulsatile flow in a deployed coronary stent, *Biorheology* **44** (2007), 91-102.

[6] Benard, N., D. Coisne, E. Donal and R. Perrault, Experimental study of laminar blood flow through an artery treated by a stent implantation: characterisation of intra-stent wall shear stress, *Journal of Biomechanics* **36** (2003), 991-998.

[7] Berry, J., A. Santamarina, J.E. Moore Jr, S. Roychowdhury and W. Routh, Experimental and computational flow evaluation of coronary stents, *Annals of Biomedical Engineering* **28** (2000), 386-398.

[8] Blasius, H., The boundary layers in fluids with little friction, *Maths and Physics* **56** (1908), 1-37.

[9] Bonert, M., R. Leask, J. Butany, C. Ethier, J. Myers, K. Johnston and M. Ojha, The relationship between wall shear stress distributions and intimal thickening in the human abdominal aorta, *BioMedical Engineering OnLine* **2** (2003), 18.

[10] Boutsianis, E., H. Dave, T. Frauenfelder, D. Poulikakos, S. Wildermuth, M. Turina, Y. Ventikos and G. Zund, Computational simulation of intracoronary flow based on real coronary geometry, *European Journal of Cardio-Thoracic Surgery* **26** (2004), 248-256.

[11] Bush, C.A., J.M. Ryan, A.R. Orsini and W.W. Hennemann, Coronary artery dilatation requiring high inflation pressure, *Catheterization and Cardiovascular Diagnosis* **22** (1991), 112-114.

[12] Butler, J., G.M. Rocker and S. Westaby, Inflammatory response to cardiopulmonary bypass, *Annals of Thoracic Surgery* **55** (1993), 552-559.

[13] Carlier, S.G., L.C.A. van Damme, C.P. Blommerde, J.J. Wentzel, G. van Langehove, S. Verheye, M.M. Kockx, M.W.M. Knaapen, C. Cheng, F. Gijsen, D.J. Duncker, N. Stergiopulos, C.J. Slager, P.W. Serruys and R. Krams, Augmentation of wall shear stress inhibits neointimal hyperplasia after stent implantation: inhibition through reduction of inflammation?, *Circulation* **107** (2003), 2741-2746.

[14] Cengel, Y.A. and J.M. Cimbala, Approximate solutions of the Navier-Stokes equation, in: *Fluid Mechanics: Fundamentals and Applications*, S. Jeans, ed, McGraw-Hill, New York, 2006, pp. 465-470.

[15] Centre-for-National-Health-Statistics, Online Article, Cardiovascular Procedure Statistics, 1979 - 2003, pp. 1 - 3.

[16] Chen, H.Y., J. Hermiller, A.K. Sinha, M. Sturek, L. Zhu and G.S. Kassab, Effects of stent sizing on endothelial and vessel wall stress:

potential mechanisms for in-stent restenosis, *Journal of Applied Physiology* **106** (2009), 1686-1691.

[17] Clowes, A.W. and M.M. Clowes, Kinetics of cellular proliferation after arterial injury. IV. Heparin inhibits rat smooth muscle mitogenesis and migration, *Circulation Research* **58** (1986), 839-845.

[18] Colombo, A., J. Drzewiecki, A. Banning, E. Grube, K. Hauptmann, S. Silber, D. Dudek, S. Fort, F. Schiele, K. Zmudka, G. Guagliumi and M.E. Russell, Randomized study to assess the effectiveness of slow- and moderate-release polymer-based paclitaxel-eluting stents for coronary artery lesions, *Circulation* **108** (2003), 788-794.

[19] Corwin, H.L., S.M. Sprague, G.A. DeLaria and M.J. Norusis, Acute renal failure associated with cardiac operations. A case-control study, *Journal of Thoracic Cardiovascular Surgery* **98** (1989), 1107-1112.

[20] Dawkins, K.D., E. Grube, G. Guagliumi, A.P. Banning, K. Zmudka, A. Colombo, L. Thuesen, K. Hauptman, J. Marco, W. Wijns, J.J. Popma, J. Koglin and M.E. Russell, Clinical efficacy of polymer-based paclitaxel-eluting stents in the treatment of complex, long coronary artery lesions from a multicenter, randomized trial: support for the use of drug-eluting stents in contemporary clinical practice, *Circulation* **112** (2005), 3306-3313.

[21] de Feyter, P.J., M. van den Brand, G.J. Laarman, R. van Domburg, P.W. Serruys, H. Suryapranata and G. Jaarman, Acute coronary artery occlusion during and after percutaneous transluminal coronary angioplasty. Frequency, prediction, clinical course, management, and follow-up [published erratum appears in Circulation 1991 Jul;84(1):446], *Circulation* **83** (1991), 927-936.

[22] DePaola, N., M.A. Gimbrone, P.F. Davies and C.F. Dewey, Vascular endothelium responds to fluid shear stress gradients, *Arteriosclerosis and Thrombosis* **12** (1992), 1254-1257.

[23] Detre, K.M., D.R. Holmes, Jr., R. Holubkov, M.J. Cowley, M.G. Bourassa, D.P. Faxon, G.R. Dorros, L.G. Bentivoglio, K.M. Kent and R.K. Myler, Incidence and consequences of periprocedural occlusion. The 1985-1986 national heart, lung, and blood institute percutaneous transluminal coronary angioplasty registry, *Circulation* **82** (1990), 739-750.

[24] Duraiswamy, N., *Effect of blood flow patterns on localized platelet adhesion under physiologic flow conditions using two-dimensional and three-dimensional stent models: an experimental and computational approach*, PhD Thesis, Florida International University, Florida, 2005.

[25] Duraiswamy, N., J.M. Cesar, R.T. Schoephoerster and J.E. Moore Jr, Effects of stent geometry on local flow dynamics and resulting platelet deposition in an in vitro model, *Biorheology* **45** (2008), 547-561.

[26] Duraiswamy, N., R.T. Schoephoerster and J.E. Moore Jr, Comparison of near-wall hemodynamic parameters in stented artery models, *Journal of Biomechanical Engineering* **131** (2009), 061006.

[27] Edelman, E.R. and C. Rogers, Pathobiologic responses to stenting, *American Journal of Cardiology* **81** (1998), 4E-6E.

[28] Encyclopedia-Britannica-Online, Electronic Article, Artheroscelerosis, 2010.

[29] Faik, I., R. Mongrain, R. Leask, J. Rodes-Cabau, E. Larose and O. Bertrand, Time-dependent 3D simulations of the hemodynamics in a stented coronary artery, *Biomedical Materials* **2** (2007), S28.

[30] Favaloro, R.G., D.B. Effler, L.K. Groves, D.J.G. Fergusson and J.S. Lozada, Double internal mammary artery-myocardial implantation: Clinical evaluation of results in 150 patients, *Circulation* **37** (1968), 549-555.

[31] Fischman, D.L., M.B. Leon, D.S. Baim, R.A. Schatz, M.P. Savage, I. Penn, K. Detre, L. Veltri, D. Ricci, M. Nobuyoshi, M. Cleman, R.

Heuser, D. Almond, P.S. Teirstein, R.D. Fish, A. Colombo, J. Brinker, J. Moses, A. Shaknovich, J. Hirshfeld, S. Bailey, S. Ellis, R. Rake and S. Goldberg, A randomized comparison of coronary-stent placement and balloon angioplasty in the treatment of coronary artery disease, *New England Journal of Medicine* **331** (1994), 496-501.

[32] Fontaine, A.B., D.G. Spigos, G. Eaton, S.D. Passos, G. Christoforidis, H. Khabiri and S. Jung, Stent-induced intimal hyperplasia: Are there fundamental differences between flexible and rigid stent designs?, *Journal of Vascular and Interventional Radiology* **5** (1994), 739-744.

[33] Frank, A.O., P.W. Walsh and J.E. Moore Jr, Computational fluid dynamics and stent design, *Artificial Organs* **26** (2002), 614-621.

[34] Garasic, J.M., E.R. Edelman, J.C. Squire, P. Seifert, M.S. Williams and C. Rogers, Stent and artery geometry determine intimal thickening independent of arterial injury, *Circulation* **101** (2000), 812-818.

[35] García, J., A. Crespo, J. Goicolea, M. Sanmartín and C. García, Study of the evolution of the shear stress on the restenosis after coronary angioplasty, *Journal of Biomechanics* **39** (2006), 799-805.

[36] Gaston, R.D., S.M. Gary, D.P. Augusto, M.K. Kenneth, F.S. Lowell, J.P. Jeffrey, S.C. Wong and B.L. Martin, Small stent size and intimal hyperplasia contribute to restenosis: A volumetric intravascular ultrasound analysis, *Journal of the American College of Cardiology* **26** (1995), 720-724.

[37] Gerald, M.F., P.K. Henryk, J.L. Alan, J.K. Wilbert, G.D. Hooper and R.B. Jeffrey, Coronary bypass graft fate and patient outcome: Angiographic follow-up of 5,065 grafts related to survival and reoperation in 1,388 patients during 25 years, *Journal of the American College of Cardiology* **28** (1996), 616-626.

[38] GlobalData, Global Coronary Stents Pipeline Analysis, Opportunity Assessment and Market Forecasts to 2016, 2010.

[39] Grube, E., S. Silber, K.E. Hauptmann, R. Mueller, L. Buellesfeld, U. Gerckens and M.E. Russell, TAXUS I: six- and twelve-month results from a randomized, double-blind trial on a slow-release paclitaxel-eluting stent for de novo coronary lesions, *Circulation* **107** (2003), 38-42.

[40] Gruentzig, A., Transluminal dialation of coronary-artery stenosis, *Lancet* **311** (1978), 263-263.

[41] Harnek, J., E. Zoucas, E. Carlemalm and W. Cwikiel, Differences in endothelial injury after balloon angioplasty, insertion of balloon-expanded stents or release of self-expanding stents: An electron microscopic experimental study, *Cardiovascular and Interventional Radiology* **22** (1999), 56-61.

[42] He, Y., N. Duraiswamy, A.O. Frank and J.E. Moore Jr, Blood flow in stented arteries: a parametric comparison of strut design patterns in three dimensions, *Journal of Biomechanical Engineering* **127** (2005), 637-647.

[43] Himburg, H.A., D.M. Grzybowski, A.L. Hazel, J.A. LaMack, X.-M. Li and M.H. Friedman, Spatial comparison between wall shear stress measures and porcine arterial endothelial permeability, *American Journal of Physiology: Heart and Circluatory Physiology* **286** (2004), H1916-1922.

[44] Hirsch, C., Numerical solutions of viscous laminar flows, in: *Numerical computation of internal and external flows*, Elsevier, 2007, pp. 618-625.

[45] Hoffmann, R., G.S. Mintz, G.R. Dussaillant, J.J. Popma, A.D. Pichard, L.F. Satler, K.M. Kent, J. Griffin and M.B. Leon, Patterns and mechanisms of in-stent restenosis: A serial intravascular ultrasound study, *Circulation* **94** (1996), 1247-1254.

[46] Holmes Jr, D.R., R.E. Vlietstra, H.C. Smith, G.W. Vetrovec, K.M. Kent, M.J. Cowley, D.P. Faxon, A.R. Gruentzig, S.F. Kelsey and K.M. Detre, Restenosis after percutaneous transluminal coronary angioplasty (PTCA): a report from the PTCA Registry of the National Heart, Lung,

and Blood Institute, *American Journal of Cardiology* **53** (1984), 77C-81C.

[47] Huittinen, T.S., *Chlamydia pneumoniae infection, inflammation and heat shock protein 60 immunity in asthma and coronary heart disease*, University of Oulu, 2003.

[48] Hyun, S., C. Kleinstreuer and J.P. Archie, Hemodynamics analyses of arterial expansions with implications to thrombosis and restenosis, *Medical Engineering & Physics* **22** (2000), 13-27.

[49] Iakovou, I., T. Schmidt, E. Bonizzoni, L. Ge, G.M. Sangiorgi, G. Stankovic, F. Airoldi, A. Chieffo, M. Montorfano, M. Carlino, I. Michev, N. Corvaja, C. Briguori, U. Gerckens, E. Grube and A. Colombo, Incidence, predictors, and outcome of thrombosis after successful implantation of drug-eluting stents, *Journal of the American Medical Association* **293** (2005), 2126-2130.

[50] Ischinger, T.A., R.J. Solar and E. Hitzke, Improved outcome with novel device for low-pressure PTCA in de novo and in-stent lesions, *Cardiovascular Radiation Medicine* **4** (2003), 2-6.

[51] Jang, I., G. Tearney and B. Bouma, Visualization of tissue prolapse between coronary stent struts by optical coherence tomography: comparison with intravascular ultrasound, *Circulation* **104** (2001), 2754.

[52] Jin, S., Y. Yang, J.N. Oshinski, A.R. Tannenbaum, J. Gruden and D.P. Giddens, Flow Patterns and Wall Shear Stress Distributions at Atherosclerotic-Prone Sites in a Human Left Coronary Artery - An Exploration Using Combined Methods of CT and Computational Fluid Dynamics, Georgia Institute of Technology, 2004.

[53] Kastrati, A., J. Mehilli, J. Dirschinger, F. Dotzer, H. Schuhlen, F.J. Neumann, M. Fleckenstein, C. Pfafferott, M. Seyfarth and A. Schomig, Intracoronary stenting and angiographic results: strut thickness effect on

restenosis outcome (ISAR-STEREO) trial, *Circulation* **103** (2001), 2816-2821.

[54] Kastrati, A., J. Mehilli, J. Dirschinger, J. Pache, K. Ulm, H. Schuhlen, M. Seyfarth, C. Schmitt, R. Blasini, F.J. Neumann and A. Schomig, Restenosis after coronary placement of various stent types, *American Journal of Cardiology* **87** (2001), 34-39.

[55] Kleinstreuer, C., S. Hyun, J.R. Buchanan, P.W. Longest, J.P. Archie and G.A. Truskey, Hemodynamic parameters and early intimal thickening in branching blood vessels, *Critical Reviews in Biomedical Engineering* **29** (2001), 1-64.

[56] Ku, D.N., D.P. Giddens, C.K. Zarins and S. Glagov, Pulsatile flow and atherosclerosis in the human carotid bifurcation. Positive correlation between plaque location and low oscillating shear stress, *Arteriosclerosis* **5** (1985), 293-302.

[57] Ku, D.N., Blood flow in arteries, *Annual Review of Fluid Mechanics* **29** (1997), 399 - 434.

[58] Kute, S.M. and D.A. Vorp, The effect of proximal artery flow on the hemodynamics at the distal anastomosis of a vascular bypass graft: computational study, *Journal of Biomechanical Engineering* **123** (2001), 277-283.

[59] LaDisa, J., L. Olson, H. Douglas, D. Warltier, J. Kersten and P. Pagel, Alterations in regional vascular geometry produced by theoretical stent implantation influence distributions of wall shear stress: analysis of a curved coronary artery using 3D computational fluid dynamics modeling, *BioMedical Engineering OnLine* **5** (2006), 40.

[60] LaDisa, J.F., I. Guler, L.E. Olson, D.A. Hettrick, J.R. Kersten, D.C. Warltier and P.S. Pagel, Three-dimensional computational fluid dynamics modeling of alterations in coronary wall shear stress produced

by stent implantation, *Annals of Biomedical Engineering* **31** (2003), 972-980.

[61] LaDisa, J.F., L.E. Olson, I. Guler, D.A. Hettrick, S.H. Audi, J.R. Kersten, D.C. Warltier and P.S. Pagel, Stent design properties and deployment ratio influence indexes of wall shear stress: a three-dimensional computational fluid dynamics investigation within a normal artery, *Journal of Applied Physiology* **97** (2004), 424-430.

[62] LaDisa, J.F., L. Olson, D. Hettrick, D. Warltier, J. Kersten and P. Pagel, Axial stent strut angle influences wall shear stress after stent implantation: analysis using 3D computational fluid dynamics models of stent foreshortening, *BioMedical Engineering OnLine* **4** (2005), 59.

[63] LaDisa, J.F., L.E. Olson, I. Guler, D.A. Hettrick, J.R. Kersten, D.C. Warltier and P.S. Pagel, Circumferential vascular deformation after stent implantation alters wall shear stress evaluated with time-dependent 3D computational fluid dynamics models, *Journal of Applied Physiology* **98** (2005), 947-957.

[64] LaDisa, J.F., L.E. Olson, R.C. Molthen, D.A. Hettrick, P.F. Pratt, M.D. Hardel, J.R. Kersten, D.C. Warltier and P.S. Pagel, Alterations in wall shear stress predict sites of neointimal hyperplasia after stent implantation in rabbit iliac arteries, *American Journal of Physiology: Heart and Circluatory Physiology* **288** (2005), H2465-2475.

[65] Lally, C., F. Dolan and P.J. Prendergast, Cardiovascular stent design and vessel stresses: a finite element analysis, *Journal of Biomechanics* **38** (2005), 1574-1581.

[66] Langseth, L., Oxidants, antioxidants and disease prevention, *Monograph of the International Life Science Institute*, Belgium, 1996.

[67] Lansky, A.J., G.S. Roubin, C.D. O'Shaughnessy, P.B. Moore, L.S. Dean, A.E. Raizner, R.D. Safian, J.P. Zidar, J.L. Kerr, J.J. Popma, R. Mehran, R.E. Kuntz and M.B. Leon, Randomized comparison of GR-II stent and

Palmaz-Schatz stent for elective treatment of coronary stenoses, *Circulation* **102** (2000), 1364-1368.

[68] Lei, M., C. Kleinstreuer and G.A. Truskey, A focal stress gradient-dependent mass transfer mechanism for atherogenesis in branching arteries, *Medical Engineering and Physics* **18** (1996), 326-332.

[69] Lin, E.C., R.P. Bredeweg and P.L. Sicuro, Coronary CT angiography, *Medscape article*, 2010.

[70] Longest, P.W. and C. Kleinstreuer, Computational haemodynamics analysis and comparison study of arterio-venous grafts, *Journal of Medical Engineering and Technology* **24** (2000), 102-110.

[71] Malek, A. and S. Izumo, Physiological fluid shear stress causes down regulation of endothelin-1 mRNA in bovine aortic endothelium, *American Journal of Physiology: Cell Physiology* **263** (1992), C389-396.

[72] Malek, A.M., S.L. Alper and S. Izumo, Hemodynamic shear stress and its role in atherosclerosis, *Journal of the American Medical Association* **282** (1999), 2035-2042.

[73] McFadden, E.P., E. Stabile, E. Regar, E. Cheneau, A.T.L. Ong, T. Kinnaird, W.O. Suddath, N.J. Weissman, R. Torguson, K.M. Kent, A.D. Pichard, L.F. Satler, R. Waksman and P.W. Serruys, Late thrombosis in drug-eluting coronary stents after discontinuation of antiplatelet therapy, *Lancet* **364** (2004), 1519-1521.

[74] Mehran, R., G. Dangas, A.S. Abizaid, G.S. Mintz, A.J. Lansky, L.F. Satler, A.D. Pichard, K.M. Kent, G.W. Stone and M.B. Leon, Angiographic patterns of in-stent restenosis: classification and implications for long-term outcome, *Circulation* **100** (1999), 1872-1878.

[75] Mintz, G.S., J.J. Popma, A.D. Pichard, K.M. Kent, L.F. Satler, S. Chiu Wong, M.K. Hong, J.A. Kovach and M.B. Leon, Arterial remodeling after coronary angioplasty: A serial intravascular ultrasound study, *Circulation* **94** (1996), 35-43.

[76] Morice, M.-C., P.W. Serruys, J.E. Sousa, J. Fajadet, E. Ban Hayashi, M. Perin, A. Colombo, G. Schuler, P. Barragan, G. Guagliumi, F. Molnar, R. Falotico and R.S.G. the, A randomized comparison of a sirolimus-eluting stent with a standard stent for coronary revascularization, *New England Journal of Medicine* **346** (2002), 1773-1780.

[77] Moses, J.W., M.B. Leon, J.J. Popma, P.J. Fitzgerald, D.R. Holmes, C. O'Shaughnessy, R.P. Caputo, D.J. Kereiakes, D.O. Williams, P.S. Teirstein, J.L. Jaeger and R.E. Kuntz, Sirolimus-eluting stents versus standard stents in patients with stenosis in a native coronary artery, *New England Journal of Medicine* **349** (2003), 1315-1323.

[78] Mudra, H., E. Regar, V. Klauss, F. Werner, K.-H. Henneke, E. Sbarouni and K. Theisen, Serial follow-up after optimized ultrasound-guided deployment of Palmaz-Schatz stents: In-stent neointimal proliferation without significant reference segment response, *Circulation* **95** (1997), 363-370.

[79] Murphy, J. and F. Boyle, Application of advanced computational modelling in the numerical prediction of the haemodynamic impact of coronary stent implantation, *Proceedings of the 6th world scientific and engineering academy and society international conference on applied computer science*, Puerto de la Cruz, Tenerife, 2006.

[80] Murphy, J. and F. Boyle, Evaluation of stent design based on the haemodynamic effect of coronary stenting, *Proceedings of the 13th bioengineering in Ireland conference*, Fermanagh, Ireland, 2007.

[81] Murphy, J. and F. Boyle, Application of advanced three-dimensional modelling to compare flow disturbances induced by implantation of the Palmaz-Schatz and Gianturco-Roubin II coronary stents, *Proceeding of the 5th international conference on biomedical engineering* Innsbruck, Austria, 2007.

[82] Murphy, J. and F. Boyle, Comparison of stent design using computational fluid dynamics, *Proceedings of the 10th annual sir Bernard Crossland symposium*, Galway, Ireland, 2007.

[83] Murphy, J. and F. Boyle, Assessment of the effects of increasing levels of physiological realism in the computational fluid dynamics analyses of implanted coronary stents., *Proceedings of the Engineering in Medicine and Biology Society, 30th Annual International Conference of the IEEE*, Vancouver, 2008, pp. 5906-5909.

[84] Murphy, J. and F. Boyle, Evolution of a computational domain for numerical analysis of fluid mechanical disturbance induced by coronary stent deployment, *Proceedings of the 14th bioengineering in Ireland conference*, Sligo, Ireland, 2008.

[85] Murphy, J. and F. Boyle, Development of a three-dimensional prolapse model to simulate physiological haemodynamics in a stented coronary artery, *Proceedings of the 6th international conference on biomedical engineering*, Innsbruck, Austria, 2008.

[86] Murphy, J. and F. Boyle, Comparing stent design using computational fluid dynamics to predict wall shear stress based parameters, *Proceedings of the 15th bioengineering in Ireland conference*, Limerick, Ireland, 2009.

[87] Murphy, J. and F. Boyle, A full-range, multi-variable, CFD-based methodology to identify abnormal near-wall haemodynamics in a stented coronary artery, *Biorheology* **47** (2010), 1-16.

[88] Murphy, J. and F. Boyle, A numerical methodology to fully elucidate the altered wall shear stress in a stented coronary artery, *Cardiovascular Engineering and Technology* **1** (2010), 256-268.

[89] Murphy, J. and F. Boyle, A multi-variable analysis of transient near-wall haemodynamics in a stented coronary artery, *Proceedings of the 16th bioengineering in Ireland conference*, Dublin, Ireland, 2010.

[90] Murphy, J. and F. Boyle, Predicting neointimal hyperplasia in stented arteries using time-dependant computational fluid dynamics: A review, *Computers in Biology and Medicine* **40** (2010), 408-418.

[91] Nichols, W.W. and M.F. O'Rourke, The coronary circulation, in: *McDonald's blood flow in arteries theoretical, experimental and clinical principles*, J. Koster, S. Burrows and N. Wilkinson, eds, Hodder Arnold, London, 2005, pp. 326-327.

[92] Ojha, M., Spatial and temporal variations of wall shear stress within an end-to-side arterial anastomosis model, *Journal of Biomechanics* **26** (1993), 1377-1388.

[93] Pache, J.U., A. Kastrati, J. Mehilli, H. Schuhlen, F. Dotzer, J.O. Hausleiter, M. Fleckenstein, F.J. Neumann, U. Sattelberger, C. Schmitt, M. Muller, J. Dirschinger and A. Schomig, Intracoronary stenting and angiographic results: strut thickness effect on restenosis outcome (ISAR-STEREO-2) trial, *Journal of the American College of Cardiology* **41** (2003), 1283-1288.

[94] Pfisterer, M.E., Late stent thrombosis after drug-eluting stent implantation for acute myocardial infarction: A new red flag is raised, *Circulation* **118** (2008), 1117-1119.

[95] Popma, J.J., R.M. Califf and E.J. Topol, Clinical trials of restenosis after coronary angioplasty, *Circulation* **84** (1991), 1426-1436.

[96] Prandtl, L., Fluid flow in very little friction, *Third International Mathematical Congress*, Germany, 1904.

[97] Prendergast, P.J., C. Lally, S. Daly, A.J. Reid, T.C. Lee, D. Quinn and F. Dolan, Analysis of prolapse in cardiovascular stents: a constitutive equation for vascular tissue and finite-element modelling, *Journal of Biomechanical Engineering* **125** (2003), 692-699.

[98] Prosi, M., K. Perktold, Z. Ding and M.H. Friedman, Influence of curvature dynamics on pulsatile coronary artery flow in a realistic bifurcation model, *Journal of Biomechanics* **37** (2004), 1767-1775.

[99] Rajamohan, D., R.K. Banerjee, L.H. Back, A.A. Ibrahim and M.A. Jog, Developing pulsatile flow in a deployed coronary stent, *Journal of Biomechanical Engineering* **128** (2006), 347-359.

[100] Release-Notes-ANSYS(12.0), Discretisation and Solution Theory, *ANSYS CFX-Solver Release 12.0: Theory*, pp. 243-245.

[101] Release-Notes-ANSYS(12.0), Basic Solver Capability Theory, *ANSYS CFX Release 12.0*, pp. 56-58.

[102] Rensing, B.J., W.R. Hermans, B.H. Strauss and P.W. Serruys, Regional differences in elastic recoil after percutaneous transluminal coronary angioplasty: A quantitative angiographic study, *Journal of the American College of Cardiology* **17** (1991), 34-38.

[103] Rogers, C. and E.R. Edelman, Endovascular stent design dictates experimental restenosis and thrombosis, *Circulation* **91** (1995), 2995-3001.

[104] Rogers, C., S. Parikh, P. Seifert and E.R. Edelman, Endogenous cell seeding: Remnant endothelium after stenting enhances vascular repair, *Circulation* **94** (1996), 2909-2914.

[105] Rogers, C., F.G.P. Welt, M.J. Karnovsky and E.R. Edelman, Monocyte recruitment and neointimal hyperplasia in rabbits: coupled inhibitory effects of heparin, *Arteriosclerosis Thrombosis and Vascular Biology* **16** (1996), 1312-1318.

[106] Schampaert, E., E.A. Cohen, M. Schluter, F. Reeves, M. Traboulsi, L.M. Title, R.E. Kuntz and J.J. Popma, The Canadian study of the sirolimus-eluting stent in the treatment of patients with long de novo lesions in small native coronary arteries (C-SIRIUS), *Journal of the American College of Cardiology* **43** (2004), 1110-1115.

[107] Schofer, J., M. Schlüter, A.H. Gershlick, W. Wijns, E. Garcia, E. Schampaert and G. Breithardt, Sirolimus-eluting stents for treatment of patients with long atherosclerotic lesions in small coronary arteries: double-blind, randomised controlled trial (E-SIRIUS), *The Lancet* **362** (2003), 1093-1099.

[108] Schulz, C., R.A. Herrmann, C. Beilharz, J. Pasquantonio and E. Alt, Coronary stent symmetry and vascular injury determine experimental restenosis, *Heart* **83** (2000), 462 - 467.

[109] Schwartz, R.S., K.C. Huber, J.G. Murphy, W.D. Edwards, A.R. Camrud, R.E. Vlietstra and D.R. Holmes, Restenosis and the proportional neointimal response to coronary artery injury: results in a porcine model, *Journal of the American College of Cardiology* **19** (1992), 267-274.

[110] Schwartz, R.S., Cellular mechanisms of restenosis: conventional dogma and novel theory, in: *Handbook of drug-eluting stents*, P.W. Serruys and A.H. Gershlick, eds, Taylor and Francis, London, 2005.

[111] Seo, T., L.G. Schachter and A.I. Barakat, Computational study of fluid mechanical disturbance induced by endovascular stents, *Annals of Biomedical Engineering* **33** (2005), 444-456.

[112] Serruys, P.W., P. de Jaegere, F. Kiemeneij, C. Macaya, W. Rutsch, G. Heyndrickx, H. Emanuelsson, J. Marco, V. Legrand, P. Materne, J. Belardi, U. Sigwart, A. Colombo, J.J. Goy, P. van den Heuvel, J. Delcan and M. Morel, A comparison of balloon-expandable-stent implantation with balloon angioplasty in patients with coronary artery disease, *New England Journal of Medicine* **331** (1994), 489-495.

[113] Serruys, P.W., B. van Hout, H. Bonnier, V. Legrand, E. Garcia, C. Macaya, E. Sousa, W. van der Giessen, A. Colombo, R. Seabra-Gomes, F. Kiemeneij, P. Ruygrok, J. Ormiston, H. Emanuelsson, J. Fajadet, M. Haude, S. Klugmann and M. Morel, Randomised comparison of implantation of heparin-coated stents with balloon angioplasty in

selected patients with coronary artery disease (Benestent II), *The Lancet* **352** (1998), 673-681.

[114] Serruys, P.W., M. Degertekin, K. Tanabe, A. Abizaid, J.E. Sousa, A. Colombo, G. Guagliumi, W. Wijns, W.K. Lindeboom, J. Ligthart, P.J. de Feyter and M. Morice, Intravascular ultrasound findings in the multicenter, randomized, double-blind RAVEL (randomized study with the sirolimus-eluting velocity balloon-expandable stent in the treatment of patients with de novo native coronary artery lesions) trial, *Circulation* **106** (2002), 798-803.

[115] Shroyer, A.L., F.L. Grover, B. Hattler, J.F. Collins, G.O. McDonald, E. Kozora, J.C. Lucke, J.H. Baltz and D. Novitzky, On-pump versus off-pump coronary-artery bypass surgery, *New England Journal of Medicine* **361** (2009), 1827-1837.

[116] Sigwart, U., J. Puel, V. Mirkovitch, F. Joffre and L. Kappenberger, Intravascular stents to prevent occlusion and restenosis after transluminal angioplasty, *New England Journal of Medicine* **316** (1987), 701-706.

[117] Smedby, O., J. Johansson, J. Molgaard, A.G. Olsson, G. Walldius and U. Erikson, Predilection of atherosclerosis for the inner curvature in the femoral artery: A digitized angiography study, *Arteriosclerosis, Thrombosis, and Vascular Biology* **15** (1995), 912-917.

[118] Stemerman, M.B., T.H. Spaet, F. Pitlick, J. Cintron, I. Lejnieks and M.L. Tiell, Intimal healing. The pattern of reendothelialization and intimal thickening, *American Journal of Pathology* **87** (1977), 125-142.

[119] Stokes, G.G., On the theories of internal friction of fluids in motion, *Transactions of the Cambridge Philosophical Society* **8** (1845), 287-305.

[120] Stone, G.W., S.G. Ellis, D.A. Cox, J. Hermiller, C. O'Shaughnessy, J.T. Mann, M. Turco, R. Caputo, P. Bergin, J. Greenberg, J.J. Popma and M.E. Russell, A polymer-based, paclitaxel-eluting stent in patients with

coronary artery disease, *New England Journal of Medicine* **350** (2004), 221-231.

[121] Stone, G.W., M. Midei, W. Newman, M. Sanz, J.B. Hermiller, J. Williams, N. Farhat, K.W. Mahaffey, D.E. Cutlip, P.J. Fitzgerald, P. Sood, X. Su and A.J. Lansky, Comparison of an everolimus-eluting stent and a paclitaxel-eluting stent in patients with coronary artery disease: A randomized trial, *Journal of American Medical Association* **299** (2008), 1903-1913.

[122] Takagi, H., M. Matsui and T. Umemoto, Off-pump coronary artery bypass may increase late mortality: A meta-analysis of randomized trials, *Annals of Thoracic Surgery* **89** (2010), 1881-1888.

[123] Tardy, Y., N. Resnick, T. Nagel, M.A. Gimbrone, Jr. and C.F. Dewey, Jr., Shear stress gradients remodel endothelial monolayers in vitro via a cell proliferation-migration-loss cycle, *Arteriosclerosis, Thrombosis, and Vascular Biology* **17** (1997), 3102-3106.

[124] The Writing Group for the Bypass Angioplasty Revascularization Investigation, Five-year clinical and functional outcome comparing bypass surgery and angioplasty in patients with multivessel coronary disease: A multicenter randomized trial, *Journal of the American Medical Association* **277** (1997), 715-721.

[125] Thomas, J.P., P.G. Geiger and A.W. Girotti, Lethal damage to endothelial cells by oxidized low density lipoprotein: role of selenoperoxidases in cytoprotection against lipid hydroperoxide- and iron-mediated reactions, *Journal of Lipid Research* **34** (1993), 479-490.

[126] Thury, A., J.J. Wentzel, R.V.H. Vinke, F.J.H. Gijsen, J.C.H. Schuurbiers, R. Krams, P.J. de Feyter, P.W. Serruys and C.J. Slager, Focal in-stent restenosis near step-up: roles of low and oscillating shear stress, *Circulation* **105** (2002), 185-187.

[127] Toutouzas, K., A. Colombo and C. Stefanadis, Inflammation and restenosis after percutaneous coronary interventions, *European Heart Journal* **25** (2004), 1679-1687.

[128] Tuman, K.J., R.J. McCarthy, H. Najafi and A.D. Ivankovich, Differential effects of advanced age on neurologic and cardiac risks of coronary artery operations, *Journal of Thoracic and Cardiovascular Surgery* **104** (1992), 1510-1517.

[129] Turco, M.A., J.A. Ormiston, J.J. Popma, L. Mandinov, C.D. OShaughnessy, T. Mann, T.F. McGarry, C.-J. Wu, C. Chan, M.W.I. Webster, J.J. Hall, G.J. Mishkel, L.A. Cannon, D.S. Baim and J. Koglin, Polymer-based, paclitaxel-eluting TAXUS Liberte stent in de novo lesions: The pivotal TAXUS ATLAS trial, *Journal of the American College of Cardiology* **49** (2007), 1676-1683.

[130] Vanhoutte, P.M., Endothelial dysfunction the first step toward coronary arteriosclerosis, *Circulation Journal* **73** (2009), 595-601.

[131] Waller, B.F. and C.A. Pinkerton, Coronary balloon angioplasty restenosis: pathogenesis and treatment strategies from a morphological perspective, *Journal of Interventional Cardiology* **2** (1989), 167-178.

[132] Waller, B.F., C.M. Orr, J. Vantassel, T. Peters, E. Fry, J. Hermiller and L.D. Grider, Coronary artery and saphenous vein graft remodeling: A review of histologic findings after various interventional procedures - Part IV, *Clinical Cardiology* **19** (1996), 960-966.

[133] Wentzel, J.J., D.M. Whelan, W.J. van der Giessen, H.M. van Beusekom, I. Andhyiswara, P.W. Serruys, C.J. Slager and R. Krams, Coronary stent implantation changes 3-D vessel geometry and 3-D shear stress distribution, *Journal of Biomechanics* **33** (2000), 1287 - 1295.

[134] Wentzel, J.J., R. Krams, J.C.H. Schuurbiers, J.A. Oomen, J. Kloet, W.J. van der Giessen, P.W. Serruys and C.J. Slager, Relationship between

neointimal thickness and shear stress after wallstent implantation in human coronary arteries, *Circulation* **103** (2001), 1740-1745.

[135] Yoshitomi, Y., S. Kojima, M. Yano, T. Sugi, Y. Matsumoto, M. Saotome, K. Tanaka, M. Endo and M. Kuramochi, Does stent design affect probability of restenosis? A randomized trial comparing Multilink stents with GFX stents, *American Heart Journal* **142** (2001), 445 - 451.

[136] Young, D.F., Effect of a time dependant stenosis on flow through a tube, *Journal of Engineering for Industry* **90** (1968), 7.

[137] Zacharias, A., R.H. Habib, T.A. Schwann, C.J. Riordan, S.J. Durham and A. Shah, Improved survival with radial artery versus vein conduits in coronary bypass surgery with left internal thoracic artery to left anterior descending artery grafting, *Circulation* **109** (2004), 1489-1496.

[138] Zarins, C.K., D.P. Giddens, B.K. Bharadvaj, V.S. Sottiurai, R.F. Mabon and S. Glagov, Carotid bifurcation atherosclerosis. Quantitative correlation of plaque localization with flow velocity profiles and wall shear stress, *Circulation Research* **53** (1983), 502-514.